CFD Simulations and Thermal Design for Application to Compressed Air Energy Storage

A THESIS
SUBMITTED TO THE FACULTY OF
UNIVERSITY OF MINNESOTA
BY

Chao Zhang

IN PARTIAL FULFILLMENT OF THE REQUIREMENTS
FOR THE DEGREE OF
DOCTOR OF PHILOSOPHY/EDUCATION

Terrence W. Simon, Adviser

June 2015

Acknowledgements

I would like to thank NSF (Grant number: NSF EFRI-1038294) and the University of Minnesota Institute of Renewable Energy and Environment for funding this project. I would also like to thank the Minnesota Supercomputing Institute for the computational resources.

It was a great learning experience studying in the Ph.D. program in the Mechanical Engineering Department at the University of Minnesota working with Prof. Terrence Simon. Regular meetings and discussions with Prof. Simon greatly helped me enhance my knowledge in the field of fluid mechanics and heat transfer as well as applying the knowledge to solve engineering problems. Prof. Simon's patience and engaging approach in discussing research related issues taught me the importance of being patient and perseverant while conducting research.

I would also like to thank Prof. Perry Li and Prof. James Van de Ven for their encouraging discussions and comments on my presentations, papers, and reports during my Ph.D. study, which greatly helped me improve my academic skills. I also thank Prof. Krishnan Mahesh for giving me valuable comments on my research program and teaching me a course in fluid mechanics which was important for conducting this research.

Working on the Compressed Air Energy Storage Project required a team of efficient and capable students. I would like to thank Bo Yan, Jacob Wieberdink, Mohsen Sadaat, Shawn Wilhelm, Hao Tian, and Pieter Gagnon for their collaboration and providing valuable ideas from different perspectives.

To all of my other friends and family, thank you for your encouragement and support. Special thanks go to my parents, Ying and Zhengquan, for giving me the genes and for everything they have done to prepare me for a life of service.

Abstract

The present computational research focuses on fluid flow analysis and heat transfer enhancement in support of the design of a hydraulic Compressed Air Energy Storage (CAES) system. A CAES system compresses air to high pressure during high power generation periods, stores the compressed air, and expands it to generate power during high power demand periods. The main benefit of using CAES is that it overcomes the mismatch between power generation and power demand. An innovative liquid piston method is used in the present research, where liquid (water) is pumped into the lower section of a compression chamber, and the gas (air) is compressed by the rising liquid-gas interface.

Important to the efficient operation of CAES is reducing the temperature rise during compression. The work input process for compressing the air requires two main steps. In the first step, compression work compresses the air to a high pressure. The air temperature rises during compression, and this leads to a second step, where the compressed air cools. In order to maintain the work potential, the pressure of the compressed air is maintained during cooling, volume decreases and cooling work is done. As a result, higher temperature rise during compression requires greater amount of total work input for a given amount of air and a given pressure ratio. For similar reasons, it is also desirable to reduce the temperature drop during expansion of compressed air. The use of a liquid piston offers opportunities to insert heat exchanger matrices into the compression chamber to improve heat transfer. Computational Fluid Dynamics (CFD) and design analyses on the heat exchangers are done in the present research.

Two main types of heat exchangers, a commercially available, open-cell metal foam and an in-house designed interrupted plate matrix, are investigated, mainly through computational methods, and with experimental validations. CFD modeling of the liquid piston chamber inserted with exchanger matrices requires closure models that characterize the heat transfer and flow resistance characteristics of the heat exchanger elements. For the metal foam matrix, characterization is done by measuring the flow pressure drop and comparing existing heat transfer models to a liquid piston experiment. For the interrupted

plate matrix, large numbers of CFD simulations on the unit cells of the exchanger and experiments are applied for developing correlations for these terms. Based on the unit cell simulations, models for three-dimensionally anisotropic heat transfer behavior of porous media have been developed. Using these models, 3-D global-scale CFD simulations of the liquid piston chamber have been done. As the liquid chamber represents an application of two-phase flow through porous media, the simulation combines a VOF (Volume of Fluid) method and a two-energy-equation modeling method for porous media.

The choice of the interrupted plate matrix offers flexibility to vary the shape (e.g. plate height, thickness and separation distance) based on an optimum design to further improve CAES efficiency. Design sensitivity analyses typically require large numbers of computational runs and would demand extraordinary computational resources if combined with 2-D or 3-D CFD simulations. Developed in the present research is a simplified, one-dimensional (1-D) code that is much less computationally expensive, and preserves the main physics of the two-phase flow in porous media. The 1-D code is used for the design analysis of the heat exchanger shape distribution along the axial direction of the chamber.

CFD Simulations have been done to also compare a no-insert chamber to chambers with exchanger inserts, for both compression and expansion processes. The expansion process allows the expanding compressed gas to push the liquid out of the chamber to generate power. It is shown that in both the compression and expansion processes, using a heat exchanger matrix in the liquid piston chamber can significantly reduce the rise or drop in gas temperature, thus reducing the losses. Using the CFD modeling tools, a design exploration is also done to investigate the effect of changing the profile of the chamber's cross sectional radius along the axial direction to design a gourd-like shaped chamber to agitate flow and enhance heat transfer.

Table of Contents

List of Tables

List of Figures

Nomenclature

a_V	surface area per volume	(/m)
b	inertial coefficient	(/m)
b_{f1}	anisotropic inertial coefficient for x direction	(/m)
b_{f2}	anisotropic inertial coefficient for y direction	(/m)
b_{f3}	anisotropic inertial coefficient for z direction	(/m)
$\bar{\bar{b}}$	anisotropic inertial matrix	(/m)
$\mathscr{b}$	half distance between plates	(m)
c	specific heat	(J/(kgK))
$\mathcal{D}$	mass diffusivity	()
d_1, d_2	coefficients for mixing effect on heat transfer	(-)
E_s	storage energy	(J)
f_1, f_2	coefficients for mixing effect on heat transfer	(-)
H	pressure resistance term due to mixing effects	(-)
h	surface heat transfer coefficient	(W/(m^{2}K))
h_V	volumetric heat transfer coefficient	(W/(m^{3}K))
K	permeability	(m^2)
k	thermal conductivity	(W/(mK))
k_{eff}	effective thermal conductivity	(W/(mK))
L	characteristic pores size	(m)
$\mathbb{L}$	chamber length	(m)
ℓ	plate length	(m)
M	molecular weight	(kg/mol)
m	mass	(kg)
n	polytropic exponent	
Nu	Nusselt number	(-)
P	averaged pressure	(Pa)
P_f	final pressure	(Pa)
$\mathscr{p}$	periodic pore-scale pressure	(Pa)
p	local pressure of flow	(Pa)
Pr	Prandtl number	(-)
R	radius	(m)
$\Re$	ideal gas constant	(J/(kgK))
Re	Reynolds number	(-)

$\vec{S}_m$	momentum source term	(Pa/m)
T	temperature	(K)
t	time	(s)
t_f	final time	(s)
t	thickness	(m)
U_p	piston speed	(m/s)
u	velocity	(m/s)
V	air volume	(m^3)
V_f	final air volume	(m^3)
W_{in}	work input	(J)
Y	mass concentration of a species	(-)

Greek symbols

α	angle between mean velocity vector and x axis	(-)
β	angle between mean velocity vector and y axis	(-)
γ	angle between mean velocity vector and z axis	(-)
ϵ	porosity	(-)
η	efficiency	(-)
θ	angle between mean velocity vector and xOy plain	(-)
κ	turbulence kinetic energy	(W/(mK))
μ	viscosity	(Pa s)
ρ	density	(kg/m^3)
τ	shear stress	(Pa)
φ	angle between the projection of mean velocity vector on the xOy plane and x axis	(-)
χ	a symbol representing a flow variable (velocity, temperature or pressure)	

subscript

a	air
f	fluid
REV	representative elementary volume
REV, f	fluid region of a representative elementary volume
s	solid

v	vapor

superscript

f	fluid region
s	solid region
*	dimensionless variable

Chapter 1: Introduction

A mismatch between power generation and demand often exists in power generation systems. To overcome this mismatch, the Compressed Air Energy Storage (CAES) approach can be used, by integrating it into a power generation system, e.g. a wind farm. An isothermal CAES system has a theoretical thermodynamics efficiency of 100%, if perfect heat transfer between the compressed gas and the heat exchange media is achieved. However, in practice, temperature rise during compression and temperature drop during expansion are unavoidable. Enhancing heat transfer during compression of the gas to achieve a near-isothermal CAES process is a key to improve efficiency. The present study provides insight to the physical processes and numerical models for heat transfer and thermal design analyses for application to Compressed Air Energy Storage (CAES). In this chapter, literature with regard to CAES, heat transfer enhancement, and numerical modeling of heat exchanger matrices will be discussed.

1.1. Compressed Air Energy Storage (CAES)

Using the CAES approach, excess amount of energy is stored during low power demand periods by compressing air and storing the pressurized air, and this energy is extracted by expanding the compressed air during high power demand periods. The CAES approach for application to a wind energy power plant has been modeled, with regard to two scenarios, the “business-as-usual,” and the “20% penetration of wind by 2030” [1]. It shows that, in the “business-as-usual” scenario, with the addition of CAES, the energy capacity can be increased to 351GW in 2050, compared to 302GW without storage. In the “20% penetration of wind by 2030” scenario, the electricity price can be lowered with the addition of CAES. The study concluded that the CAES method is more economically advantageous than hydroelectric pump storage (HPS) and batteries.

Two large-scale CAES plants have been built in the world, one in Huntorf, Germany [2], and the other in Mclntosh, Alabama [3], both storing the compressed air in underground caverns and burning it in combustion turbines for work extraction. The Huntorf plant has

a power of 320MW over 2 hours of operation, and an efficiency of 42%; the Mclntosh plant has a power of 110MW over 26 hours of operation, and a higher efficiency as it recovers the waste heat from the combustion turbine exhaust to preheat the compressed air. A newer CAES system uses multi-stage compressors with inter-cooling between stages, and multi-stage expansion turbines to enhance heat transfer, which, as a result, made effective improvements on the cost, storage power, and NOx emission [4].

An open accumulator design [5] and a liquid piston concept [6] enabled the design of a novel CAES system that uses hydraulics to transmit mechanical power from the energy source, and to compress air using a liquid piston. After compression, the pressurized air is stored in open accumulators. Accumulators in general are used in fluid power applications to store energy by compressing gas in a chamber. Conventional accumulators are closed such that the gas is always inside the accumulator, and the energy density is thus restricted by the volume of the accumulator. In the open accumulator, however, the gas is allowed to enter and exit the accumulator chamber during compression and expansion cycles. As a result, the storage energy density is improved by an order of magnitude [5]. The liquid piston is created by pumping liquid into the lower section of a chamber and utilizing the rising water-air interface as a piston surface to compress air. It has been shown that liquid piston compressors have an advantage over solid pistons in terms of efficiency and work consumption of the pump [6]. Further, a liquid piston compressor is compatible with the use of heat transfer matrices inside the compressor to cool the gas, as liquid can flow through the matrix gaps. A fluid-power-driven CAES system that utilizes the open accumulator and the liquid piston also has the advantage of zero-emission, since no combustion turbine is used.

A practical perspective of the hydraulic CAES system is that it can be integrated into offshore wind power generation systems using the vastly available sea water, as in the U.S., the country's most electric-demanding places are near the coasts. According to the U. S. Offshore Wind Collaborative [7], the total amount of U. S. offshore wind energy capacity is almost equal to the current total installed capacity.

A concept design of a CAES system employing hydraulic components, open accumulators, and liquid piston chambers was presented in [8]. The main components of this system are shown in Fig.1.1. When electricity demand is small, the system operates in a storage mode; the mechanical power input on the wind turbine is transmitted through hydraulic transformers consisting of specialized hydraulic pumps and valves to the liquid piston chamber to compress air. The compressed air is stored in the open accumulator. When electricity demand is high, the system switches to generation mode; the compressed air is withdrawn from the open accumulator and is expanded in the liquid piston chamber to generate power output.

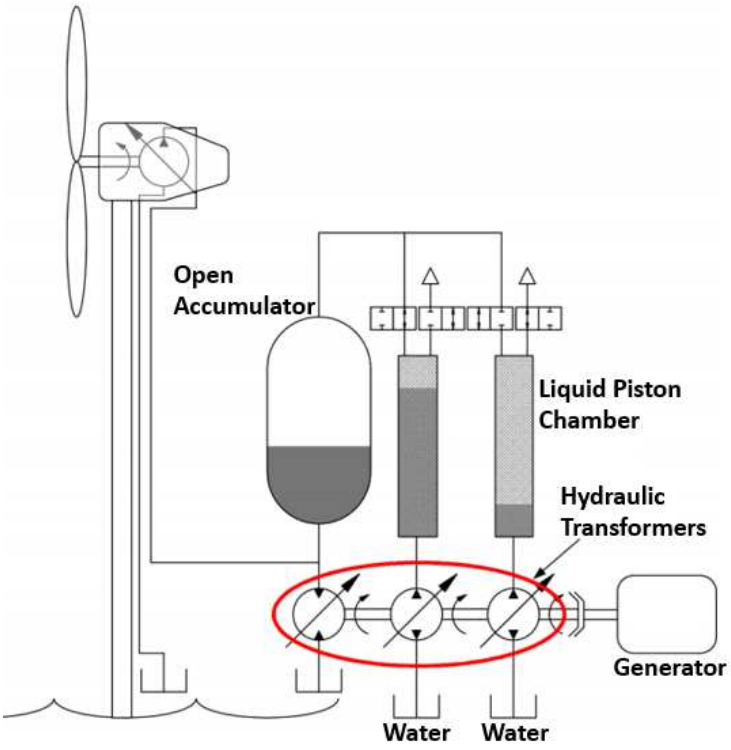

Fig.1.1 Schematic of CAES system for offshore wind energy storage and generation [8]

The compression process utilizes the mechanical energy to increase the work potential of the air by increasing its pressure. During compression, air temperature tends to rise;

however, as the air temperature rises, part of the compression work is converted into the internal energy, which is wasted later during the storage period when the compressed air cools. Therefore, minimizing the temperature rise is a key to reduce the total work input. For similar reasons, it is also important to reduce the temperature drop during expansion of air in order to obtain an effective work extraction. An example of the liquid piston chamber is shown in Fig.1.2, which is one of the experimental prototypes built in the Mechanical Engineering department at the University of Minnesota. The chamber is made of PVC plastic tube. Water is pumped into it from the bottom during compression. This particular setup was used for low pressure compression (up to around 13bar). Previous experimental results have been obtained by measuring the overall pressure vs. volume change during compression in a chamber inserted with porous media [9]. In the present study, detailed flow analyses and heat transfer characterizations will be completed; heat transfer enhancement methods will be investigated computationally, with experimental validations.

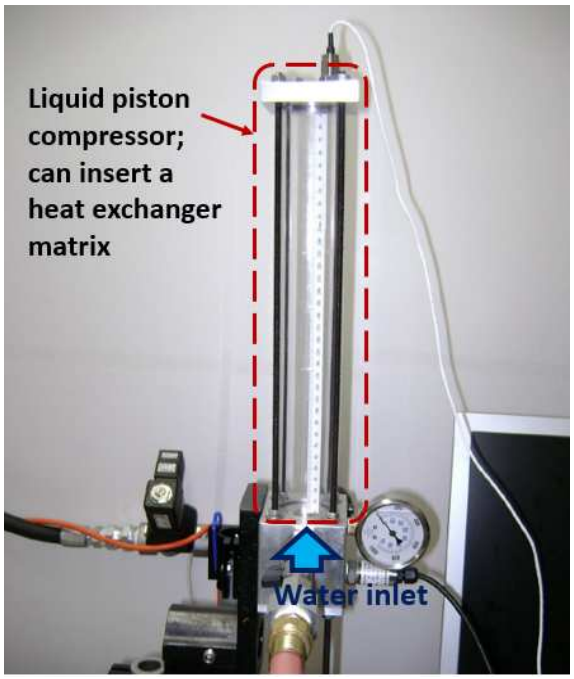

Fig.1.2 A low-pressure liquid piston compression chamber for lab-scale experiments [10]

1.2. Heat Transfer during Piston Compression

Heat transfer during piston compression is accompanied with rapid changes in density, temperature and pressure, and the formation of vortices. The vortices are formed due to interactions between the flow and the solid boundaries. The vortex in a moving corner as a result of piston movement, has been studied though flow visualization [11]. The "moving corner" was created by two pistons travelling in the same direction and at the same velocity. It is found that the vortex is stable when the Reynolds number is below 1.25×10^4, and fully turbulent if it is above 1.75×10^4, where the Reynolds number is based on piston diameter and velocity.

Early studies on heat transfer calculations focus on analytically solving a boundary layer flow. In a study where compression was induced by a short pulse movement of the piston, the analytical solution of a boundary layer flow was obtained and shown to agree well with experimental measurements [12, 13]. A similar analytical solution was obtained to compare with an experimental study of a sinusoidal compression trajectory [14]. However, it was found that when the ratio of the thickness values of the momentum boundary layer to thermal boundary layer is 0.44, the analytical solution agrees the most with the measured results. The same boundary layer analysis was used in a study of piston-induced shock waves, where a mismatch between the measurements and the analytical solution was observed [15].

Studies on heat transfer during piston compression often are targeted at internal combustion engine applications. One of the early results was the Hohenberg equation, which is an empirical heat transfer correlation based on bulk flow variables in the cylinder [16]. In more recent years, CFD has been applied to study piston cylinder compression. Sinusoidal trajectories of piston compression from 1000 to 3500 rpm have been simulated on a 2-D axisymmetric domain using a coordinate transformation method [17]. In another study, heat transfer coefficients were calculated based on CFD simulations on a four-stroke engine and compared with data from experiments [18]. Commercially available CFD codes

are capable of solving most engine application problems today. The commercial software ANSYS Fluent was used to model the reciprocating compression with inclusion of gas suction and discharge processes [19]. The engine CFD code KIVA-4 was used to simulate the droplet spray combustion coupled with heat conduction in the engine wall [20]. The CFD code ANSYS CFX was used to model the sinusoidal compression and expansion of a gas spring using different turbulence closure models [21].

Compression processes in the present study are realized through a liquid piston approach. The liquid piston compression can be simulated based on multiphase flow modeling techniques. Two Eulerian multiphase flow approaches are the Volume Of Fluid (VOF) model [22] and the mixture model [23]. Both use volume fraction variables to numerically represent the spatial occupations of different fluid phases, and solve the momentum and energy equations for the mixture flow based on averaged properties. The difference between the two is that the VOF model solves individual continuity equations for each phase while the mixture model solves continuity equations for the mixture flow and the secondary phase(s). The VOF model can be coupled with a Level-Set function, which tracks the dynamics of the phase interface [24]. Phase change processes, such as condensation and evaporation, can be combined with the Lee model [25], which calculates a mass source term in the continuity equation based on comparison between the local fluid temperature and the saturation temperature.

1.3. Flow and Heat Transfer in Porous Media

Porous media, or heat exchanger matrices, are used in the present liquid piston chamber to enhance heat transfer capabilities. A method of modeling fluid flow and heat transfer through porous media is by solving the volume-averaged transport equations [26, 27, 28, 29]. The model treats the porous medium region as a continuum region in the computational domain. The continuity, momentum, and energy equations are volume averaged within a unit cell that is a Representative Elementary Volume (REV) of the porous medium. The REV has a length scale greater than the pore size and much smaller

than the global length scale. The intrinsic averaged variables are based on averaging on the phase volume inside an REV,

$$\langle \chi \rangle^f = \frac{1}{V_{REV,f}} \int_{V_{REV,f}} \chi \, dV \tag{1.1}$$

where "χ" represents variables such as velocity, temperature, and pressure. Therefore, any variable, χ can be decomposed into an average term, $\langle \chi \rangle^f$, and a spatially fluctuating term, $\tilde{\chi}$,

$$\chi = \langle \chi \rangle^f + \tilde{\chi} \tag{1.2}$$

A superficial variable can also be defined, which is is averaged on the total volume of the REV,

$$\langle \vec{u}_f \rangle = \frac{1}{V_{REV}} \int_{V_{REV}} \vec{u}_f \, dV = \epsilon \langle \vec{u}_f \rangle^f \tag{1.3}$$

where ϵ is the porosity of void volume over the total volume. The continuity and momentum equations are volume-averaged on an REV scale, based on the above concept:

$$\nabla \cdot \langle \vec{u}_f \rangle^f = 0 \tag{1.4}$$

$$\rho_f \frac{\partial}{\partial t} \left(\langle \vec{u}_f \rangle^f \right) + \rho_f \nabla \cdot \left(\langle \vec{u}_f \rangle^f \langle \vec{u}_f \rangle^f \right) = -\nabla \langle p_f \rangle^f + \nabla \cdot \langle \bar{\bar{\tau}} \rangle^f + \rho_f \vec{g} + S_M \tag{1.5}$$

The stress tensor, $\langle \bar{\bar{\tau}} \rangle^f$, can be expressed, based on Cartesian tensor notation and the Kronecker delta, by:

$$\langle \tau_{i,j} \rangle^f = \mu \partial_j \langle u_i \rangle^f + \mu \partial_i \langle u_j \rangle^f - \frac{2}{3} \delta_{i,j} \mu \partial_k \langle u_k \rangle^f \tag{1.6}$$

The momentum sink term, S_M, in Eq.(1.5) results from spatial fluctuations of velocity on the pore scale. In isotropic porous media, the momentum sink term represents resistance of the porous medium to the flow. It has been modeled using a viscous and an inertial term [30]. Another term proportional to $-(\rho\mu|\vec{u}|)^{\frac{1}{2}}\vec{u}$ was added to capture flow transient effects, based on curve-fitting of experimental data of steady and oscillating flows through wire screens [31]. The full model is given by,

$$\vec{S}_m = -\frac{\mu\langle\vec{u}\rangle}{K} - \rho b|\langle\vec{u}\rangle|\langle\vec{u}\rangle - \frac{H}{K^{3/4}}(\rho\mu|\langle\vec{u}\rangle|)^{\frac{1}{2}}\langle\vec{u}\rangle \tag{1.7}$$

The volume-averaging technique is also applied on the energy equations to derive the energy equations for the porous continuum region. Two methods are available for modeling the energy transport, the one-energy-equation model and the two-energy-equation model. The one-energy-equation model solves an artificial temperature field that is a representation of the average local temperatures between the solid and the fluid, based on the assumption of local thermal equilibrium,

$$\frac{\partial}{\partial t}\left[\epsilon c_{p,f}\langle\rho_f\rangle^f\langle T\rangle + (1-\epsilon)c_s\rho_s\langle T\rangle\right] + \epsilon\nabla\cdot\left[\langle\vec{u}_f\rangle^f\left(c_{p,f}\langle\rho_f\rangle^f\langle T\rangle + \langle p_f\rangle^f\right)\right] = \nabla\cdot(k_{eff}\nabla\cdot\langle T\rangle + \epsilon\langle\bar{\bar{\tau}}\rangle^f\cdot\langle\vec{u}_f\rangle^f) \tag{1.8}$$

This method is often used when the temperature difference between the solid and the fluid is insignificant compared to global temperature difference. In a study of flow in round tubes inserted with a rolled copper mesh, good agreements were found between one-energy-equation solutions and experimental data [32]. The one-energy-equation model was applied also in another study of a liquid rocket propulsion system where the global temperature variation in the propulsion system is much greater than the temperature variation on the pore scale [33]. Solid piston compression in a porous-medium-inserted chamber was modeled using the one-energy-equation model, which showed that vortices develop during compression and they are affected by the Reynolds number, Darcy number ($Da = \frac{K}{D^2}$) and

the porous insert length [34]. The one-energy equation model was also validated against experiments in another application which showed that heat transfer rate of a tube with porous inserts is 1.6-5.5 times larger than that of a clear tube [35].

The other method, the two-energy-equation model, solves individual energy equations for the fluid and solid. The equations are given by:

$$\epsilon\rho_f \frac{\partial}{\partial t}\left(c_{p,f}\langle T_f\rangle^f\right) + \epsilon\nabla\cdot\left[\langle\vec{u}_f\rangle^f\left(c_{p,f}\rho_f\langle T_f\rangle^f + \langle p_f\rangle^f\right)\right]$$
$$= \nabla\cdot(\epsilon k_f\nabla\cdot\langle T_f\rangle^f - c_{p,f}\rho_f\langle\tilde{\vec{u}}_f\tilde{T}_f\rangle + \epsilon\langle\bar{\bar{\tau}}\rangle^f\cdot\langle\vec{u}_f\rangle^f) + ha_V(\langle T_s\rangle^s - \langle T_f\rangle^f) \quad (1.9)$$

$$(1-\epsilon)c_s\rho_s\frac{\partial\langle T_s\rangle^s}{\partial t} = (1-\epsilon)\nabla\cdot k_s\nabla\langle T_s\rangle^s - ha_V(\langle T_s\rangle^s - \langle T_f\rangle^f) \quad (1.10)$$

Heat transfer between the solid and fluid is represented by the interfacial heat transfer term, $ha_V(\langle T_s\rangle^s - \langle T_f\rangle^f)$, that couples the two energy equations. Volume-averaging the fluid energy equation also results a thermal dispersion term, $-\rho\nabla\cdot c_p\langle\tilde{\vec{u}}\tilde{T}\rangle^f$, which represents the amount of thermal energy fluctuation advected by the velocity fluctuation. Applications of the two-energy-equation method can be found in a number of studies. Analytical solutions of the two-energy-equation model were obtained for a fully developed flow through a pipe filled with a metal foam [36]. The two-energy-equation model was also used in laminar flow through a porous channel filled with particles [37], which showed that high Reynolds number, low particle diameter, and low solid to thermal conductivity ratio promotes thermal equilibrium between the solid and fluid, and enhances heat transfer with the channel wall. A double-pipe heat exchanger featuring two concentric pipes inserted with metal foam is modeled using the two-energy-equations model and the simulation results led to optimal design of the radius ratio of the two concentric pipes [38]. The two-energy-model was also used to study flow through a porous foam ceramic structure as part of a solar energy receiver [39]. When thermal dispersion effects are included in the two-

energy-equation simulations, they are modeled using an effective thermal energy diffusion term, the coefficient of which is closed by a correlation based on the Peclet number of the flow [40].

An interfacial heat transfer model is required in the two-energy-equation model to couple the fluid and solid energy equations. Over the years, different interfacial heat transfer models for porous media have been developed. A correlation for packed beds of 0.4 porosity is given in [41], by:

$$Nu = 2 + 1.1Re^{0.6}Pr^{\frac{1}{3}} \tag{1.11}$$

where the Nusselt and Reynolds numbers are based on particle size of the packed bed. An improved correlation was developed to account for the packed bed's porosity's effect [42]:

$$Nu = 1 + \frac{4(1-\epsilon)}{\epsilon} + \frac{1}{2}(1-\epsilon)^{\frac{1}{2}}Re^{0.6}Pr^{\frac{1}{3}} \tag{1.12}$$

When modeling a metal foam porous medium, heat transfer correlations developed for staggered cylinders [43] was used:

$$Nu = \frac{hd}{k_f} = 0.76{Re_d}^{0.4}Pr^{0.37}, \quad (1 \leq Re_d \leq 40) \tag{1.13}$$

$$Nu = \frac{hd}{k_f} = 0.52{Re_d}^{0.5}Pr^{0.37}, \quad (40 \leq Re_d \leq 10^3) \tag{1.14}$$

$$Nu = \frac{hd}{k_f} = 0.26{Re_d}^{0.6}Pr^{0.37}, \quad (10^3 \leq Re_d \leq 2 \times 10^5) \tag{1.15}$$

When applied to metal foam, the characteristic length, d, is defined as follows, to account for then non-circular cross sections of the metal foam filaments.

$$d = (1 - e^{-\frac{1-\epsilon}{0.04}})d_f \tag{1.16}$$

where d_f is the diameter of the strut of the metal foam. Other porous media correlations are based on the mean pore diameter, d_m, and the surface area per total volume, a_V [44, 45]:

$$Nu = \frac{ha_V {d_m}^2}{k_f} = 0.07\left(\frac{\epsilon}{1-\epsilon}\right)^{\frac{2}{3}} Re_{d_m}\mathrm{Pr}$$

$$(0.7 < \epsilon < 0.95,\ \ 3 < Re_{d_m} < 1000) \tag{1.17}$$

$$Nu = \frac{ha_V {d_m}^2}{k_f} = 0.124(\frac{3\pi\epsilon}{4(1-\epsilon)})^{0.605}(Re_{d_m}Pr)^{0.791}$$

$$(0.811 < \epsilon < 0.916) \tag{1.18}$$

Two more correlations were proposed based on conversion of the existing correlations into the mean pore diameter:

Kamiuto and Yee

$$\frac{h_V {d_m}^2}{k} = 0.996(\frac{\rho u_D d_m}{\mu}Pr)^{0.791} \qquad (\epsilon = 0.93) \tag{1.19}$$

Fu, et al.

$$\frac{h_V {d_m}^2}{k} = 0.275(\frac{\rho u_D d_m}{\mu})^{1.01} \qquad (Pr = 0.72) \tag{1.20}$$

When a porous medium is anisotropic, modeling of the flow resistance and heat transfer must account for the flow direction. Modeling of two-dimensional (2-D) cross flow through an anisotropic medium made of arrays of aligned cylinders of square cross sections

was developed based on permeability and inertial tensors [46]. The Darcy's Law defines a permeability tensor, $K_{i,j}$, as follows,

$$v_i = -\frac{1}{\mu} K_{i,j} \partial_j p \tag{1.21}$$

Based on earlier studies, when the coordinate system of flow domain is aligned with the principal axes of the porous medium, the permeability tensor is a diagonal tensor [47]. Therefore, the pressure gradient is given by,

$$\partial_j p = -\frac{\delta_{i,j}\mu}{K_{i,j}} v_i \tag{1.22}$$

The pressure drop in an arbitrary flow direction $\vec{n}$, where $\vec{n} = (cos\alpha,\ cos\beta,\ cos\gamma)$, is thus given by,

$$\partial_n p = \partial_j p \cdot \vec{n} = -\left(\frac{cos^2\alpha}{K_{1,1}} + \frac{cos^2\beta}{K_{2,2}} + \frac{cos^2\gamma}{K_{3,3}}\right)\mu|v| \tag{1.23}$$

When the Reynolds number is sufficiently large, the pressure drop is due to the inertial effect, modeled by:

$$\partial_j p = -\rho b_{i,j}|v|v_i\ . \tag{1.24}$$

For a 2-D cross flow through square cylinders, the inertial tensor is symmetric, and the following equation was proposed to use for accounting the anisotropic flow effect [46]:

$$\partial_j p = -\rho \begin{bmatrix} b_{f1} & bb_{f1}cos\alpha cos\beta & bb_{f1}cos\alpha cos\gamma \\ bb_{f1}cos\alpha cos\beta & b_{f2} & bb_{f2}cos\beta cos\gamma \\ bb_{f1}cos\alpha cos\gamma & bb_{f2}cos\beta cos\gamma & b_{f3} \end{bmatrix} |v|v_i \tag{1.25}$$

For modeling heat transfer in this anisotropic porous medium, the following correlation was proposed [46]:

$$\mathrm{Nu} = c_f + d_f \mathrm{Re}^{0.6} \mathrm{Pr}^{\frac{1}{3}} \tag{1.26}$$

where c_f and d_f are dependent upon flow direction, $\vec{n}$, given by:

$$c_f = c_{f1} cos^2\alpha + c_{f2} cos^2\beta + c_{f3} cos^2\gamma \tag{1.27}$$

$$d_f = (d_{\mathrm{f1}} \cos^2\alpha + d_{\mathrm{f2}} \cos^2\beta + d_{\mathrm{f3}} \cos^2\gamma)^{0.3} \tag{1.28}$$

In a later study [48], a quasi-three-dimensional flow field was solved using the same formulations, where the square cylinders had infinite lengths along the axial direction. In numerical modeling and simulations of porous media, the pressure drop and heat transfer models can first be resolved based on microscopic simulations on the REV, and then these models can be used to solve the global scale flow based on the volume-averaged equations. This method was used in a study of flow through a serpentine heat exchanger [49, 50].

1.4. Modeling of Heat Exchangers Made of Porous Media

Porous media provide large surface areas within small volumes and thus have superior heat transfer capabilities to other heat transfer methods such as fins or baffles. Porous media, or heat exchanger matrices, are often used in thermal regenerators to absorb or release thermal energy for the purpose of cooling or heating a volume of fluid. One-dimensional models have been used in the past for numerical simulations of flows in heat transfer applications consisting of heat exchanger matrices, to obtain fast calculations of transient temperature distributions and to be used for optimizations. An early 1-D model for a regenerator was proposed by simply coupling the spatial advection of fluid energy and the transient energy storage in the solid [51]. Solutions of the regenerator problem were extended to solve different inlet conditions by using superposition methods [52]. A regenerator with a by-

pass flow that offered opportunities to control the gas temperature at the outlet of the exchanger section was modeled in [53]. The effects of two bulk average heat transfer coefficients, one being linearly proportional to the gas flow rate, and the other being linearly proportional to a surface heat transfer coefficient, have been studied using 1-D modeling in [7]. An improved numerical method to solve the same governing equations employing Richardson extrapolation was introduced in [54]. The transient effect of the fluid temperature and heat conduction in the solid were added into the 1-D model in the studies of [55, 56]. Thermal conduction in the fluid phase was later added into the model in a study of the decomposition of nitrous oxide in a regenerative heat exchanger [57]. The more advanced 1-D model were used to simulate different applications related to heat exchanger matrices, such as a study on the effects of entrained fluid [58], and an active magnetic regenerator, in which the warming and cooling were induced by the magnetocaloric effect [59]. A novel numerical technique that combines short-cut methods was introduced to solve the 1-D model to improve the computational time [60]. Some methods for comparing the performance of different regenerators based on simulation results were shown in [61].

From a numerical perspective, the 1-D modeling approach in the aforementioned literature treats the heat exchanger matrix as a porous medium, and solves an energy equation for the fluid and another energy equation for the solid, similar to an approach for solving 2-D and 3-D fluid flow through porous media [29, 30]. The present study focuses on the liquid-piston application, in which a heat exchanger matrix is inserted, and the flow is two-phase (water and air). For the purpose of fast calculation and thermal design, a 1-D model is developed based on the same concept of modeling the porous medium flow, but incorporated with the Volume Of Fluid (VOF) method [22] to model also the two-phase flow with a moving interface.

Two-D and 3-D CFD can be applied to simulate heat exchanger applications to validate/improve the 1-D models. A rotary regenerator for in a helicopter engine, which recovers heat from the exhaust gas to increase temperature of the inlet gas, is studied through CFD analysis using commercial CFD software CFX [62]. Two-D and 3-D CFD

models have been developed using the commercial CFD code CFD-ACE for a porous medium Stirling converter in NASA [63]. In another study of a regenerator that features layers of involute-foils stacked together, 2-D and 3-D CFD analyses are done to support the experiments and design [64, 65, 66]. The same concept of using interrupted plates to induce new flow boundary layers for the purpose of enhancing heat transfer was applied in the present study to design an interrupted plate heat exchanger.

1.5. Motivation

The importance of having good heat transfer in the liquid piston chamber is demonstrated by a simple thermodynamic analysis that quantitatively shows the relation between heat transfer and compression efficiency. The compression efficiency for CAES systems is defined as the ratio of storage energy to work input [8]. The storage energy is defined as the amount of work extraction from compressed air as it is isothermally expanded to atmospheric pressure:

$$E_s = m\Re T_0(lnP^* - 1 + \frac{1}{P^*}) \tag{1.29}$$

Compression of air is completed in two steps: compress the air from atmospheric pressure to a high pressure, typically resulting in temperature increase, and allow the air to cool while compressing at the storage pressure so that the work potential (storage energy) is maintained as volume decreases. Work of the latter stage is identified as “cooling work.” The total work input is the sum of the work done in the two steps. It is given by,

$$W_{in} = -\int_{V_0}^{V_f}(P - P_0)dV + (P_f - P_0)(V_f - \frac{V_0}{P^*}) \tag{1.30}$$

The compression efficiency is given by the ratio of the storage energy to the total work input,

$$\eta = \frac{E_s}{W_{in}} = \frac{m\Re T_0 (lnP^* - 1 + \frac{1}{P^*})}{-\int_{V_0}^{V_f} (P - P_0) dV + (P_0\zeta - P_0)(V_f - \frac{V_0}{\zeta})} \tag{1.31}$$

Assuming that the compression process can be characterized as a polytropic process, we can relate pressure and volume change to heat transfer, which is characterized by a polytropic exponent, n:

$$PV^n = P_0 {V_0}^n \tag{1.32}$$

When $n = 1$, it represents isothermal processes with perfect heat transfer, and when $n = 1.4$, it represents adiabatic processes with no heat transfer. Substituting Eq. (1.32) into Eq. (1.31), and writing in terms of dimensionless pressure and volume based on their initial values, we get,

$$\eta = \frac{lnP^* - 1 + \frac{1}{P^*}}{\frac{P^{*(n-1)/n} - 1}{n-1} + P^{*-1/n} - 1 + (P^* - 1)(P^{*-1/n} - \frac{1}{P^*})} \tag{1.33}$$

The above equation shows that the compression efficiency is dependent on the pressure compression ratio, P^* and heat transfer, given by n. The efficiency is plotted against the final pressure ratio and the polytropic exponent in Fig.1.3. It shows that for the same pressure compression ratio, decreasing n, which means enhancing heat transfer from the compressed air, significantly improves efficiency.

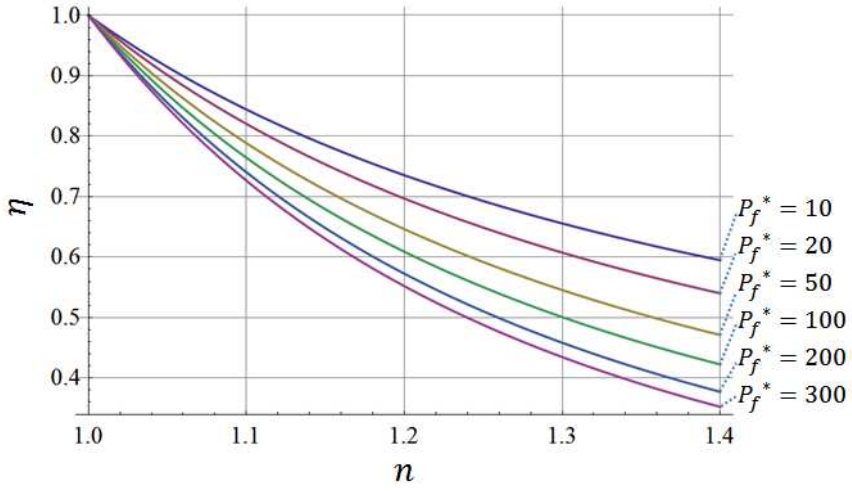

Fig.1.3 Effects of heat transfer on compression efficiency with different pressure compression ratios

As shown, enhancing the heat transfer process to maintain the temperature of the air during compression is an essential technique to improve the efficiency of the CAES system, and to reduce cost. The present study focuses on fluid flow and heat transfer analyses to understand the physics of the liquid piston chamber and provide thermal design solutions for enhancing heat transfer.

Chapter 2: Piston Compression without Exchanger Inserts

In this chapter, piston compression processes in chambers without any heat exchanger insert are analyzed. The results show that the formation of flow vortices during compression and temperature rise of gas are affected by chamber aspect ratio as well as the compression trajectory. The CFD results show the necessity of using heat exchanger inserts in the chamber, which will be discussed in the following chapters.

2.1. Low-Pressure Compression in Chambers with Different Aspect Ratios

We first discuss low speed, low pressure compression processes in solid piston cylinders of different aspect ratios.

2.1.1. Simulation Cases and Numerical Procedures

Twelve compression cases are simulated, all having the same volume compression ratio, 0.1 (final volume to initial volume), and having relatively low pressure compression ratios, generally in the range between 12 to 22. The cases are varied by the cylinder aspect ratio and compression speeds. The aspect ratio is represented by the parameter, $\frac{L}{R}$; four different values have been studied, $0.1,\ 0.5,\ 2$ and 10. The compression speed is represented in a dimensionless manner by a piston Reynolds number, based on initial gas property values; three different Reynolds numbers have been studied, $500,\ 1000$ and 2000. The actual compression speeds investigated are generally small, with the compression time varying from 6 to 120 seconds. These twelve cases are listed in Table 2.1.

The continuity, momentum and energy equations in the cylindrical coordinate are solved using the finite-volume-based CFD solver ANSYS Fluent. The movement of the piston in the simulation is realized using a dynamic mesh, based on a “layering” method. At each time step, the location of the moving boundary (the piston surface) is updated according to the piston speed, and the height of the first layer of computational cells next to the moving boundary decreases. If the height of this layer is smaller than a critical height, which is defined as 0.2 times the average cell size, it is merged with the second layer of

cells. The finite volume approach utilized first-order upwind scheme for differencing spatial derivative terms in the governing equations, and the first-order implicit method for transient discretization. The Pressure-Implicit Split Operator (PISO) algorithm is used for pressure and velocity coupling [67]. The Least Squares Cell Based method is used for calculating discretized spatial derivatives [68]. The Pressure Staggering Option scheme is used for calculating discretized pressure at each face center of the discretized cells [69]. These numerical methods are made available in the commercial solver ANSYS Fluent.

Table 2.1 CFD simulations of solid piston compression for low pressure compression ratios

Case name	$\mathbb{L}\ (m)$	$R\ (m)$	$U_p\ (m/s)$	$t_f\ (s)$	Re_p
Re500_0.1	0.1	1	0.0038	23.8	500
Re1000_0.1	0.1	1	0.0076	11.9	1000
Re2000_0.1	0.1	1	0.0151	6.0	2000
Re500_0.5	0.5	1	0.0038	119.1	500
Re1000_0.5	0.5	1	0.0076	59.6	1000
Re2000_0.5	0.5	1	0.0151	29.8	2000
Re500_2	1	0.5	0.0076	119.1	500
Re1000_2	1	0.5	0.0151	59.6	1000
Re2000_2	1	0.5	0.0302	29.8	2000
Re500_10	1	0.1	0.0378	23.8	500
Re1000_10	1	0.1	0.0756	11.9	1000
Re2000_10	1	0.1	0.1511	6.0	2000

A detailed analysis was done to study convergence with grid and time step sizes. Two parameters that characterize the effects of grid and time step size are used: the ratio of the average discretized cell area to the total area of the computational domain and a Courant number, defined as:

$$\mathbb{C} = \frac{\Delta x \Delta r}{\mathbb{L} R} \tag{2.1}$$

$$\mathbb{C}_t = \frac{u \Delta t}{\Delta x} + \frac{v \Delta t}{\Delta r} \tag{2.2}$$

The case Re1000_2 is used for grid and time step size analysis. Thirteen CFD runs of different combinations of grid and time step sizes are computed. In these thirteen runs, the number of grid cells in the axial direction varies from 38 to 304 and the number of grid cells in the radial direction varies from 29 to 232 and the time step size varies from 0.012s to 0.001s. The solutions from the different runs at the times when the piston has traveled 31% of the total length of the cylinder are compared. The error in conservation of mass, and the volume-averaged temperature and pressure are compared vs. $\mathbb{C}$ and $\mathbb{C}_t$ for each case. As shown in Fig.2.1 (a) and (b), for the triangular points, $\mathbb{C}_t$ is too large and for the square points, $\mathbb{C}$ is too large. From Fig.2.1 (c) and (d), it can be seen that when $\mathbb{C}$ and $\mathbb{C}_t$ are sufficiently small, the results converge. Based on this analysis, criteria for grid and time step size independence are: $\mathbb{C}_t < 0.01$ and $\mathbb{C} < 0.0004$. The simulations of the twelve cases in Table 2.1 all meet this criterion.

2.1.2. CFD Results

Although compression processes are slow compared to real applications, CFD simulations reveal fundamental flow physics and heat transfer during compression. The volume-averaged pressure and temperature are calculated for each case. They are shown in Fig.2.2 and Fig.2.3. In general, the piston speed has a stronger effect on the temperature rise than the aspect ratio. The processes can be represented by the polytropic exponents:

$$P^* V^{*n} = 1 \tag{2.3}$$

or,

$$T^* V^{*n-1} = 1 \tag{2.4}$$

The polytropic exponents for different Reynolds numbers and different aspect ratios are given in Fig.2.4. As expected, the effect of Reynolds number on n is relatively larger than that of the geometry aspect ratio. When the Reynolds number increases, the polytropic exponent increases for the same aspect ratio, meaning that heat transfer decreases. When the aspect ratio is above 0.5, the influence of it on n is relatively small. However, if the aspect ratio is decreased to 0.1, n drops significantly for the same Reynolds number. This means that for aspect ratios approaching 0.1, there is a significant advantage toward enhancing heat transfer, compared to larger aspect ratio cases.

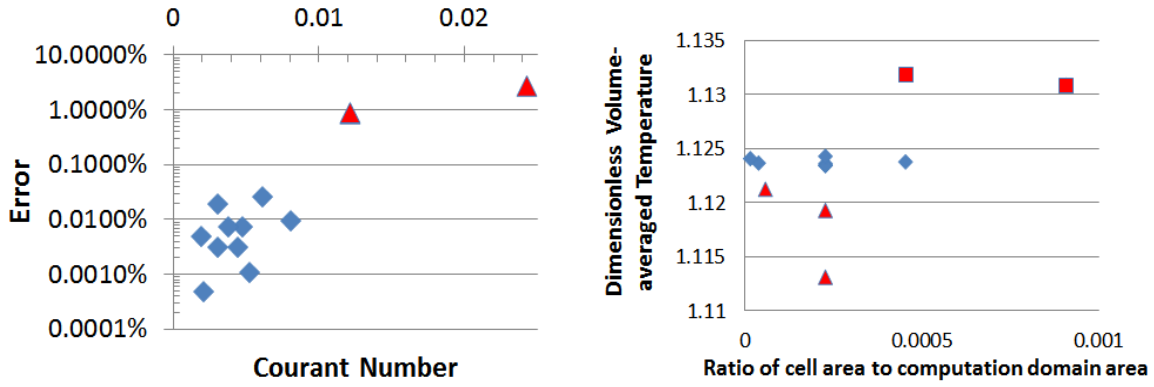

(a) Error in conservation of mass (b) Volume-averaged temperature

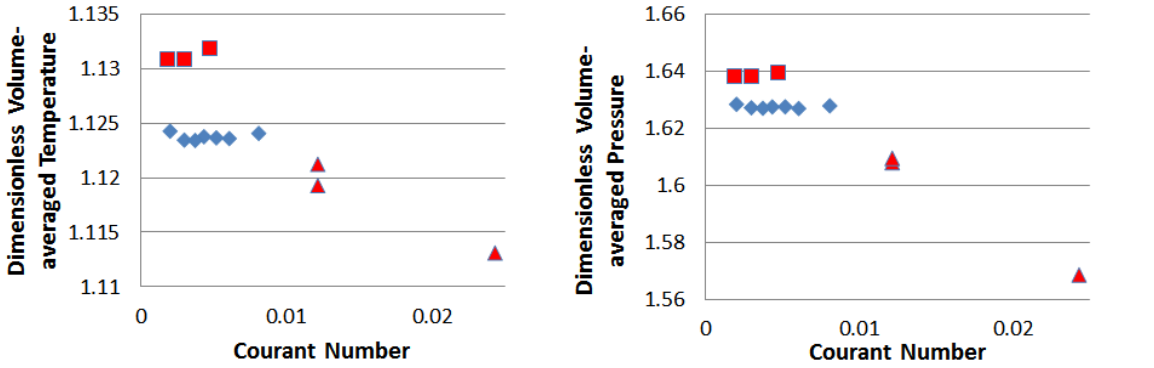

(c) Volume-averaged pressure (d) Volume-averaged temperature

Fig.2.1 Results computed from cases with various grid and time step sizes (each point represents a grid independence study run), for triangular points $\mathbb{C}_t$ is too large; for square points $\mathbb{C}$ is too large

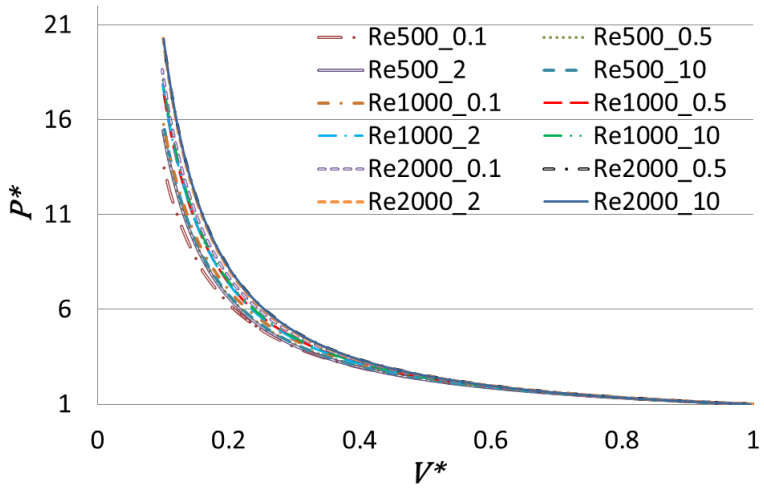

Fig.2.2 Dimensionless pressure vs. dimensionless volume for different cases (pressure and volume are normalized by their initial values; cases are named according to the piston Reynolds number which is based on the piston velocity and initial air properties, and the aspect ratio)

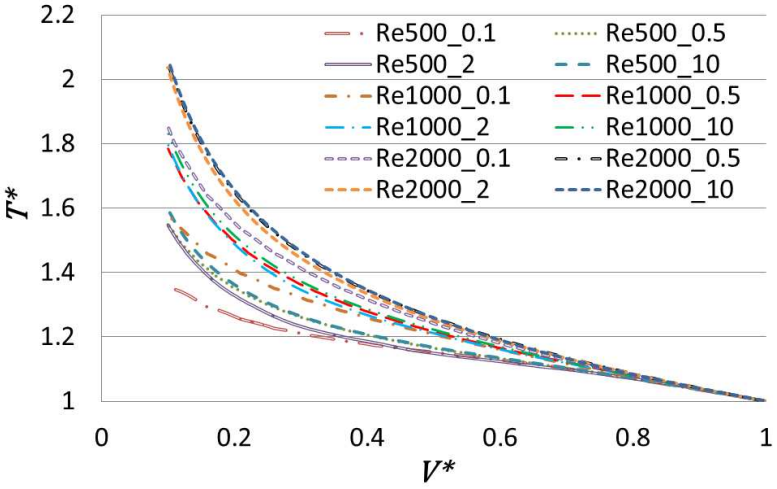

Fig.2.3 Dimensionless temperature vs. dimensionless volume (temperature and volume are normalized by their initial values; cases are named according to the piston Reynolds number which is based on the piston velocity and initial air properties, and the aspect ratio)

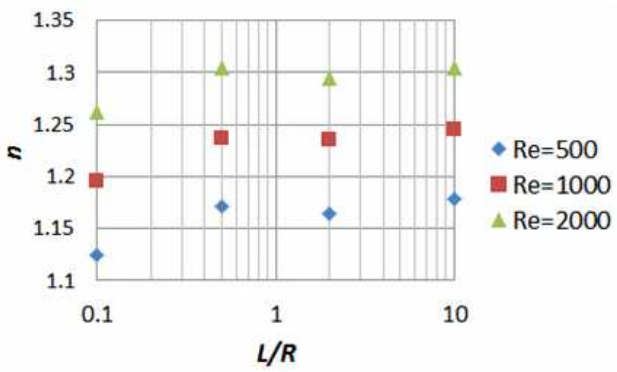

Fig.2.4 Polytropic exponents for slow compression processes with different chamber aspect ratios and piston Reynolds numbers

2.1.3. Flow Field

The flow field during compression for case Re2000_2 is shown in Fig.2.5. A stream of flow close to the cylinder wall that goes in the opposite direction to the piston motion is developed in the early stage of compression. A vortex is formed in the corner between the piston and the cylinder wall, as shown in Fig.2.5 (a). The shape of this vortex has some similarity to those studied in [11]. The flow is most energetic from 10s to 20s. At 10s, some small vortices develop near the cap (right side) due to flow deceleration as it approaches the wall. These vortices help mix the colder fluid near the wall with the hotter fluid in the inner region of the chamber. The vortex that was previously in the corner between the piston and the cylinder wall, together with the near-wall counter stream, have developed strong mixing effects near the piston side (left side). This mixing effect cools nearly half the chamber on the piston side. At 15s, the vortices that developed near the cap (right side) become larger in scale, carrying more cold fluid from the wall to mix with hot fluid inside. At 20s, shrinking of the axial length leads to dampening of the fluid motion near the walls. In the later stages of compression, when the mixing effect of vortices has subsided, the temperature field begins to appear more uniform in the inner region, but cold on the boundaries.

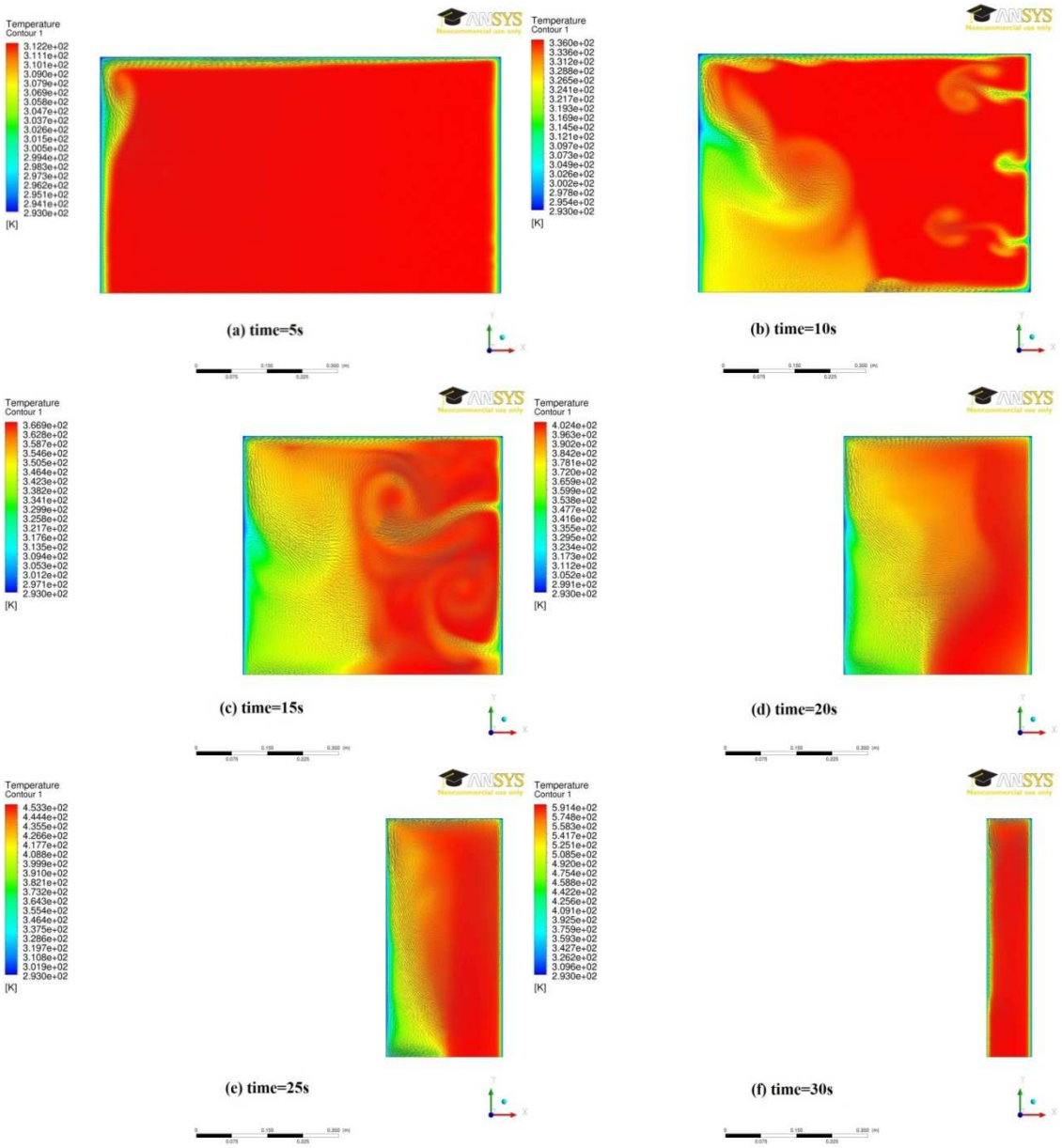

Fig.2.5 Temperature field of the flow during compression (in each plot, the left boundary is the piston surface, and the gravity points horizontally from right to left)

The CFD simulations of low pressure compression show that these processes in general follow a polytropic process and can thus be characterized by a polytropic exponent, n, an indication of less heat transfer. Larger piston Reynolds numbers results in larger n,.

The influence of aspect ratio on n is generally small, except when the aspect ratio is decreased toward 0.1. Vortices developed during compression tend to decrease the rate of temperature rise, due to more effective mixing of the colder fluid near the wall with the hotter fluid in the inner region.

2.2. High-Pressure Compression with Different Trajectories

Next, we discuss high pressure compression cases using the liquid piston approach, with relatively faster compression speeds.

2.2.1. Simulation Cases and Numerical Procedure

A liquid piston compression chamber of a high-pressure ratio is studied. The application is for a second stage CAES compressor, in which compression process starts with air and 7bar and ends when it is compressed 210 bar. The chamber has a length of 0.4826m and a radius of 0.0381m. Different compression trajectories are tested. One constant speed trajectory (0.15m/s) is simulated with two different wall boundary conditions, isothermal and adiabatic. Two trajectories are simulated with consideration of the pump. The pump has a maximum power output. At low pressure conditions, the pump can provide a constant maximum flow rate; when pressure rises, the maximum flow rate decreases as the power output rises with pressure. This characteristic of the pump is shown in Fig.2.6. These two trajectories utilizes maximum power output of the pump in the beginning and later switch to a constant speed compression trajectory. Another trajectory is simulated that utilizes a constant speed compression in the beginning and a constant power compression in the later period. The aforementioned trajectories all have slower compression speeds near the end. For comparison, an additional fast-slow-fast trajectory is simulated, which has a fast speed near the end. These different trajectories are given in Table 2.2.

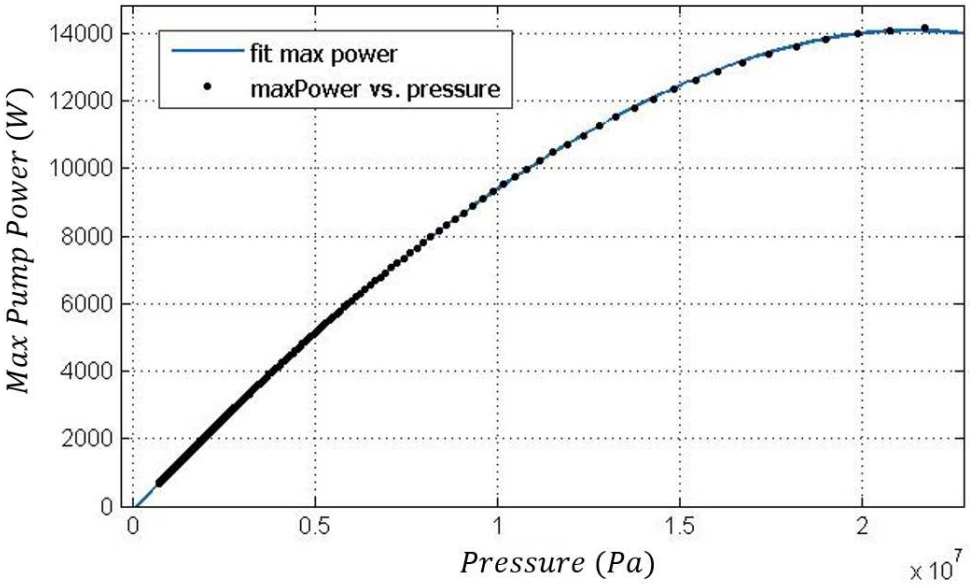

Fig.2.6 Pump power vs pressure

Table 2.2 Compression Trajectories

Case Name	Description
Const-Spd	Constant speed compression, 0.15m/s
Const-Spd_ADB-w	Constant speed compression with adiabatic walls (all other simulations have isothermal walls)
Max-Pw_Cons-Spd	Maximum power trajectory according to the pump, and then switch to constant speed compression at pressure ratio of 15
Max-Pw_Cons-Spd2	Maximum power compression according to the pump, and then switch to constant speed compression at pressure ratio of 8
Const-Spd_Const-Pw	Constant speed trajectory in the beginning, and then switch to constant power compression at pressure ratio of 15
Fast-Slow-Fast	A fast-slow-fast trajectory

Computed are compression processes from 700kPa to 21MPa. Due to the high pressure, a cubic equation of state for air treated as a real gas is used to relate air pressure to density and temperature [70]:

$$p = \frac{\rho \Re T}{M - \rho \mathfrak{b}} - \frac{\mathfrak{a}\rho^2}{M^2 + \mathfrak{b}M\rho} \tag{2.5}$$

where,

$$\mathfrak{b} = \frac{0.08664 \Re T_c}{P_c} \tag{2.6}$$

$$\mathfrak{a} = \frac{0.42727 \Re^2 {T_c}^2}{P_c} \left\{ 1 + \mathfrak{n} \left[1 - \left(\frac{T}{T_c} \right)^{0.5} \right] \right\}^2 \tag{2.7}$$

$$\mathfrak{n} = 0.48 + 1.574\omega - 0.176\omega^2 \tag{2.8}$$

The acentric factor, ω, is taken to be 0.033. For air, the critical pressure, critical temperature and molecular weight are respectively, 3.758MPa, 132.3K and 29g/mol. The universal gas constant is 8.314J/(mol K). The specific heat for a real gas is modeled using a departure specific heat [70, 71]:

$$c_{p,1} = c_{p,1,\text{ideal}} - c_{p,1,\text{dep}} \tag{2.9}$$

where the $c_{p,1,\text{ideal}}$ is for an ideal gas. For air, $c_{p,1,\text{ideal}}$ is taken as a function of temperature based on a curve fit of the data from [72]. The departure specific heat is based on the following equation,

$$c_{p,1,dep} = -\frac{p}{\rho T} + \frac{\Re}{M} - \frac{\frac{\partial \mathfrak{a}}{\partial T} - \frac{\mathfrak{a}}{T}}{M\mathfrak{b}} ln\left(1 + \frac{\mathfrak{b}\rho}{M}\right) \tag{2.10}$$

In the rest of this text, where compression is in the high pressure range (from 700kPa to 21MPa), the same real gas model is used.

The liquid piston compressor is simulated on a two-dimensional (2-D) domain. The computational domain and mesh for the compressor are shown in Fig.2.7. The water enters from the left boundary and compresses air. The left boundary in Fig.2.7 represents the bottom of the chamber and the gravity points from right to left. The chamber is initially filled with air at 7 bar, 293K. The walls have no-slip velocity boundary conditions. As this is a two-phase flow simulation, the VOF method is used; solved are two continuity equations for each of the two phases, along with the momentum and energy equations for

the mixture flow. The governing equations are based on the standard VOF formulations given by [22]. The simulations are done using ANSYS Fluent. Different compression trajectories are implemented through user defined functions (UDF) that calculate the instantaneous water inlet velocity values based on volume averaged pressure of the compressed air. The pump characteristic is implemented in the UDF using a fitted curve based on Fig.2.6. The 1st order implicit method is used on the transient discretization. Spatial differencing is based on a 2nd order upwind scheme. The PISO scheme is used for pressure-velocity coupling. The gradient terms are solved using the Green-Gauss Cell-Based method, which calculates the face value of a variable based on the arithmetic average of the values at its adjacent cell centers. In each time step, convergence is satisfied when the residual is smaller than 10^{-9}. The number of grid cells is 66,648 with progressively small cell sizes as walls are approached, and time step size is 0.00002s. Grid independence is verified by doubling the number of cells.

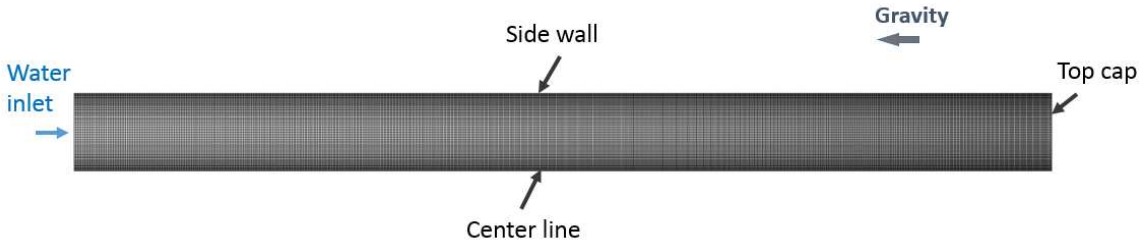

Fig.2.7 Computational domain and mesh for 2-D high-pressure compression simulations

Compression trajectories for the non-constant-speed cases are shown in Fig.2.8. Based on the pump power and instantaneous pressure relation, trajectories "Max-Pw_Cons-Spd," "Const-Spd_Const-Pw," and "Max-Pw_Cons-Spd2" are calculated simultaneously with other flow variables during CFD simulations.

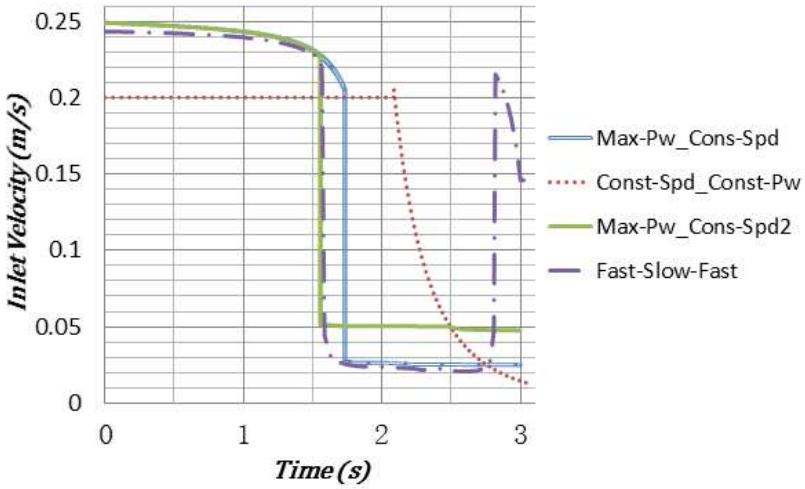

Fig.2.8 Compression trajectories

2.2.2. Flow Filed and Efficiency

The CFD simulations reveal different flow fields at the end of compression when pressure reaches 210 bar, as shown in Fig.2.9. The flow field of the case with adiabatic chamber walls is substantially different from the rest of the cases. The adiabatic walls lead to uniform temperature distributions; the only temperature gradient in the gas region is next the water-air interface. As the air heats up uniformly, there is no buoyancy effect that drives the secondary flows to mix the cold near-wall flow with the hot core region flow.

The other isothermal wall (with the walls being kept at 293K) cases reveal similar flow features as shown in the low speed, low pressure compression (Fig.2.5). Although different trajectories do not have strong effects on the overall gas temperature rise, close observation of Fig.2.9 shows that the active levels of secondary flow features are not the same in all cases. With reference to Fig.2.8, one sees that the faster the compression speed, the more active the secondary flows; as shown, the secondary flow features in Fig.2.9 (d) and (f) are more active than those in Fig.2.9 (a) and (e).

The instantaneous pressure vs. volume curves for different cases are given in Fig.2.10. As shown, the Fast-Slow-Fast case has the smallest slope, indicating it may require less

amount of total work input. The compression efficiency for different cases are calculated based on Eq.(1.31), and the results are shown in Fig.2.11. The differences in efficiency values among different compression cases are small. However, it can be seen that having a fast compression speed at the end of compression may help agitate the flow to promote mixing, as the higher efficiency values in Fig.2.11 are linked to those cases that have more active secondary flows in Fig.2.9. This indicates that a further study of trajectory optimization may be done to improve efficiency. The storage power values are given in Fig.2.12, for comparing the liquid piston compressors to other engineering applications that the readers might be interested. The storage energy values for these cases are the same, as they are compressed to the same final pressure. The storage power is defined as the storage energy divided by the compression time. Differences in the storage power values are caused by different compression times.

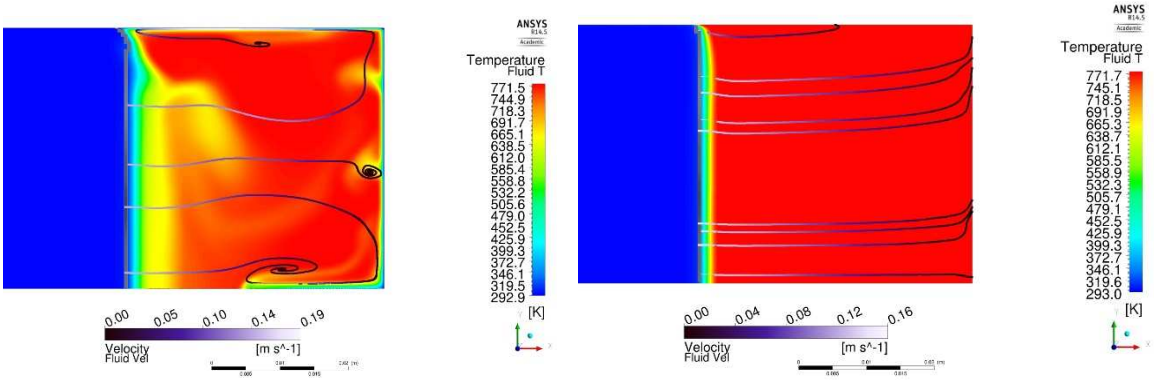

(a) Const-Spd

(b) Const-Spd_ADB-w

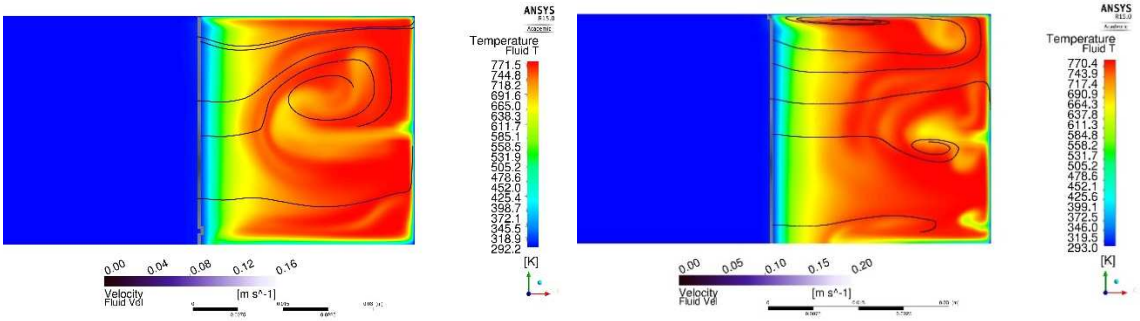

(c) Max-Pw_Cons-Spd

(d) Max-Pw_Cons-Spd2

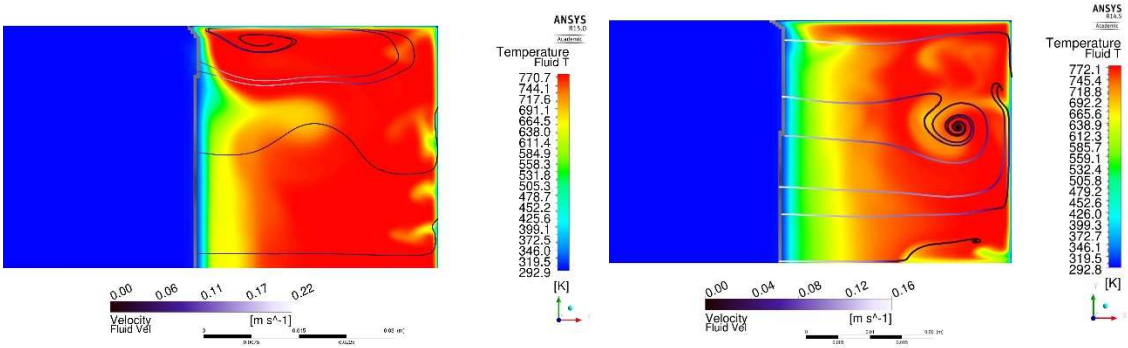

(e) Const-Spd_Const-Pw

(f) Fast-Slow-Fast

Fig.2.9 Temperature field and streamline of different compression trajectories at 210bar (only the top region of the chamber is shown; the interface between the dark blue and colorful regions represents the water-air interface)

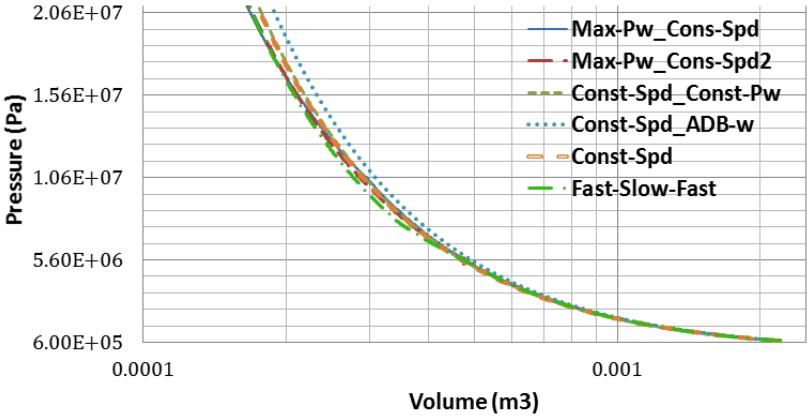

Fig.2.10 Pressure vs. volume for different cases

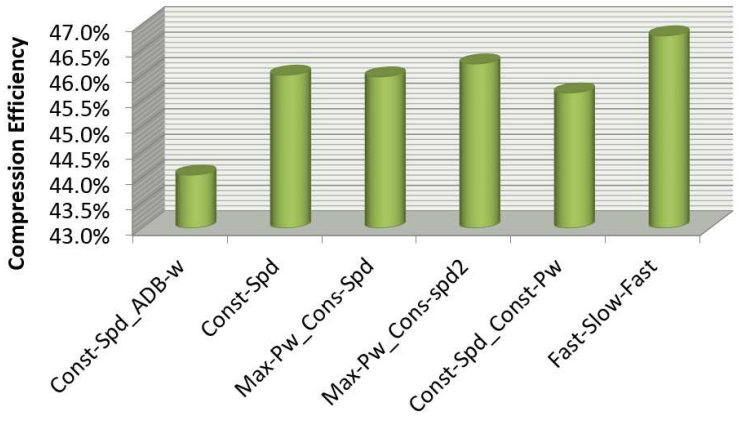

Fig.2.11 Compression efficiency

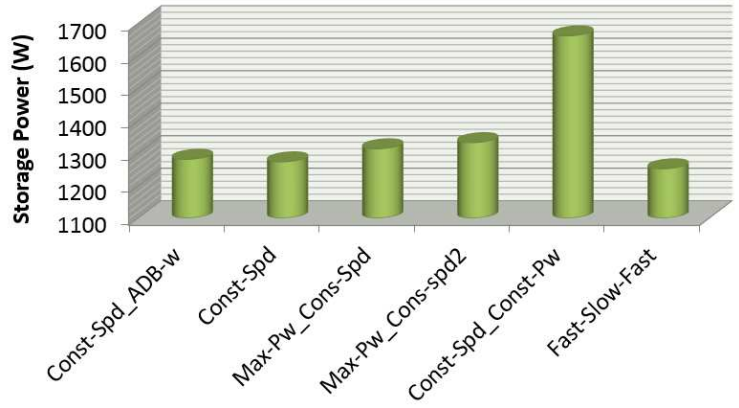

Fig.2.12 Storage Power

2.3. High-Pressure Compression with Phase Change Modeling

The same compression problem with a constant compression speed in section 2.2 is modeled by including the water condensation and evaporation effects. The gas phase now has two species, air and water vapor. Initially the chamber is filled by air with saturated vapor at 700,000Pa. The saturation vapor partial pressure at 293K and 700,000Pa is 2338Pa. The corresponding mass fraction of vapor is 0.002073.

A multiphase mixture model combined with species transport formulation is used. The basic concept of the mixture model is the same as the VOF model; volume fraction variables for both phases are solved. The difference is that, in the mixture model a continuity equation of the fluid mixture and another continuity equation for the secondary phase are solved, as opposed to solving two individual phase continuity equations in the VOF model. One set of momentum and energy equations are shared by the two phases. To model condensation and evaporation, a species transport formulation is incorporated in the mixture model. The gas phase has two species, air and water vapor, each represented by its own mass concentration (Y) in the gas phase (represented by subscript 1). Thus the species transport equations of the gas phase are given by:

$$\frac{\partial(\rho_1 Y_a)}{\partial t} + \nabla \cdot (\rho_1 \vec{u} Y_a) = -\nabla \cdot \rho_1 \mathcal{D}_{a-v} \nabla Y_a \tag{2.11}$$

$$\frac{\partial(\alpha_1 \rho_1 Y_v)}{\partial t} + \nabla \cdot (\alpha_1 \rho_1 \vec{u} Y_v) = -\nabla \cdot \alpha_1 \rho_1 D_{v-a} \nabla Y_v + \dot{m}_{evap} \tag{2.12}$$

In the species transport of the vapor, a source term, $\dot{m}_{evap}$, represents the amount of vapor generation due to evaporation. If condensation takes place, then $\dot{m}_{evap}$ has a negative value. The continuity equation for the liquid phase (water) has a corresponding source term $\dot{m}_{cond}$:

$$\frac{\partial(\alpha_2 \rho_2)}{\partial t} + \nabla \cdot (\alpha_2 \rho_2 \vec{u}) = \dot{m}_{cond} \tag{2.13}$$

The following conditions must be satisfied:

$$\dot{m}_{cond} = -\dot{m}_{evap} \tag{2.14}$$

The Lee model [25] is used for modeling the condensation and evaporation based on the local saturation temperature, which is calculated from the Clausius-Clapeyron equation. If the local liquid temperature is greater than the saturation temperature, then phase change happens in the direction of evaporation:

$$\dot{m}_{evap} = c\alpha_2\rho_2 \frac{T-T_{sat}}{T_{sat}} \tag{2.15}$$

If the local vapor temperature is less than the saturation temperature, then phase change happens in the direction of condensation:

$$\dot{m}_{cond} = c\alpha_1\rho_1 Y_v \frac{T_{sat}-T}{T_{sat}} \tag{2.16}$$

The coefficient c is set at 0.4. An energy source term due to latent heat is added in the energy equation.

Like observed before, secondary flows form during compression, water droplets (or cloud) in the gas space are carried by the secondary flows in the gas phase. The temperature distribution and water droplets in the gas region near the end of compression are shown in Fig.2.13 and Fig.2.14 As the pressure rises during compression, the partial pressure of vapor drops, and thus condensation takes place in the gas space. The condensed water droplets (or cloud) in the gas has an additional cooling effect. As a result, the final gas temperature at the end of compression is lower than that in the case where no phase change is modeled. Comparing the temperature distribution in Fig.2.14 to that in Fig.2.9 (a), one sees that the overall secondary flow features are very similar, but in the case with phase change modeling, the temperature is less uniform due to the presence of liquid water (as a "cloud") in the gas phase.

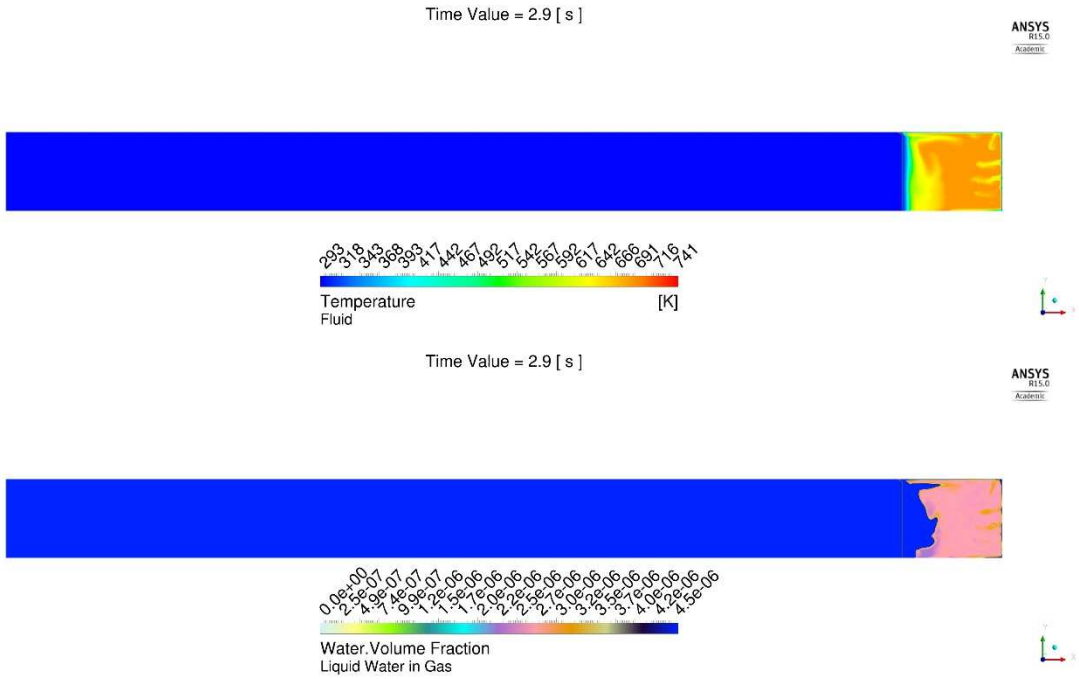

Fig.2.13 Temperature distribution and liquid water in the gas region, time=2.9s (Gravity points from right to left)

Of interest to compressed air energy storage is the work input, and efficiency. The inlet pressure profile during compression calculated from CFD results is compared to its counterpart in the same case without phase change modeling, as shown in Fig.2.15. The two inlet pressure profiles are very similar; the case with the phase change modeling has a slightly smaller slop in pressure rise. Based on the CFD simulation, the compression efficiency is 46.5% (as opposed to 46.0% of the case without phase change modeling).

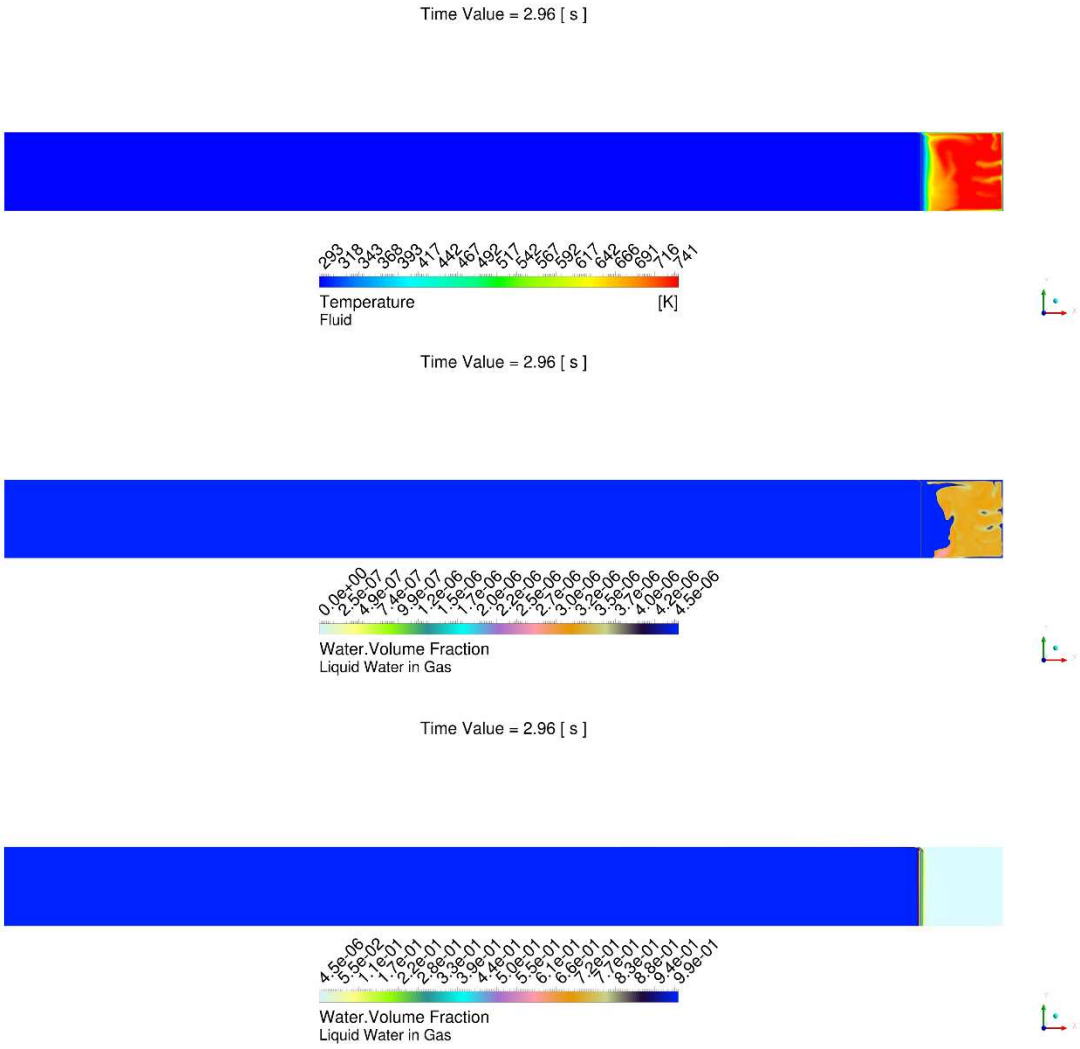

Fig.2.14 Temperature distribution and liquid water in the gas region, time=2.96s, final compression stage. (Gravity points from right to left)

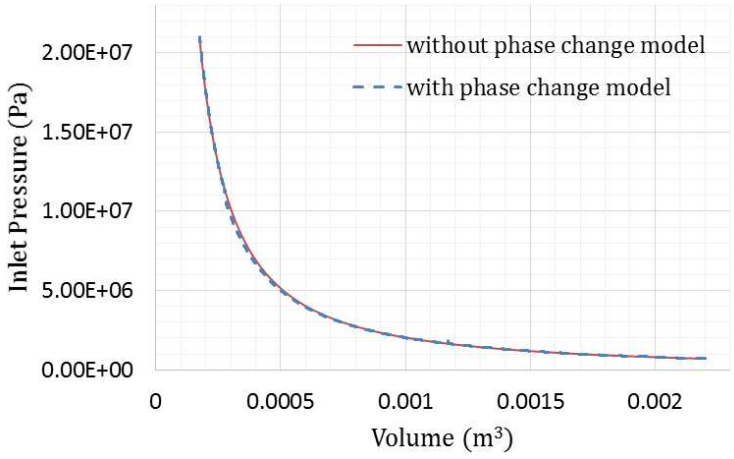

Fig.2.15 Comparison of inlet pressure profiles between the simulations with and without phase change modeling

2.4. Summary

In this chapter, preliminary simulation analyses have been done on compression chambers without any assistance of heat transfer media. It shows that complex flow features are present during compression of gas and that different trajectories influence the formation of secondary flows. The high temperature rise and low efficiency values show the requirement for enhancing heat transfer in the chamber, which will be discussed in the following chapters. The phase change process is modeled based on comparing the local gas temperature to the local saturation temperature and tracks only the volume fraction of the condensed water droplets in gas. This model is an appropriate approximation for the no-insert chamber. For a chamber inserted with a heat exchanger matrix, when the temperature and pressure conditions for condensation are met, the water vapor tends to condense on the colder surfaces of the matrix and liquid films are formed. This is a complex phenomenon and cannot be modeled using the previous model. Although the study of the phase change on porous medium surfaces is out of the scope of the present research, it is believed that the amount of heat interaction due to phase change is much smaller than the heat generated by compression or the heat transferred by the exchanger matrix. When the liquid piston chamber is inserted with a porous matrix, phase change is not modeled.

Chapter 3: Metal Foam Used for Heat Transfer Enhancement

Metal foam provides large surface area per volume. It can be used to absorb thermal energy in a liquid piston compressor for Compressed Air Energy Storage (CAES) applications. The use of the liquid piston, as opposed to a solid piston, provides the possibility for inserting heat transfer media into the chamber, like the metal foam, as the liquid piston can run through the gaps of the porous media without interfering with it.

The CFD simulations with porous media require modeling of a negative momentum source term (drag), and an interfacial heat transfer term. The first one is the pressure drop due to the metal foam, which is obtained from experimental measurements. To obtain the interfacial heat transfer term, a compression experiment is done, which provides instantaneous pressure and volume data. These data are compared to solutions of a zero-dimensional compression model based on different heat transfer correlations from published references. By this comparison, a heat transfer correlation that is most suitable for the present study is chosen for use in the CFD simulation.

Using these models that represent the hydro thermal properties of the metal foam, CFD simulations are run for global-scale simulations on the liquid piston compressor for low and high pressure compression cases. An exploratory design analysis is done on the shape of the chamber with a metal foam insert. In the last section of this chapter, studies are also done on some expansion processes with the application of metal foam.

3.1. Hydro-Thermal Characterization of Metal Foam

3.1.1. Pressure Drop

The pressure drop values of metal foams are measured. A schematic of the experimental setup is shown in Fig.3.1. A fan moves air as shown. Two kinds of metal foam blocks are inserted and measured for pressure drop: one with 10 pores per inch (10PPI), and one with 40PPI. They both have 93% porosity. A picture of the metal foam blocks is shown in Fig.3.2. The flow rate of air can be adjusted by a manual valve. A Sierra TopTrack 822S flow meter is used to measure the volumetric flow rate. The gauge pressure, also considered

as the pressure drop of the porous foam, is measured from the pressure tap by a micro-manometer. The experiment measures pressure drop values at different velocities.

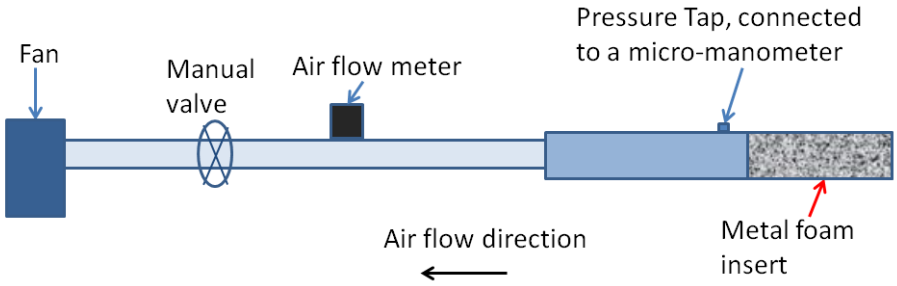

Fig.3.1 Schematic of experimental setup for pressure drop measurement

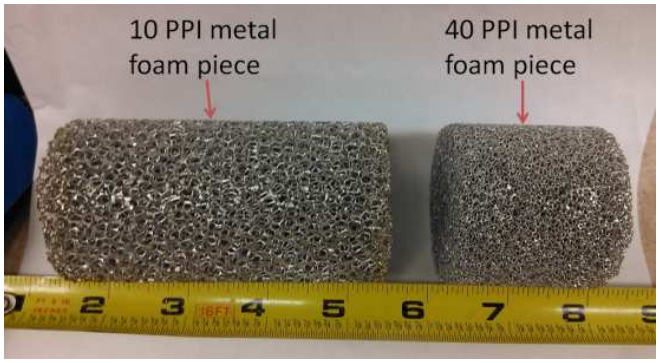

Fig.3.2 Metal foam blocks used

Results are shown in Fig.3.3. The micro-manometer has an uncertainty of 0.125Pa. The uncertainty of the measured Darcian velocity is 1.5%. The data are fit into the following equation that represents the pressure drop term in the momentum equation:

$$\vec{S}_m = -\frac{\mu\epsilon\vec{u}}{K} - b\rho|\epsilon\vec{u}|\epsilon\vec{u} \tag{3.1}$$

The permeability, K, and the coefficient in the inertial term, b, are obtained:

10PPI metal foam: $K = 2.397 \times 10^{-7} m^2$, $b = 285/m$

40PPI metal foam: $K = 9.913 \times 10^{-8} m^2$, $b = 576/\text{m}$

Equation (3.1) represents the pressure drop of the metal foam medium. It can be used to represent the momentum sink term in the global-scale CFD simulations of the metal foam where the domain is treated as a continuum.

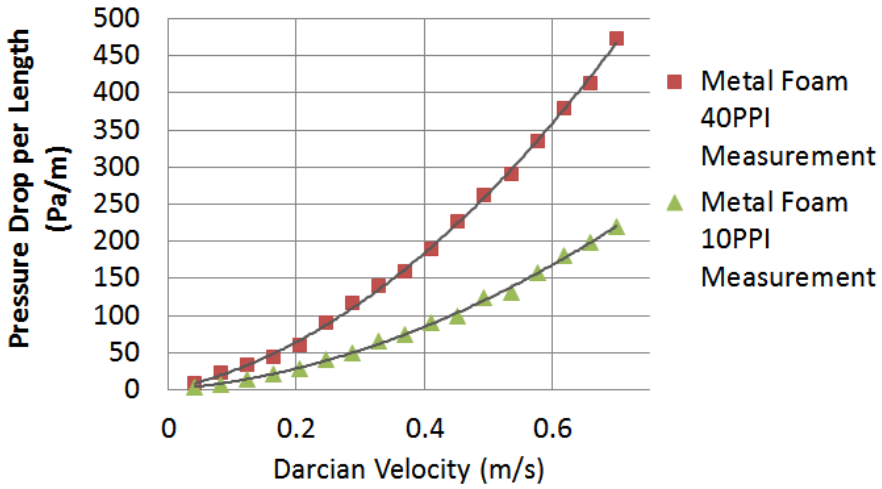

Fig.3.3 Pressure drop vs. Darcian velocity from experiments

3.1.2. An Experiment on Compression Using Metal Foam

Several porous media heat transfer correlations are available in the literature. To find one heat transfer correlation suitable for the metal foam media shown in Fig.3.2, experiments which measure the instantaneous pressure and volume during compression in a liquid-piston chamber with metal foam inserts were completed [73, 74]. To compare different heat transfer correlations with the experimental results, selected correlations are substituted into a Zero-D model to solve for the temperature trajectories during the compression processes. The trajectories were compared with the experimental data.

Shown in Fig.3.4 is a photo of an experimental liquid piston compressor setup, built in the Fluid Power Lab at the University of Minnesota [73, 74]. Water is circulated in a clockwise direction. A relief valve is installed between the pump and the rest of the system

to limit pressure to a maximum of 165 psi. An Omega FTB-1412 turbine flowmeter is used to measure the volume of water that enters the compression chamber. This flowmeter is capable of measuring flow rates from 47cm^3/s to 470cm^3/s. The control valve is used to maintain an approximately constant upstream pressure, thus regulating the flow rate. The control of this valve is done in MATLAB/Simulink using the built-in Proportional Integrator (PI) Controller. Due to the nature of the control valve, the flow rate is only approximately constant. Downstream of the control valve is the compression chamber. The chamber is apolycarbonate pipe with a length of 353 mm and an internal diameter of 50.8 mm. It is marked with graduations so that the water level in the chamber can be recorded. A PCI-DAS1602/16 16-bit analog input board is used to send and receive signals. Using xPC target, the I/O board is connected to a MATLAB/Simulink model for control and data acquisition. The sampling frequency is chosen to be 4000 Hz to correctly acquire the signal from the turbine meter. The three measured signals are: upstream pressure, turbine meter flow rate, and chamber pressure.

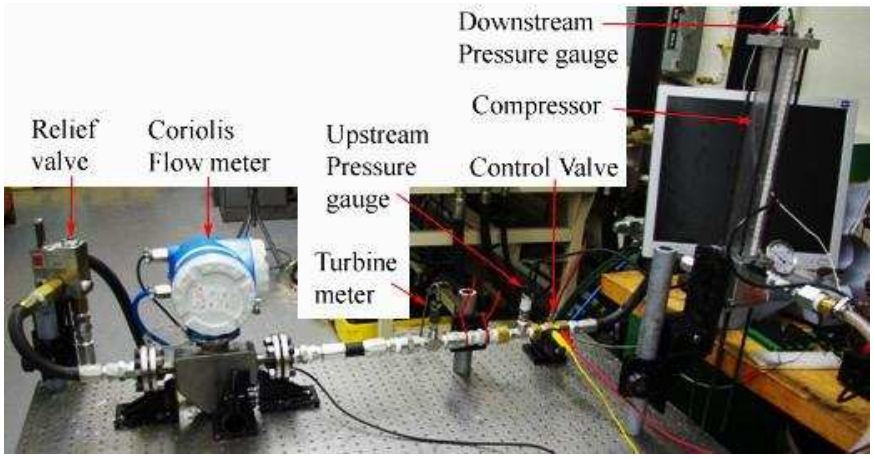

Fig.3.4 Experimental setup of liquid-piston compression
(taken from [73, 74])

Two experimental runs are made, one with the chamber filled with 10PPI metal foam, and the other with 40PPI metal foam. The conditions for these runs are given in Table 3.1. Due to a difference in the lengths of the compression chamber and the metal foam inserts, there remains at the bottom of the chamber a region that does not have insert material. In these experiments, the liquid piston is brought to the bottom of the metal foam at the beginning of compression so that the entire active length of chamber is filled with the metal foam insert. The instantaneous volume of air in the compression chamber is found by subtracting the cumulative amount of water added to the chamber from the initial volume of air. The instantaneous pressure of the compression chamber air is found directly from the pressure transducer at the top of the chamber. The instantaneous temperature is not measured directly; it is calculated from pressure and volume measurements using the ideal gas law. Although previous efforts had been made to measure the air temperature using a thermocouple, the ideal gas law method is preferred for several reasons. A thermocouple measurement is only one point in a thermal field that contains large thermal gradients. Additionally, the relatively fast temperature change during the transient process is difficult to capture accurately with the relatively slow responding thermocouple.

Table 3.1 Conditions of experimental runs

Experimental Runs	Initial length of air region (m)	Chamber radius (m)	Initial and ambient temperature (K)
10PPI Run	0.294	0.0254	297
40PPI Run	0.272	0.0254	297
	Initial Pressure (Pa)	Compression time (s)	Average Flow Rate (m3/s)
10PPI Run	101644	2.54	1.942×10^{-4}
40PPI Run	102632	3.78	1.210×10^{-4}

3.1.3. Zero-Dimensional (0-D) Compression Model and Interfacial Heat Transfer

To quickly compare performance with different exchangers in the compression chamber, a 0-D model representing the compression process in a chamber with an inserted exchanger is solved. The model is based on the first law of thermodynamics, using the heat transfer results obtained from the previous CFD simulations. For the air phase, the energy conservation gives,

$$Q = mc_v \frac{dT_a}{dt} + P\varepsilon \frac{dV}{dt} \tag{3.2}$$

After substituting the ideal gas law for the temperature term, and using a constant liquid piston velocity for the volume flow rate term, and assuming heat transfer is only between the air and the metal foam insert, the above equation becomes,

$$\bar{h}_V V(T_a - T_s) = (\frac{c_v}{R} + 1)\varepsilon A U_{in} P + \frac{c_v}{R} \varepsilon A U_{in} V \frac{dP}{dV} \tag{3.3}$$

where A is the cross sectional area of the chamber. The energy conservation for the solid phase is:

$$c_s \rho_s (1 - \varepsilon) A U_{in} \frac{dT_s}{dV} = -\bar{h}_V (T_a - T_s) \tag{3.4}$$

The ODE system formed by Eqns. (3.3) and (3.4) requires input of an averaged volumetric heat transfer coefficient, $\bar{h}_V$.

$$\bar{h}_V = a_V \bar{h} = a_V \frac{k\overline{Nu}_{Dh}}{D_h} \tag{3.5}$$

Equations. (3.3) and (3.4) are solved by the finite difference method. An iterative implicit scheme is used:

$$\bar{h}_V{}^{(i)} V^{(n+1)} \left(\frac{V^{(n+1)}\varepsilon}{mR} P^{(i+1)} - T_s{}^{(i)}\right)$$

$$= (\frac{c_v}{R} + 1)\varepsilon A U_{in} P^{(i+1)} + \frac{c_v}{R} \varepsilon A U_{in} V^{(n+1)} \frac{P^{(i+1)} - P^{(n)}}{\Delta V} \tag{3.6}$$

Superscript (n) represents the volume marching step, and superscript (i) represents numerical iteration step within one volume step. During each iteration, $P^{(i+1)}$ is solved from Eq.(25), and then ${T_s}^{(i+1)}$ is solved from:

$$c_s\rho_s(1-\varepsilon)AU_{in}\frac{{T_s}^{(i+1)}-{T_s}^{(n)}}{\Delta V}=-{\bar{h}_V}^{(i)}\left(\frac{V^{(n+1)}\varepsilon}{mR}P^{(i+1)}-{T_s}^{(i+1)}\right) \tag{3.7}$$

Next, the index of iteration step, i, increases by 1 and Eqns.(25) and (26) are solved again. Once convergence of this iterative process is reached, $P^{(n+1)}=P^{(i+1)}$, and ${T_s}^{(n+1)}={T_s}^{(i+1)}$. Then the computation marches to the next volume step, by increasing the index of volume step, n, by 1.

A number of references have given interfacial heat transfer correlations often used for porous media, as discussed in Chapter 1. These correlations are given by Eqns.(1.11)-(1.20). The Zero-D model is solved to simulate the experimental runs by substituting the different heat transfer correlations. When evaluating the average Reynolds number in the heat transfer correlations, a velocity that is half the piston velocity is used to approximate the overall mean velocity of the air in the chamber. The physical properties of air and metal foam (solid) used in the computation are given in Table 3. The metal foam is aluminum. The average cell size is used as the characteristic pore; for the 10PPI and 40PPI metal foam blocks, they are, respectively, 3.61mm and 2.38mm. An average filament size of 0.6mm is used. The values of surface area per volume for the 10PPI and 40PPI metal foams are, respectively, 697/m and 1677/m. The air Prandtl number is 0.713. A fit of conductivity data (from [72]) with temperature over 273K to 573K is used.

Table 3.2 Physical properties used for computation

$\mathcal{R}=287.06J/(kgK)$	$\mu_2=1.002\times10^{-3}Pa\cdot s$	$c_2=4181.3J/(kgK)$
$\rho_s=2719\,\mathrm{kg}/m^3$	$\rho_2=1000\,\mathrm{kg}/m^3$	$k_2=0.56W/(mK)$
$k_s=205W/(mK)$	$c_{p,1}=1005J/(kgK)$	$c_s=871J/(kgK)$
$\mu_1=1.716\times10^{-5}\times\left(\frac{T}{273K}\right)^{2/3}Pa\cdot s$		

$$k_1 = (0.00468506 + \frac{7.16557\times10^{-5}T}{K})\, W/(\mathrm{mK})$$

The computed and the experimentally measured air temperature values are normalized based on the initial temperature. The results are shown in Fig.3.5. In the experiment, the temperature is calculated from the ideal gas law, based on instantaneous pressure and volume measurements. The uncertainties of the initial volume and initial temperature measurements are respectively $1.013cm^3$ and 0.8 K. The uncertainties in the transient pressure and volume measurements are, respectively, 1724Pa and $3cm^3$. Using an uncertainty propagation equation yields a temperature of 15 – 17K. Despite local mismatches and uncertainties in the experiments, one sees from Fig. 6 that the solutions obtained based on the Kamiuto and Yee correlation agree with experimental measurements best throughout the whole compression process. Therefore, the Kamiuto and Yee correlation (Eq. (1.19)) is chosen for CFD modeling to calculate interfacial heat transfer coefficients.

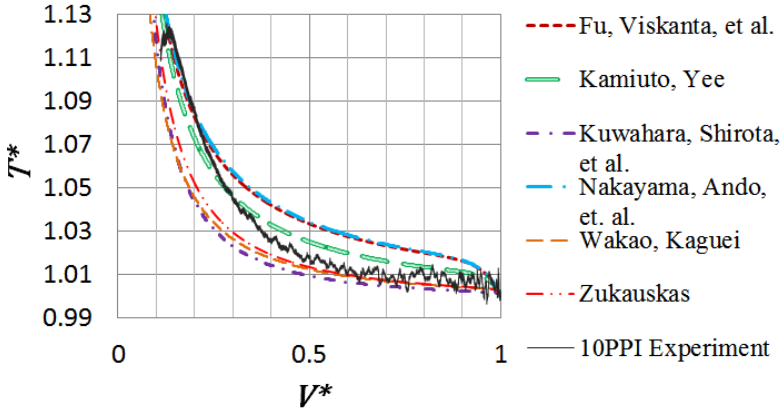

(a) 10PPI metal foam insert

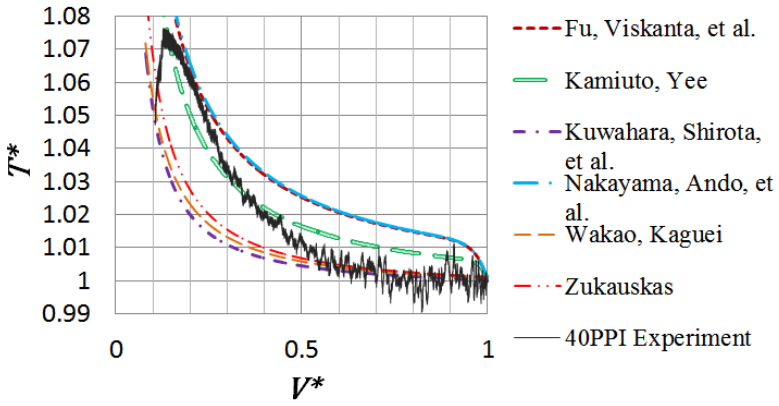

(b) 40PPI metal foam insert

Fig.3.5 Comparison of experimental results to Zero-D model solutions obtained by using different heat transfer correlations (Variables are normalized by their initial values) (taken from [74])

3.2. Two-D Simulations of Low-Pressure Compression in Chambers that are Fully and Partially Filled with Insert Material

The following CFD simulations investigate two types of metal foam inserts, two different layouts of the insert (partial vs. full), and two different liquid piston speeds. The results show the influence of the metal foam on secondary flows and temperature distributions.

3.2.1. Problem Description

A cylindrical, liquid-piston compression chamber is occupied by a porous metal foam. The present study investigates two situations: foam in the entire volume and foam in a portion of the chamber. A schematic of a partially occupied chamber is shown in Fig.3.6. The fully occupied case uses the same coordinate system and coordinate layout. The compression chamber is studied in cylindrical coordinates. The x axis is along the centerline of the compression chamber. The gravitational field points opposite to the axis direction x. At time = 0, water pumping into the chamber at location $x = 0$ begins. Boundaries $x = \mathbb{L}$ and $r = R$ represent walls of the chamber. For the partial insert case, the metal foam is inserted

over the region of length $\mathbb{L}_{ins}$; for the full insert case, the metal foam is inserted over the entire length $\mathbb{L}$. The material of the metal foam is aluminum.

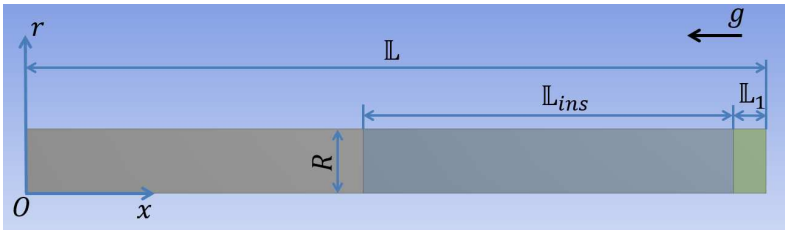

Fig.3.6 Schematic of compression chamber with partial insert

During compression, liquid water, air, and solid coexist in the chamber. The transport equations are based on the two-energy equation model for porous media and the VOF method. The water does not change phase in the simulation. The continuity equation for each of the two fluid phases is solved. The fluid density of a particular phase that is transported by the continuity equation is the phase density times its phase volume fraction, α. Let subscripts 1 and 2 represent air and water, respectively. Then, for air:

$$\frac{\partial \alpha_1 \rho_1}{\partial t} + \nabla \cdot (\alpha_1 \rho_1 \vec{u}) = 0 \tag{3.8}$$

For water, since the density is a constant, the continuity equation becomes a transport equation of volume fraction only,

$$\frac{\partial \alpha_2}{\partial t} + \nabla \cdot (\alpha_2 \vec{u}) = 0 \tag{3.9}$$

The velocity field and temperature field are shared by air and water. Thus, one set of momentum and fluid energy equations is solved, based on the properties of the fluid mixture.

$$\frac{\partial \rho \vec{u}}{\partial t} + \nabla \cdot (\rho \vec{u} \vec{u}) = -\nabla p + \nabla \cdot \bar{\bar{\tau}} + \rho \vec{g} + \vec{S}_m \tag{3.10}$$

where

$$\rho = \alpha_1 \rho_1 + \alpha_2 \rho_2 \tag{3.11}$$

The stress tensor, $\bar{\bar{\tau}}$, is based on viscosity of the fluid that is made up of air and water,

$$\mu = \alpha_1 \mu_1 + \alpha_2 \mu_2 \tag{3.12}$$

The negative momentum source term, $\vec{S}_m$, represents the resistance of the metal foam to the flow. It is formulated based on Eq. (3.1), using values measured in section 3.1.1. The energy equation for the fluid is,

$$\frac{\partial \epsilon(\rho c_p T)}{\partial t} + \epsilon \nabla \cdot \left(\vec{u} \rho c_p T\right) = \epsilon \nabla \cdot k_f \nabla T + h_V (T_s - T) + \epsilon \frac{\partial p}{\partial t} \tag{3.13}$$

where

$$\rho c_p = \alpha_1 \rho_1 c_{p,1} + \alpha_2 \rho_2 c_{p,2} \tag{3.14}$$

$$k_f = \alpha_1 k_1 + \alpha_2 k_2 \tag{3.15}$$

The volumetric heat transfer coefficient can be written in terms of surface heat transfer coefficient,

$$h_V = a_V h_{sf} \tag{3.16}$$

The air density follows the ideal gas law,

$$\rho_1 = \frac{p}{\mathcal{R} T} \tag{3.17}$$

The energy equation for the solid is

$$(1 - \epsilon) \frac{\partial}{\partial t} (\rho_s c_s T_s) = (1 - \epsilon) \nabla \cdot k_s \nabla T_s - h_V (T_s - T) \tag{3.18}$$

The boundary conditions for velocity and temperature variables are given in Table 3.3.

Table 3.3 Boundary conditions for velocity and temperature

$\vec{u}(x = \mathbb{L}) = \vec{u}(r = R) = 0, \vec{u}(x = 0) = (U_0, 0)$
$T(x = 0) = T(x = \mathbb{L}) = T(r = R) = 297\text{K}$
$T_s(x = 0) = T_s(x = \mathbb{L}) = T_s(r = R) = 297\text{K}$
$\alpha_1(x = 0) = 0, \alpha_2(x = 0) = 1$
$\frac{\partial T}{\partial r}|_{r=0} = \frac{\partial T_s}{\partial r}|_{r=0} = \frac{\partial u}{\partial r}|_{r=0} = 0, T_s(r = R) = T_0$
For full insert: $T_s(x = 0) = T(x = \mathbb{L}) = T_0$
For partial insert: $T_s(x = \mathbb{L} - \mathbb{L}_1) = T(x = \mathbb{L} - \mathbb{L}_1)$,
$T_s(x = \mathbb{L} - \mathbb{L}_1 - \mathbb{L}_{\text{ins}}) = T(x = \mathbb{L} - \mathbb{L}_1 - \mathbb{L}_{\text{ins}})$

CFD simulations based on the above formulation require models for the negative momentum source term, $\vec{S}_m$, and the interfacial heat transfer coefficient, h_V. These two terms have been obtained in the previous sections. Eight CFD runs are calculated by varying the inlet water velocity, the layout of the insert (full-insert vs. partial-insert), and the pore size. The cases are shown in Table 4. The schematic of the chamber is shown in Fig.3.6. In all cases, the dimensions of the chamber are: $\mathbb{L} = 0.294m$, $R = 0.0254m$. For the four full-insert cases, the entire chamber length $\mathbb{L}$ is occupied by the insert. For the four partial-insert cases, the insert length is: $\mathbb{L}_{ins} = \frac{\mathbb{L}}{2} = 0.147m$, and the distance between the top boundary of the insert and the top cap of the chamber is: $\mathbb{L}_1 = 0.013\text{m}$. The initial temperature (for both fluid and solid) and pressure are: 297K and 101644Pa. The initial air velocity is 0.0, and air volume fraction is 1.0 in the chamber.

Table 3.4 CFD Runs

Cases	Insert	t_f (s)	U_0 (m/s)	No. of Grid Cells	Δt (s)
Run1	10PPI, Full	2.6	0.103	26,000	0.0002
Run2	40PPI, Full	2.6	0.103	26,000	0.0002
Run3	10PPI, Full	1.3	0.206	26,000	0.0001
Run4	40PPI, Full	1.3	0.206	26,000	0.0001
Run5	10PPI, Partial	2.6	0.103	44,485	0.00005

Run6	40PPI, Partial	2.6	0.103	44,485	0.00005
Run7	10PPI, Partial	1.3	0.206	44,485	0.000025
Run8	40PPI, Partial	1.3	0.206	44,485	0.000025

3.2.2. Numerical Method, Verification, and Validation

The commercial CFD Software ANSYS Fluent is used. The default VOF model is used, interfaced with User-Defined-Function (UDF) codes to incorporate the solid energy equation for the two-energy equation model. The same numerical treatment as used in the previous chapter is used. The convergence is satisfied when the residual is smaller than 10^{-9} in each time step. The physical properties given in Table 3.2 are used. The number of grid cells is 26,000 for the full-insert cases, and 44,485 for the partial-insert cases. The time step size is 0.0002s for the full insert cases with the smaller inlet velocity. The time step size decreases as the number of nodes and the velocity increase.

Run1, which has a relatively small number of grid cells and a large time step size compared to other runs, is tested for grid independence. The grid-independence run is done on the mesh that has 65,600 cells, using a time step size of 0.0001s.The average air pressure and temperature at the final compression time calculated from Run1 and its grid-independence run are, respectively: 1,317,934Pa and 1,318,324Pa, and 345.8K and 345.6K. The temperature contour plots of the two at their final compression times also display identical features. Therefore, grid independence is satisfied.

Two validation methods have been done. The first validation is a comparison with experimental results. Since CFD Run1 simulates the same experimental conditions as the 10PPI run shown in Table 2, the bulk air pressure rise and temperature rise calculated from CFD can be compared to the experimental results (shown in Fig.3.7). In the CFD simulation, the total compression time is slightly longer than in the experiment. In the experiment, the flow rate slows at the end due to the valve behavior, causing the air temperature to drop slightly. Overall, the two agree.

In the second validation, the problem of case Run 1 is simulated with several modifications. The first change is that thermal boundary conditions are changed from isothermal to adiabatic.

$$\frac{\partial T}{\partial r}|_{r=R} = \frac{\partial T_s}{\partial r}|_{r=R} = \frac{\partial T}{\partial x}|_{x=L} = \frac{\partial T_s}{\partial x}|_{x=L} = 0 \tag{3.19}$$

In order to make the water piston adiabatic, the thermal conductivity is manipulated to become $10^{-6}W/(mK)$. Additionally, the heat transfer between solid and fluid is made zero by setting the interfacial heat transfer coefficient, h_V, to zero. As expected, the CFD simulates adiabatic compression of air. In theory, the pressure vs. volume trajectory of adiabatic compression has a polytropic exponent of 1.4. The CFD result shows that the bulk pressure verse volume follows the same adiabatic trend as shown in Fig. 8. At the end of compression, the pressure calculated from CFD is slightly smaller than that from the theory. This is because the liquid piston still conducts a small amount of heat for its conductivity is not exactly made to zero for numerical stability reasons.

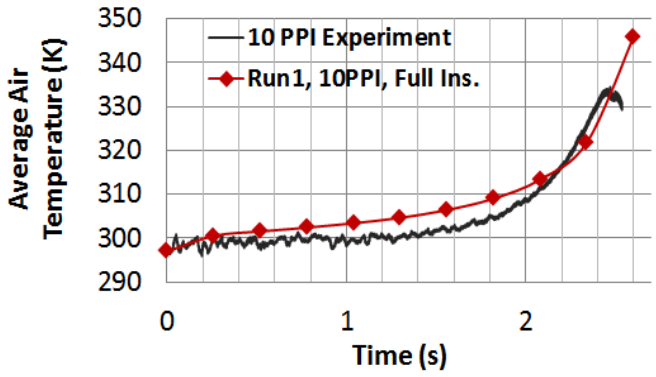

(a) Pressure vs. time

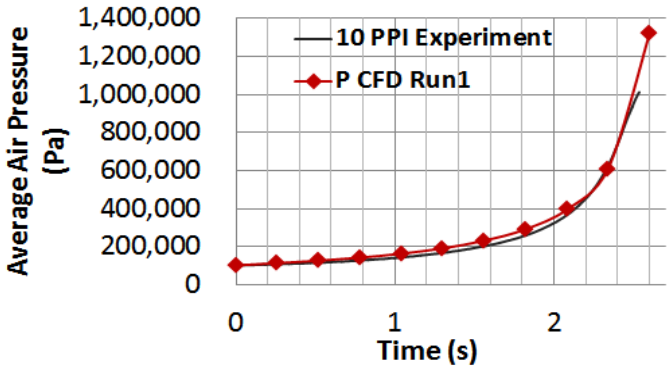

(b) Temperature vs. time

Fig.3.7 Experimental validation of CFD Run1
(in collaboration with B. Yan [74])

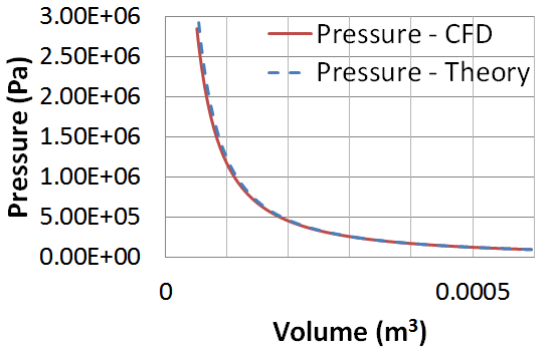

Fig.3.8 Validation of CFD using adiabatic compression

3.2.3. CFD Results

The eight CFD cases in Table 4 are simulated. The bulk air temperature during compression is calculated and shown in Fig. 9. In most cases, the metal foam does a good job of suppressing the air temperature rise during compression. The smallest bulk air temperature rise during compression is 35K (Run2), which is compressed by the smaller liquid-piston speed and has a chamber that is fully occupied by the finer-mesh metal foam. For the same porous insert, higher compression speeds result in larger temperature rises. For the same compression speed, the full insert case has an advantage over the partial insert case, and

40PPI foam has an advantage over the 10PPI foam for reducing the temperature rise. In the partial insert situations, since the foam is inserted in the upper half of the chamber region, the bulk air temperature rises fast in the beginning. As the air is being pushed from the non-porous region into the porous region, its temperature cools due to heat transfer with the metal foam. This causes the bulk air temperature to drop by a few degrees in the middle of the compression process.

The computed fluid temperature field and streamlines are shown in Fig.3.10-Fig.3.12. An arrow with a note “Interface” indicates the instantaneous location of water-air interface. In addition to the full scale contour plots, enlarged air region plots at later compression times are shown on the right of each figure.

The velocity streamlines in the fully occupied chambers appear to be straight as shown in Fig.3.10; very small and weak secondary flows are present near the top corner of the chamber. The pressure drop of the flow through the metal foam is small compared to the absolute pressure of air, yet it is large enough to overcome small local pressure instabilities that could otherwise results in vortices. In the partially occupied chambers, vortices are formed outside the porous region, yet, inside the porous region, the flow is stable, as shown in Fig.3.11 and Fig.3.12. With the same metal foam, smaller compression speeds result in larger vortex sizes. The effects of the two different metal foams (10PPI vs. 40PPI) are shown to be insignificant on the size of the vortices formed outside the metal foam regions.

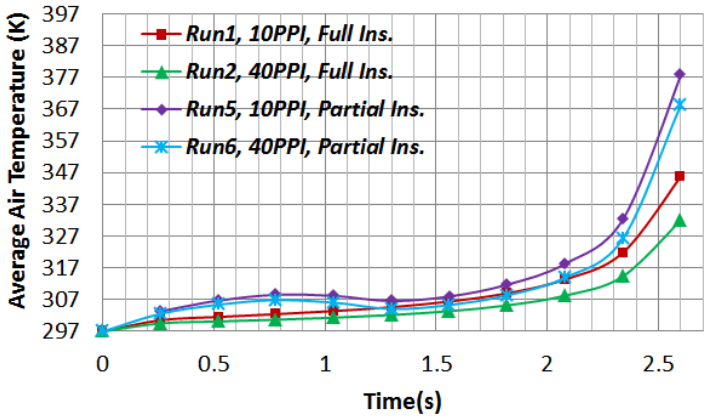

(a) Water inlet velocity: 0.103m/s

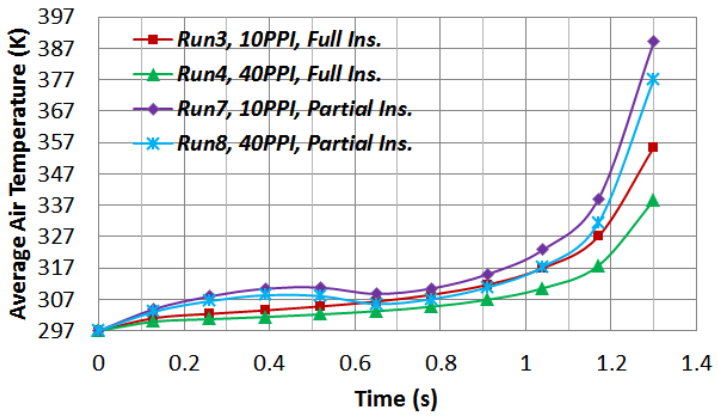

(b) Water inlet velocity: 0.206m/s

Fig.3.9 Air temperature rise during compression

At the end of compression, the air temperature distribution becomes highly non-uniform, as volume decreases. Relatively high local temperature values are seen in regions very close to the top cap. In fully-occupied chambers, the high local air temperature values at the end of compression are mainly due to the stagnant flow. Since Nusselt numbers between the flow and the porous medium depend on Reynolds number, stagnant flow impedes heat transfer. In partially occupied chambers, the high local air temperature values at the end of compression are high due to lack of heat transfer surfaces; even though, the local flow is relatively active, as shown by a vortex that has been formed since the earlier stage of compression.

The computed solid temperature fields at the end of compression for various cases are shown in Fig.3.13. In the fully occupied chambers, the largest local temperature rise in the solid is less than 1K. In the partially occupied chambers, the largest local temperature rise is 57.4K, which occurs at the top surface of the metal foam. The bulk of the solid material is maintained at a low temperature. Great differences in local temperature values between the air and the solid are found in certain regions. This confirms the advantage of using the

two-energy equation formulation instead of the one-energy, equilibrium formulation for this kind of problem.

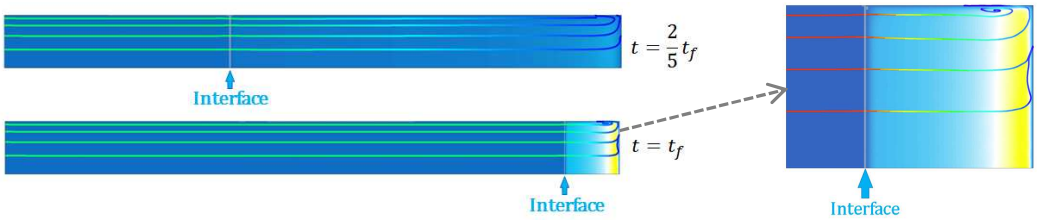

(a) Run1, 10PPI, Full Insert, $U_0 = 0.103m/s$, $t_f = 2.6$s

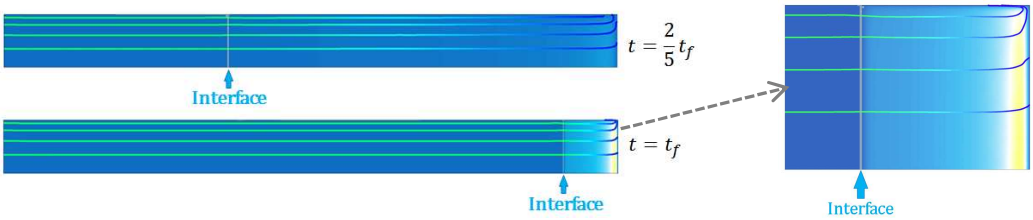

(b) Run2, 40PPI, Full Insert, $U_0 = 0.103m/s$, $t_f = 2.6$s

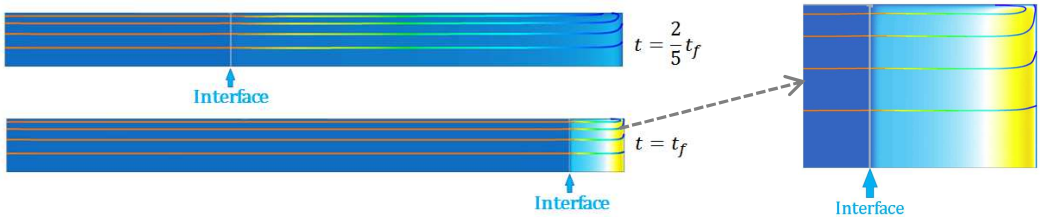

(c) Run3, 10PPI, Full Insert, $U_0 = 0.206m/s$, $t_f = 1.3$s

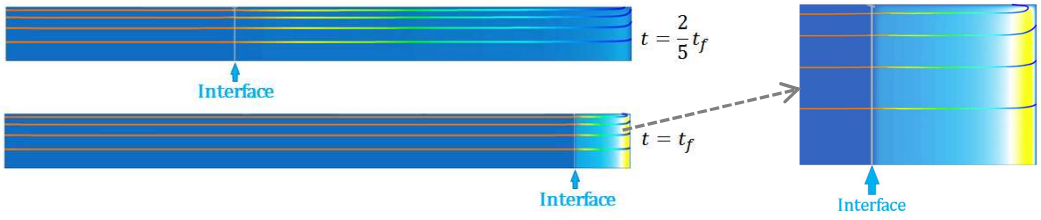

(d) Run4, 40PPI, Full Insert, $U_0 = 0.206m/s$, $t_f = 1.3$s

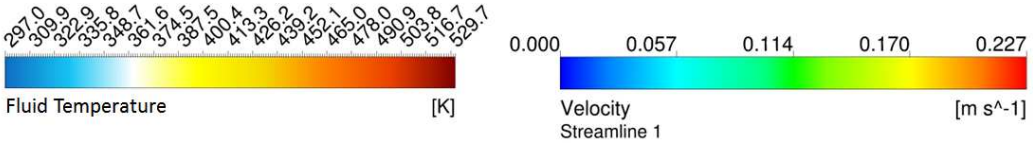

Fig.3.10 Temperature field and velocity streamline at different times during compression, fully occupied chambers. (Gravity points from right to left)

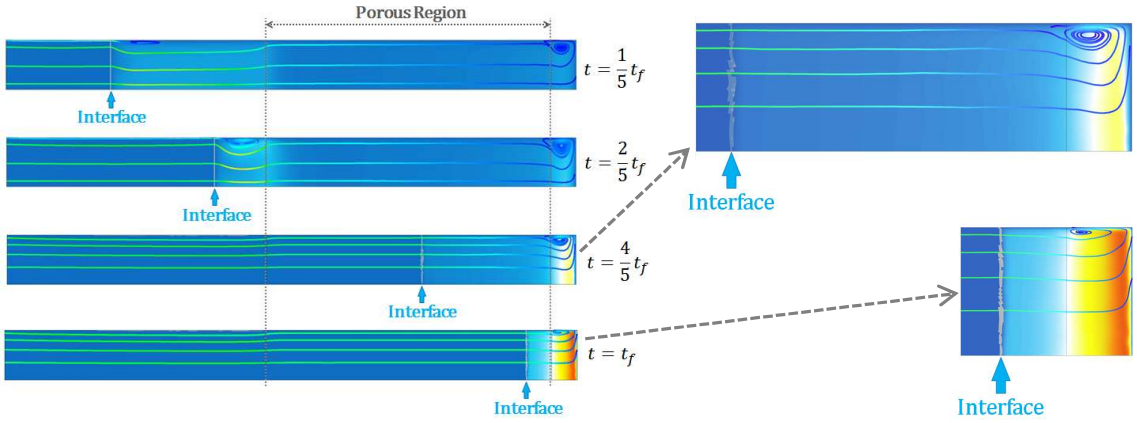

(a) Run5, 10PPI, Partial Insert, $U_0 = 0.103m/s$, $t_f = 2.6$s

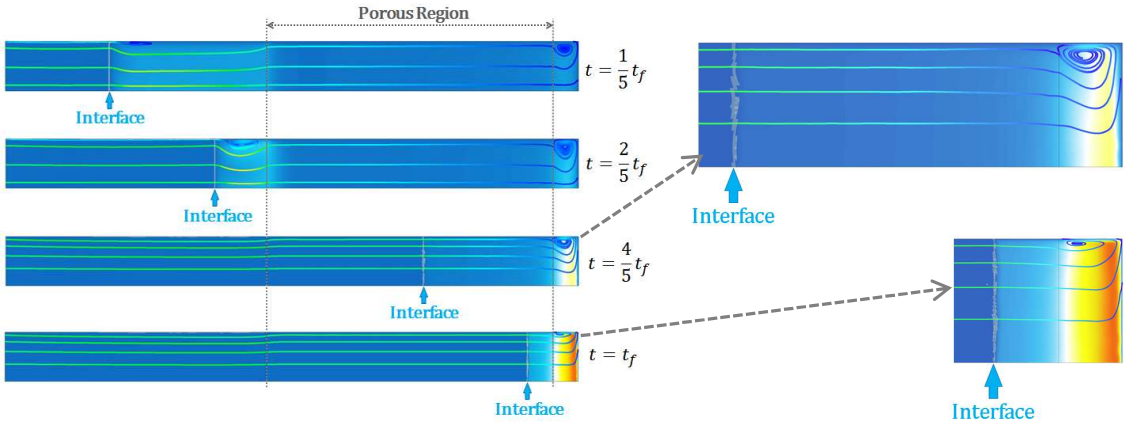

(b) Run6, 40PPI, Partial Insert, $U_0 = 0.103m/s$, $t_f = 2.6$s

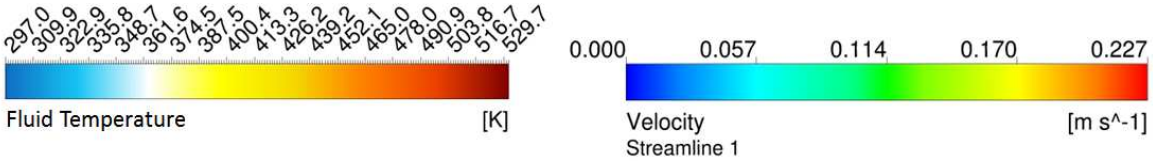

Fig.3.11 Temperature field and velocity streamline at different times during compression, partially occupied chambers, low compression speed. (Gravity points from right to left)

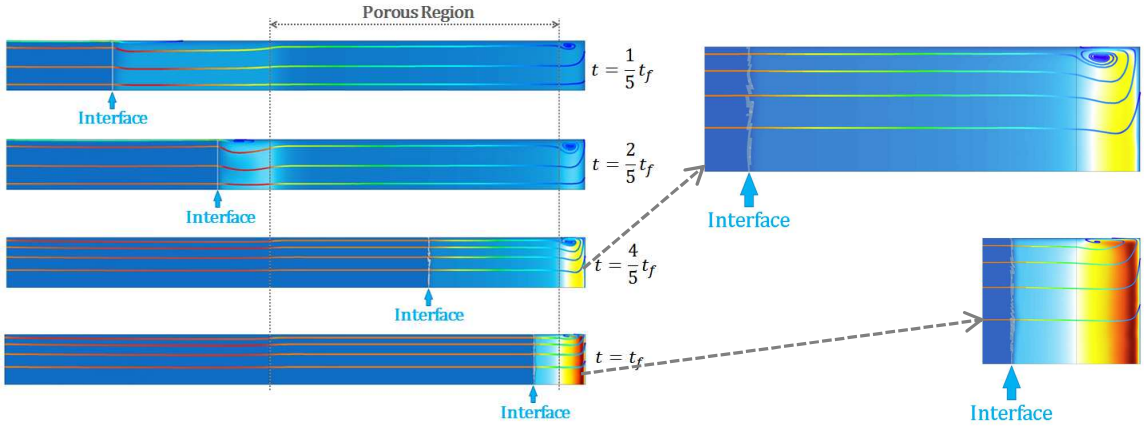

(a) Run7, 10PPI, Partial Insert, $U_0 = 0.206m/s$, $t_f = 1.3$s

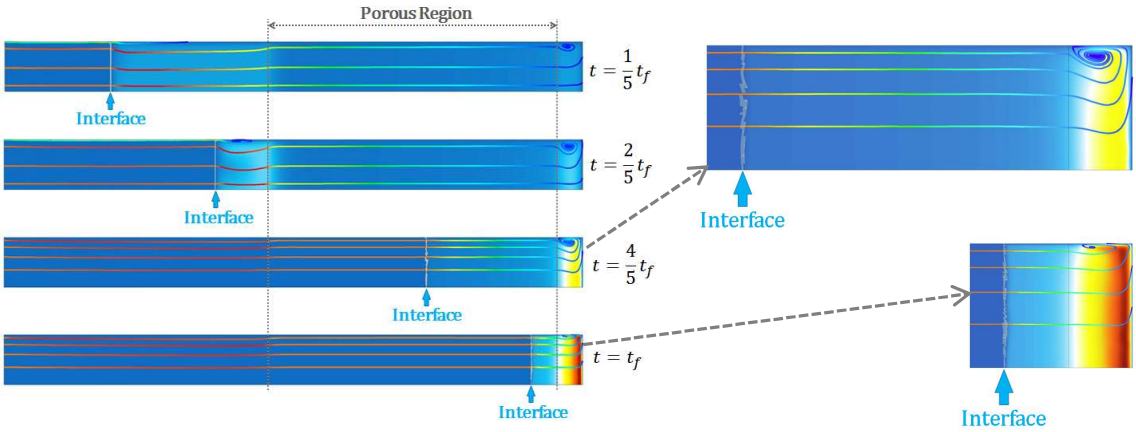

(b) Run8, 40PPI, Partial Insert, $U_0 = 0.206m/s$, $t_f = 1.3$s

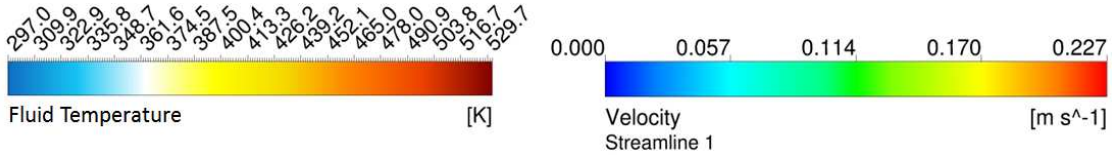

Fig.3.12 Temperature field and velocity streamline at different times during compression, partially occupied chambers, high compression speed. (Gravity points from right to left)

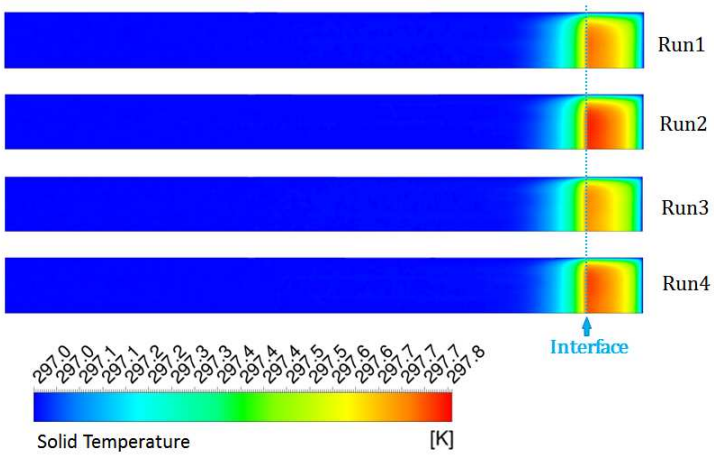

(a) Fully occupied chambers

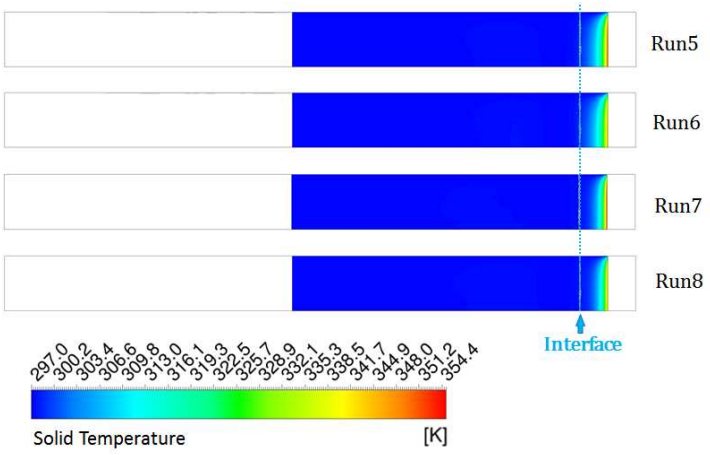

(b) Partially occupied chambers

Fig.3.13 Temperature distributions in the metal foam at the end of compression, $t = t_f$. (Gravity points from right to left)

3.2.4. Adding Dispersion Effect

In this section, a CFD simulation of one of the previous faster compression cases is conducted, but thermal dispersion is added. The chamber is fully occupied by the 10 PPI foam. The compression speed and total compression time are: 0.206 m/s and 1.3 s. The continuity, momentum, and energy equations for the solid phase are the same. The energy equation for the fluid mixture is:

$$\frac{\partial \epsilon\left(c_p \langle\rho\rangle^f \langle T\rangle^f\right)}{\partial t} + \epsilon\nabla \cdot \left(\langle\vec{u}\rangle^f \langle\rho\rangle^f c_p \langle T\rangle^f\right)$$

$$= \epsilon\nabla \cdot k_f \nabla\langle T\rangle^f - \nabla \cdot \rho c_p \langle\vec{\tilde{u}}\tilde{T}\rangle^f + h_V(\langle T_s\rangle^s - \langle T\rangle^f) + \epsilon\frac{\partial\langle p\rangle^f}{\partial t} \tag{3.20}$$

The thermal dispersion term is modeled as,

$$-\rho c_p \langle\vec{\tilde{u}}\tilde{T}\rangle^f = \bar{\bar{k}}_{\text{dis}} \nabla\langle T\rangle \tag{3.21}$$

The following dispersion closure model is used [40]

$$\frac{k_{\text{dis,XX}}}{k_f} = 0.022\frac{\text{Pe}_D{}^2}{(1-\epsilon)} \qquad (\text{Pe}_D < 10) \tag{3.22}$$

$$\frac{k_{\text{dis,YY}}}{k_f} = 0.022\frac{\text{Pe}_D{}^{1.7}}{(1-\epsilon)^{1.4}} \qquad (\text{Pe}_D < 10) \tag{3.23}$$

$$\frac{k_{\text{dis,XX}}}{k_f} = 2.7\frac{\text{Pe}_D}{\epsilon^{1/2}} \qquad (\text{Pe}_D > 10) \tag{3.24}$$

$$\frac{k_{\text{dis,YY}}}{k_f} = 0.052(1-\epsilon)^{1/2}\text{Pe}_D \qquad (\text{Pe}_D > 10) \tag{3.25}$$

where XX is the local streamwise direction and YY is the local cross-streamwise direction. In this example, this model is implemented in the transport equation for the CFD simulation.

The bulk temperature rise of the air is computed and compared to a simulation of the same case but without thermal dispersion (Fig.3.14). Results of both cases show that, though the compression time is very short and isentropic compression would lead to a temperature of 575K, the insert is effective in suppressing the temperature rise. Further, they show that during the latter period of compression, the calculated temperature of the case with dispersion is less. This is due to larger thermal gradients in the flow for that case and the resulting higher heat transfer. Thermal dispersion has an influence on the bulk temperature when temperatures and temperature gradients rise to the point where dispersion becomes significant. The flow fields at two times during compression are shown

in Fig.3.15. The warmer region is in the upper portion of the chamber in which the velocities, heat transfer coefficients and thermal dispersion coefficients are low.

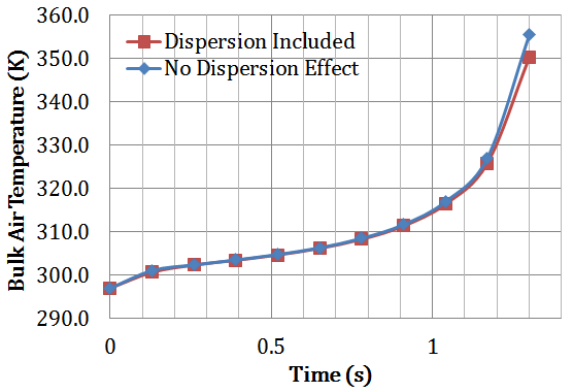

Fig.3.14 Bulk temperature of air

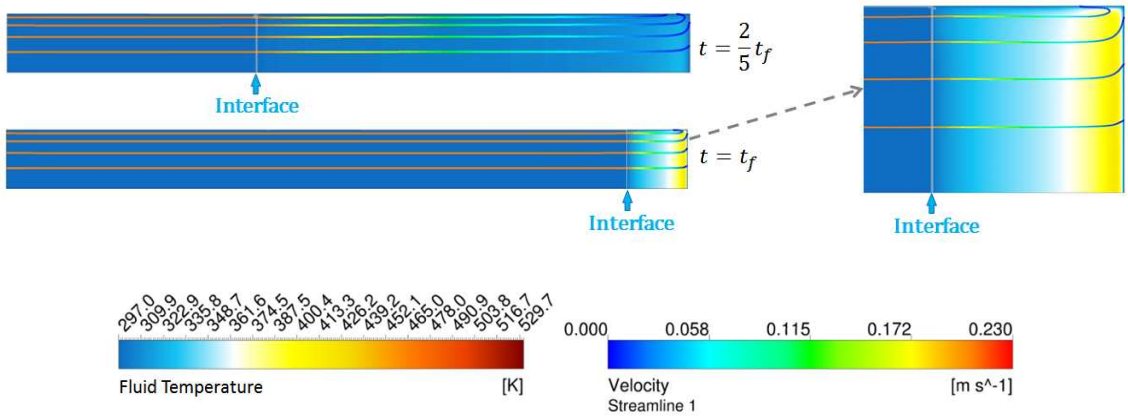

Fig.3.15 Temperature field and velocity streamline (note that up is to the right in this figure)

3.3. Two-D Simulation of High-Pressure Compression with Metal Foam Insert

A simulation of high-pressure compression is done. The chamber is completely inserted with the 10PPI metal foam. The chamber has a length of 0.4826m and a radius of 0.0381m. This is the same geometry as discussed in section 2.2.1, and same computational mesh is

used. The energy transport equation for the solid phase in the porous media modeling was implemented in the Fluent solver as a User-Defined-Function.

The constant speed (15cm/s) compression starts from 7bar and stops when the gas pressure reaches 210bar after 3.08. The fluid mixture temperature distribution and streamlines in the air phase are shown in Fig.3.16. Comparing the flow field of this case to the previous compression simulation cases where the chamber had no insert (Fig.2.9), one sees a distinctive difference that is the lack of secondary flows in the metal-foam inserted chamber. This is caused by the flow resistive effect of the metal foam. The temperature of the air is also much lower due to cooling provided by the metal foam surface area. The mass-averaged temperature of air at the final compression state is 389.2K, much lower than the previous empty chamber compression cases. This leads to a compression efficiency of 66.5%, which is a 20% improvement to the non-inserted chamber.

The temperature distribution in the metal foam is shown in Fig.3.17. The metal foam above the water-air interface has the highest local temperature because it has been previously heated up by air, and also because it is farthest from the chamber walls; the metal foam region submerged in water is effectively cooled by water. Metal foams can effectively cool the air during compression.

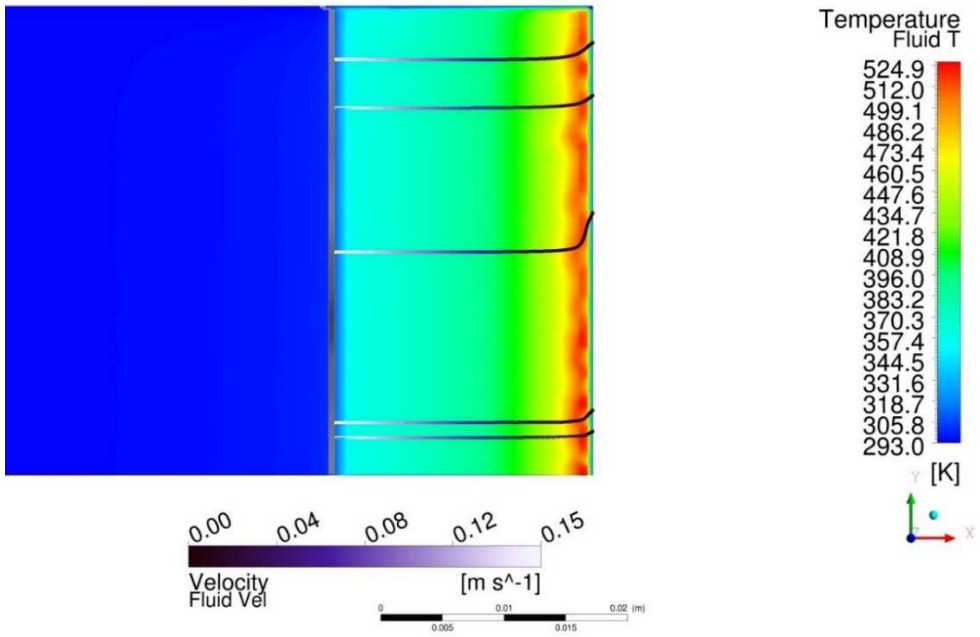

Fig.3.16 Temperature of the fluid mixture and streamlines in the air phase at 210bar (gravity points from right to left; bottom boundary is the centerline of the cylinder, the streamline start from the water-air interface and stop at the top cap of the chamber)

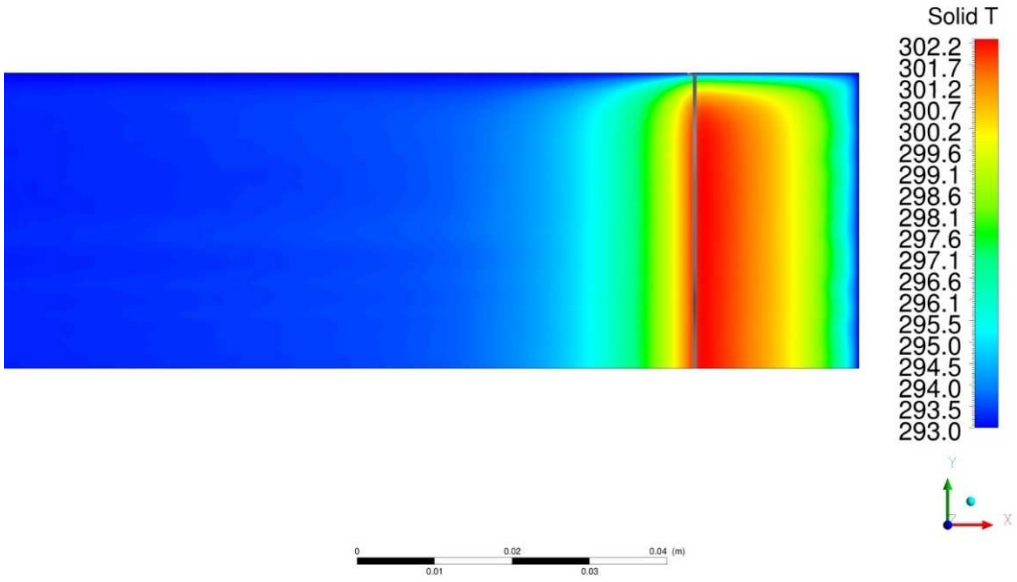

Fig.3.17 Temperature of the metal foam at 210bar (gravity points from right to left; bottom boundary is the centerline of the cylinder; vertical gray line in the contour plot indicates water-air interface location)

3.4. Design Analysis of the Liquid Piston Chamber Shape

3.4.1. Introduction

Traditionally, the compression chamber has a cylindrical shape. In this section, we explore the compression efficiency change as a result of varying profiles of cross-sectional diameter along the axis of the chamber. This leads to a compression chamber with an axisymmetric curved side wall that makes it assume a gourd-like shape. The advantage of such shape is that it offers an opportunity for more complex flow features in the chamber during compression that enhance mixing and heat transfer. To analyze the wall shape effect, the shape is parameterized and a series of design exploration cases based on orthogonal arrays is created. The orthogonal arrays of experiments have been often used with the Taguchi optimization method [75], and shown to be capable of reducing the number of realizations, whether experimental or numerical [76, 77]. In this section, four shape parameters are recognized, each having four different values of parameters of interest. Based on the orthogonal array method, sixteen orthogonal arrays of the design are created, each is analyzed by a CFD run. The results give insight into the fluid flow and heat transfer characteristics in the compression chamber and lead to an optimized chamber shape within the chosen parameter domain.

The effects of the shape of a liquid piston compression chamber are studied. A schematic of a randomly shaped chamber is shown in Fig.3.18. The 10PPI and 93% porosity metal foam studied in section 3.1 is inserted in the chamber. As water is pumped into the chamber (on the left of the figure – note that gravity is from right to left in this figure), a rising water-air interface acts as a piston surface that compresses the air in the chamber. The compression process starts with pre-compressed air at 7 bars and 293 K, and ends at 210 bars after 3 seconds. The chamber volume is fixed at $2.19 \times 10^{-3}\, m^3$. These are the same conditions as studied for the cylindrical chamber volume in the previous

section. The chamber's main shape is governed by five parameters, as labelled in Fig.3.18: the length, the inlet radius, the maximum radius, the top cap radius and the location of the maximum radius with respect to the inlet. Of interest to the design is analysis with the different ratios of these five shape parameters, since the chamber volume is fixed. Four dimensionless shape parameters based on these five length scales are created:

$$\mathcal{P}_1 = \frac{\mathbb{L}}{R_m} \tag{3.26}$$

$$\mathcal{P}_2 = \frac{R_m}{R_i} \tag{3.27}$$

$$\mathcal{P}_3 = \frac{X_m}{\mathbb{L}} \tag{3.28}$$

$$\mathcal{P}_4 = \frac{R_m}{R_t} \tag{3.29}$$

The domains of interest for these parameters are: $1 \leq \mathcal{P}_1 \leq 8$, $1.5 \leq \mathcal{P}_2 \leq 6$, $0.333 \leq \mathcal{P}_3 \leq 0.8$, $1.5 \leq \mathcal{P}_4 \leq 6$. Four levels (values) for each parameter within its own domain are chosen for investigation. They are given in Table 3.1. Using the "L'16 Array," based on the Taguchi design method [75], sixteen orthogonal exploratory shape designs are created, and given in Table 3.4. A design is an array of shape parameter values, and it is orthogonal to other arrays of parameter values. The orthogonal array method can be proven mathematically. A practical perspective is that (1) each design is most different from the others, and (2) in all 16 designs, each level of each parameter has been combined with all other levels of other parameters. CFD simulations are done for different designs.

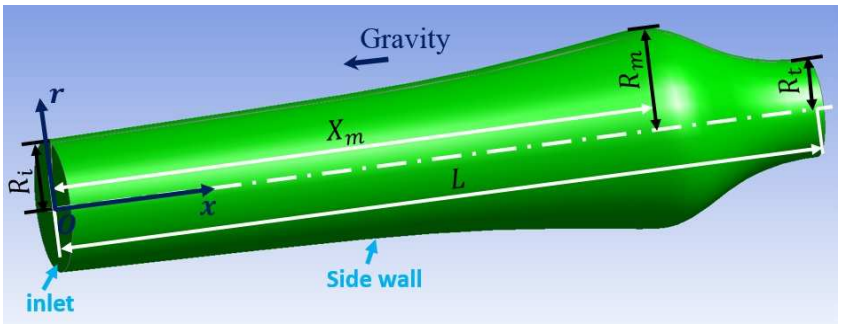

Fig.3.18 Schematic of liquid piston chamber and shape parameters

The CFD simulations are done using commercial CFD Software ANSYS Fluent. Used are the same approach that combines the VOF and porous media models, and the same numerical discretization methods as used in the previous sections. For the sixteen runs, the computational grids vary from 60,790 cells to 78,794 cells, all having progressively fine grids near the wall. The time step sizes of all simulations vary from $1 \times 10^{-5}s$ to $2.5 \times 10^{-5}s$. (The liquid piston speeds vary from 0.049m/s to 1.87m/s.) The choice of grid and time step size are in line with previous studies on grid independence [78].

Table 3.5 Levels of investigation for different parameters

	$\mathcal{L}_1$	$\mathcal{L}_2$	$\mathcal{L}_3$	$\mathcal{L}_4$
$\mathcal{P}_1$	1	2	4	8
$\mathcal{P}_2$	1.5	2	4	6
$\mathcal{P}_3$	0.333	0.5	0.65	0.8
$\mathcal{P}_4$	1.5	2	4	6

Table 3.6 Exploratory designs based on orthogonal arrays

	$\mathcal{P}_1$	$\mathcal{P}_2$	$\mathcal{P}_3$	$\mathcal{P}_4$
Design 1	1 $(\mathcal{L}_1)$	1.5 $(\mathcal{L}_1)$	0.333 $(\mathcal{L}_1)$	1.5 $(\mathcal{L}_1)$
Design 2	1 $(\mathcal{L}_1)$	2 $(\mathcal{L}_2)$	0.5 $(\mathcal{L}_2)$	2 $(\mathcal{L}_2)$
Design 3	1 $(\mathcal{L}_1)$	4 $(\mathcal{L}_3)$	0.65 $(\mathcal{L}_3)$	4 $(\mathcal{L}_3)$
Design 4	1 $(\mathcal{L}_1)$	6 $(\mathcal{L}_4)$	0.8 $(\mathcal{L}_4)$	6 $(\mathcal{L}_4)$
Design 5	2 $(\mathcal{L}_2)$	1.5 $(\mathcal{L}_1)$	0.5 $(\mathcal{L}_2)$	4 $(\mathcal{L}_3)$
Design 6	2 $(\mathcal{L}_2)$	2 $(\mathcal{L}_2)$	0.333 $(\mathcal{L}_1)$	6 $(\mathcal{L}_4)$
Design 7	2 $(\mathcal{L}_2)$	4 $(\mathcal{L}_3)$	0.8 $(\mathcal{L}_4)$	1.5 $(\mathcal{L}_1)$
Design 8	2 $(\mathcal{L}_2)$	6 $(\mathcal{L}_4)$	0.65 $(\mathcal{L}_3)$	2 $(\mathcal{L}_2)$
Design 9	4 $(\mathcal{L}_3)$	1.5 $(\mathcal{L}_1)$	0.65 $(\mathcal{L}_3)$	6 $(\mathcal{L}_4)$
Design 10	4 $(\mathcal{L}_3)$	2 $(\mathcal{L}_2)$	0.8 $(\mathcal{L}_4)$	4 $(\mathcal{L}_3)$
Design 11	4 $(\mathcal{L}_3)$	4 $(\mathcal{L}_3)$	0.333 $(\mathcal{L}_1)$	2 $(\mathcal{L}_2)$
Design 12	4 $(\mathcal{L}_3)$	6 $(\mathcal{L}_4)$	0.5 $(\mathcal{L}_2)$	1.5 $(\mathcal{L}_1)$
Design 13	8 $(\mathcal{L}_4)$	1.5 $(\mathcal{L}_1)$	0.8 $(\mathcal{L}_4)$	2 $(\mathcal{L}_2)$
Design 14	8 $(\mathcal{L}_4)$	2 $(\mathcal{L}_2)$	0.65 $(\mathcal{L}_3)$	1.5 $(\mathcal{L}_1)$
Design 15	8 $(\mathcal{L}_4)$	4 $(\mathcal{L}_3)$	0.5 $(\mathcal{L}_2)$	6 $(\mathcal{L}_4)$
Design 16	8 $(\mathcal{L}_4)$	6 $(\mathcal{L}_4)$	0.333 $(\mathcal{L}_1)$	4 $(\mathcal{L}_3)$

3.4.2. CFD Results

The temperature distributions at the end of the compression processes for different chamber designs are shown in Fig.3.19 - Fig.3.34. In these plots, the bottom boundary is the centerline of the chamber and gravity points horizontally from right to left. Water enters the chamber from the left boundarys as shown in the figures. The water rises in temperature only very slightly during compression and is occupying regions colored by dark blue, as shown in these plots. Large temperature gradients are present in the air phase. The different chamber shapes affect air temperature distributions differently.

The air temperature distribution in the radial direction at the end of compression is mostly affected by how abruptly the chamber's radius changes near the top cap, or the parameter $\mathcal{P}_4$. As shown in Fig.3.21-Fig.3.23, Fig.3.27, and Fig.3.28, when the wall slope is large near the top cap, flow near the side wall next to the water-air interface has a lower temperature due to a radial velocity component, and heat transfer is thus enhanced.

Large air temperature gradients in the axial direction commonly exist in all the chambers. The reason is that flow near the top cap of the chamber is generally near stagnation, which limits the amount of heat transfer between the metal foam and the top cap, and flow near the water-air interface has a high velocity and, thus, offers good heat transfer. However, when the chamber is longer, or has a larger aspect ratio, $\mathcal{P}_1$, a relatively smaller percentage of the air volume is in stagnation next to the top cap and a larger portion of the air volume continues to have good heat transfer to the metal foam insert, as shown by Fig.3.27, Fig.3.29, Fig.3.32, and Fig.3.33.

Although the chamber's shape has complicated effects on the flow and temperature fields, these preliminary observations based on Fig.3.19-Fig.3.34 show that, in general, large aspect ratios $(\frac{\mathbb{L}}{R_m})$ and abrupt changes in radius may agitate the flow, which is beneficial for heat transfer and cooling of the compressed air.

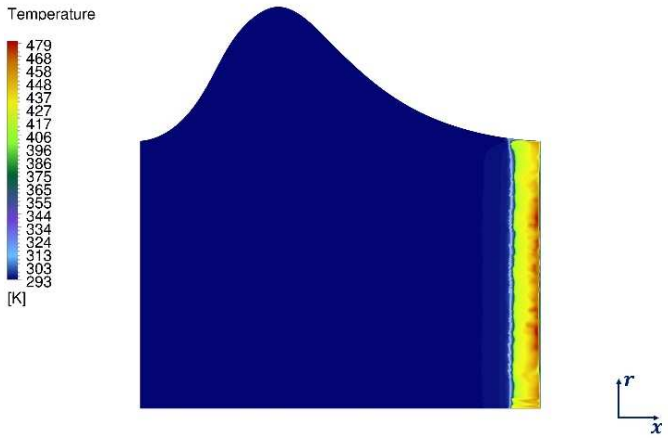

Fig.3.19 Temperature field at the end of compression - Design 1. (Gravitation points to the left; bottom boundary is centreline)

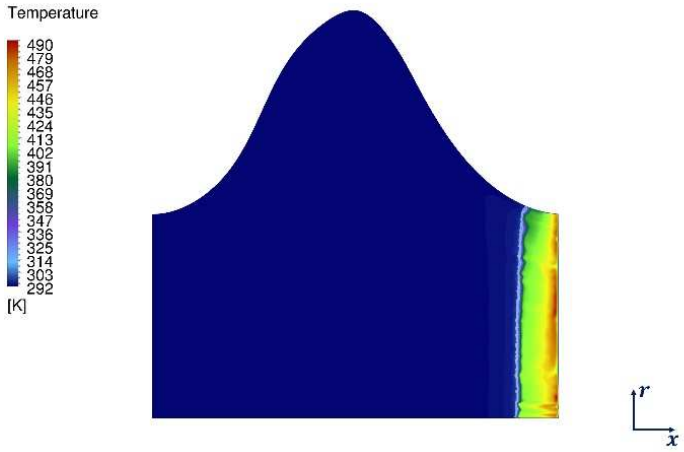

Fig.3.20 Temperature field at the end of compression - Design 2. (Gravitation points to the left; bottom boundary is centreline)

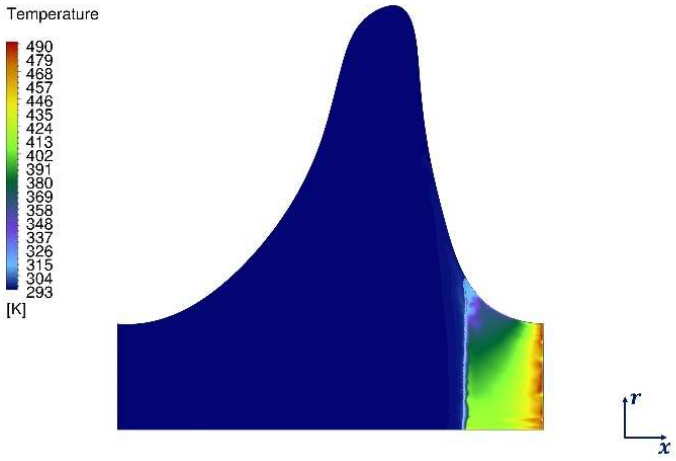

Fig.3.21 Temperature field at the end of compression - Design 3. (Gravitation points to the left; bottom boundary is centreline)

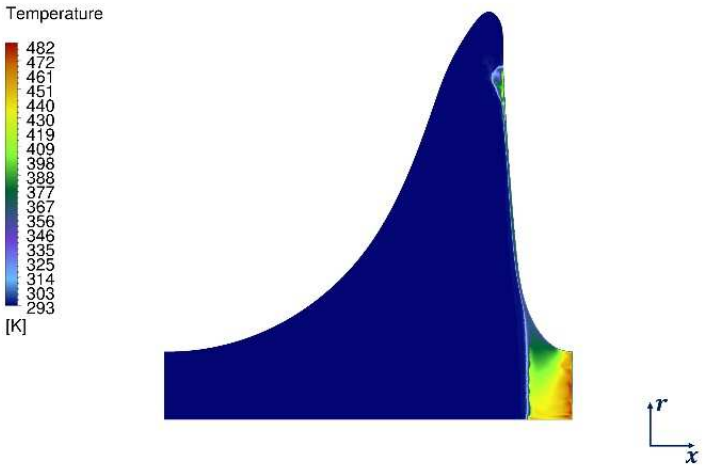

Fig.3.22 Temperature field at the end of compression - Design 4. (Gravitation points to the left; bottom boundary is centreline)

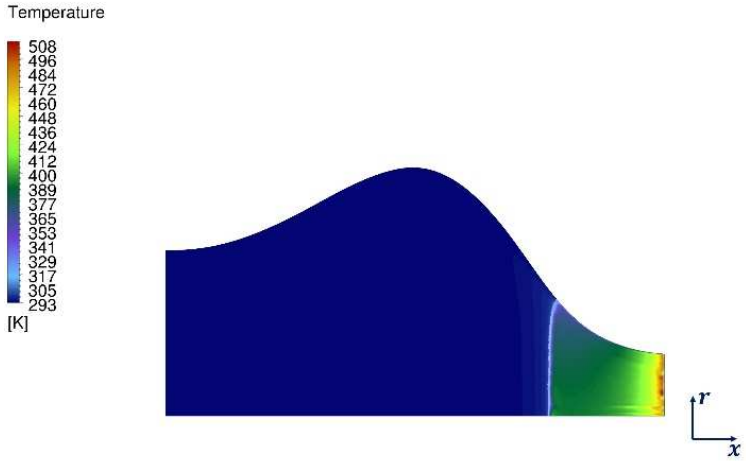

Fig.3.23 Temperature field at the end of compression - Design 5. (Gravitation points to the left; bottom boundary is centreline)

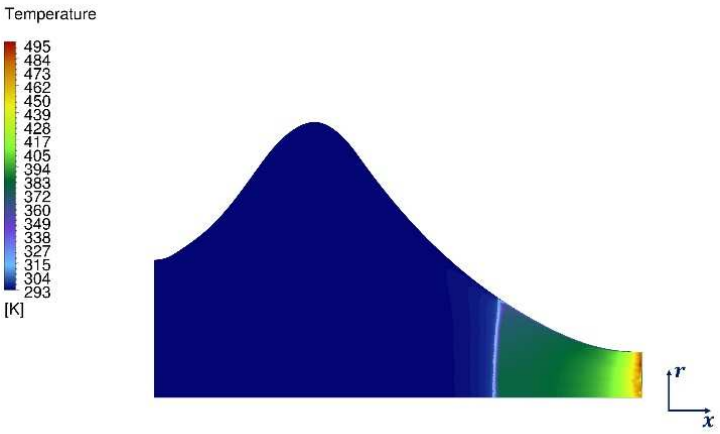

Fig.3.24 Temperature field at the end of compression - Design 6. (Gravitation points to the left; bottom boundary is centreline)

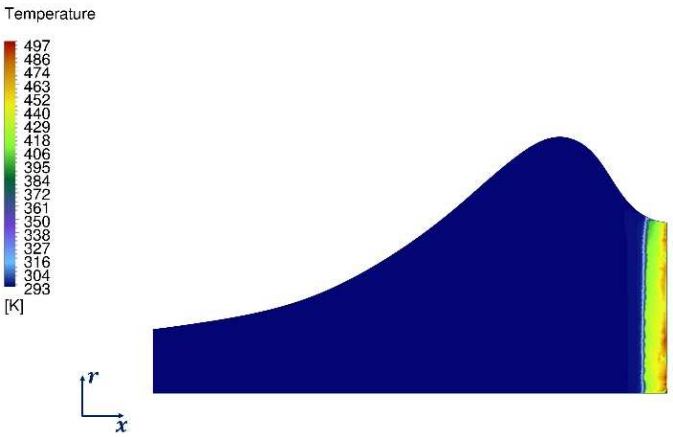

Fig.3.25 Temperature field at the end of compression - Design 7. (Gravitation points to the left; bottom boundary is centreline)

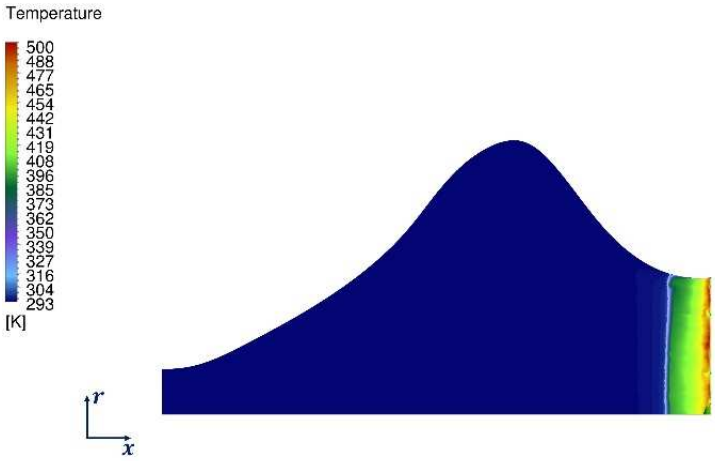

Fig.3.26 Temperature field at the end of compression - Design 8. (Gravitation points to the left; bottom boundary is centreline)

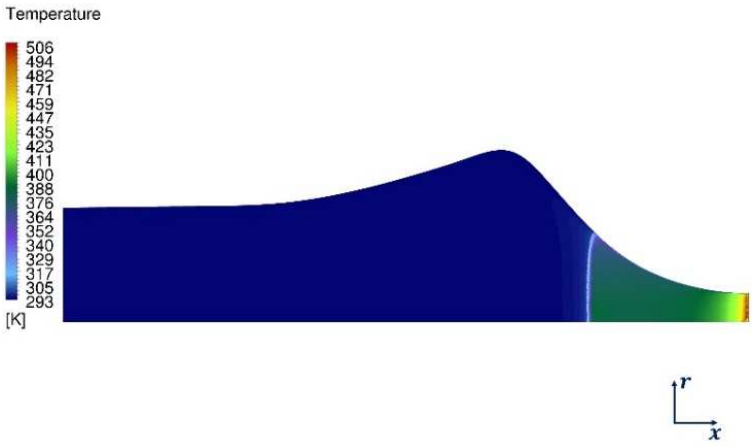

Fig.3.27 Temperature field at the end of compression - Design 9. (Gravitation points to the left; bottom boundary is centreline)

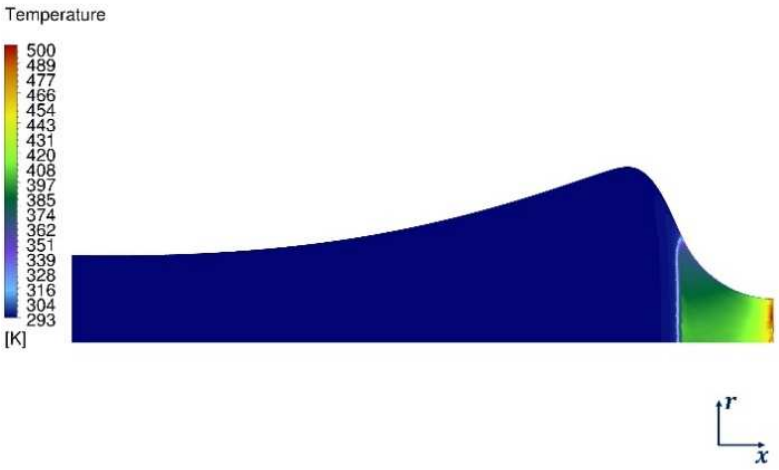

Fig.3.28 Temperature field at the end of compression - Design 10. (Gravitation points to the left; bottom boundary is centreline)

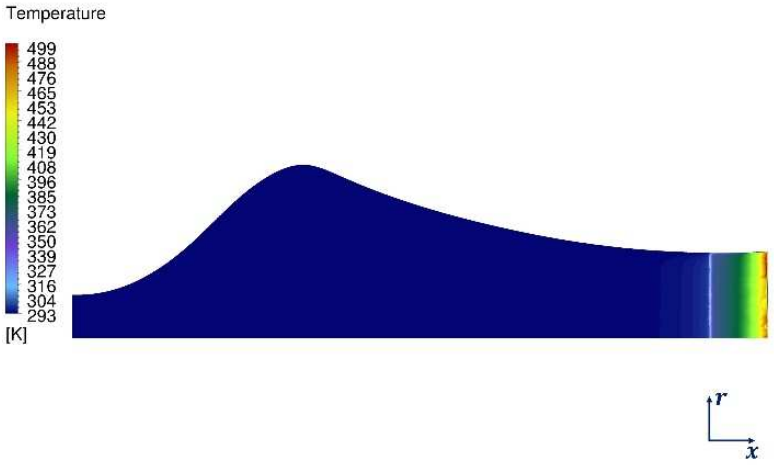

Fig.3.29 Temperature field at the end of compression - Design 11. (Gravitation points to the left; bottom boundary is centreline)

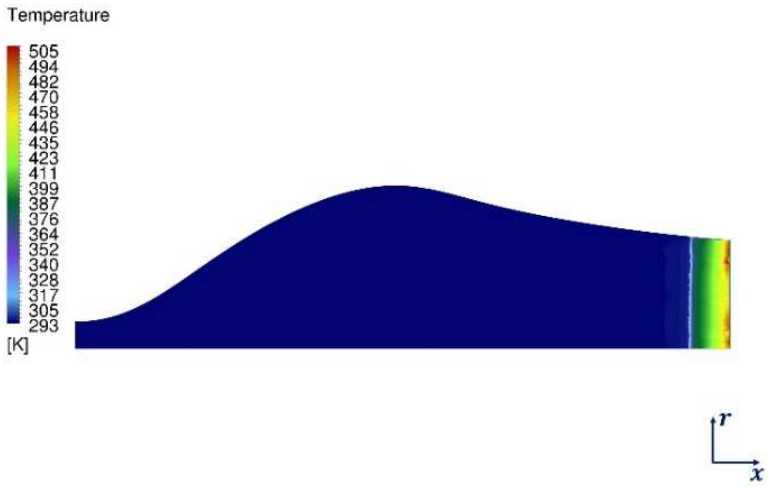

Fig.3.30 Temperature field at the end of compression - Design 12. (Gravitation points to the left; bottom boundary is centreline)

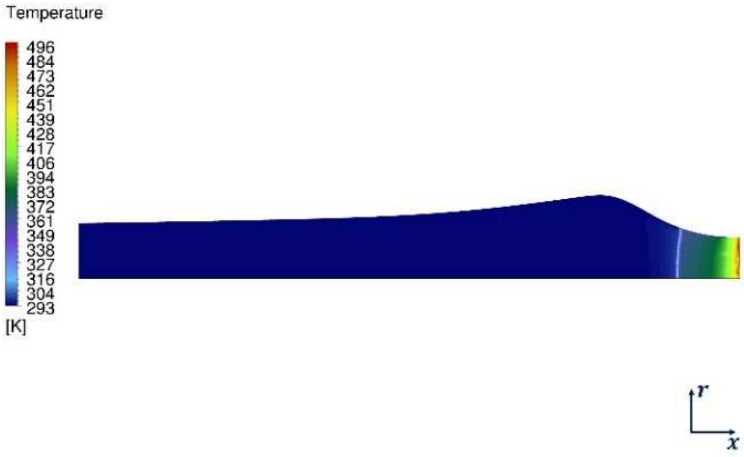

Fig.3.31 Temperature field at the end of compression - Design 13. (Gravitation points to the left; bottom boundary is centreline)

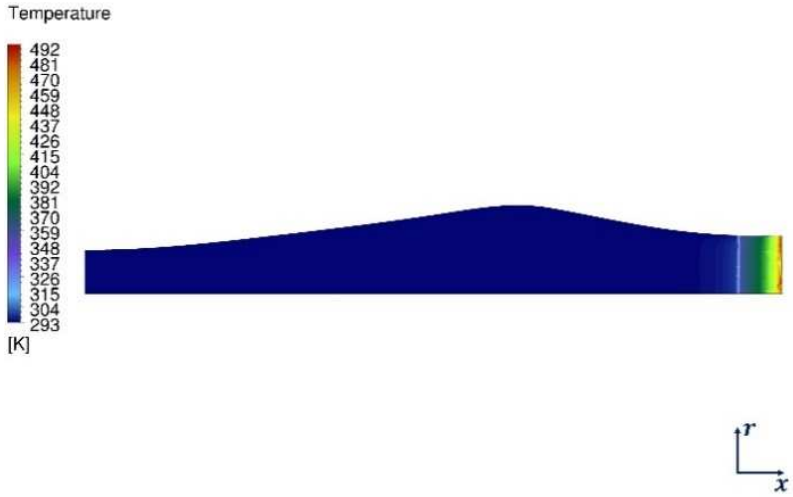

Fig.3.32 Temperature field at the end of compression - Design 14. (Gravitation points to the left; bottom boundary is centreline)

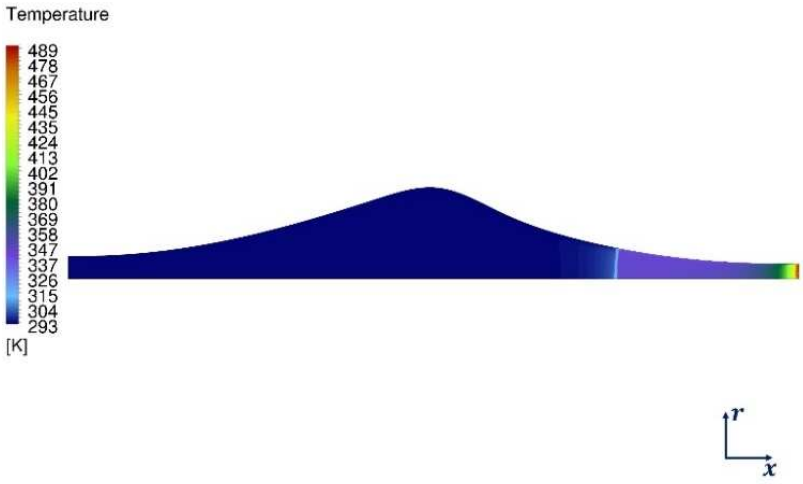

Fig.3.33 Temperature field at the end of compression - Design 15. (Gravitation points to the left; bottom boundary is centreline)

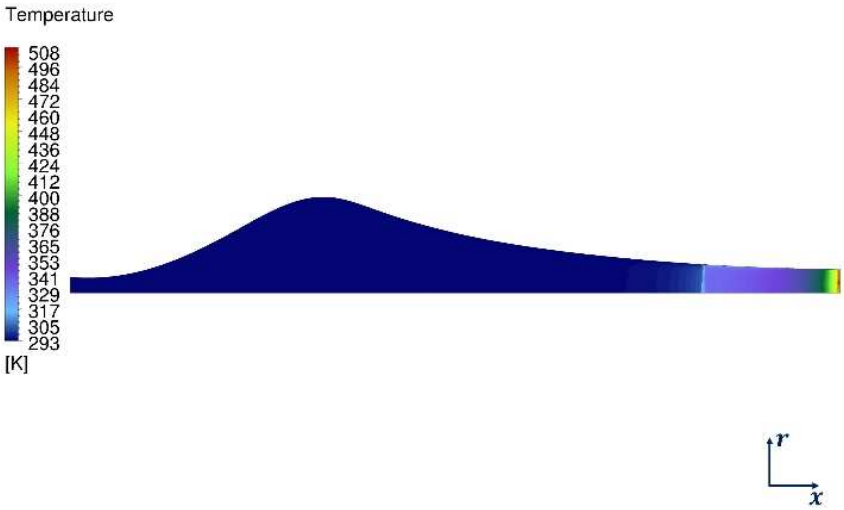

Fig.3.34 Temperature field at the end of compression - Design 16. (Gravitation points to the left; bottom boundary is centreline)

The thermodynamics efficiencies of different chamber designs are calculated based on the CFD results. The compression efficiency is defined according to Eq.(1.31). The efficiency values for different chamber designs are calculated and shown in Fig.3.35. A comparison of efficiencies among different chambers is in line with the observations made in the previous section. Keeping the chamber longer and making the cross-sectional radius change steeper are beneficial for achieving higher efficiency (Designs 16 and 15). In general, the steep change of cross-sectional radius results in more radial flow, which enhances mixing; the long, thin shape on the top increases the length that the flow travels, and, thus, its speed, which offers more opportunity for heat transfer.

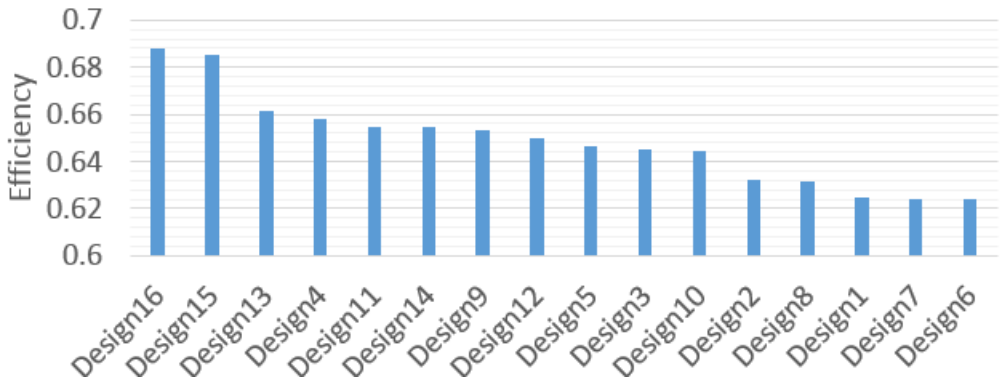

Fig.3.35 Efficiency of different chamber designs

Note that in the definition of efficiency, the work that ejects the compressed air from the compression chamber into the storage vessel is not included as part of the storage energy. The CAES system may be designed to recover this ejection work and use it for the next compression cycle, which results in an increase in efficiency of about 20%, but the comparison among different chambers remains the same.

3.4.3. Design Exploration

The individual effect of each parameter at each level is calculated. Table 3.6 shows the sixteen orthogonal arrays with each level of each parameter appearing in four designs. Therefore, the effect of a parameter at a certain level is the average of the efficiency values of the corresponding four designs in which this level of the parameter appears. For example, the effect of $\mathcal{P}_1$ at $\mathcal{L}_1$ is:

$$\eta_{\mathcal{P}_1\_\mathcal{L}_1} = \frac{1}{4}\left(\eta_{Design1} + \eta_{Design2} + \eta_{Design3} + \eta_{Design4}\right) \tag{3.30}$$

Similarly, the effects of all other parameters at different levels are calculated. The results are shown in Fig.3.36. For each parameter, the relation between its levels and the efficiency is non-linear. For parameters $\mathcal{P}_1$ and $\mathcal{P}_2$, the minimum efficiencies correspond to their middle levels, in both cases a parameter value of 2, and the maximum efficiencies correspond to the maximum levels within their own parameter domains. For parameters $\mathcal{P}_3$

and $\mathcal{P}_4$, the maximum efficiencies correspond to their middle levels, $\mathcal{L}_2$ for $\mathcal{P}_3$, and $\mathcal{L}_3$ for $\mathcal{P}_4$. Therefore, the best design of the chamber would have the following shape parameters:

$$\mathcal{P}_1 = 8, \quad \mathcal{P}_2 = 6, \quad \mathcal{P}_3 = 0.5, \quad \mathcal{P}_4 = 4$$

In designing the chamber, changing one shape parameter may not be as effective toward improving the efficiency as changing another. The effects of different parameters are thus compared. For each parameter, a relative effect is calculated by taking the difference between maximum and minimum efficiencies and dividing it by the difference between the maximum and minimum levels. The calculated relative effects: $\frac{\Delta\eta}{\Delta\mathcal{P}_1}$, $\frac{\Delta\eta}{\Delta\mathcal{P}_2}$, $\frac{\Delta\eta}{\Delta\mathcal{P}_3}$, and $\frac{\Delta\eta}{\Delta\mathcal{P}_4}$, are, respectively: 0.0058, 0.0040, 0.0016, and 0.0039. As can be seen, the aspect ratio of the chamber (the length to the maximum radius ratio) is the most important parameter; the effects of the maximum radius to the inlet radius and to the top radius are similar and less important than the aspect ratio; the axial location of the maximum radius is the least important of the four shape parameters.

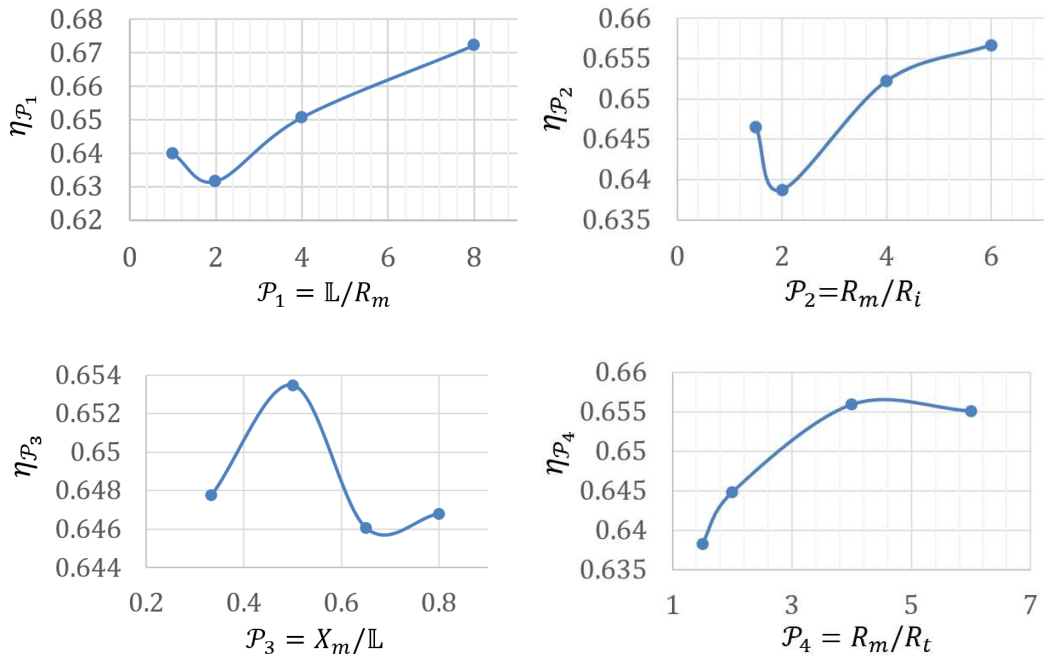

Fig.3.36 Individual effects of shape parameters on efficiency

3.5. Application of the Metal Foam in the Expansion Process

3.5.1. Problem Description

In this section, the expansion process is studied. Expansion is essential for extracting work from the compressed air. The expansion process takes place in the same liquid piston chamber. Initially, a small portion of the chamber ($6.82 \times 10^{-5} m^3$, 3.1% of the chamber volume) is occupied by compressed air at 210bar, and the rest filled with water. Then the high-pressure air is expanded and pushes water out of the chamber to generate power, until the gas pressure reaches 7bar. Two different expansion trajectories, constant power output and constant speed, are studied for each of the two situations: a chamber inserted with a 10 PPI metal foam matrix, and a no-insert chamber. The chamber has the same dimensions are the one studied in section 3.3; the length is 0.4826m and the radius is 0.0381m. Details of the cases are listed in Table 3.7. In addition, a no-insert case is simulated with inclusion of the phase change modeling. The formulation of the phase change process is the same as described in section 2.3. The computational mesh is the same as used in section 2.2 for the compression simulations. A schematic of the mesh and the boundaries are shown in Fig.3.37. During expansion, the temperature of air tends to drop. It is shown from the simulation that as air temperature drops, the metal foam quickly heats the air, and, thus, increases the power output. The CFD simulation results of these cases will be discussed in the following.

Table 3.7 Simulation cases for expansion study

Case Name	Description
Empt_ConstPow	No insert; constant power output, 1746.6W, at the water outlet
Empt_ConstU	No insert; constant speed expansion, 0.15m/s
Empt_ConstU_Cond-Evap	No insert; constant speed expansion, 0.15m/s; phase change modeling included
10PPI_ConstPow	Chamber inserted with 10PPI metal foam; constant power output, 1746.6W, at the water outlet
10PPI_ConstU	Chamber inserted with 10PPI metal foam; constant speed expansion, 0.15m/s

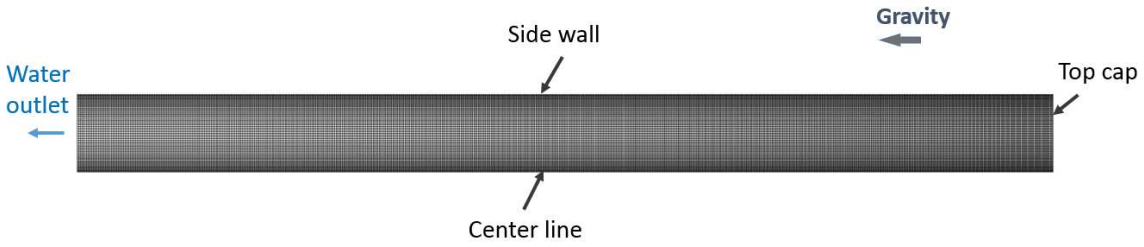

Fig.3.37 Computational domain for 2-D high-pressure expansion simulations

3.5.2. No-Insert Chamber with Constant Power Output

In the case "Empt_ConstPow," a User-Defined-Function is used to calculate the instantaneous velocity boundary condition at the outlet based on the required power output value and the instantaneous pressure. The calculated expansion trajectory and the pressure at the outlet are shown in Fig.3.38 and Fig.3.39. In order to maintain constant power output, the outlet flow speed increases as the pressure drops during expansion. Near the end of expansion, the very small pressure difference between the gas and the outlet requires a

large expansion speed in order to maintain the same power, thus causing unstable fluctuations as shown in plots.

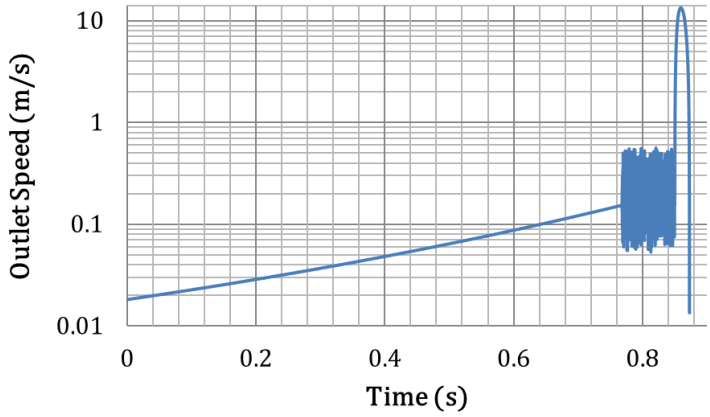

Fig.3.38 Expansion piston trajectory for case Empt_ConstPow

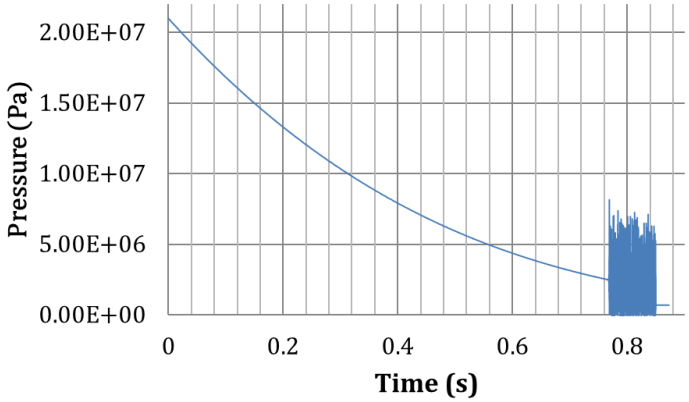

Fig.3.39 Instantaneous outlet pressure of case Empt_ConstPow

Temperature distributions in water and air are shown for selected times in Fig.3.40 to Fig.3.43. In the beginning, as the expansion speed is small, the air temperature drop is slow. Near the end of expansion, when the speed increases and becomes unstable, the water-air interface breaks up (at 0.856s), accompanied by a rapid drop in air temperature.

This slow-fast expansion trajectory only is beneficial to the beginning phase of the expansion as the piston movement is slow and the temperature drops. The fast expansion near the end led to steep temperature drop and break-up of the water-air interface.

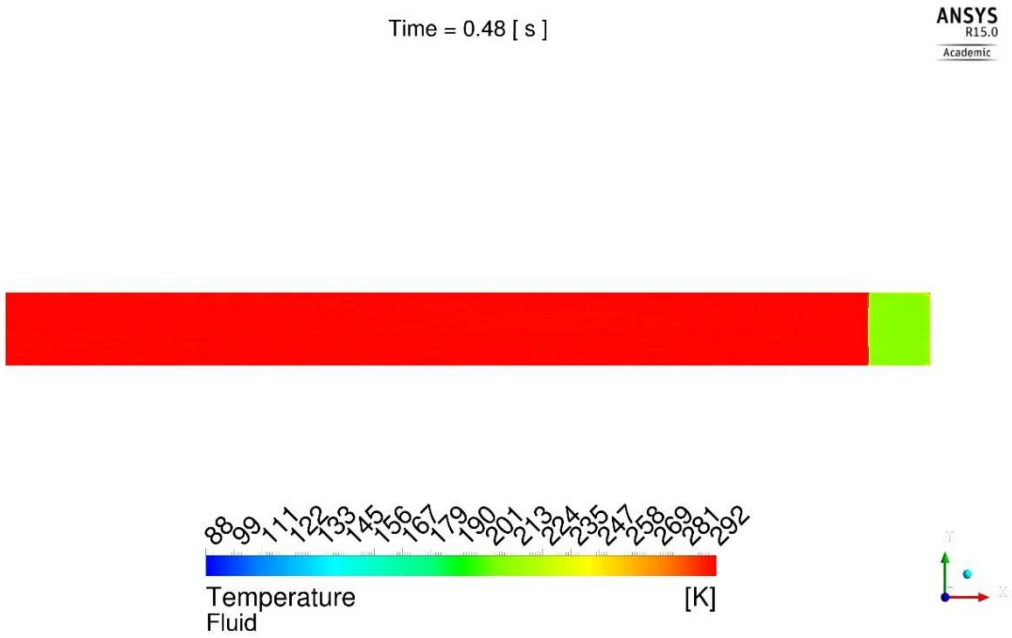

Fig.3.40 Temperature distribution, case Empt_ConstPow, 0.48s. (Gravity points to the left; the bottom boundary represents centerline)

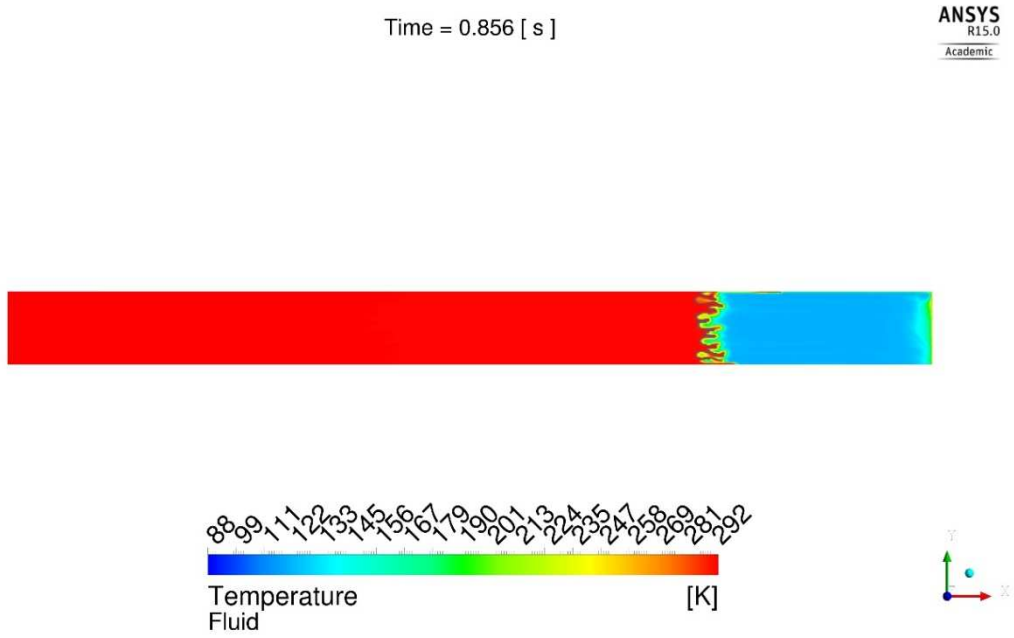

Fig.3.41 Temperature distribution, case Empt_ConstPow, 0.856s. (Gravity points to the left; the bottom boundary represents centerline)

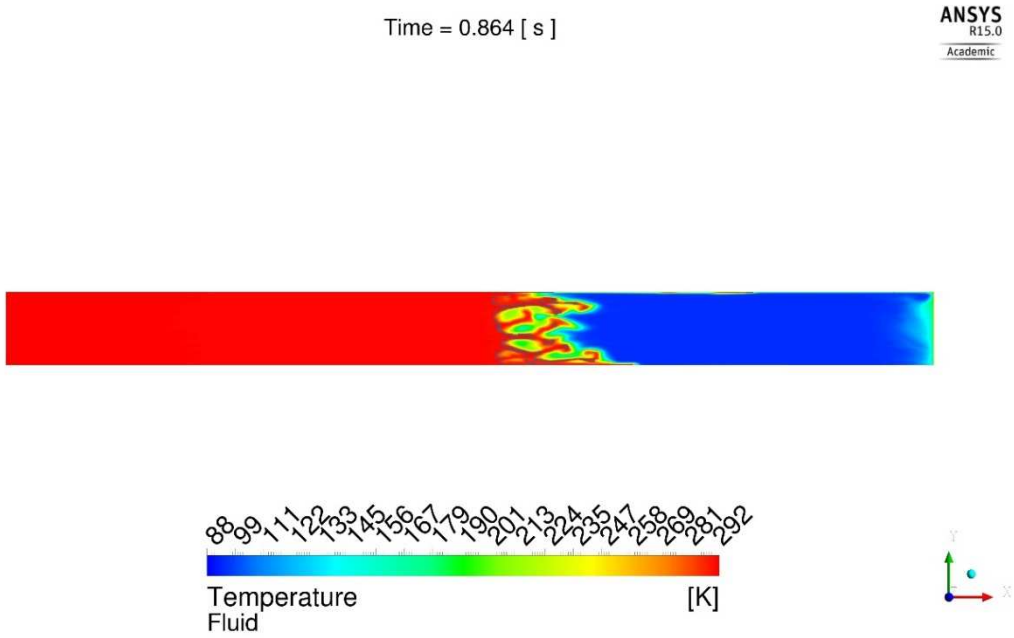

Fig.3.42 Temperature distribution, case Empt_ConstPow, 0.864s. (Gravity points to the left; the bottom boundary represents centerline)

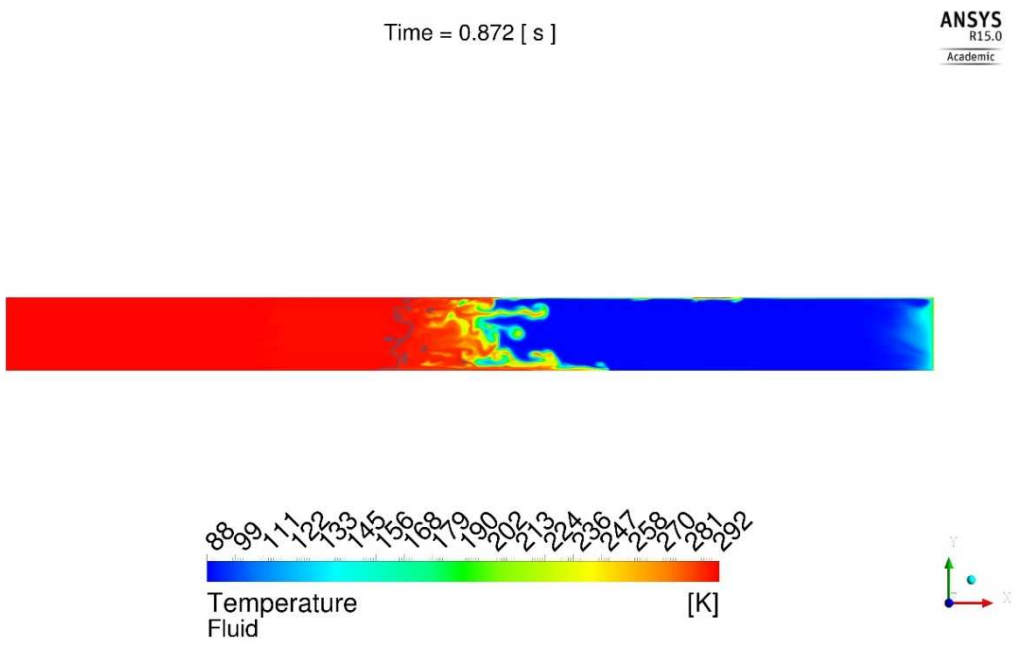

Fig.3.43 Temperature distribution, case Empt_ConstPow, 0.872s. (Gravity points to the left; the bottom boundary represents centerline)

3.5.3. No-Insert Chamber with Constant Speed Expansion

In the case "Empt_ConstU," a constant speed, 0.15m/s, is applied on the outlet boundary condition. The calculated outlet pressure vs. time is shown in Fig.3.44. Comparing to the outlet pressure profile of the previous case, Empt_ConstPow, we observe that when the outlet speed is a constant, the pressure drop is significant in the first half of the expansion process. This is due to the relatively faster expansion speed in the beginning leading to a more rapid temperature drop that leads to a more rapid pressure drop, which, eventually causes a loss of power output.

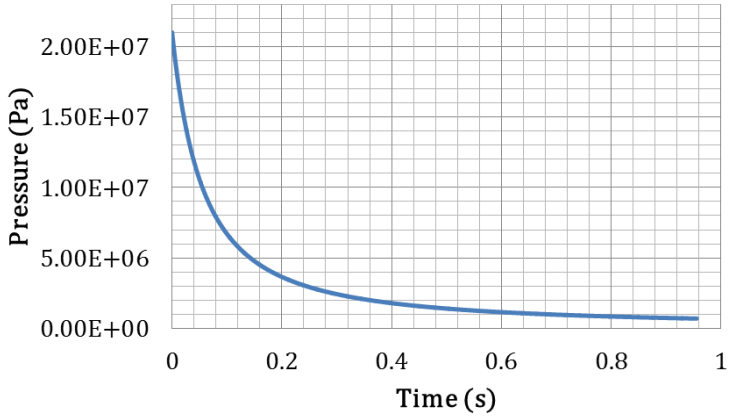

Fig.3.44 Instantaneous outlet pressure of case Empt_ConstU

Temperature distributions in water and air are shown for selected times in Fig.3.45 to Fig.3.48. The air flow field is also different in the present case from the previous constant power output case. At about 0.515s, secondary flows start to develop near the top cap region of the chamber, which eventually lead to the formation of a vortex in the top corner near the end of expansion. Although the secondary flows helped mix some of the hotter, near-wall fluid with the colder fluid from the inner regions of the chamber, this effect is rather insignificant in improving the overall heat transfer of the entire air volume. At the end of expansion, the lowest air temperature in the constant-speed expansion case is higher than that of the previous constant-power output case.

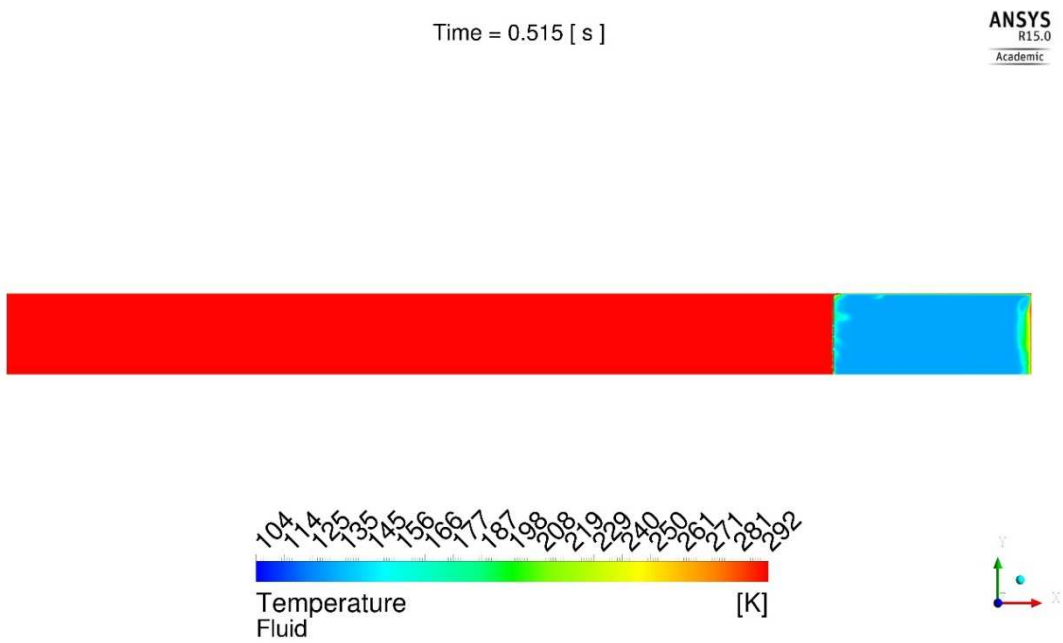

Fig.3.45 Temperature distribution, case Empt_ConstU, 0.515s. (Gravity points to the left; the bottom boundary represents centerline)

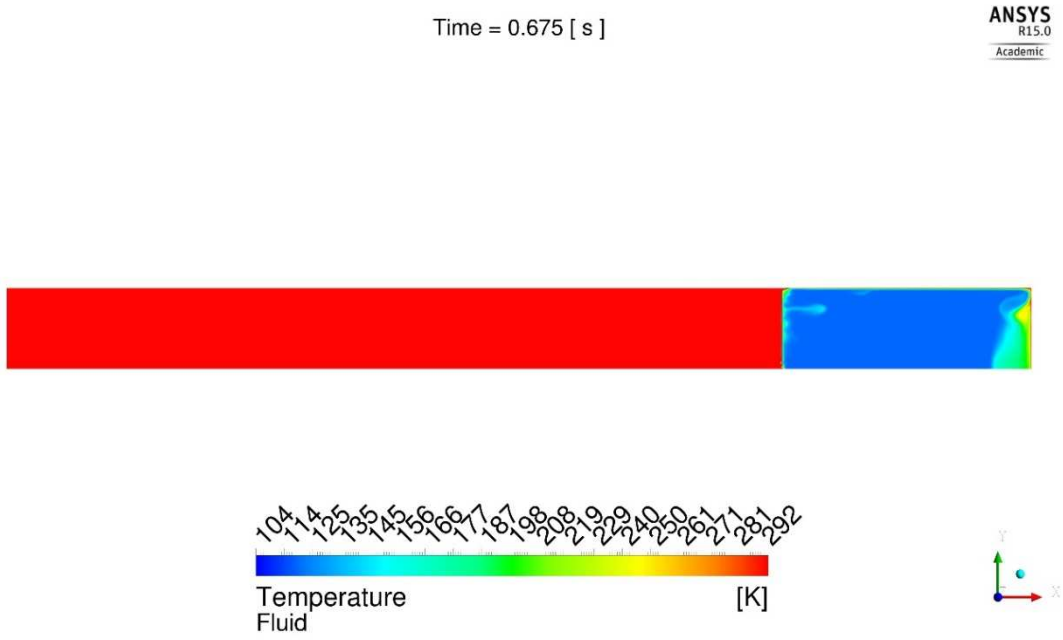

Fig.3.46 Temperature distribution, case Empt_ConstU, 0.675s. (Gravity points to the left; the bottom boundary represents centerline)

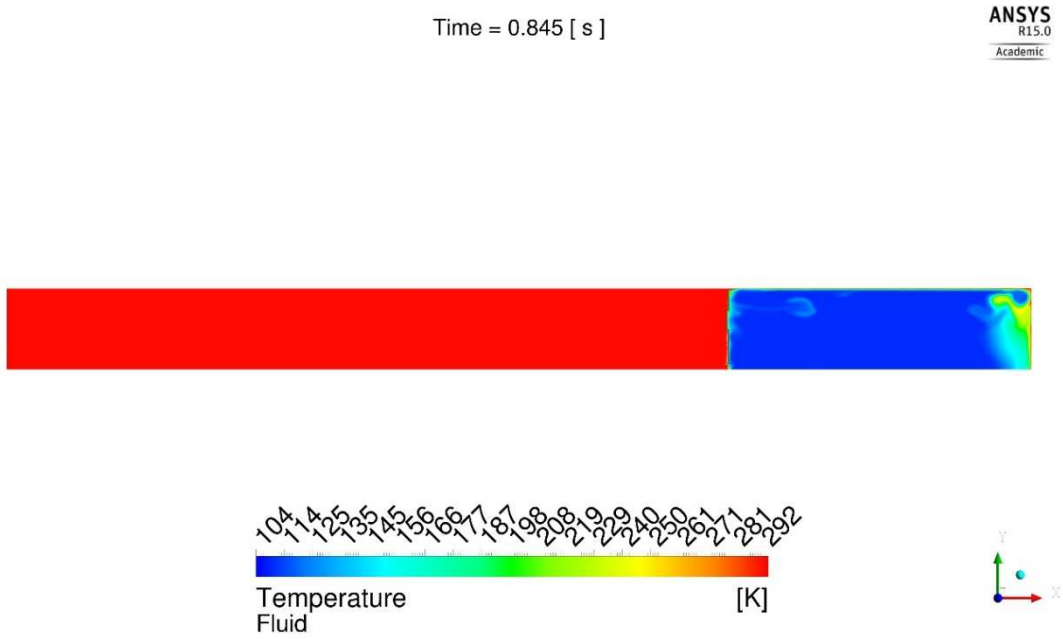

Fig.3.47 Temperature distribution, case Empt_ConstU, 0.845s. (Gravity points to the left; the bottom boundary represents centerline)

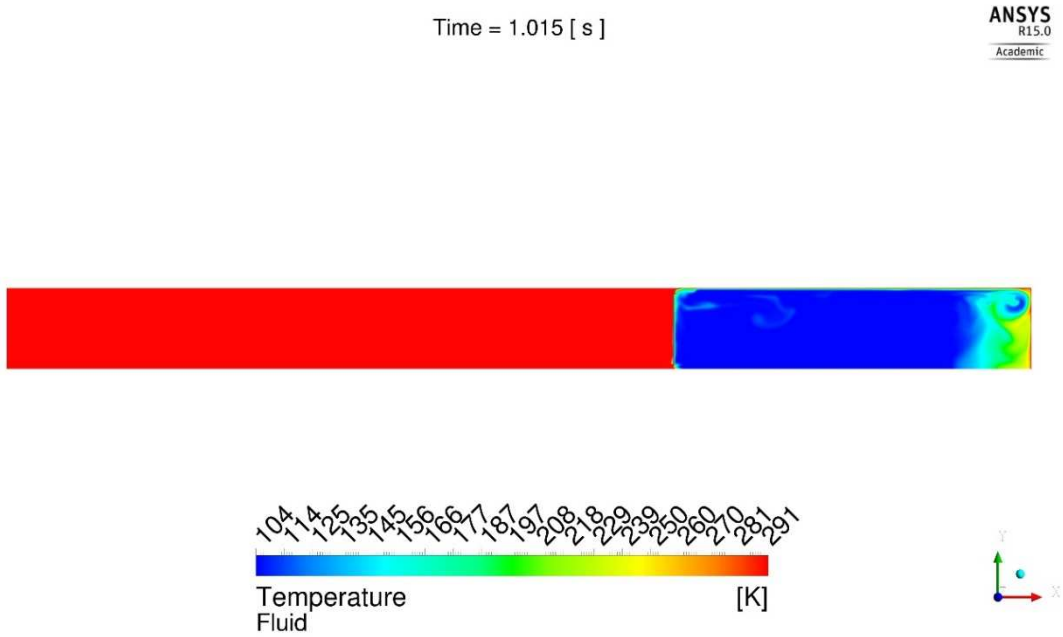

Fig.3.48 Temperature distribution, case Empt_ConstU, 1.015s. (Gravity points to the left; the bottom boundary represents centerline)

3.5.4. No-Insert Chamber with Constant Speed Expansion and Phase Change Modeling

In the case "Empt_ConstU_Cond-Evap," simulated is the same problem as discussed in the preceding section, but with consideration of a phase change process. The same phase change modeling approached as detailed in section 2.3 is applied in this simulation case. The saturation pressure of vapor at 293K is 2338Pa, which gives an initial vapor mass fraction of 0.0000691. Including the phase change has no significant effect on the overall pressure output. As shown in Fig.3.49, the two outlet pressure profiles with and without modeling of phase change almost collapse on one another.

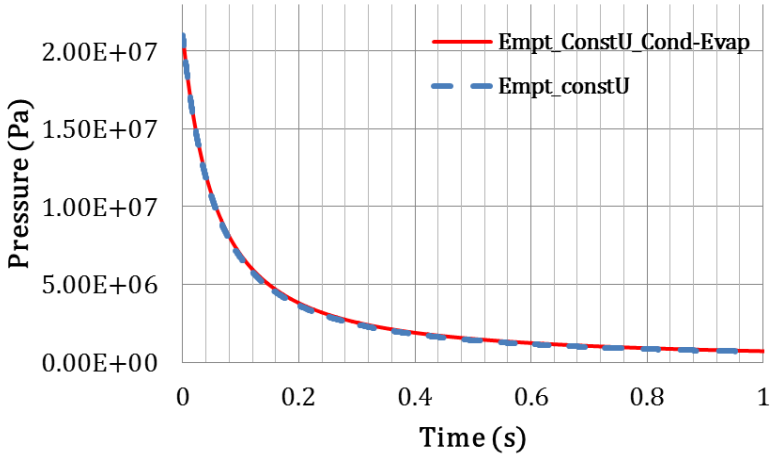

Fig.3.49 Comparison of outlet pressure profiles for the no-insert chambers with and without inclusion of phase change

During expansion, the air temperature drops. As vapor is present in the air region, condensation occurs and clouds of liquid water are formed in the gas phase. In the simulation, this "cloud" is represented numerically by the volume fraction of liquid water in the mixture. The calculated temperature distributions and the "cloud" distributions are shown at selected times in Fig.3.50 to Fig.3.53. The temperature field shows similar secondary flow features as observed in the previous simulation case, Empt_ConstU. The

condensation process starts around 0.515s, at a location of low temperature near the top cap. As the expansion process proceeds, the condensed “water cloud” is carried and transported by the secondary flows. It develops into a larger vortex in later times. The latent heat released from condensation reduces the temperature drop of the gas, but its effect is rather small in the present case.

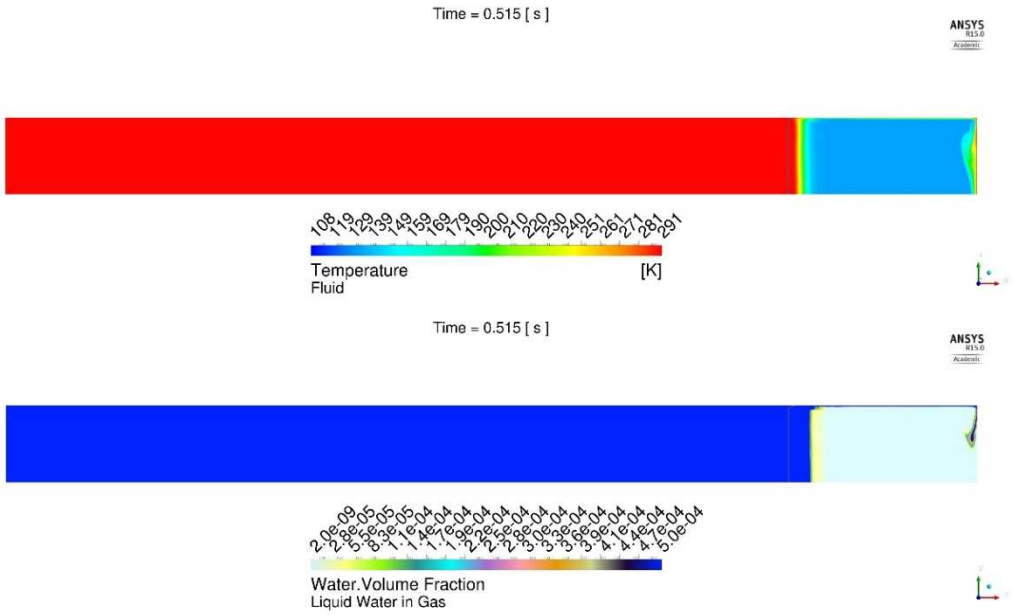

Fig.3.50 Temperature distribution (upper plot) and “cloud” (lower plot), Empt_ConstU_Cond-Evap, 0.515s. (Gravity points to the left; the bottom boundary represents centerline)

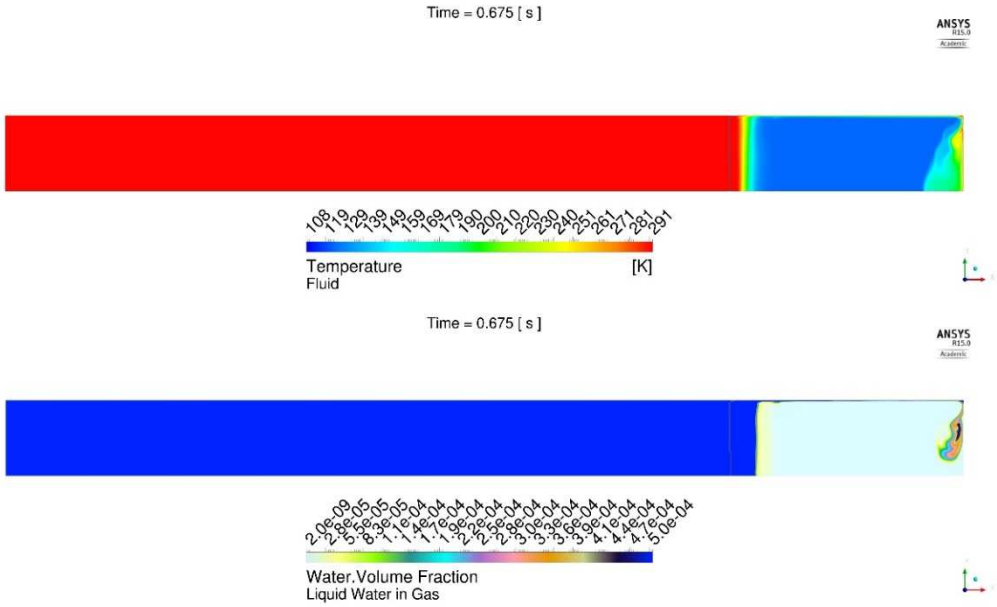

Fig.3.51 Temperature distribution (upper plot) and "cloud" (lower plot), Empt_ConstU_Cond-Evap, 0.657s. (Gravity points to the left; the bottom boundary represents centerline)

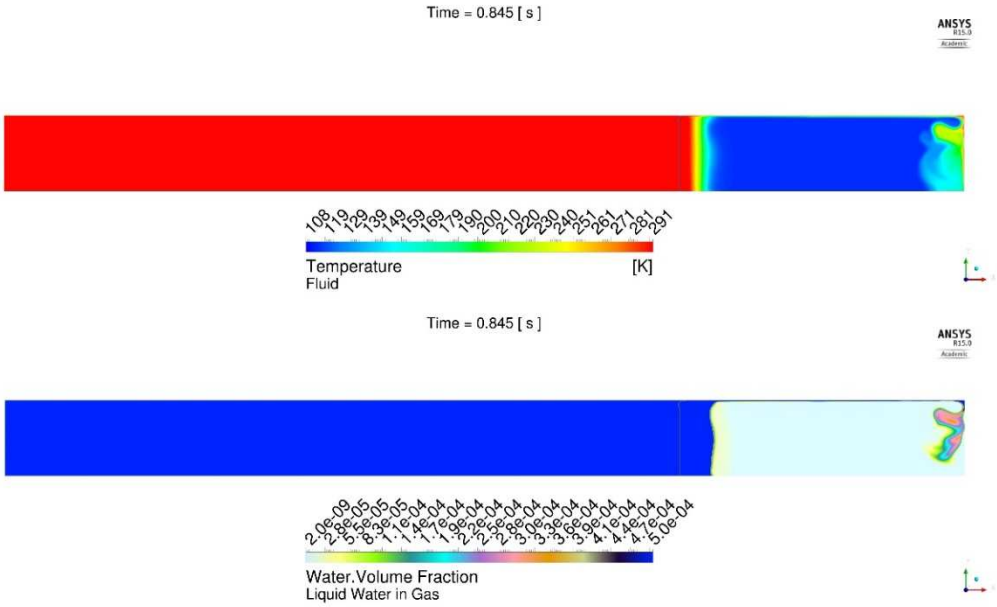

Fig.3.52 Temperature distribution (upper plot) and "cloud" (lower plot), Empt_ConstU_Cond-Evap, 0.845s. (Gravity points to the left; the bottom boundary represents centerline)

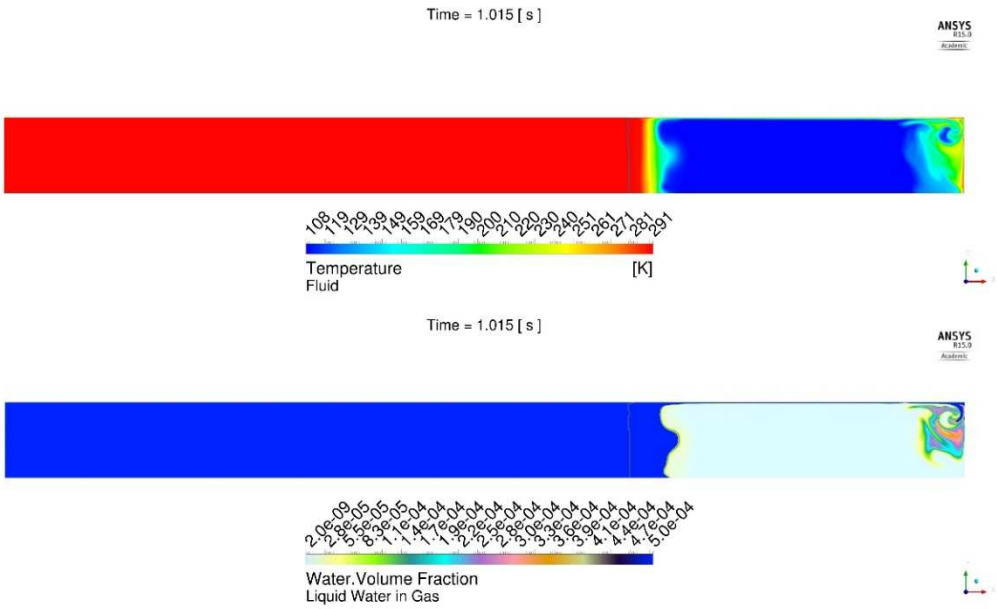

Fig.3.53 Temperature distribution (upper plot) and "cloud" (lower plot), Empt_ConstU_Cond-Evap, 1.015s. (Gravity points to the left; the bottom boundary represents centerline)

3.5.5. Metal-Foam-Inserted Chamber with Constant Power Output

In case "10PPI_ConstPow," the instantaneous velocity boundary condition at the outlet is based on the required power output and the instantaneous pressure. No phase change of the water is modeled. The calculated expansion velocity trajectory and the outlet pressure are shown in Fig.3.54 and Fig.3.55. A similar phenomenon as shown in case "Empty_ConstPow" is observed here, in order to maintain constant power output, the outlet flow speed is increased near the end of expansion as the pressure drops. Fluctuations in the velocity and outlet pressure are seen near the end.

Temperature distributions in the solid matrix and in the water and air at selected times are shown in Fig.3.56 to Fig.3.59. When using the metal foam insert, the lowest air temperature during expansion process is 222K, which is 114K higher than that in the no-insert case. Although the gas cools to very low temperature, the cold gas does not cool the

water piston to the freezing point due to a much greater thermal capacitance of water than air. In the expansion process, the air temperature drops in the beginning and reaches its lowest value at around 0.82s, and then starts to heat up due to heat transfer from the metal foam matrix. The reason for this is that the water piston speed is very small in the beginning, resulting in little heat transfer between the air and its surrounding metal foam matrix. The most active heat transfer processes occur near the end of expansion when the air speed is higher; as shown in Fig.3.59, the metal foam matrix reaches its lowest temperature at the end of expansion. This indicates that with the use of a metal foam matrix in the chamber, a better heat transfer process can be achieved if a higher expansion speed is applied near the beginning of expansion.

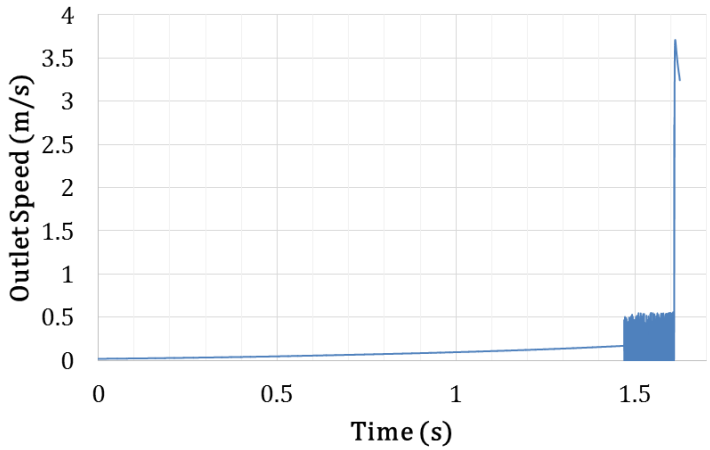

Fig.3.54 Liquid piston trajectory of case 10PPI_ConstPow

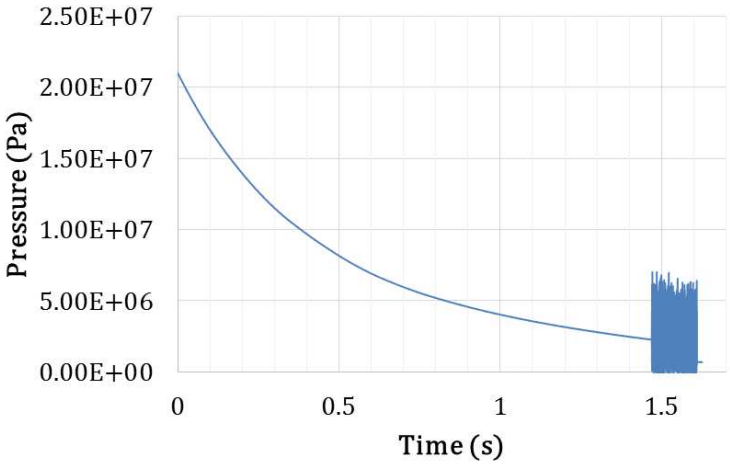

Fig.3.55 Outlet pressure of case 10PPI_ConstPow

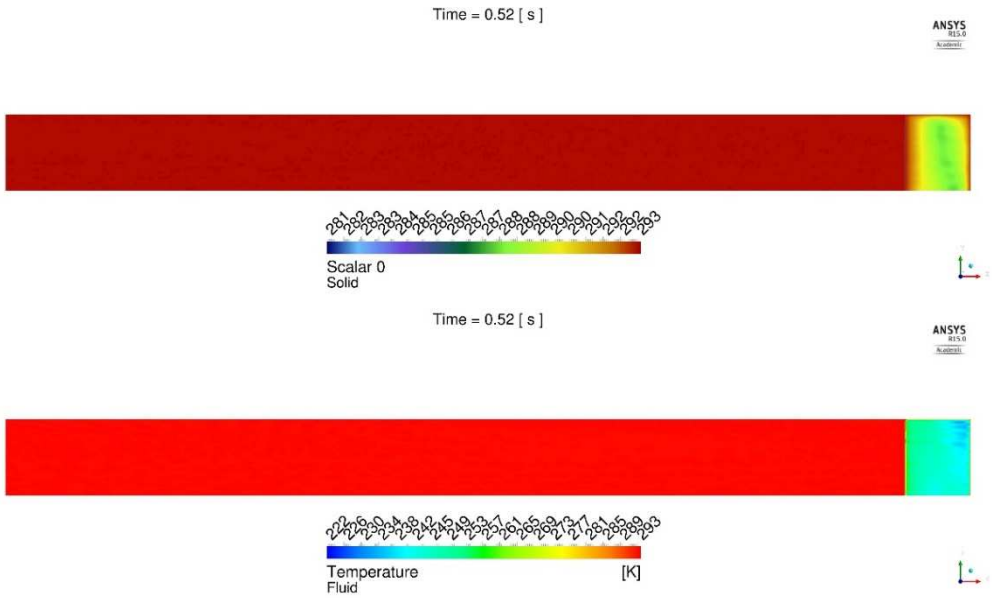

Fig.3.56 Solid temperature (upper plot) and fluid temperature (lower plot), 10PPI_ConstPow, 0.52s. (Gravity points to the left; the bottom boundary represents centerline)

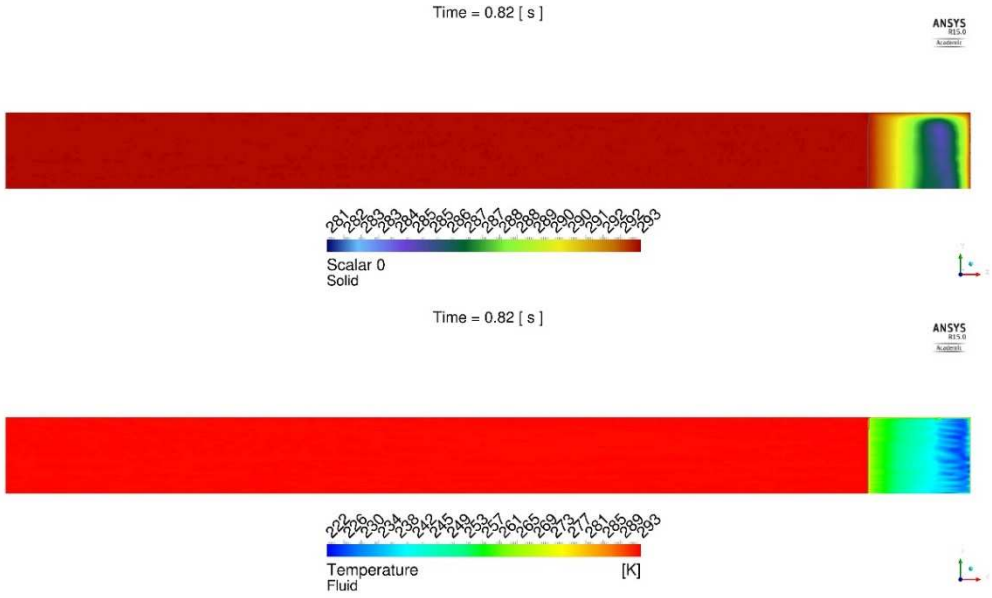

Fig.3.57 Solid temperature (upper plot) and fluid temperature (lower plot), 10PPI_ConstPow, 0.82s. (Gravity points to the left; the bottom boundary represents centerline)

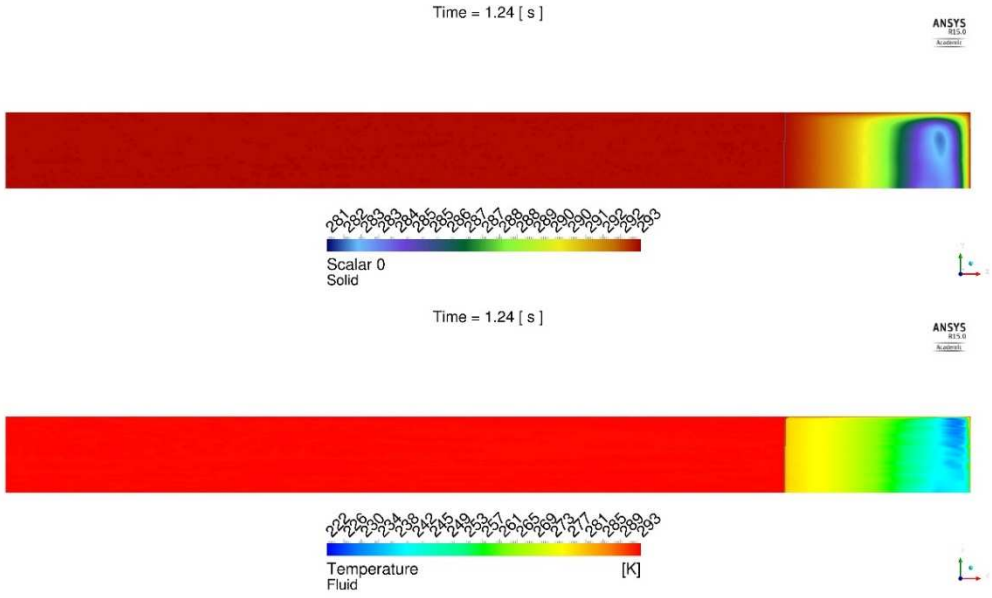

Fig.3.58 Solid temperature (upper plot) and fluid temperature (lower plot), 10PPI_ConstPow, 1.24s. (Gravity points to the left; the bottom boundary represents centerline)

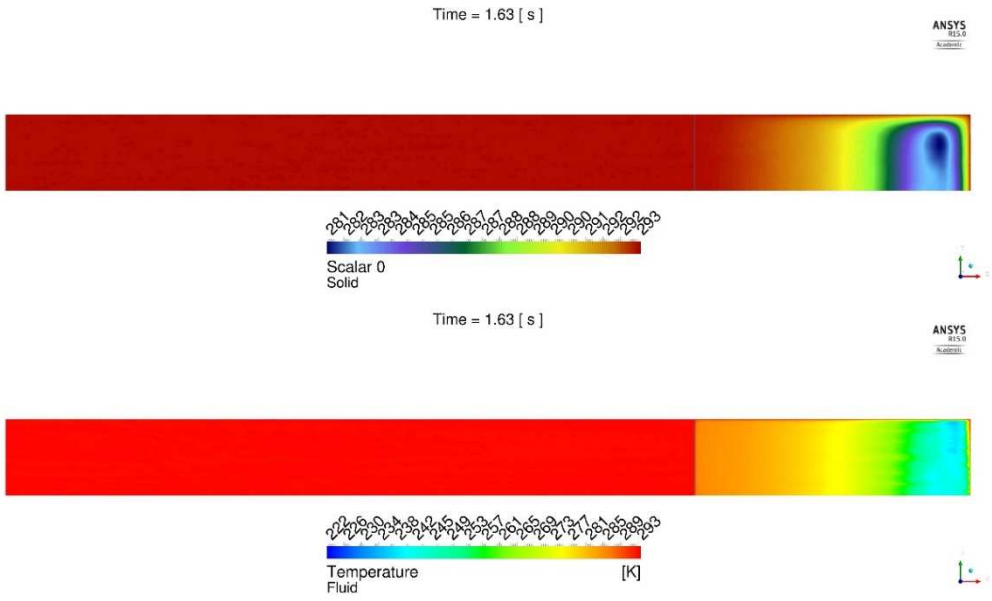

Fig.3.59 Solid temperature (upper plot) and fluid temperature (lower plot), 10PPI_ConstPow, 1.63s. (Gravity points to the left; the bottom boundary represents centerline)

3.5.6. Metal-Foam-Inserted Chamber with Constant Speed Expansion

In this simulation, the same liquid piston chamber is simulated with a constant expansion speed at 0.15m/s. The outlet pressure during expansion is shown in Fig.3.60. The expansion time in this case is the longest of all five expansion simulations. Using a 10PPI metal foam and a constant expansion speed results in a process with enhanced heat transfer that reduces the power loss due to rapid temperature drop. When comparing this case with the previous 10PPI_ConstPow case, one sees that the performance of the current case is better because of sufficient air flow in the beginning of the expansion which promotes heat transfer from the air to the solid matrix.

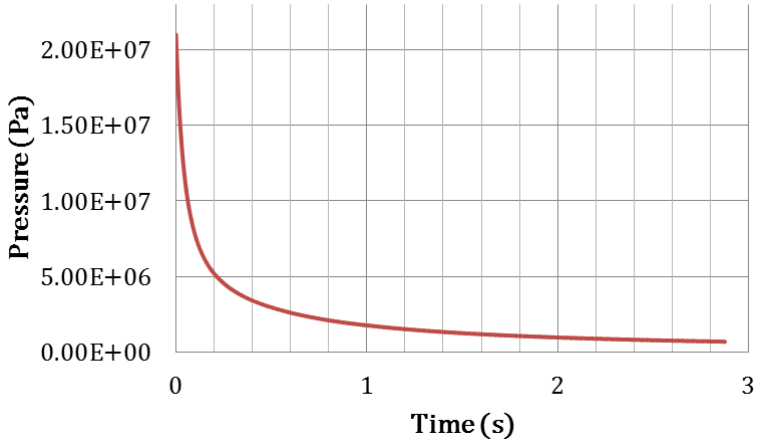

Fig.3.60 Outlet pressure of case 10PPI_ConstU

Temperature distributions in the solid and fluids at selected times are shown in Fig.3.61 to Fig.3.64. Due to constant expansion speed, the air temperature drops rapidly in the first 0.33s. This, appearing to be a disadvantage, is, however, beneficial to the process, as it sets a suitable temperature difference between the air and the solid matrix. The 0.15m/s piston speed provides good agitation to the air flow for convective heat transfer between the solid and air. After 0.33s, the solid matrix starts to heat the air, enabling the expansion process to last longer. At the end of expansion, the minimum local air temperature is only 25K lower than the air temperature before expansion.

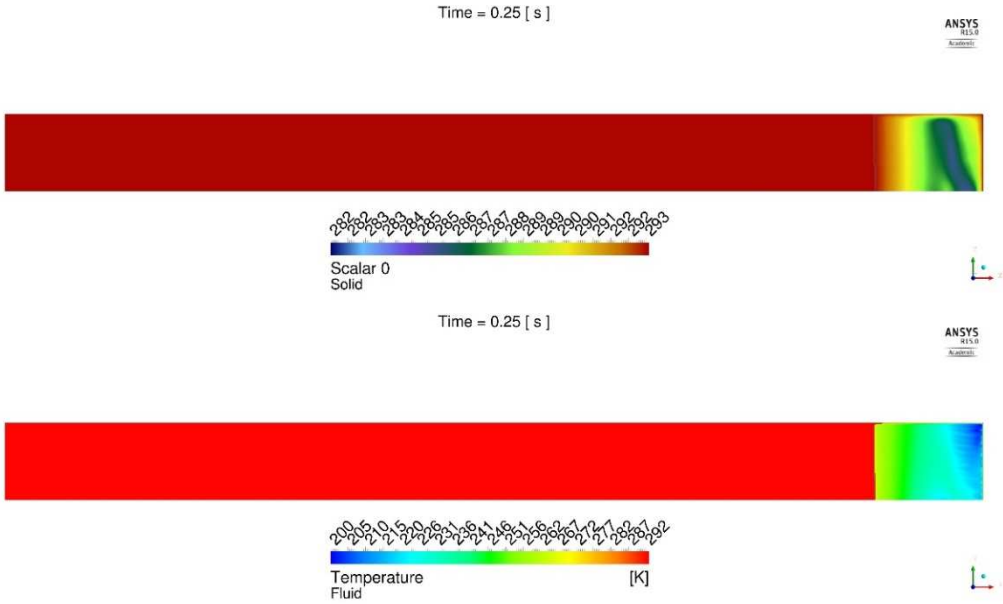

Fig.3.61 Solid temperature (upper plot) and fluid temperature (lower plot), 10PPI_ConstU, 0.25s. (Gravity points to the left; the bottom boundary represents centerline)

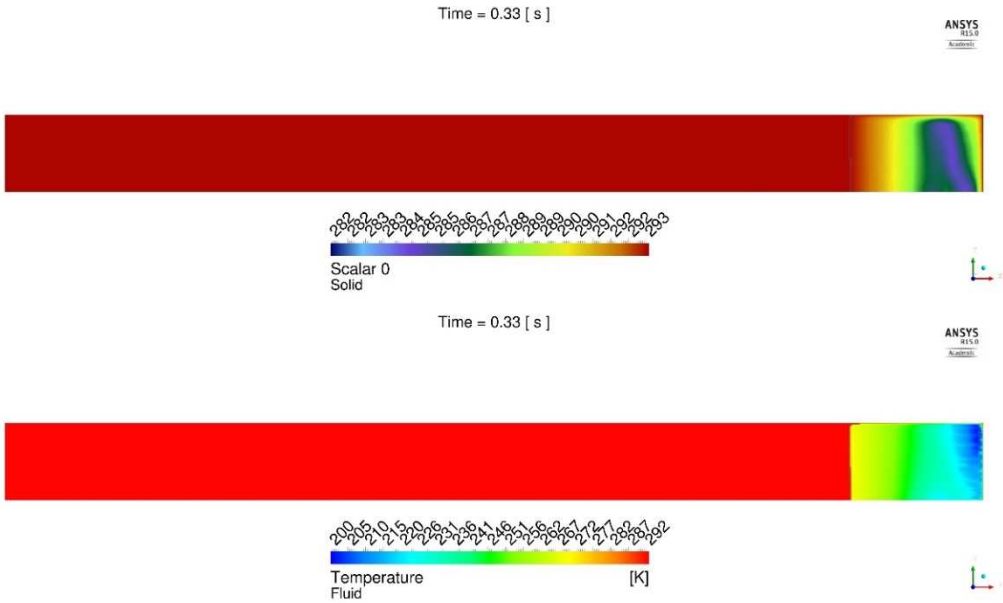

Fig.3.62 Solid temperature (upper plot) and fluid temperature (lower plot), 10PPI_ConstU, 0.33s. (Gravity points to the left; the bottom boundary represents centerline)

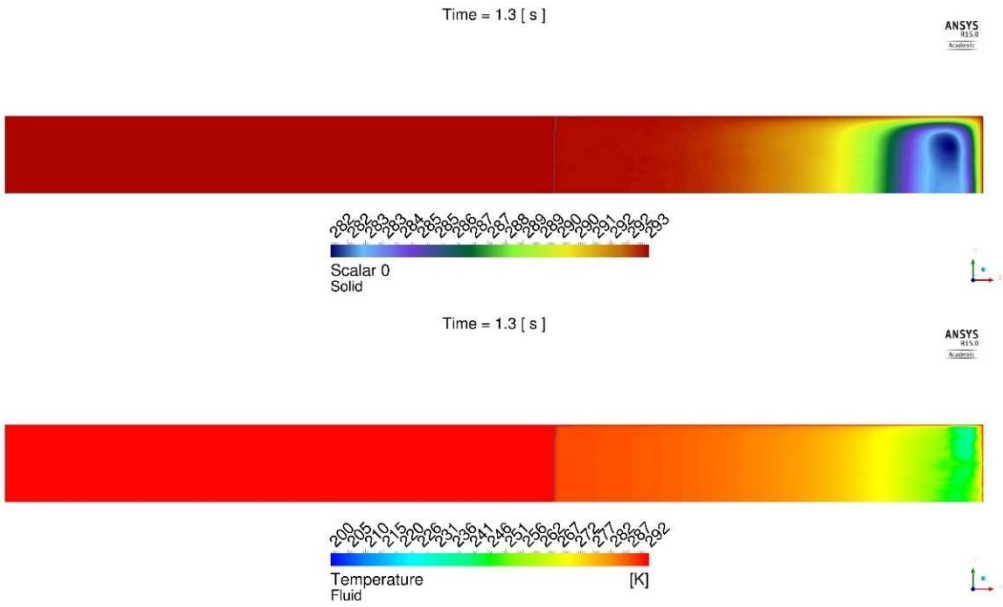

Fig.3.63 Solid temperature (upper plot) and fluid temperature (lower plot), 10PPI_ConstU, 1.3s. (Gravity points to the left; the bottom boundary represents centerline)

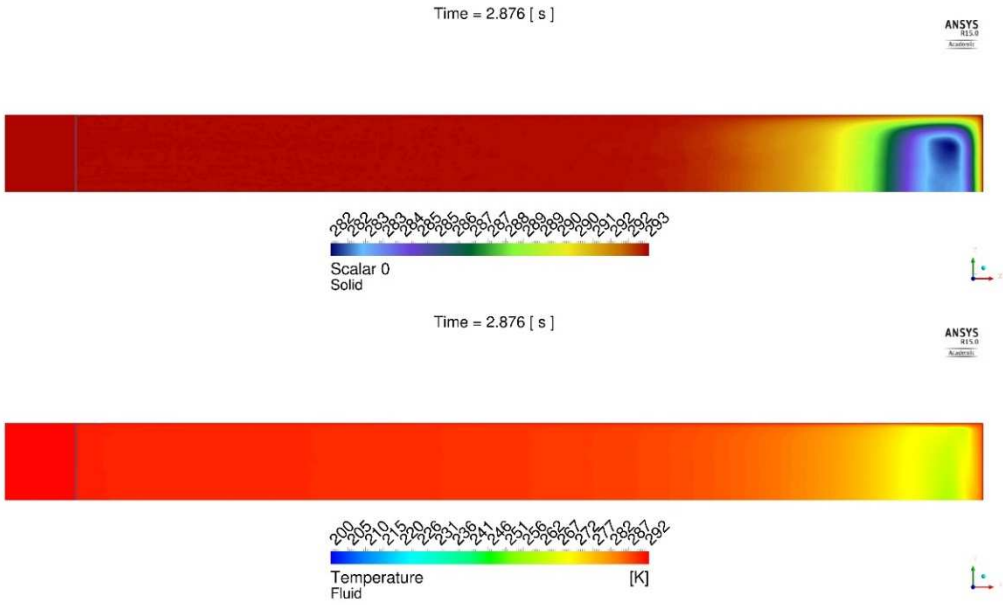

Fig.3.64 Solid temperature (upper plot) and fluid temperature (lower plot), 10PPI_ConstU, 2.876s. (Gravity points to the left; the bottom boundary represents centerline)

3.5.7. Summary of Expansion Simulations

Different performance factors of the previous simulation cases are calculated and compared in Fig.3.65. In general, metal foam enhances heat transfer capabilities for the liquid piston expander by providing large heat transfer surface areas and large thermal capacity. The expansion trajectory is also an important factor, and its effect is different depending on whether the chamber has a matrix insert. In the no-insert case, it is preferred to expand slowly in the beginning, since in the beginning the air volume is small and sudden expansion results in fast volume ratio change, leading to rapid temperature drop. Without the aid of any heat transfer medium, this loss in power cannot be recovered. On the other hand, in the matrix-inserted chamber, it is preferred to have a substantial expansion speed in the beginning, for two purposes: (1) setting the temperature difference between the air and its surrounding matrix, and (2) providing enough agitation to the air flow so that convective heat transfer between the air and the matrix can take place. This is in line with the results shown in Fig.3.65. In a 10PPI metal foam inserted chamber, the constant speed expansion has a higher efficiency (or greater work output) than the constant power expansion case. In a no-insert chamber, the constant speed expansion has a lower efficiency (or less work output) than the constant power expansion.

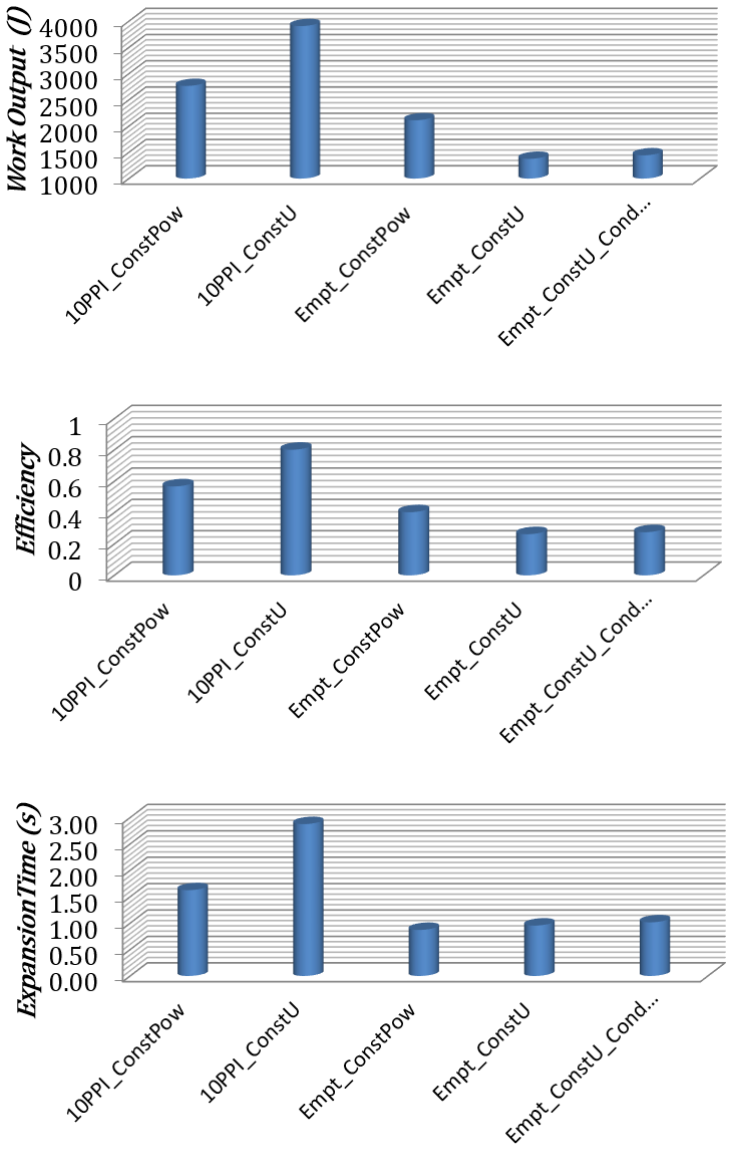

Fig.3.65 Performance comparisons of different expansion cases

Chapter 4: Interrupted Plates Used for Heat Transfer Enhancement

The porous medium, or heat exchanger matrix, investigated in this chapter is an interrupted-plate heat exchanger, which features layers of parallel, separated plates stacked together. In each successive layer, the plates are rotated such that they are perpendicular to the previous layer, as shown in Fig.4.1. This particular shape that features interrupted plates has shown in an earlier study to have a superior heat absorbing capability for application in a Stirling engine [65]. The shape of the exchanger matrix is governed by three shape parameters, the plate height, separation distance, and thickness. The first part of this chapter uses unit cell CFD simulations to develop heat transfer and pressure drop models that are functions of the matrix's shape parameters and different Reynolds numbers with the mean flow angle aligned to the chamber's axial direction. These models will be used later for designing a heat exchanger matrix that has a varying shape along the axial direction of the compression chamber. The purpose of varying the shape distribution along the chamber is to allocate heat transfer capabilities and pressure drop to different locations. The second part of this chapter uses unit cell CFD simulations to develop anisotropic heat transfer and pressure drop models that resolve the effects of different mean flow angle in an REV, for an exchanger shape with parameters that have middle values in the parameter domain. The heat transfer correlations and pressure drop models developed will also be used later in 3-D simulations of the liquid piston chamber where the exchangers are used.

4.1. Shape Analysis

4.1.1. Simulation Cases

The schematic of an REV, as shown in Fig.4.1 (b), represents a unit cell of the exchanger. The periodic features of the exchanger shape are the same in the y and z directions. Three dimensions of the exchanger are: plate length, ℓ, plate thickness, t, and plate distance, $2b$. Twenty-seven shapes are analyzed with various combinations of ℓ, t, and $2b$. The list of parameters for the various shapes is shown in Table 4.1. All CFD simulations cases done for investigating different shapes can be categorized into three sets.

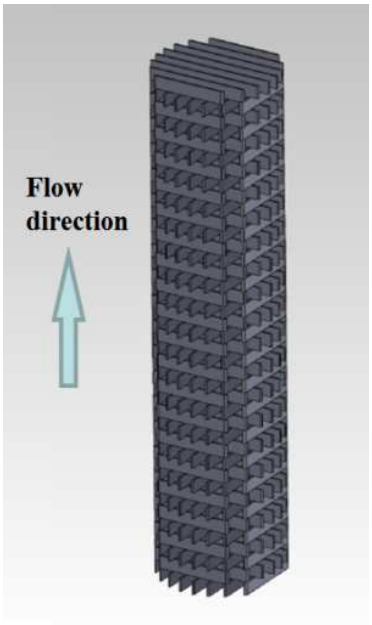

(a) Schematic of the exchanger matrix for insertion into a liquid piston chamber

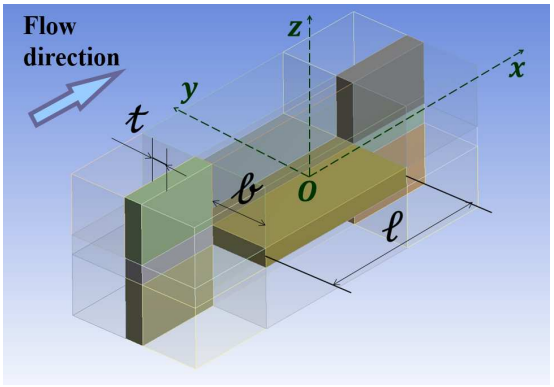

(b) Schematic of an REV of the exchanger (a unit cell)

Fig.4.1 Interrupted-plate exchanger shape and parameters (the arrow with the label "flow direction" indicates the mean flow direction in the liquid piston chamber)

The first set of CFD simulations was done for a low Reynolds number regime, A total number of 58 CFD runs were computed. This group of simulations will be referred to as "Set I." Two different Reynolds numbers, $Re_{l,f} = 1$ and $Re_{l,f} = 400$, are simulated for each shape listed in Table 4.1. In addition, four CFD runs are computed for four randomly chosen shapes with gradually increasing Reynolds number between 1 and 400: REV21 with $Re_{l,f} = 9.4$, REV23 with $Re_{l,f} = 13.1$, REV22 with $Re_{l,f} = 81.7$, and REV11 with $Re_{l,f} = 363.1$. The Reynolds number, $Re_{l,f}$, is defined as,

$$Re_{l,f} = \frac{\rho\, \ell\, u_{REV,f}}{\mu_{REV,f}} \tag{4.1}$$

where $u_{REV,f}$ is the volume-averaged fluid velocity in the fluid domain of an REV

$$u_{REV,f} = |\langle \vec{u} \rangle^f| \tag{4.2}$$

Table 4.1 List of parameters of different shapes studied

Cases	REV1	REV2	REV3	REV4	REV5	REV6	REV7	REV8	REV9
l (mm)	7.5	7.5	15	15	7.5	7.5	7.5	15	15
t (mm)	0.4	0.8	0.4	0.8	0.4	0.8	1.6	0.4	0.8
$2b$ (mm)	5	10	5	10	2.5	5	10	2.5	5

Cases	REV10	REV11	REV12	REV13	REV14	REV15	REV16	REV17	REV18
l (mm)	15	7.5	7.5	15	15	4	4	2	4
t (mm)	1.6	0.8	1.6	0.4	1.6	0.8	0.4	0.4	1.6
$2b$ (mm)	10	2.5	5	2.5	5	2.5	2.5	2.5	10

Cases	REV19	REV20	REV21	REV22	REV23	REV24	REV25	REV26	REV27
l (mm)	4	3	2	3	2	5.5	5.5	5.5	5.5
t (mm)	0.6	0.4	0.8	0.8	1.6	0.8	0.8	0.4	0.4
$2b$ (mm)	2.5	2.5	5	5	10	5	2.5	5	2.5

A second set of simulations runs are computed for the exchanger shape REV11 ($\ell = 7.5mm,\ t = 0.8mm,\ 2b = 2.5mm$), with eleven different Reynolds numbers, $Re_{Dh,f}$, ranging from 0.67 to 5333. These simulation cases will be referred to as "Set II." Three different runs are computed at $Re_{Dh,f} = 5333$ while varying the density of the air flow and the mass flow rate. The reason that this shape was chosen for extra analysis is that it has parameters with values in the middle of the parameter domain. The Reynolds number Re_{Dh} is defined as

$$Re_{Dh,f} = \frac{\rho D_h u_{REV,f}}{\mu_{REV,f}} \tag{4.3}$$

where the hydraulic diameter is

$$Dh = 4\mathscr{b} \tag{4.4}$$

The third set of simulations was done focusing on a variation of the shape REV11 with seven different Reynolds numbers, $Re_{L,f}$, ranging from 1 to 49628, and also shapes REV8 with three different Reynolds numbers and REV20 with four different Reynolds numbers from intermediate to high values ($2000 < Re_{L,f} < 53000$). The variation of the shape REV11 will be referred to as REV11_1, which has the following parameters: $\ell = 7.5mm$, $t = 0.55mm$, $2\mathscr{b} = 2.75mm$. The pore size (L) Reynolds number is defined as

$$Re_{L,f} = \frac{\rho L u_{REV,f}}{\mu_{REV,f}} \tag{4.5}$$

where L is a characteristic length of the pore size,

$$L = \sqrt[\frac{1}{3}]{\frac{V_{REV,f}}{2}} = \sqrt[\frac{1}{3}]{2\mathscr{b}(2\mathscr{b} + t)\ell} \tag{4.6}$$

4.1.2. Governing Equations and Numerical Procedure

The continuity, momentum, and energy equations are solved for flow in an REV. The computational domain is the transparent region in Fig.4.1 (b). The transient equations based on the RANS modeling are given in the following (with the overbars representing averaging being omitted):

$$\frac{\partial u_i}{\partial x_i} = 0 \tag{4.7}$$

$$\rho \frac{\partial u_i}{\partial t} + \rho \frac{\partial (u_i u_j)}{\partial x_j} = -\frac{\partial p}{\partial x_i} + \frac{\partial}{\partial x_j}\left[\mu\left(\frac{\partial u_i}{\partial x_j} + \frac{\partial u_j}{\partial x_i} - \frac{2}{3}\delta_{ij}\frac{\partial u_k}{\partial x_k}\right)\right] + \frac{\partial}{\partial x_j}\left(-\rho\overline{u_i{}' u_j{}'}\right) \tag{4.8}$$

$$\rho \frac{\partial}{\partial t}\left(c_p T + \frac{u_i u_i}{2}\right) + \rho \frac{\partial}{\partial x_j}\left[u_j\left(c_p T + \frac{u_i u_i}{2} + p\right)\right] \tag{4.9}$$

$$= \frac{\partial}{\partial x_j}\left[k\frac{\partial T}{\partial x_j} + u_i\mu\left(\frac{\partial u_i}{\partial x_j} + \frac{\partial u_j}{\partial x_i} - \frac{2}{3}\delta_{ij}\frac{\partial u_k}{\partial x_k}\right) + \frac{c_p\mu_t}{Pr_t}\frac{\partial T}{\partial x_j}\right]$$

Steady state simulations are done for all the cases in the simulation Sets I, three cases with $Re_{Dh,f}$ values of 0.7, 133, and 389 from Set II, and two cases with $Re_{L,f}$ values of 1 and 213 in Set III; the rest of the simulations are transient. In RANS simulations, the Boussinesq hypothesis is used to relate the Reynolds stresses to the mean velocity gradients,

$$-\rho\overline{u_i{}'u_j{}'} = \mu_t(\frac{\partial u_i}{\partial x_j} + \frac{\partial u_j}{\partial x_i} - \frac{2}{3}\delta_{ij}\frac{\partial u_k}{\partial x_k}) - \frac{2}{3}\rho\kappa\delta_{ij} \tag{4.10}$$

An RNG (renormalization group) $k-\varepsilon$ model [79] is used for cases in Set I with $Re_{l,f} = 400$, and for cases in Set II with $Re_{Dh,f} \geq 879$. The Transition SST model [80] is used for cases in the Set III with $Re_{L,f} \geq 2116$. The model couples the SST $k-\omega$ model with two other transport equations, one for the intermittency, and one for the momentum thickness Reynolds number, which is used as a transition onset criterion. A comparison of some closure models will be shown in the next section.

To characterize a heat exchanger matrix using the REV simulation, one must impose a periodic flow in the REV, to simulate a condition of flow that is repeating, or fully developed in the matrix, such that no inlet or outlet effects influence the characterization of the matrix. On the solid-fluid interfaces, no-slip velocity condition. For simulation Sets I and II, constant and uniform temperature at 293K are imposed on the solid-fluid interface. Periodic velocity and thermal boundary conditions are imposed on the entering-flow boundary ($x = -l$) and on the exiting-flow boundary ($x = l$),

$$\chi|_{x=-l} = \chi|_{x=l}, \qquad \chi = \vec{u}, \mathbb{T} \tag{4.11}$$

where $\mathbb{T}$ is a dimensionless temperature based on bulk flow temperature and wall temperature,

$$\mathbb{T} = \frac{T - T_{\text{bulk}}}{T - T_0} \tag{4.12}$$

The cross-sectional bulk temperature is defined as

$$T_{\text{bulk}} = \frac{\int_{cross} \rho c_p u T dA}{\int_{cross} \rho c_p u dA} \tag{4.13}$$

A bulk temperature boundary condition at the inlet is defined in the simulation. The Reynolds number in different cases is varied by imposing different mass flow rates in the REV:

$$\dot{m} = Re_{l_c} \frac{\mu}{l_c} A_{cross,f} \tag{4.14}$$

The remaining boundaries of the flow domain are symmetric,

$$\left(\frac{\partial \chi}{\partial y}\right)|_{y=\pm(b+\frac{t}{2})} = 0, \qquad \chi = \vec{u}, T \tag{4.15}$$

$$\left(\frac{\partial \chi}{\partial z}\right)|_{z=\pm(b+\frac{t}{2})} = 0, \qquad \chi = \vec{u}, T \tag{4.16}$$

Another imposed condition is the mass flow rate, which is specified according to the Reynolds number value.

For simulations in Set III, a boundary condition of a constant and uniform wall heat flux, $q_w{''}$, is imposed on the fluid-solid interface. Therefore, the thermal boundary condition for these simulations are:

$$\frac{T|_{x=\ell} - T|_{x=-\ell}}{2\ell} = \frac{q_w{''} a_V}{\rho c_p u_{REV,f}} \tag{4.17}$$

where a_V is the specific area (surface area per volume) of the REV,

$$a_V = \frac{4(2b+t)\ell + 8bt}{2(2b+t)^2 \ell} \tag{4.18}$$

Periodic boundaries are also applied to the paring boundaries $y = \pm(\mathscr{b} + \frac{t}{2})$ and $z = \pm(\mathscr{b} + \frac{t}{2})$.

$$\Gamma|_{y=-(\mathscr{b}+\frac{t}{2})} = \Gamma|_{y=\mathscr{b}+\frac{t}{2}}, \qquad \Gamma = u_i, \mathrm{T} \tag{4.19}$$

$$\Gamma|_{z=-(\mathscr{b}+\frac{t}{2})} = \Gamma|_{z=\mathscr{b}+\frac{t}{2}}, \qquad \Gamma = u_i, \mathrm{T} \tag{4.20}$$

Simulations are done in the commercial CFD solver ANSYS Fluent using the SIMPLE algorithm. The 2nd-order upwind method is used for differencing spatial derivative terms. A first-order implicit scheme is used for transient discretization. The convergence criteria for residuals of all equations are set to 10^{-9}.

In all cases in the three simulation sets, the computational domain is discretized into rectangular hexahedra cells. The cell size gradually decreases as the walls are approached in order to resolve accurately the rapidly changing, near-wall flows. In simulation Set I, the maximum edge size of cells is four times the minimum edge size of cells. Different cell sizes are used for different REV models due to different geometries and sizes. Among the twenty-seven REV models, the number of computation cells varies from 251,712 (case REV5) to 1,850,688 (case REV10), while the number of computation cells per volume varies from 532/mm^3 (case REV10) to 7658/mm^3 (case REV17). In simulation Set II, The number of computational cells varies with Reynolds number; specifically: 169,632 for $Re_{Dh,f} < 150$, 588,816 for $150 \leq Re_{Dh,f} < 2000$, 1,357,056 for $2000 \leq Re_{Dh,f} < 5000$, and 2,024,352 for $Re_{Dh,f} \geq 5000$. In simulation Set III, the number of computational cells increases from 707,840 to 2,743,320 as $Re_{L,f}$ increases from 213 to 52893. In the turbulent RANS simulations, as a wall treatment is used, the maximum value of the dimensionless wall distance (y^+) of the first cell adjacent to the wall is between 2 and 6.

4.1.3. Verification and Validation

This section covers topics on verification and validation of the simulations runs: (1) grid independence analyses by running the same simulation on refined grids of chosen cases, (2) comparisons of CFD results to experimental measurements of the pressure drop of the matrix, and (3) comparisons of different RANS models to LES for selected cases.

A set of simulations are done for the grid independence verification of the cases with constant wall temperature conditions. In the simulation Set I, the case with the smallest amount of cells and the case with the smallest cells per volume are simulated with finer meshes, at $Re_{l,f} = 400$. Comparisons between the original cases and the grid-independence verification cases are shown in Table 4.2. Cases with name extension "_i" represent verification cases corresponding to the original cases. It shows that a total number of 251,712 cells and a number of 532 cells per mm^3 are sufficient. In the current study, all simulations are done with a grid cell number and a grid cells per volume density larger than these values.

For grid-independence verification of the constant wall heat flux simulations, CFD runs are studied after refining the computational grids of selected cases in simulation Set III. For the case with 213 Reynolds numbers, the calculated Nusselt number and pressure drop (normalized on two times the mean flow kinetic energy) for 707,840 and 1,916,480 grid cells are, respectively: 22.3 and 22.2, -0.2092 and -0.2084. For the case with 8309 Reynolds number, the calculated Nusselt number and pressure drop for 1,469,139 and 2,584,833 grid cell simulations are, respectively: 180.6 and 182.4, -0.0956 and -0.0969. These calculations verify that the chosen grid sizes are sufficient.

Table 4.2 Grid-Independence Verification for Constant Wall Temperature Simulations

Cases	Number of Cells	Cells per Volume (/mm3)	Pressure Drop (Pa/m)	Mean Flow Temp. T (K)	Average Heat Transfer Coefficient h(W/m2K)
REV5	251,712	2315	-56.135	298.88	75.25

REV5_i	788,640	7252	-54.743	298.84	73.20
REV10	1,850,688	532	-2.724	300.30	24.28
REV10_i	7,098,224	2040	-2.621	300.23	23.28

Experimental measurement of the pressure drop across the interrupted-plate matrix is done to validate the CFD results. Two interrupted-plate models (REV6 and REV11) are fabricated using rapid prototyping. One model is made for REV6, and two are made for REV11 (namely REV11_1 and REV11_2). A picture of them is shown in Fig.4.2. The interrupted-plate models are made by two different 3-D rapid prototype printers, model REV6 and model REV11_1 by Dimension sst1200es, and REV11_2 by Stratasys Print Plus. Model REV11_2 and model REV6 are used for pressure drop measurements to compare with the CFD calculations.

The same experimental setup used to measure the metal foam pressure drop was used also for the interrupted-plate matrix (Fig.3.1). A fan withdraws air from the right side to the left side as shown in Fig.3.1. The fabricated interrupted-plate model is inserted in the pipe, at the right end. The flow rate of air can be adjusted by the manual valve. A Sierra Top Track 822S flow meter is used to measure the volumetric flow rate. The gauge pressure is measured from the pressure tap by a micro-manometer, and is considered as the pressure drop of the interrupted plate. The measurement is taken at the Turbulent Convective Heat Transfer Lab at the University of Minnesota.

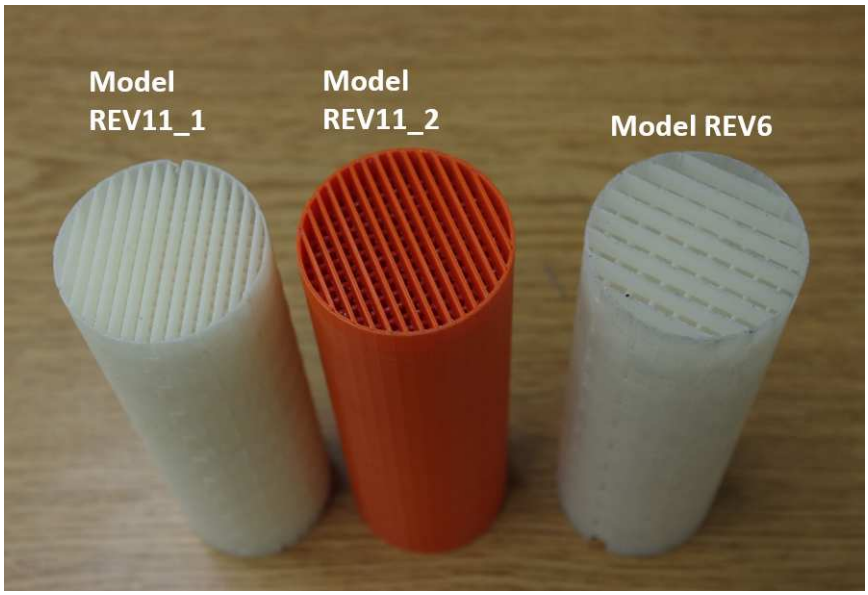

Fig.4.2 Three-D printed exchanger models

Due to fabrication variation, model REV6 has a plate thickness of 0.6mm and Model REV11_2 has a plate thickness of 0.9mm, while the design thickness is 0.8mm for both. For the purpose of comparison, CFD simulations are done by changing the REV geometries to the exact geometries of those fabricated models for the experiment. Based on the simulations, the computed permeability and Forchheimer coefficients for experimental models REV6 and REV11 are calculated. The pressure drop is then calculated according to:

$$\frac{\partial p}{\partial x} = -\frac{\mu}{K}\langle u\rangle - \frac{F\rho|\langle u\rangle|}{K^{\frac{1}{2}}}\langle u\rangle \tag{4.21}$$

The calculated results are shown in Fig.4.3, compared with the results from experimental measurements. The uncertainty associated with the pressure measurement by the micro-manometer is 0.125Pa. The relative uncertainty associated with the measured mean velocity is 1.5%, given by the flow meter manufacturer. Overall agreement is shown between CFD and experiment.

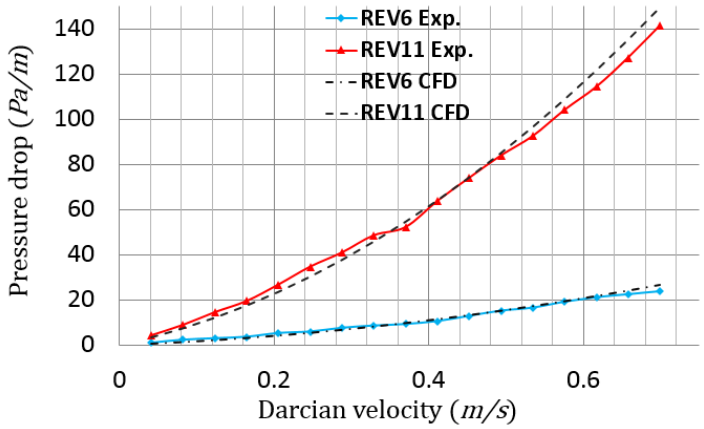

Fig.4.3 Interrupted-plate exchanger pressure drop comparison, experiment vs. CFD (Darcian velocity is the same as u_{REV}, or $|\langle\vec{u}\rangle|$)

The choice of using the Transition SST model for the high Reynolds number runs in is based on a study comparing various RANS simulations to LES simulations. Before we discuss the results for the comparisons of pressure drop and heat transfer, we first give the definition of a Reynolds number based on the superficial REV mean velocity,

$$Re_L = \frac{\rho u_{REV} L}{\mu} = \frac{\rho |\langle\vec{u}\rangle| L}{\mu} = \epsilon Re_{L.f} \tag{4.22}$$

The porosity of the interrupted-plate matrix can be obtained based on:

$$\epsilon = \frac{2\mathscr{b}}{2\mathscr{b}+t} \tag{4.23}$$

At $Re_L = 1777$, both the $k-\omega$ model and the Transition SST model yield pressure drop values close to that from the LES; the Transition SST model results in the closest Nusselt number to that of the LES, as shown in Fig.4.4. The LES in this calculation uses a dynamic Smagorinsky-Lily model [81]; it is done on a grid of 8,264,256 cells wherein the maximum y^+ value of the first layer of cells next to the wall is 2.59. The other RANS calculations are done on a grid of 1,022,720 cells wherein the maximum y^+ values of the first layer of cells next to the wall vary from 1 to 4 among different RANS calculations. At $Re_L = 41{,}667$, the pressure drop value calculated from the Transition SST model is slightly less

accurate than those from the other two models when comparing with the WMLES (Wall-Modeled LES, [82]) result, but the Transition SST model calculates the closest Nusselt number to the WMLES, as shown in Fig.4.5. The WMLES simulation in this calculation is done on the same grid of the previous LES simulation (8,264,256 cells); the maximum y^+ value of the cells in the first layer next to the wall is 17.7. The RANS calculations are done on a grid of 2,584,833 cells, wherein the maximum y^+ values of the cells in the first layer adjacent to the wall vary from 7 to 9 among different cases. From the comparisons given in Fig.4.4 and Fig.4.5, the Transition SST model gives better results than the other models when benchmarked against LES results.

Flow field comparisons between the LES and RANS calculations are given in Fig.4.6 to Fig.4.11. For each of the two Reynolds numbers, two of the better RANS results are shown along with the LES results. In the LES simulation, the flow is strongly agitated by the interrupting feature of the plates. Though the average motion of the fluid is along the plates in the x direction, the pore-scale fluid exhibits strong unsteadiness and mixing effects, characterized by the cascade of eddies generated as a result of the fluid being periodically interrupted by the plates. The flow is effectively cooled by the interrupted-plate medium.

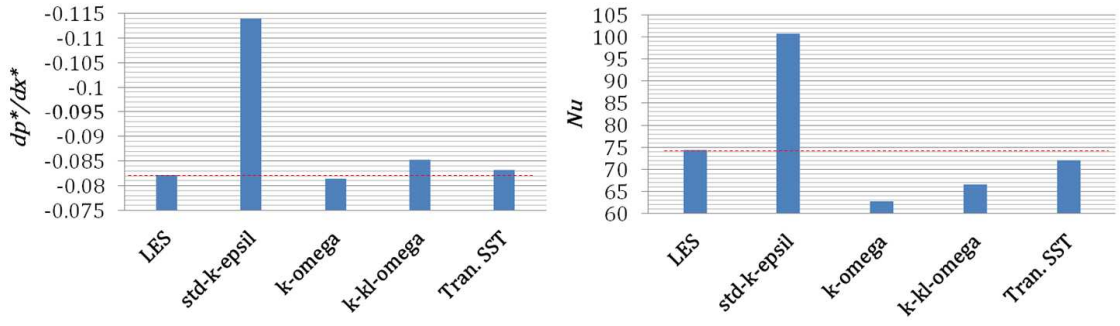

(a) Dimensionless pressure drop (b) Nusselt number

Fig.4.4 Comparison of various turbulence closure models with LES, $Re_L = 1777$ (Models being compared are: Standard $k-\epsilon$, $k-\omega$, $k-kl-\omega$, and Transition SST)

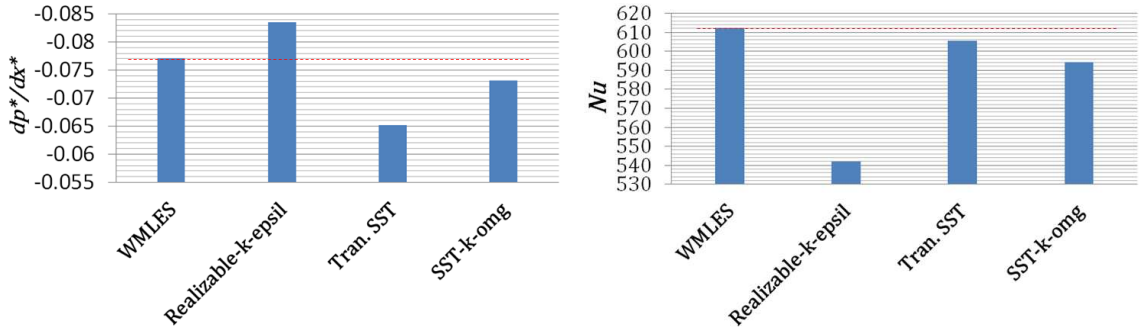

(a) Dimensionless pressure drop (b) Nusselt number

Fig.4.5 Comparison of various turbulence closure models with LES, $Re_L = 41{,}667$
(Models being compared are: Realizable $k-\epsilon$, Transition SST, and SST $k-\omega$)

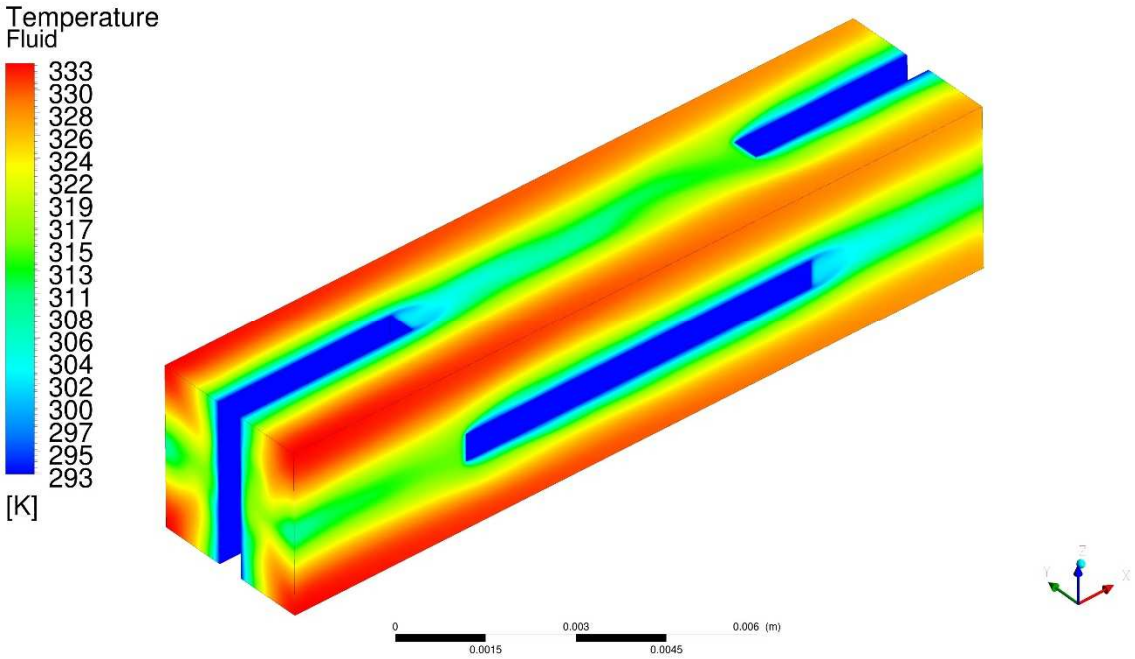

Fig.4.6 $k-\omega$ calculation, $Re_L = 1777$

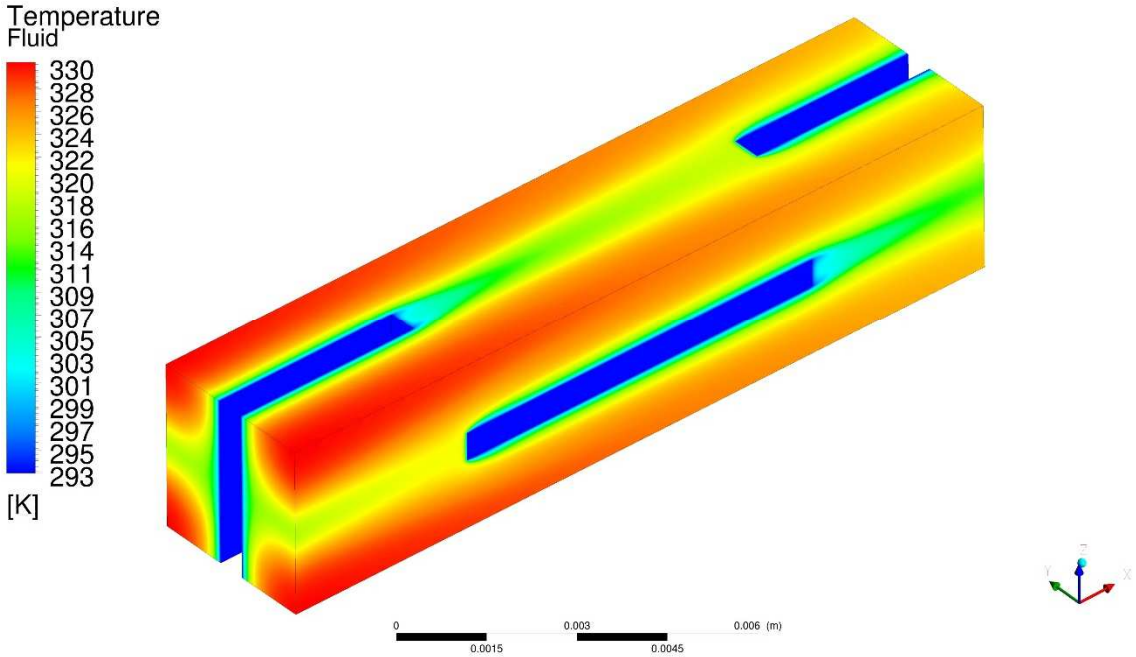

Fig.4.7 Transition SST calculation, $Re_L = 1777$

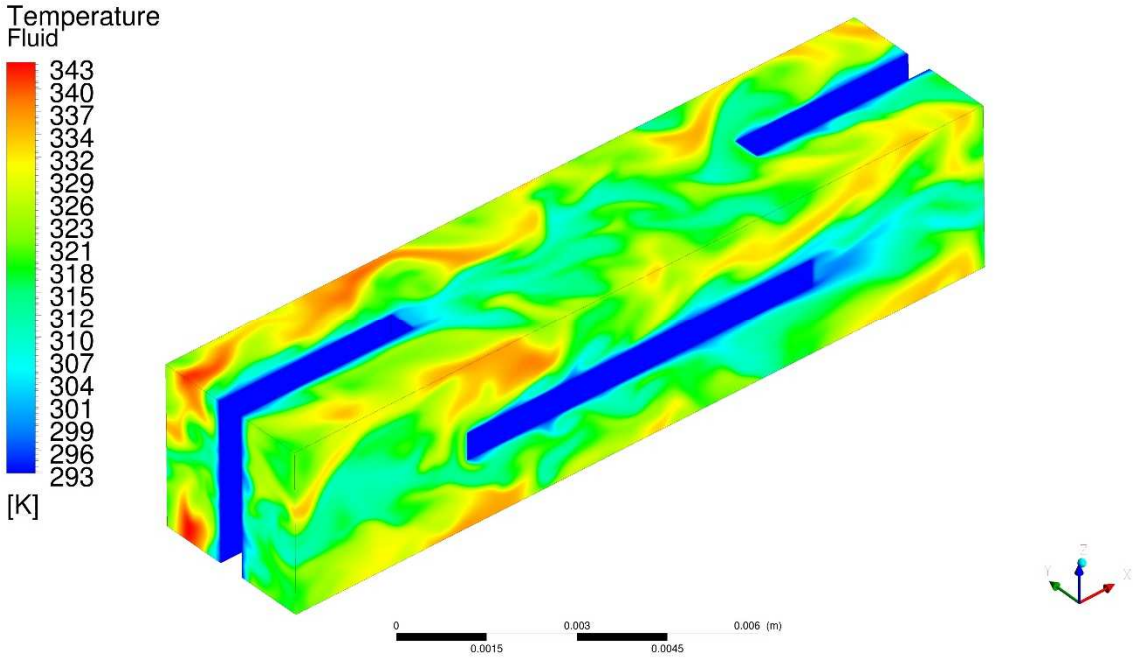

Fig.4.8 LES calculation, $Re_L = 1777$

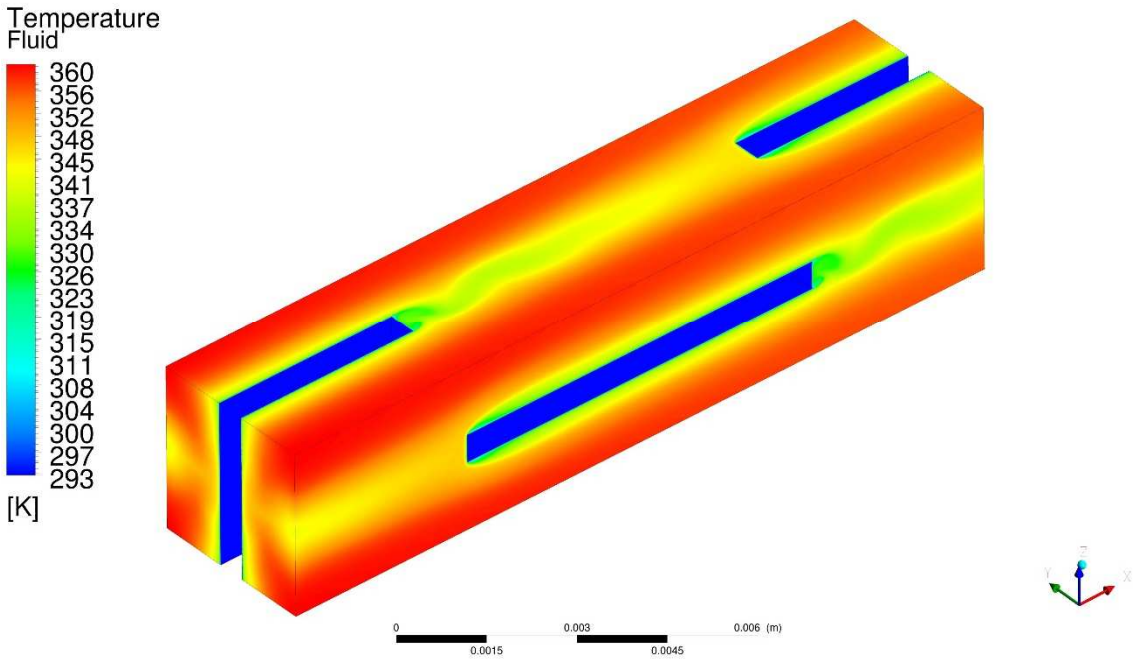

Fig.4.9 SST $k-\omega$ calculation, $Re_L = 41{,}667$

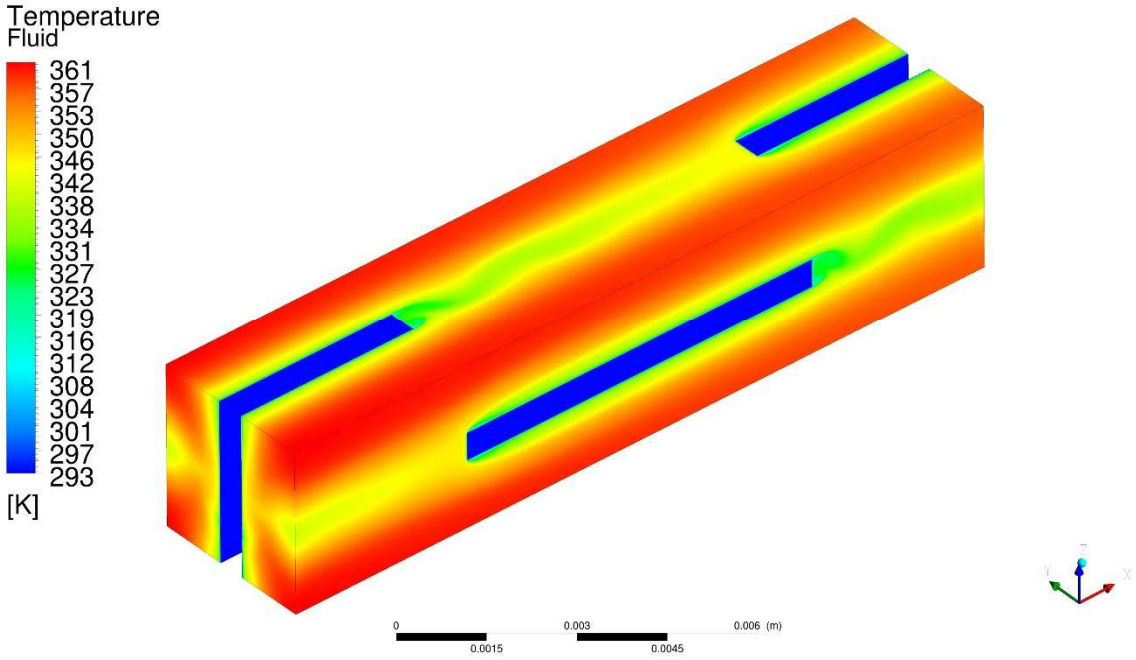

Fig.4.10 Transition SST calculation, $Re_L = 41{,}667$

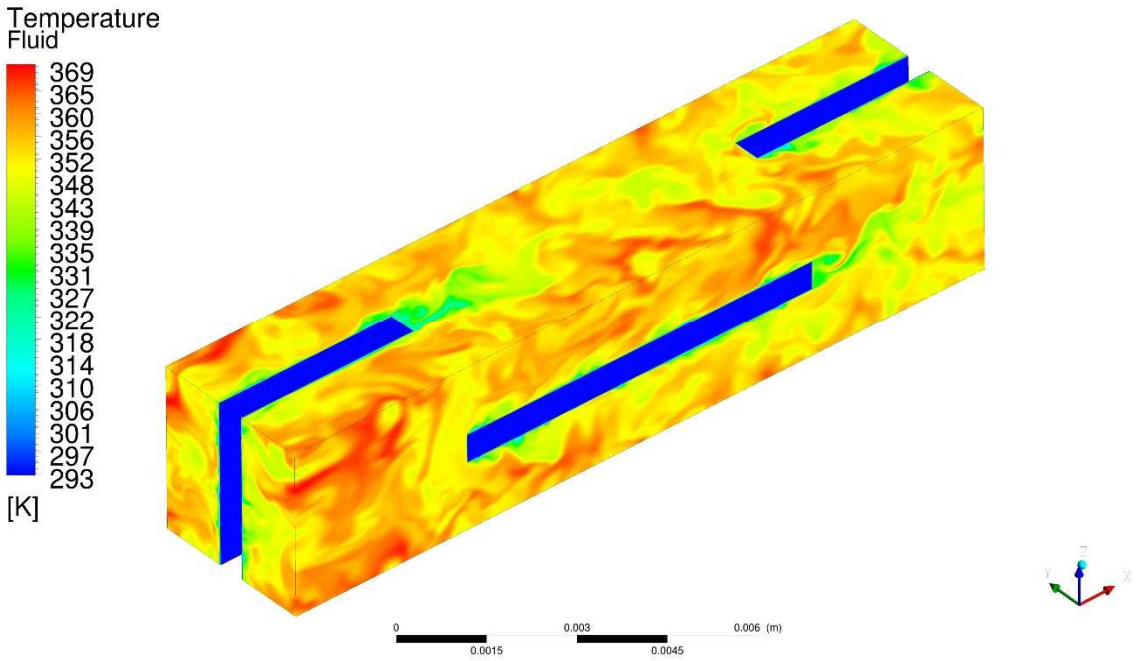

Fig.4.11 LES calculation, $Re_L = 41{,}667$

4.1.4. Modeling of Pressure Drop

The interrupted-plate exchanger is considered as a porous medium. The pressure drop is modeled using a Darcian and a Forchheimer extension term according to Eq.(4.21) using CFD results from simulation Set I. For each shape, the permeability, K, is calculated using the pressure drop value computed from the $Re_{l,f} = 1$ run, by neglecting the inertial term.

$$\frac{\partial p}{\partial x}\Big|_{Re_{l,f}=1} = -\frac{\mu}{K} u_{REV} \tag{4.24}$$

The Forchheimer coefficient, F, is calculated using the total pressure drop value computed from the $Re_l = 400$ run less the Darcian pressure drop based on the computed permeability coefficient. The computed permeability values for all exchanger shapes are given (by the dots) in Fig.4.12. The corresponding Forchheimer coefficients are given in Fig.4.13. For a given separation plate distance, the permeability and Forchheimer coefficients are fit to a function of plate height and plate thickness as shown by each of the surfaces in Fig.4.12 and Fig.4.13. These functions are:

$$K_{2.5} = \left[0.115 \lg\left(\frac{\ell}{\mathbb{L}}\right) - 5.18\frac{\ell}{\mathbb{L}} - 174\frac{t}{\mathbb{L}} + 1.03\right] \times 10^{-6}\mathrm{m}^2 \tag{4.25}$$

$$K_5 = \left[0.345 \lg\left(\frac{\ell}{\mathbb{L}}\right) + 1.29\frac{\ell}{\mathbb{L}} - 394\frac{t}{\mathbb{L}} + 3.20\right] \times 10^{-6}\mathrm{m}^2 \tag{4.26}$$

$$K_{10} = \left[-0.0344 \lg\left(\frac{\ell}{\mathbb{L}}\right) + 155\frac{\ell}{\mathbb{L}} - 984\frac{t}{\mathbb{L}} + 3.84\right] \times 10^{-6}\mathrm{m}^2 \tag{4.27}$$

$$F_{2.5} = -0.00998 \lg\left(\frac{\ell}{\mathbb{L}}\right) + 62.6\left(\frac{t}{\mathbb{L}}\right)^{1.06} - 0.0496 \tag{4.28}$$

$$F_5 = 0.00321 \lg\left(\frac{\ell}{\mathbb{L}}\right) - 1.13\frac{\ell}{\mathbb{L}} + 403\left(\frac{t}{\mathbb{L}}\right)^{1.49} + 0.0368 \tag{4.29}$$

$$F_{10} = 0.00969 \lg\left(\frac{\ell}{\mathbb{L}}\right) - 1.32\frac{\ell}{\mathbb{L}} + 9.40\frac{t}{\mathbb{L}} + 0.0649 \tag{4.30}$$

where $\mathbb{L}$ is a unit length: $\mathbb{L} = 1\mathrm{m}$. The subscripts in the above permeability and Forchheimer coefficients represent the plate separation distance in the unit of mm. For the exchanger shape with parameters of middle values, REV11, the permeability and Forchheimer coefficient are:

$$K = 2.88 \times 10^{-7} m^2, \qquad F = 0.0338$$

4.1.5. Modeling of Heat Transfer

Discussions in this section will be given to using the REV simulation results to model heat transfer. Data analyses are done, on simulation Set I and Set II, and then the combination of all sets, together. Definitions of heat transfer coefficients and Nusselt numbers are given as follows,

$$h = \frac{\bar{q}}{\langle T \rangle^f - T_0} \tag{4.31}$$

$$h_V = h a_V \tag{4.32}$$

$$Nu_{Dh} = \frac{hD_h}{k} \tag{4.33}$$

$$Nu_V = \frac{h_V L^2}{k} = \frac{h a_V L^2}{k} \tag{4.34}$$

First, heat transfer is analyzed for relatively low Reynolds number flows. The hydraulic-diameter Nusselt numbers and the volumetric Nusselt numbers are calculated for the simulations runs in Set I, shown in Fig.4.14. In Fig.4.14 (a), the data cover three different hydraulic diameters, 5mm, 10mm and 20mm. When $Re_{Dh,f}$ is less than 100, the flow is laminar-like and Nu_{Dh} is nearly a constant; when Re_{Dh}becomes larger than 100, Nu_{Dh} increases with $Re_{Dh,f}$. These features have some similarity to the situation of flow in a channel. Data obtained from the simulation runs suggest the following correlation using a least square fit:

$$Nu_{Dh} = 9.700 + 0.0876 {Re_{Dh,f}}^{0.792} Pr^{\frac{1}{3}} \qquad Re_{l,f} \leq 400 \tag{4.35}$$

The correlation is plotted together with the computed data from the CFD runs, as shown in Fig.4.14 (a).

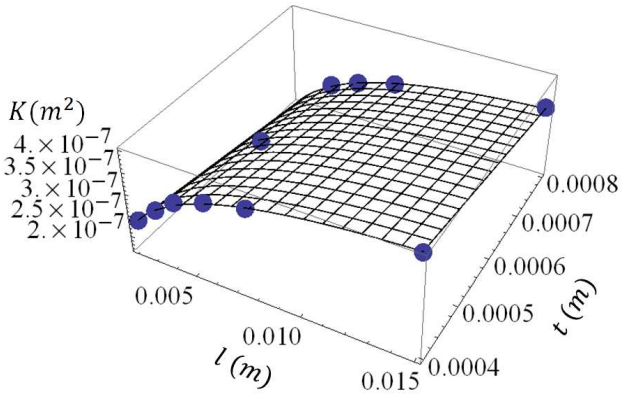

(a) $2\mathscr{b} = 2.5mm$

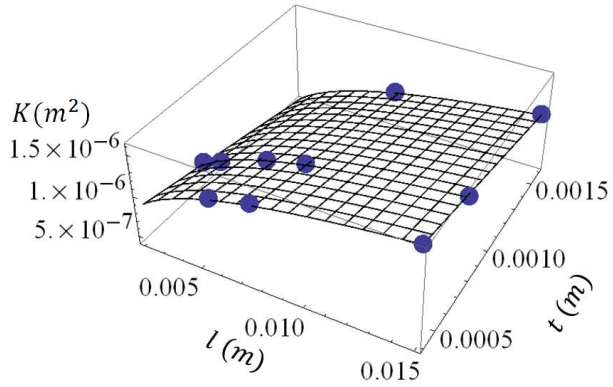

(b) $2\mathscr{b} = 5mm$

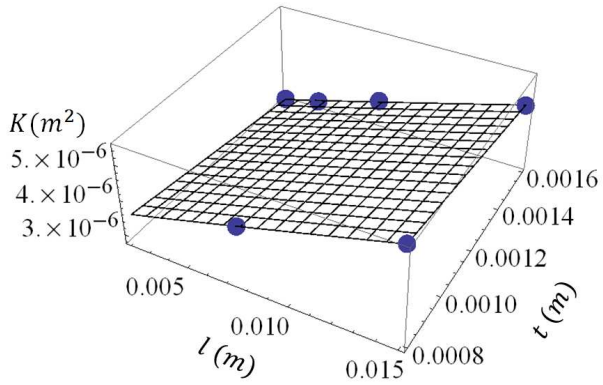

(c) $2\mathscr{b} = 10mm$

Fig.4.12 Permeability coefficient for different exchanger shapes based on CFD runs

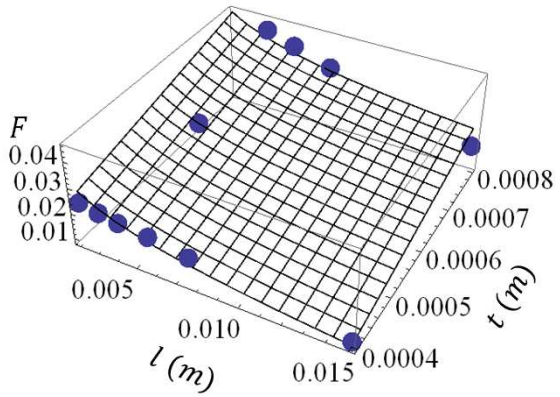

(a) $2\mathscr{b} = 2.5mm$

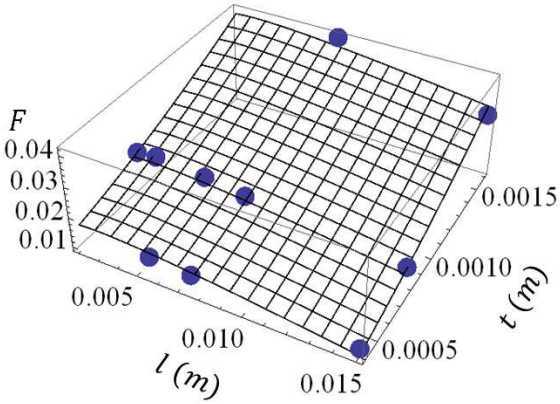

(b) $2\mathscr{b} = 5mm$

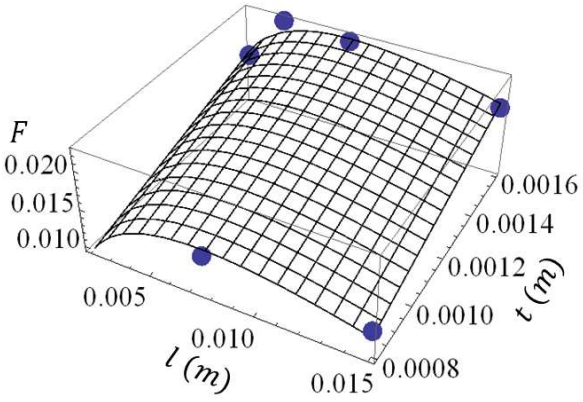

(c) $2\mathscr{b} = 10mm$

Fig.4.13 Forchheimer coefficient for different exchanger shapes based on CFD runs

In Fig.4.14 (b), the heat transfer and fluid mechanics characterizations are based on pore size, L. The pore sizes vary from case to case; they cover the range between 12.0mm (REV10) and 2.44mm (REV17). The change in $Re_{L,f}$ in these simulation runs is primarily affected by the change in the pore size. When $Re_{L,f}$ is between 0.2 and 3, Nu_L decreases as Re_L increases, similar to laminar flow over a flat plate with growing boundary layers. Strong scattering is observed when $Re_{L,f}$ is between 100 and 1000. More analysis are required to reveal the relation between $Re_{L,f}$ and Nu_V.

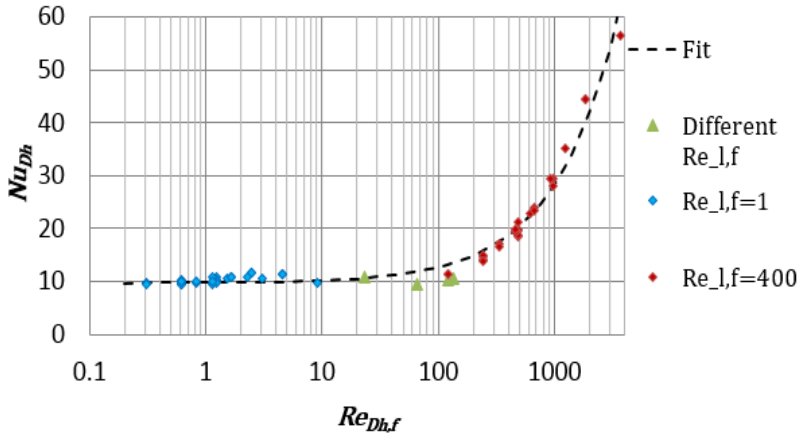

(a) Dimensionless numbers based on hydraulic diameter, D_h

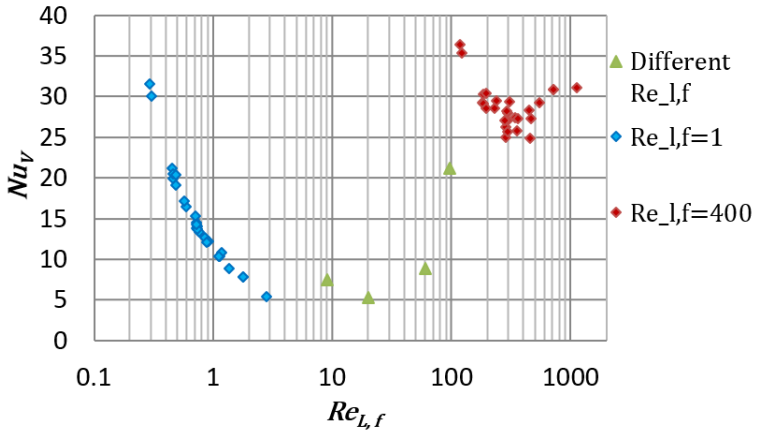

(b) Dimensionless numbers based on pore size, L

Fig.4.14 Nusselt number vs. Reynolds number for simulation Set I

Next, heat transfer at relatively large Reynolds numbers for a fixed shape is analyzed. From the simulation Set II, the area-averaged surface heat transfer coefficient depends on both flow velocity and density, as shown in Fig.4.15 (a). The Reynolds numbers and Nusselt numbers can very well capture heat transfer under different velocity and pressure conditions, as shown in Fig.4.15 (b). A least square fit reveals the following heat transfer correlation for shape REV11:

$$Nu_{Dh} = 7.96 + 0.0672{Re_{Dh,f}}^{0.844}Pr^{\frac{1}{3}} \qquad \text{for REV11} \tag{4.36}$$

The aforementioned two correlations (Eq. (4.35) and (4.36)) are based on either low Reynods number calculations or a single geometry. To expand them to a wider range of Reynolds number, results are analyzed based on simulation Sets I, II, and cases of shape REV11_1 from Set III. The hydraulic Nusselt number vs. hydraulic Reynolds number are calculated. The results are shown in Fig.4.16. The following heat transfer correlation was developed:

$$Nu_{Dh} = 8.46 + 0.325{Re_{Dh,f}}^{0.625}Pr^{\frac{1}{3}} \tag{4.37}$$

Next, all CFD results from simulation Sets I, II, and III are analyzed. The Nusselt number values for all cases are plotted against Reynolds numbers based on pore size and superficial (Darcy) mean velocity values. As shown in Fig.4.17, for the same Reynolds number, the value of Nusselt number scatters due to different shapes, especially at large Reynolds numbers. An additional shape parameter must be included to fully resolve the shape's effect on heat transfer, in addition to using the characteristic pore size for Reynolds number; this parameter is chosen to be the plate height over the plate separation distance, $\frac{\ell}{2\mathscr{b}}$. Physically, it represents the interrupting feature of the matrix. Larger $\frac{\ell}{2\mathscr{b}}$ values indicate that the flow travels in thinner and longer channels and is interrupted less frequently; small

$\frac{\ell}{2\mathscr{b}}$ values indicate that the flow travels in shorter channels and has more opportunities to be interrupted by the matrix.

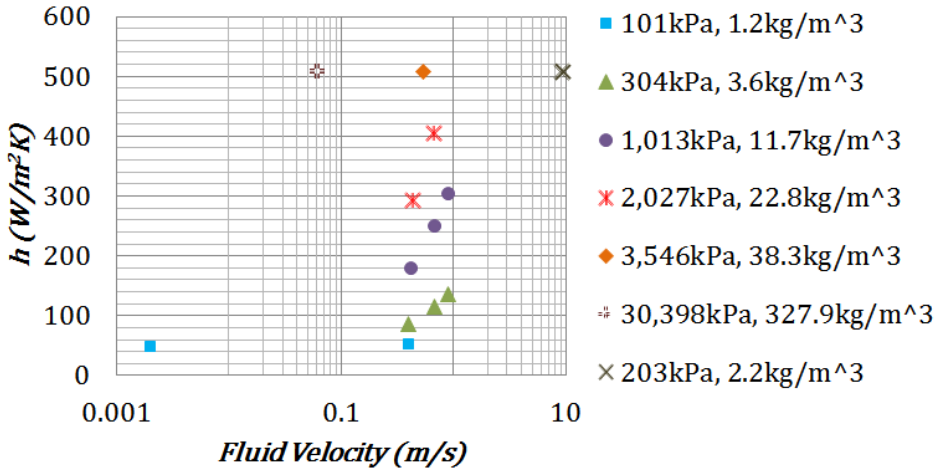

(a) Averaged wall heat transfer coefficient ("fluid velocity" refers to $|\langle\vec{u}\rangle^f|$)

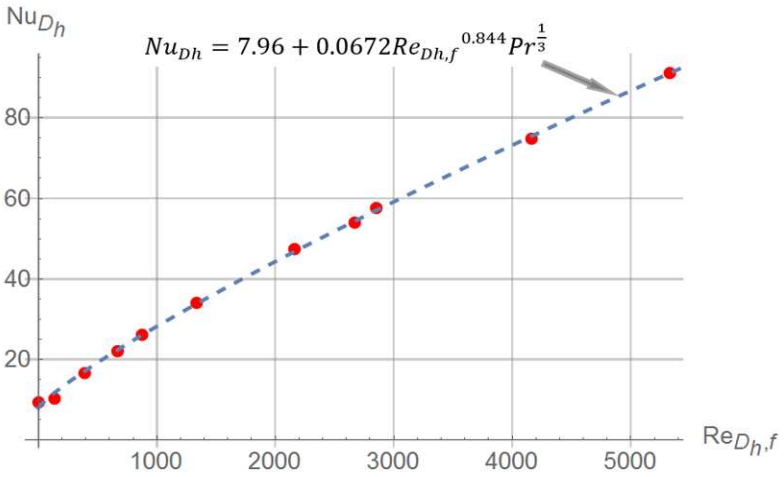

(b) Dimensionless heat transfer correlation

Fig.4.15 Heat transfer results based on simulation Set II ($\ell = 7.5mm$, $t = 0.8mm$, $2\mathscr{b} = 2.5mm$)

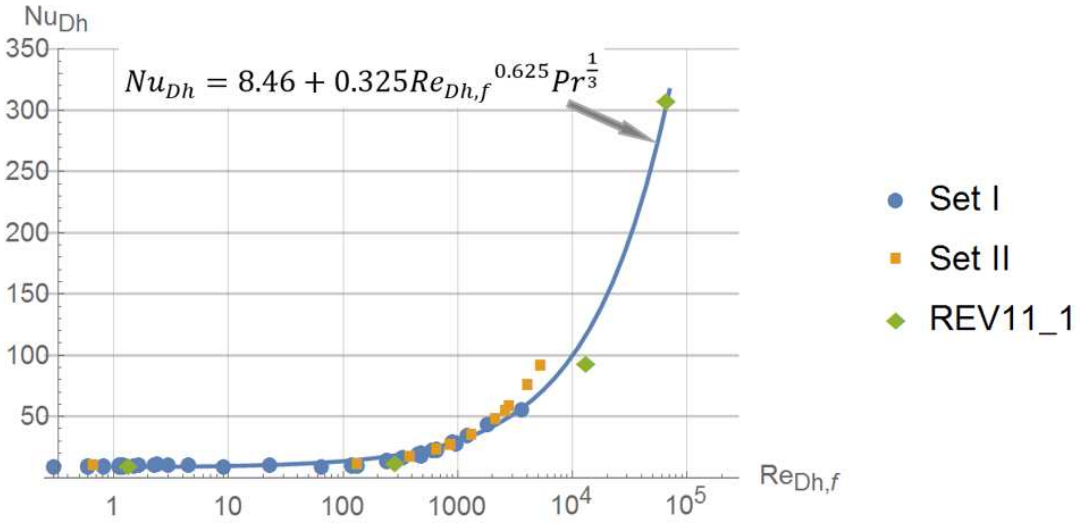

Fig.4.16 Nusselt number vs. Reynolds number based on hydraulic diameter

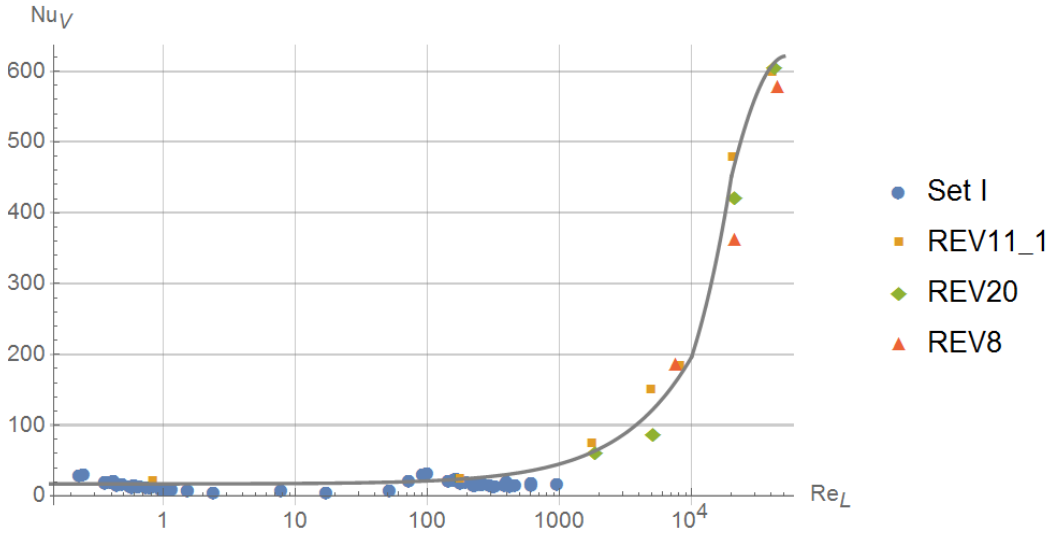

Fig.4.17 Nusselt number vs. Reynolds number for all cases (the curve represents a shape with $\frac{\ell}{2b} = 2.06$ based on the model)

A general form given in the following is used to relate Nusselt number to the Reynolds number and to the shape parameter, $\frac{\ell}{2b}$:

$$Nu_V(Re_L, \frac{\ell}{2\mathscr{b}}) = (\mathrm{a} + \mathrm{b}{Re_L}^{\mathrm{n}}\mathrm{Pr}^{\mathrm{m}})\left[\left(\frac{\ell}{2\mathscr{b}}\right)^{\mathrm{m}_1} + \mathrm{b}_2{Re_L}^{\mathrm{n}_1}\left(\frac{\ell}{2\mathscr{b}}\right)^{\mathrm{m}2}\right] \quad (4.38)$$

where coefficients m_1, m_2, n_1 may or may not depend on Reynolds number. For the flow regime $\mathrm{Re_L} < 10{,}000$, it is found that the function $Nu_V(Re_L, \frac{\ell}{2\mathscr{b}})$ can be written as:

$$Nu_{V,1} = \left(12.5 + 0.0816{Re_L}^{0.819}Pr^{\frac{1}{3}}\right) \cdot \left[\left(\frac{\ell}{2\mathscr{b}}\right)^{0.427} - 8.74 \times 10^{-7}Re_L\left(\frac{\ell}{2\mathscr{b}}\right)^{2.54}\right] \quad (4.39)$$

The function is plotted against CFD results in Fig.4.18. It shows that the shape parameter $\frac{\ell}{2\mathscr{b}}$ has different effects on heat transfer under different Reynolds numbers. For a relatively small Re_L, increasing $\frac{\ell}{2\mathscr{b}}$ slowly increases heat transfer; for a large Re_L, heat transfer is steeply enhanced as $\frac{\ell}{2\mathscr{b}}$ increases from 1 to 3.5, and maintains almost a constant value as $\frac{\ell}{2\mathscr{b}}$ continues to increase to 6.

For the flow regime $20{,}000 \leq \mathrm{Re_L} < 50{,}000$, it is found that $Nu_V(Re_L, \frac{\ell}{2\mathscr{b}})$ can be expressed as

$$Nu_{V,2} = \left(12.5 + 3.68{Re_L}^{0.490}Pr^{\frac{1}{3}}\right) \cdot \left[\left(\frac{\ell}{2\mathscr{b}}\right)^{-1.52\times10^{-5}Re_L+0.739} - 3.69 \times 10^5{Re_L}^{-1.51}\left(\frac{\ell}{2\mathscr{b}}\right)^{-1.35\times10^{-5}Re_L+1.67}\right] \quad (4.40)$$

The functions is plotted with CFD results in Fig.4.19. It shows that the value of the shape parameter, $\frac{\ell}{2\mathscr{b}}$, that corresponds to the maximum heat transfer shifts to small values as $\mathrm{Re_L}$ increases. For the region between 10,000 and 20,000 Reynolds numbers, one can use interpolation between $Nu_{V,1}$ and $Nu_{V,2}$.

$$Nu_{V,I} = \frac{Nu_{V,2} - Nu_{V,1}}{10000}(Re_L - 10000) + Nu_{V,1} \tag{4.41}$$

The overall heat transfer for the entire domain is plotted in Fig.4.20. The RMS values of the proposed models are calculated.

To give a quantitative estimate of the accuracy of the proposed heat transfer models, the RMS values are calculated. The RMS value for model $Nu_{V,1}$ ($\mathrm{Re_L} < 10{,}000$) is 4.44; the RMS value for model $Nu_{V,2}$ ($20{,}000 \leq \mathrm{Re_L} < 50{,}000$) is 11.9. Note that the Nusselt number values for the flow regime of $20{,}000 \leq \mathrm{Re_L} < 50{,}000$ is between 300 to 700; an RMS value of 11.7 is relatively small. The RMS value for the combination of the two models for the entire flow regime investigated is 5.42.

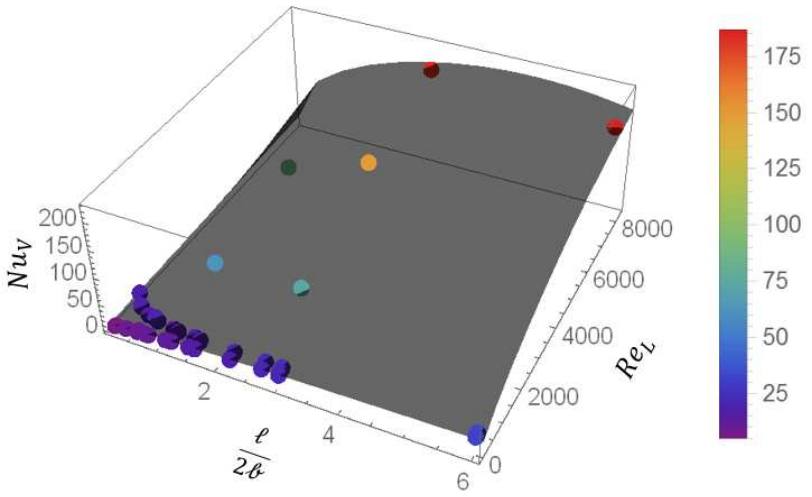

Fig.4.18 Nusselt number vs. Reynolds number and $\frac{\ell}{2\mathscr{b}}$, $\mathrm{Re_L} < 10{,}000$ (points represent CFD results; the surface represents proposed function)

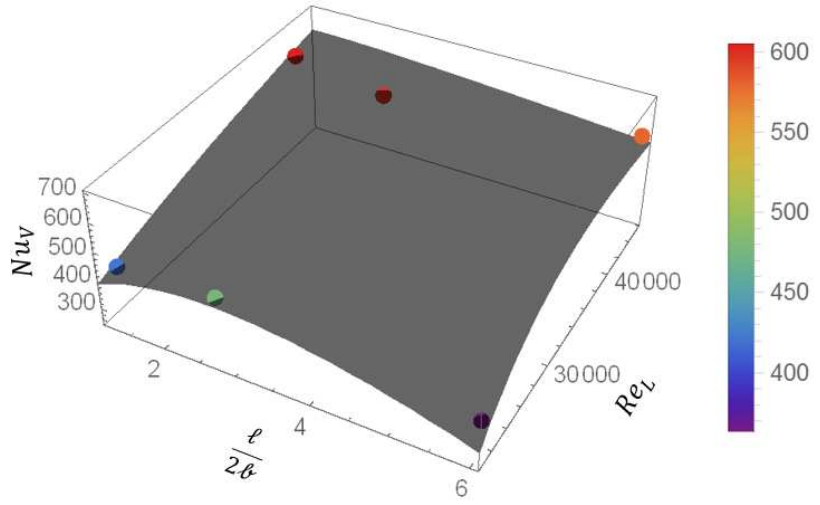

Fig.4.19 Nusselt number vs. Reynolds number and $\frac{\ell}{2b}$, $20{,}000 \leq \mathrm{Re_L} < 50{,}000$ (points represent CFD results; the surface represents proposed function)

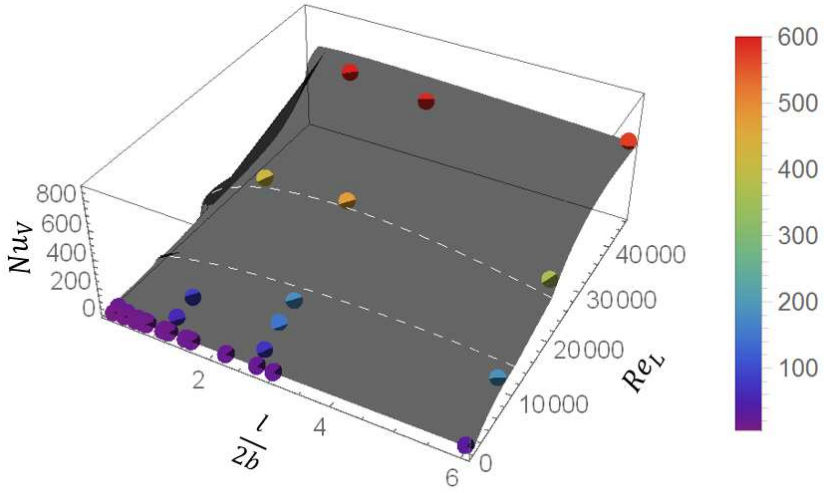

Fig.4.20 Nusselt number vs. Reynolds number and $\frac{\ell}{2b}$ for the interrupted-plate matrices (points represent CFD results; the surface represents proposed function)

4.1.6. Flow Field at Relatively High Reynolds Numbers

Flow fields of different REV shapes are compared. Three REV models with distinctively different shape are selected and two temperature fields are plotted for each model, at two

Reynolds number values. The solid plate surface has a constant heat flux boundary condition. They are shown in Fig.4.21. For comparison purposes, plotted are dimensionless temperature distributions, defined according to:

$$T^* = \frac{T - \langle T \rangle^f}{\frac{\int_{x=-\ell} T dA}{\int_{x=-\ell} dA} - \langle T \rangle^f} \tag{4.42}$$

where $x = -\ell$ is the REV upstream inlet in these cases.

For a given REV shape, a higher Reynolds number case typically has a smaller dimensionless local wall temperature value, indicating that a higher Reynolds number leads to better heat transfer. It can also be observed, by comparing the low Reynolds number run with the high Reynolds number run for each given shape, that the thermal boundary layer is much thinner in the high Reynolds number case due to a stronger turbulence effect. Comparing three different shapes at high Reynolds numbers, it can be observed that the flow is most agitated when the REV shape has an intermediate aspect ratio, $\frac{\ell}{2\mathscr{b}} = 2.73$, as shown by the eddies on the trailing edge of the plates. This observation is in line with the quantitative heat transfer results shown in Fig.4.19. As agitation enhances mixing of the fluids and hence improves heat transfer, the shape of the heat transfer surface becomes slightly concave at high Reynolds numbers (greater than 25,000); the peak heat transfer takes place when the aspect ratio of the REV, $\frac{\ell}{2\mathscr{b}}$, is between the minimum and maximum values.

The periodic heat transfer characteristics of the REV models are also shown by the local Nusselt number distribution. The local streamwise heat transfer coefficient is calculated based on the local heat flux, local wall temperature and bulk fluid temperature. Using the local streamwise heat transfer coefficient, a local Nusselt number is calculated. For selected cases, the local Nusselt number distributions are plotted against the streamwise direction x, shown in Fig.4.22. Peak heat transfer values are seen near the junctions of the interrupted plates. At a junction, the flow impinges on the frontal, cross-sectional area of a plate, resulting a steep increase in heat transfer. The impingement also causes local flow

separation at the leading edge of the plate. Therefore, immediately after the spike, the Nusselt number drops to a minimum value, but then quickly rises as the flow reattaches to the plate. As the flow moves further down the plate, a boundary layer starts to develop, and the Nusselt number gradually flattens. Clear periodic features in the local Nusselt number distributions are observed, indicating that heat transfer in the porous medium can be characterized using REV scales, thus reassuring that the Volume Averaging Technique that treats a porous medium region as a continuum is valid. The averaged local Nusselt numbers are calculated and shown with comparison to the REV-volume-averaged hydraulic Nusselt number, defined according to Eq.(4.33). For high-pressure compression up to 210bar, a constant piston speed of 15cm/s leads to a maximum Reynolds number, Re_L, of a value around 8000 near the end of compression, which is close to the lower Reynolds number values of the matrix shapes listed in Table 4.3.

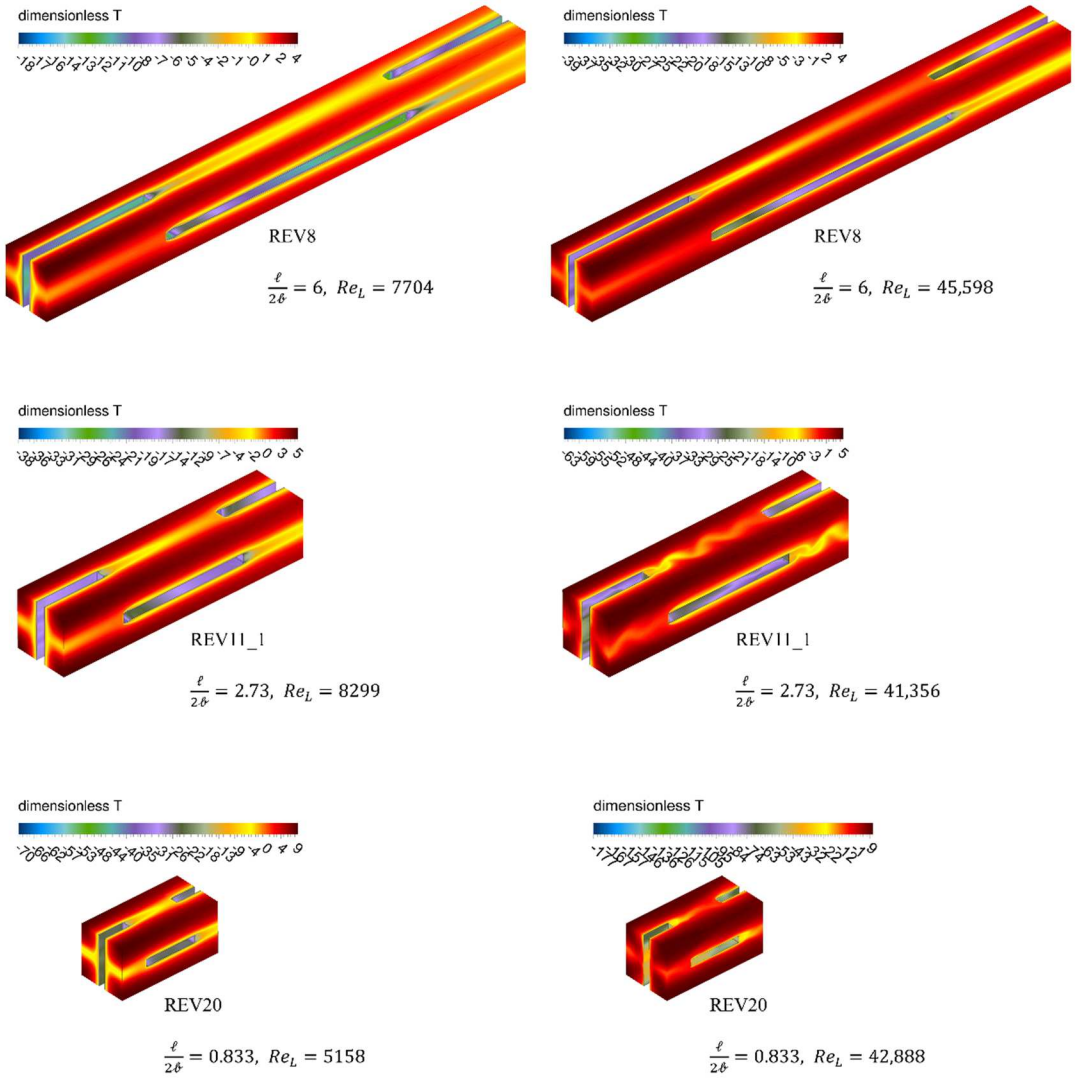

Fig.4.21 Comparison of flow fields in REV simulations (based on transient RANS) of different shape parameters and Reynolds numbers

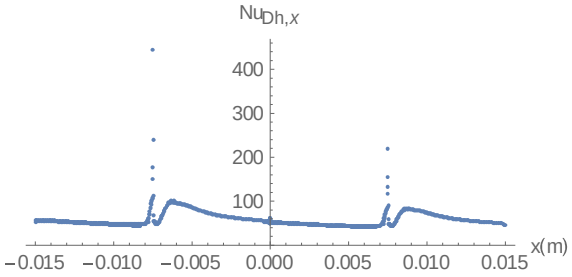

(a) REV8, $\frac{\ell}{2\mathscr{b}} = 6$, $Re_L = 7704$

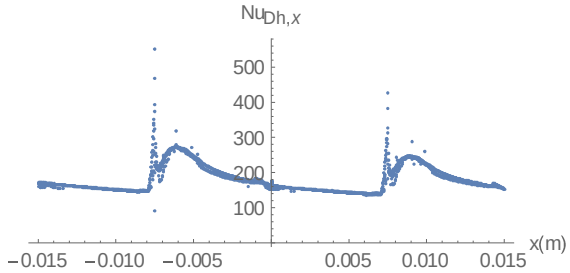

(b) REV8, $\frac{\ell}{2\mathscr{b}} = 6$, $Re_L = 45{,}598$

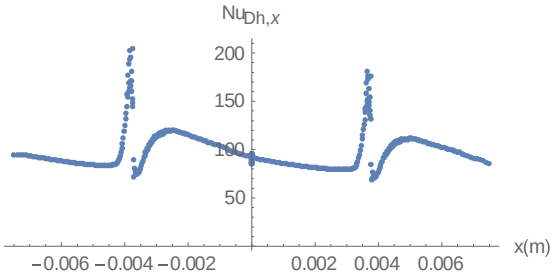

(c) REV11_1, $\frac{\ell}{2\mathscr{b}} = 2.73$, $Re_L = 8299$

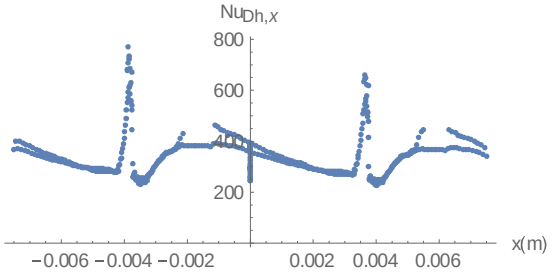

(d) REV11_1, $\frac{\ell}{2\mathscr{b}} = 2.73$, $Re_L = 41{,}356$

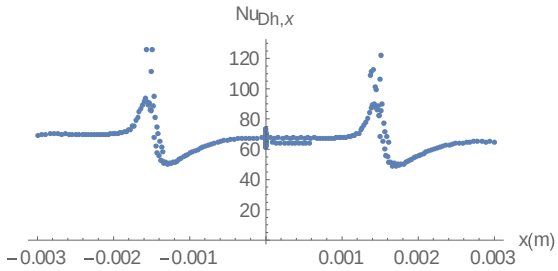

(e) REV20, $\frac{\ell}{2\mathscr{b}} = 0.833$, $Re_L = 5158$

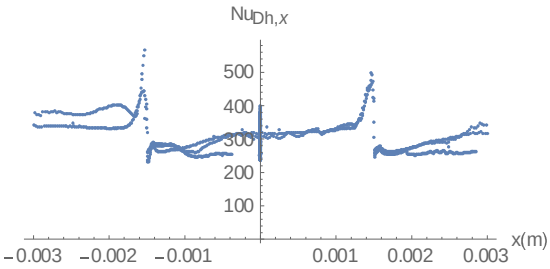

(f) REV20, $\frac{\ell}{2\mathscr{b}} = 0.833$, $Re_L = 42{,}888$

Fig.4.22 Streamwise pore-scale Nusselt number distributions in different REV models

Table 4.3 Comparison between Nusselt number based on the REV volume-averaging definition and the averaged local Nusselt number

	REV 8		REV11_1		REV20	
Re_L	7704	45,598	8299	41,356	5158	42,888
Nu_{Dh}	57.5	175	92.6	305	64.0	294
$\frac{1}{2\ell}\int_{-\ell}^{\ell} Nu_{Dh,x}dx$	58.4	180	96.7	344	66.7	316

4.1.7. Flow Field at Extremely Small Reynolds Numbers

When the Reynolds number is extremely small (around 1), the flow physics is different. In the liquid piston compressor, flow with a Reynolds number around 1 is experienced in a small fraction during the start or stop of compression, or at locations very close to the chamber wall. (Note that the flow is never completely stagnant unless it is right on the wall.) The exchanger matrix, REV11 ($\ell = 7.5\text{mm}, t = 0.8, 2b = 2.5\text{mm}$) is analyzed for this low Reynolds number study. Periodic flow condition is assumed with inclusion of gravity effect. The wall temperature is 293K. Five simulation runs are done with different inlet flow temperatures. The Reynolds number based on the plate height, $\text{Re}_{\ell,\text{f}}$, is 1 in each simulation, or, equivalently, the flow has: $\text{Re}_{\text{Dh,f}} = 0.66$ or $\text{Re}_{\text{L,f}} = 0.52$. The Prandtl numbers are fixed at 0.714 in different runs through UDF scripts that adjust the viscosity and conductivity values accordingly.

The Nusselt number for each case is calculated based on Eqns.(4.33) and (4.31), which are defined according to the standard Volume Averaging Technique. The results are shown in Table 4.4. Although in the five runs the mean flow temperatures are different from one another, the calculated Nusselt number values are close, between 9.1 and 9.5, confirming that the Nusselt number is independent of the mean flow temperature at small Reynolds numbers. This is in line with the heat transfer correlations proposed in section 4.1.5.

Table 4.4 Simulation runs and results, REV11, $\text{Re}_{\ell,\text{f}} = 1$, $\text{Pr} = 0.714$

	$(\langle T \rangle^f - T_0)/K$	Nu_{Dh}
Run1	0.43	9.5
Run2	0.85	9.2
Run3	1.6	9.1
Run4	4.0	9.1
Run5	10	9.5

The temperature field of one of the runs is shown in Fig.4.23. Comparing to previous flow features at higher Reynolds numbers, one significant difference is that due to the small Reynolds number ($\mathrm{Re}_{\ell,\mathrm{f}} = 1$), the hotter flow at the inlet is cooled by conduction before it is convected farther downstream. In the majority region of an REV cell, the flow temperature and the wall temperature are very close, which causes the temperature distribution on the outlet surface to appear uniform in Fig.4.23, where the color scale is based on the global minimum and maximum temperature values. However, the outlet surface actually has the same temperature profile as the inlet surface as required by the periodic boundary condition. When the inlet and outlet temperatures are plotted on different local scales, they show the same distribution. This is shown in Fig.4.24, along with the local wall heat flux distribution. It is observed that in the region where the temperature difference between the flow and the wall is small, the wall heat flux is also small. As the local heat transfer is a division between the local wall heat flux and local temperature difference, it becomes fluctuating due to numerical uncertainties, or round-off errors in the numerical simulation. As shown in Fig.4.23, the local temperature difference on the outlet cross section is less than $\frac{1}{1000}$K. The local Nusselt number distribution is shown in Fig.4.25. Although most of the downstream region in the REV has a local Nusselt number that is subject to fluctuations due to the denominator of the heat transfer coefficient being close to zero, in the beginning part of the REV where the temperature difference between the flow and the wall is more significant, the local Nusselt number values appear to have an approximate average close to 9, which is the expected pore-scale Nusselt number value.

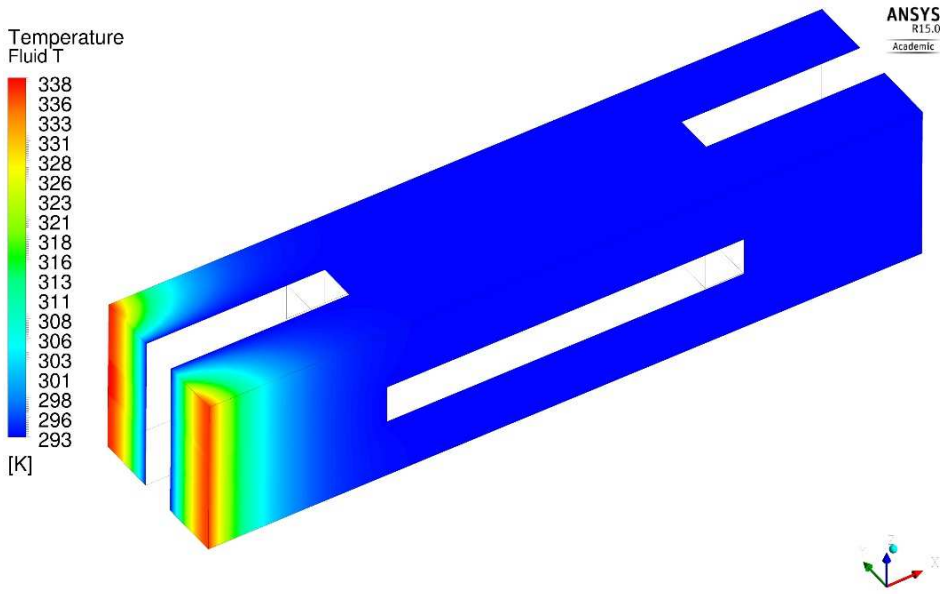

Fig.4.23 Temperature fields, Run3, $\langle T \rangle^f - T_0 = 1.6K$, $\mathrm{Re}_{\ell,\mathrm{f}} = 1$, $\mathrm{Pr} = 0.714$

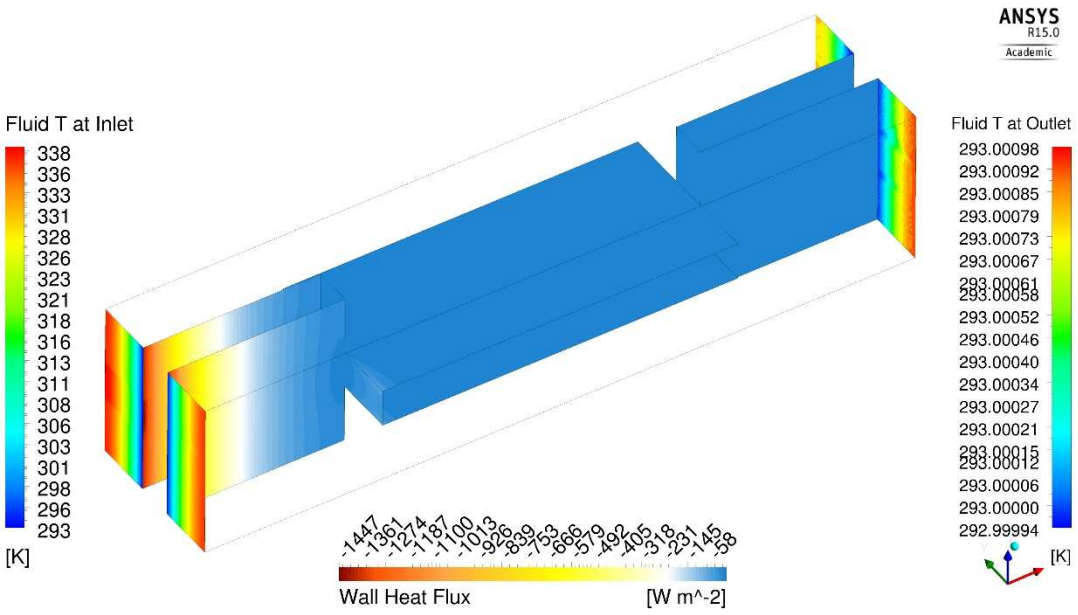

Fig.4.24 Wall heat flux and temperature distributions at the inlet and outlet, Run3, $\langle T \rangle^f - T_0 = 1.6K$, $k = 0.0254W/(mK)$, $\mathrm{Re}_{\ell,\mathrm{f}} = 1$, $\mathrm{Pr} = 0.714$

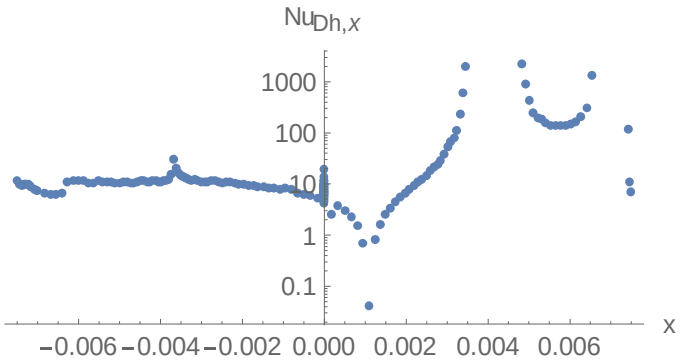

Fig.4.25 Streamwise pore-scale Nusselt number distribution, Run3, $\langle T \rangle^f - T_0 = 1.6K$, $\mathrm{Re}_{\ell,\mathrm{f}} = 1$

4.2. Anisotropic Pressure Drop and Heat Transfer

This section presents a study on the modeling of three-dimensional, anisotropic heat transfer and flow resistance properties of the interrupted-plate medium. The anisotropic pressure drop and heat transfer of the interrupted-plate medium are determined using the microscopic (pore-scale) results calculated in REV simulations using different Reynolds numbers and various flow angles.

4.2.1. Governing Equations and Numerical Procedure

The basic transport equations are the same as Eq.(4.7) - (4.9). Different flow directions in different REV simulations are set by varying the pressure gradient direction. The pressure gradient is decoupled into a macroscopic pressure gradient, which is due to the periodic interruption of the porous medium, and a microscopic (pore-scale) pressure gradient, which is due to the local flow field variation inside the REV:

$$\frac{\partial p}{\partial x_i} = \left|\frac{\partial \langle p \rangle^f}{\partial x_i}\right| \left(cos\alpha_p, cos\beta_p, cos\gamma_p\right) + \frac{\partial p'}{\partial x_i} \tag{4.43}$$

Angles α_p, β_p and γ_p are varied in different simulation runs. The pore-scale pressure gradient, $\frac{\partial p}{\partial x_i}$, and the magnitude of the global-scale pressure drop $\left|\frac{\partial \langle p \rangle^f}{\partial x_i}\right|$ are calculated. Geometrical representations of these angles are given in Fig.4.26 (a). Any direction in a 3-D space can be defined by using either the (α, β, γ) system, or a (φ, θ) system, as shown in Fig.4.26 (b).

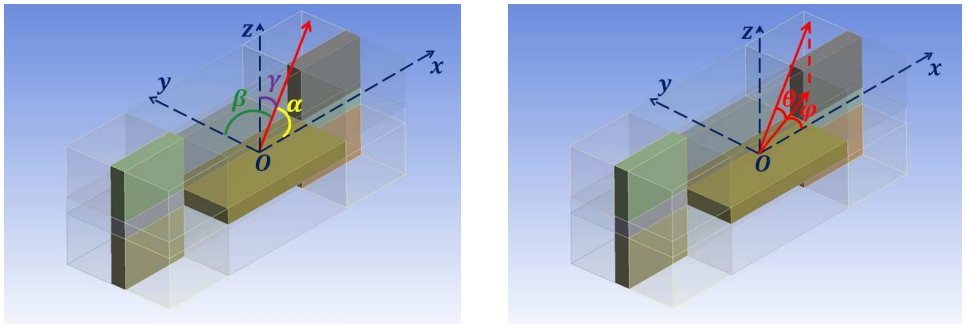

(a) α, β and γ (b) φ and θ

Fig.4.26 Schematic of two sets of angles used to characterize the direction of a vector

Periodic boundary conditions are applied all inlet and outlet paring boundaries of the REV domain:

$$\Gamma|_{x=-\ell} = \Gamma|_{x=\ell}\,, \quad \Gamma|_{y=-(b+\frac{t}{2})} = \Gamma|_{y=b+\frac{t}{2}}\,, \quad \Gamma|_{z=-(b+\frac{t}{2})} = \Gamma|_{z=b+\frac{t}{2}} \qquad \Gamma = u_i, p$$

On the interfacial boundary between the fluid and solid, the no-slip velocity and uniform-wall-heat-flux boundary conditions are used. The periodic thermal boundary condition is defined using interfacial wall heat flux and mean flow angle,

$$\frac{T|_{x=\ell} - T|_{x=-\ell}}{2\ell} = \frac{q'' a_V}{\rho c_p |\langle \vec{u} \rangle^f|} cos\alpha \qquad (4.44)$$

$$\frac{T|_{y=\mathscr{b}+\frac{t}{2}} - T|_{y=-(\mathscr{b}+\frac{t}{2})}}{2\mathscr{b}+t} = \frac{q'' a_V}{\rho c_p |\langle \vec{u} \rangle^f|} cos\beta \tag{4.45}$$

$$\frac{T|_{z=\mathscr{b}+\frac{t}{2}} - T|_{z=-(\mathscr{b}+\frac{t}{2})}}{2\mathscr{b}+t} = \frac{q'' a_V}{\rho c_p |\langle \vec{u} \rangle^f|} cos\gamma \tag{4.46}$$

where $cos\alpha$, $cos\beta$, $cos\gamma$ are projections of the unit mean velocity vector onto the x, y and z axes, respectively. The matrix is REV11_1, with the following shape parameters:

$$\ell = 7.5mm, \quad 2\mathscr{b} = 2.75mm, \quad t = 0.55mm,$$

$$\epsilon = 0.8333, \quad a_V = 643.1/m, \quad L = 4.083mm$$

Twenty different mean flow directions are used for each of the 181 and 8309 Reynolds numbers.

The transport equations are solved by the finite volume method using the commercial CFD software ANSYS Fluent, based on the SIMPLE algorithm. The first-order implicit formulation is used for transient discretization; the second-order upwind scheme is used for discretizing advective terms; central differencing is used for diffusive terms. The convergence criterion for residuals of all equations is set to 10^{-9}. The computational domain is discretized into rectangular hexahedral cells. The cell size gradually decreases as the walls are approached. The total numbers of grid cells are 1,469,139, for simulation runs with Reynolds numbers of 8309, and 707,840, for simulation runs with smaller Reynolds numbers. The maximum value of the dimensionless wall distance (y^+) of the first cell adjacent to the wall is between 2 and 6 for simulations of 8309 Reynolds number. The Transition SST model is used for modeling the turbulent viscosity and turbulent kinetic energy.

4.2.2. Anisotropic Pressure Drop

In this section, flow fields and anisotropic flow resistance of the interrupted-plate medium are discussed in specially selected scenarios, to reveal the effects of: (1) the mean velocity on the pressure drop when the velocity is aligned with the pressure gradient, (2) y-direction

velocity component on z-direction pressure drop, and (3) x-direction velocity component on y-direction pressure drop, as well as y-direction velocity component on x-direction pressure drop. Then, the pressure drop models will be tested against cases with randomly selected mean flow attack angles.

4.2.2.1. Mean flow aligned with the plate

When the mean flow direction is aligned with the plate, such as the Ox or Oy coordinate (see Fig.4.26), the pressure gradient points to the same direction as the mean flow. Velocity streamline plots are shown in Fig.4.27 and Fig.4.28 for cases with the mean flow along the Ox and Oy directions, at a Reynolds number of 8309. Because the thickness of the plate is relatively small, when the mean flow is in the Ox direction, local flow in the REV is also in the same direction as the mean flow; only very small regions of stagnation and separation are seen near the leading and trailing edges. When the mean flow is in the Oy direction, it is perpendicular to a set of vertical plates, as shown inFig.4.28. In this case, flow regions interrupted by the plates are mostly stagnation regions.

The pressure drop in these flow situations is caused by viscous and by inertial effects in, respectively, the Ox and Oy directions. It is modeled using a Darcian and an inertial term,

$$\left(\frac{\partial p^*}{\partial x^*}\right)_{Ox} = -\frac{1}{Re_L}\frac{L^2}{K_1} - Lb_1 \tag{4.47}$$

$$\left(\frac{\partial p^*}{\partial y^*}\right)_{Oy} = -\frac{1}{Re_L}\frac{L^2}{K_2} - Lb_2 \tag{4.48}$$

where the dimensionless pressure drop is based on,

$$\nabla p^* = \frac{L}{\rho|\langle\vec{u}\rangle|^2}\nabla p \tag{4.49}$$

Using calculated pressure drop values from the CFD runs, the permeability and inertial coefficients in the Ox and Oy directions are found:

$$K_1 = 4.79 \times 10^{-7} m^2, \quad K_2 = 2.59 \times 10^{-7} m^2, \quad b_1 = 24.69/m, \quad b_2 = 23.85/m$$

The model (the curve) and the CFD results (the points) are compared in Fig.4.29, which shows good agreement. The dimensionless pressure drop decreases with increasing Reynolds number, because of non-dimensionalization with the inertial terms.

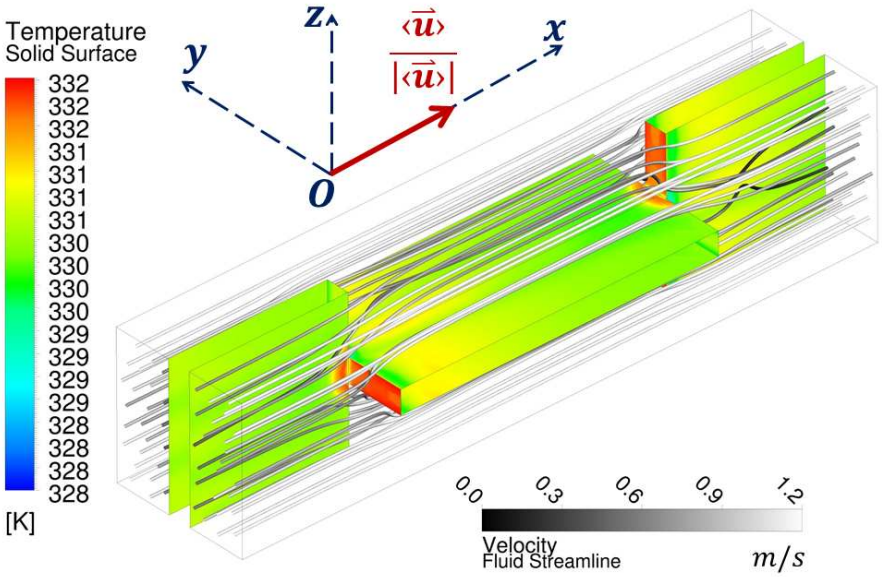

Fig.4.27 Velocity and wall temperature distributions ($Re_L = 8309, \theta = 0, \varphi = 0$)

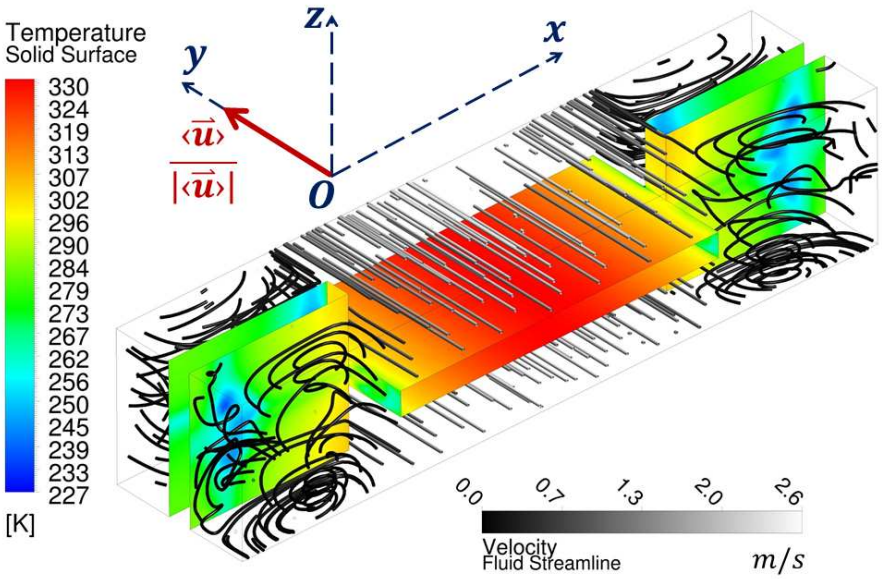

Fig.4.28 Velocity and wall temperature distributions ($Re_L = 8309, \theta = 0, \varphi = 90^o$)

4.2.2.2. Flow Parallel to the yOz Plane

Under this condition, the mean flow may impinge onto both plates in the REV. As a result, flows in different regions in the REV follow distinctively different directions, which allows the local flow to run parallel to the nearest plate to avoid direct impingement on it. As shown in Fig.4.30 and Fig.4.31, in different locations inside the REV, the flows are in a different directions, yet approximately parallel to the nearest plates.

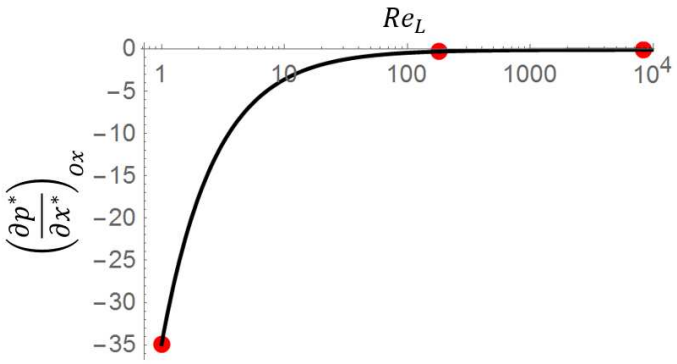

(a) Mean flow in Ox direction

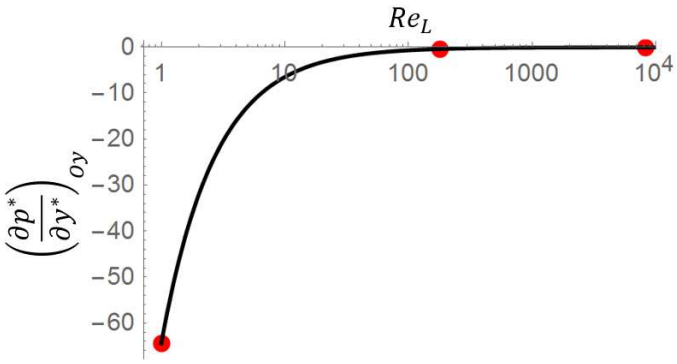

(b) Mean flow in Oy direction

Fig.4.29 Pressure drop vs. Reynolds number when the mean flow is along the symmetric lines of the plate (Curves: model; points: CFD results)

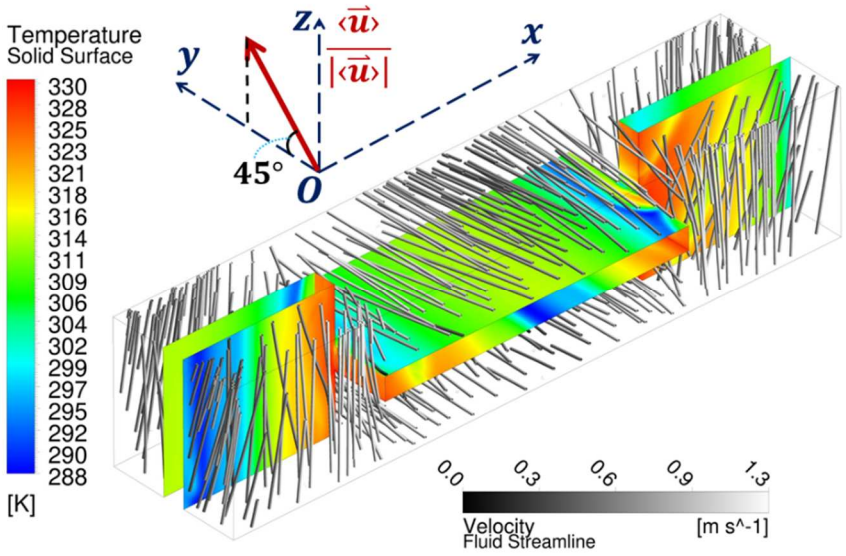

Fig.4.30 Velocity and wall temperature distributions ($Re_L = 8309, \theta = 45^o, \varphi = 90^o$)

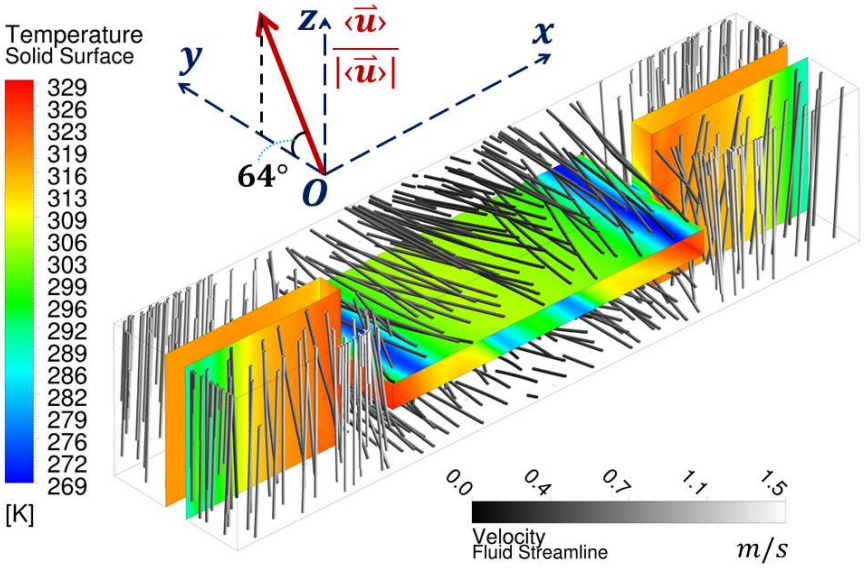

Fig.4.31 Velocity and wall temperature distributions ($Re_L = 8309, \theta = 64^o, \varphi = 90^o$)

Impingement of flow onto the plates results in flow separation and mixing effects. The pressure drop will be characterized using an inertial and an additional mixing term. The pressure drop caused by inertia is direction-dependent; the pressure drop in the Oy direction results from the inertial effect in the Oy direction, as well as that in the Oz direction. According to Eq. (3.1), the inertial effects in the Oy and Oz directions result in a pressure drop in the Oy direction, which should be modeled in a more general form, as $-\rho b_2|\langle\vec{u}\rangle|^2\langle u_3{}^*\rangle$ and $-\rho b_{23}cos\beta cos\gamma|\langle\vec{u}\rangle|^2\langle u_3{}^*\rangle$, respectively. Unsteady, mixing effects are found along with flow separation after flow impinges on a plate. A mixing term must be used in the modeling of the pressure drop to account for this effect. In [31], the term, $-\frac{H}{K^{3/4}}(\rho\mu|\langle\vec{u}\rangle|)^{\frac{1}{2}}\langle\vec{u}\rangle$, or $-\rho\mathcal{H}Re_L^{-0.5}|\langle\vec{u}\rangle|\langle\vec{u}\rangle$, was used to capture mixing effects of an oscillatory flow as it transitions from a relatively stable state to an unstable state. In the present study, varying the mean flow direction from one that is aligned with the plate to one that has an attack angle to the plate transitions the flow from a relatively stable state to an unstable state with increasing mixing effects. Thus, the amount of pressure drop caused by this mixing effect is modeled based on a variation of the term proposed in [31]: $\rho H_{23}Re_L^{m_{23}}\langle u_2\rangle\langle u_3\rangle$, or $\rho H_{23}Re_L^{m_{23}}cos\beta|\langle\vec{u}\rangle|^2\langle u_3\rangle^*$. In sum, the pressure drop in the Oy direction is:

$$\left(\frac{\partial p^*}{\partial y^*}\right)_{yOz} = -\frac{1}{Re_L}\frac{L^2}{K_2}\langle u_2\rangle^* - [Lb_2 \quad Lb_{23}cos\beta cos\gamma]\begin{bmatrix}\langle u_2\rangle^*\\ \langle u_3\rangle^*\end{bmatrix} - H_{23}Re_L^{m_{23}}cos\beta\langle u_3\rangle^* \tag{4.50}$$

Due to the identical periodic features of the shape along the Oy and Oz directions, the pressure drop in the Oz direction must be modeled as:

$$\left(\frac{\partial p^*}{\partial z^*}\right)_{yOz} = -\frac{1}{Re_L}\frac{L^2}{K_2}\langle u_3\rangle^* - [Lb_{23}cos\beta cos\gamma \quad Lb_2]\begin{bmatrix}\langle u_2\rangle^*\\ \langle u_3\rangle^*\end{bmatrix} - H_{23}Re_L^{m_{23}}cos\gamma\langle u_2\rangle^* \tag{4.51}$$

Good agreement is found between the model and the directional pressure drop values calculated from ten CFD runs with five different mean flow angles and two Reynolds numbers, as shown in Fig.4.32. A directional component of the pressure drop increases as the velocity component along the same direction increases. This is the result of an increasing amount of flow impinging onto the plate. The directional inertial coefficient and the mixing coefficients are:

$$b_{23} = -11.92/m, \quad H_{23} = 3.605 \times 10^{-2}, \quad m_{23} = 0.1050$$

4.2.2.3. Flow parallel to the xOy plane

When the mean flow direction is parallel to the xOy plane, the local flow may impinge on the plate that is perpendicular to the xOy plane. As shown in Fig.4.33 and Fig.4.34, when the mean flow has an attack angle to the vertical plates but parallel to the horizontal plane, the local flows in different regions in the REV follow different directions. The flow in the gap space between the two vertical plates in Fig.4.33, has an angle φ greater than that of the mean flow; the flows alongside the two vertical plates are nearly parallel to the plates, due to the large flow resistance; flow separation zones form due to impingement effects.

Comparing Fig.4.33 and Fig.4.34 to Fig.4.30 and Fig.4.31, one sees that if the mean flow is parallel to the yOz plane (Fig.4.30 and Fig.4.31), the local fluid follows the Oy direction in some regions of the REV while in other regions it follows the Oz direction. However, if the mean flow is parallel to the xOy plane (Figs. 9 and 10), it is not possible for the local fluid to follow the Oz direction. As a result, the impingement effects onto the vertical plates in the situation of Fig.4.33 and Fig.4.34 are much stronger than those in the situation of Fig.4.30 and Fig.4.31. Therefore, when the mean flow is parallel to the xOy plane, stronger separation zones behind those plates are created, which induces larger pressure drop in the Ox direction. As can be seen, the flow separation and mixing effect are strongly affected by mean flow angle of attack. The pressure drop must be modeled to capture these effects.

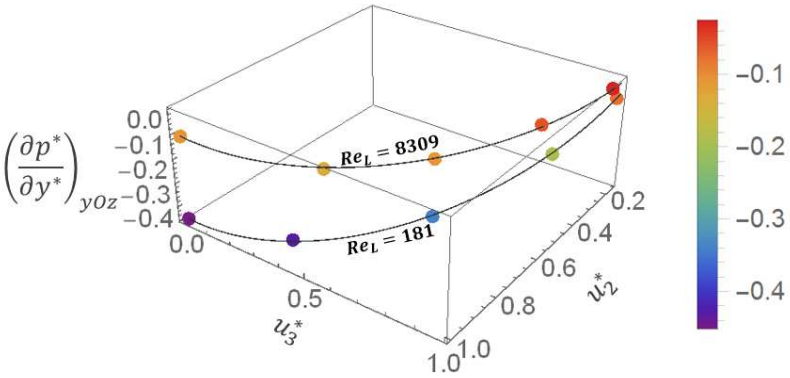

(a) y-directional pressure drop

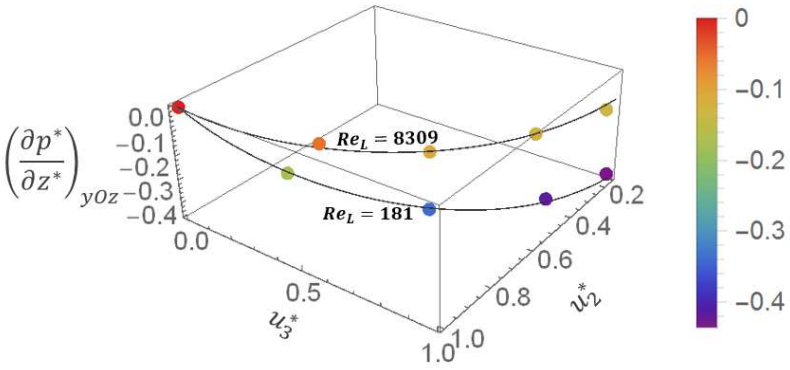

(b) z-directional pressure drop

Fig.4.32 Pressure drop for different mean flow directions with different Reynolds numbers, all parallel to the yOz plane. (Curves: model; points: CFD results)

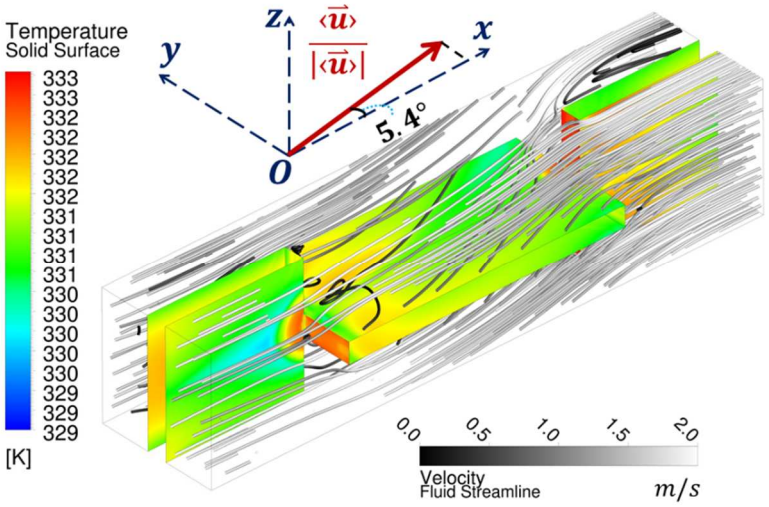

Fig.4.33 Velocity and wall temperature distributions ($Re_L = 8309, \theta = 0, \varphi = 5.4^o$)

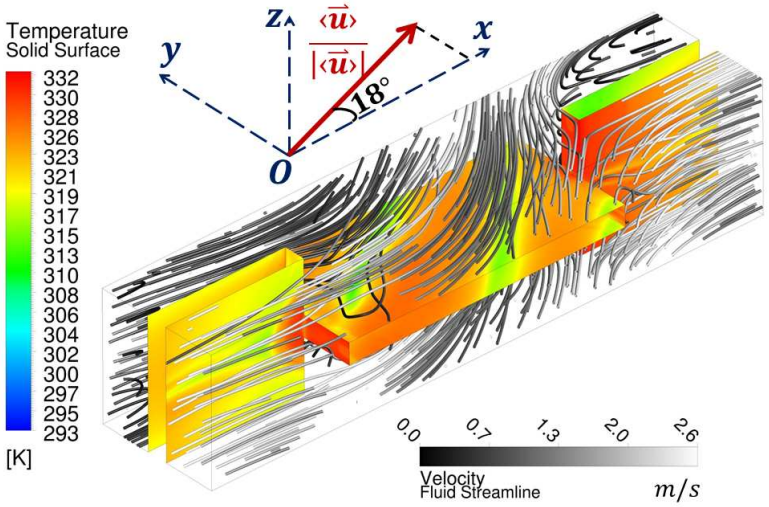

Fig.4.34 Velocity and wall temperature distributions ($Re_L = 8309, \theta = 0, \varphi = 18^o$)

The directional pressure drop is modeled using a Darcian term, an inertial term, and a mixing term representing flow separation due to impingement:

$$\left(\frac{\partial p^*}{\partial x^*}\right)_{xOy} = -\frac{1}{Re_L}\frac{L^2}{K_1}\langle u_1\rangle^* - [Lb_1 \quad Lb_{12}cos\alpha cos\beta]\begin{bmatrix}\langle u_1\rangle^* \\ \langle u_2\rangle^*\end{bmatrix}$$

$$-H_{12}Re_L^{m_{12}}cos\alpha\langle u_2\rangle^* \tag{4.52}$$

$$\left(\frac{\partial p^*}{\partial y^*}\right)_{xOy} = -\frac{1}{Re_L}\frac{L^2}{K_2}\langle u_2\rangle^* - [Lb_{21}cos\alpha cos\beta \quad Lb_2]\begin{bmatrix}\langle u_1\rangle^* \\ \langle u_2\rangle^*\end{bmatrix}$$

$$-H_{21}Re_L^{m_{21}}cos\beta\langle u_1\rangle^* \tag{4.53}$$

Results from twelve CFD runs with different mean flow angles and two different Reynolds numbers are used to find the inertial and mixing coefficients in the model.

$$b_{12} = -63.12/m, \qquad b_{21} = 221.6/m, \qquad H_{12} = 0.6252,$$

$$H_{21} = 2.271, \qquad m_{12} = -0.04198, \qquad m_{21} = 0.02699$$

The model and the CFD runs are in good agreement as shown in Fig.4.35. The maximum values for the directional components of the pressure drop, $\frac{\partial p^*}{\partial x^*}$ and $\frac{\partial p^*}{\partial y^*}$, are reached when the mean flow has an angle of attack with respect to the plates.

In the previous discussions, specially chosen CFD runs have resolved the pressure drop characteristics of the interrupted plate medium with respect to different flow angles and the directional pressure drop components are shown to be functions of directional velocity components. The full model is given by:

$$\nabla^* p^* = -\frac{1}{Re_L}\begin{bmatrix} \frac{L^2}{K_1} & 0 & 0 \\ 0 & \frac{L^2}{K_2} & 0 \\ 0 & 0 & \frac{L^2}{K_2} \end{bmatrix}\begin{bmatrix} \langle u_1 \rangle^* \\ \langle u_2 \rangle^* \\ \langle u_3 \rangle^* \end{bmatrix}$$

$$-\begin{bmatrix} Lb_1 & Lb_{12}cos\alpha cos\beta & Lb_{12}cos\alpha cos\gamma \\ Lb_{21}cos\alpha cos\beta & Lb_2 & Lb_{23}cos\beta cos\gamma \\ Lb_{21}cos\alpha cos\gamma & Lb_{23}cos\beta cos\gamma & Lb_2 \end{bmatrix}\begin{bmatrix} \langle u_1 \rangle^* \\ \langle u_2 \rangle^* \\ \langle u_3 \rangle^* \end{bmatrix}$$

$$-\begin{bmatrix} 0 & H_{12}Re_L^{m_{12}}cos\alpha & H_{12}Re_L^{m_{12}}cos\alpha \\ H_{21}Re_L^{m_{21}}cos\beta & 0 & H_{23}Re_L^{m_{23}}cos\beta \\ H_{21}Re_L^{m_{21}}cos\gamma & H_{23}Re_L^{m_{23}}cos\gamma & 0 \end{bmatrix}\begin{bmatrix} \langle u_1 \rangle^* \\ \langle u_2 \rangle^* \\ \langle u_3 \rangle^* \end{bmatrix} \quad (4.54)$$

4.2.2.4. Mean flow impinging on both plates

Twenty additional CFD runs are made for cases in which the mean flow is in a direction that is not parallel to either of the plates or the x, y, z coordinates. In this case, neither φ nor θ is 0 or 90^o. The flow fields for such cases are shown in Fig.4.36 and Fig.4.37. Even though the mean flow is in a certain direction, the local flow features do not follow this direction, and they run in very different directions to reduce impingement on the walls, leading to complex flow separation and mixing pattern. This feature is beneficial for heat transfer, as the amount of mixing that leads to heat transfer is determined by the pore-scale mixing activities.

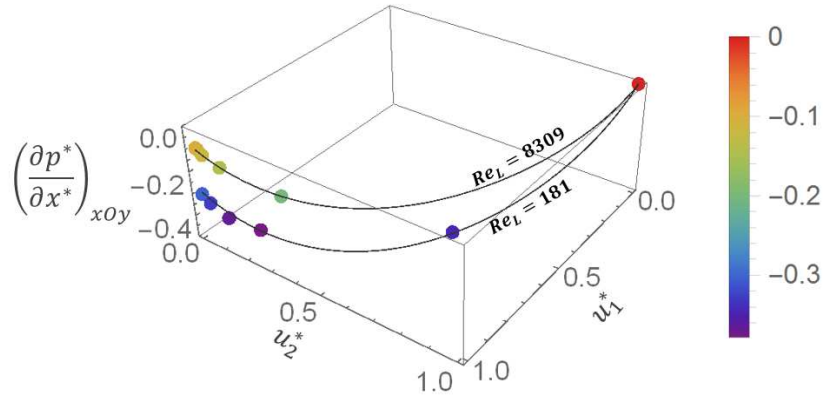

(a) x-directional pressure drop

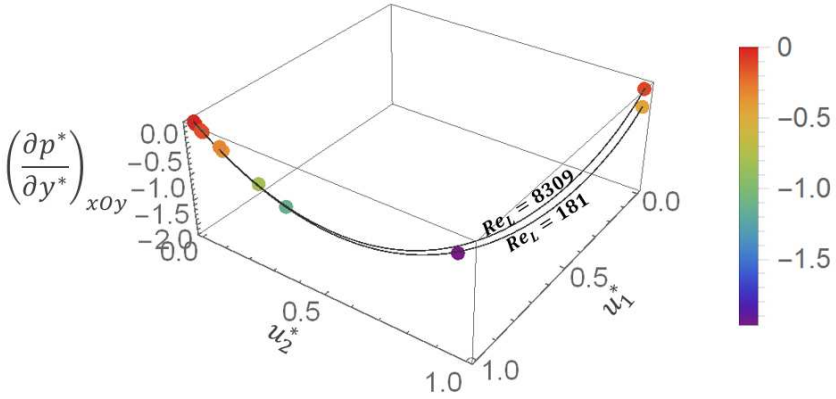

(b) y-directional pressure drop

Fig.4.35 Pressure drops with different mean flow directions with different Reynolds numbers, all parallel to the xOy plane. (Curves: model; points: CFD results)

The model (Eq.(4.54)) and pressure drop values calculated from all the simulation cases are compared in Fig.4.38. The following features of the anisotropic pressure drop of the interrupted-plate medium can be observed. For a very small θ, as φ increases from 0 to 90^o, (1) the x-direction pressure drop increases slightly when φ reaches around 30^o, due to an increase in viscous effects in the x-direction, and it then decreases to 0 as φ increases to 90^o, due to a decrease in the x-directional inertial effects, and (2) the y-directional pressure drop increases as φ increases from 0 to around 45^o, due to increasing

flow separation caused by flow impinging on the plate, and then decreases to smaller values, due to an increasing size of the flow stagnation region. For large θ values, the effects of changing φ on the pressure drop values in the Ox and Oy directions are small because the local fluid in the REV is allowed to go in the Oz direction to avoid direct impingement onto the plate, which avoids flow separation or stagnation. For very small values of φ, as θ increases from 0 to 90^{o}, the z-direction pressure drop first increases and then decreases, because impingement of flow onto the plates first causes separation and then stagnation. For a large value of φ, the effect of θ on the z-direction pressure drop is small because local fluid in the REV can avoid directly impinging upon the plates while maintaining the mean flow direction.

In the development of the model, an anisotropic mixing term (the last term on the RHS of Eq. (20)) was introduced. This term is special to the 3-D porous medium in the present study, because the plates in the porous medium cause strong separation and mixing when flow impinges on them, which is different from the flow through an open-cell or a packed bed of spheres. The RMS values of the model with inclusion of only the Darcian and inertial terms, and of the model with inclusion of all three terms are calculated. The RMS values are normalized on the differences between the maximum and minimum values of the samples. It is shown in Fig.4.39 that inclusion of the mixing term gives predicted pressure drop values closer to those of the CFD results.

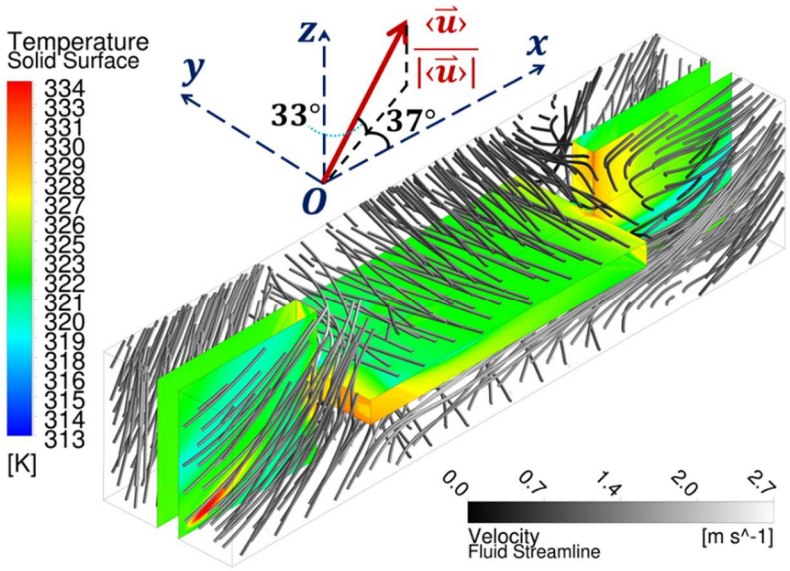

Fig.4.36 Velocity and wall temperature distributions ($Re_L = 8309, \theta = 33^o, \varphi = 37^o$)

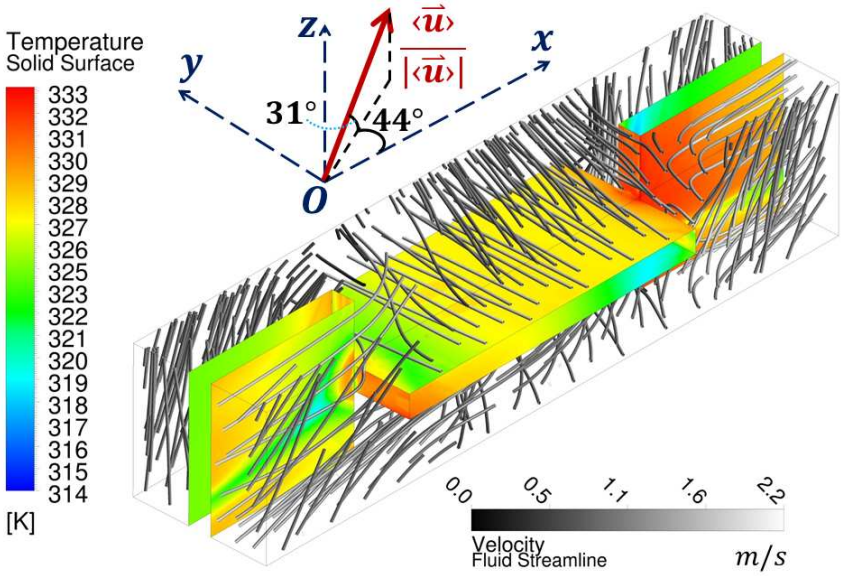

Fig.4.37 Velocity and wall temperature distributions ($Re_L = 8309, \theta = 31^o, \varphi = 44^o$)

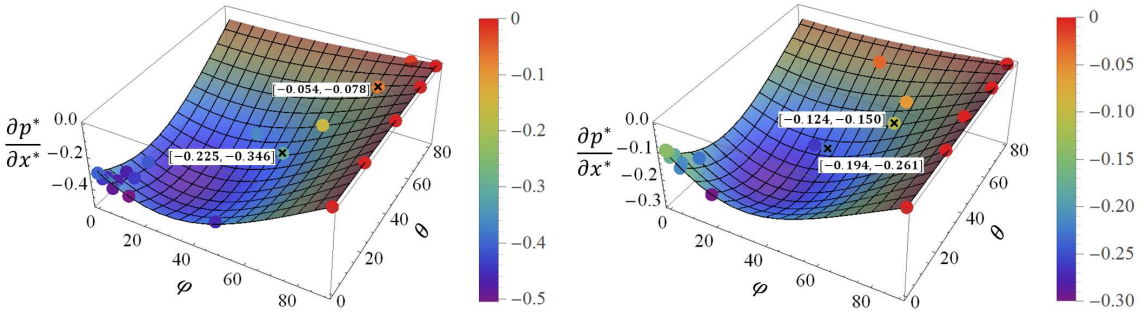

(a) x-direction pressure drop, $Re_L = 181$ (b) x-direction pressure drop, $Re_L = 8309$

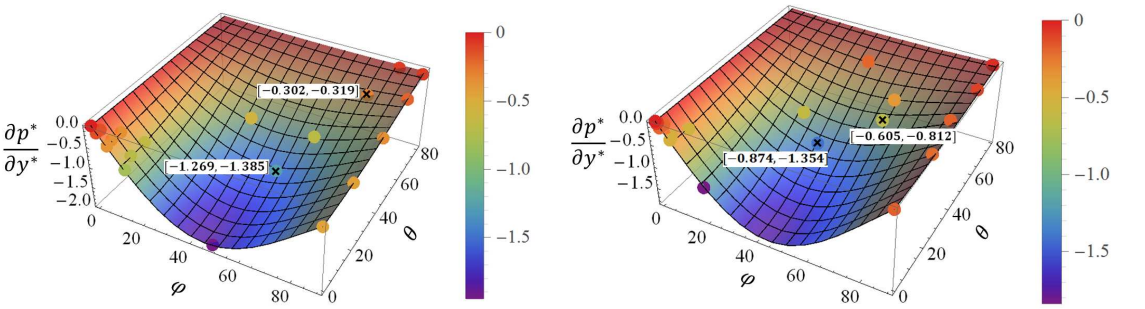

(c) y-direction pressure drop, $Re_L = 181$ (d) y-direction pressure drop, $Re_L = 8309$

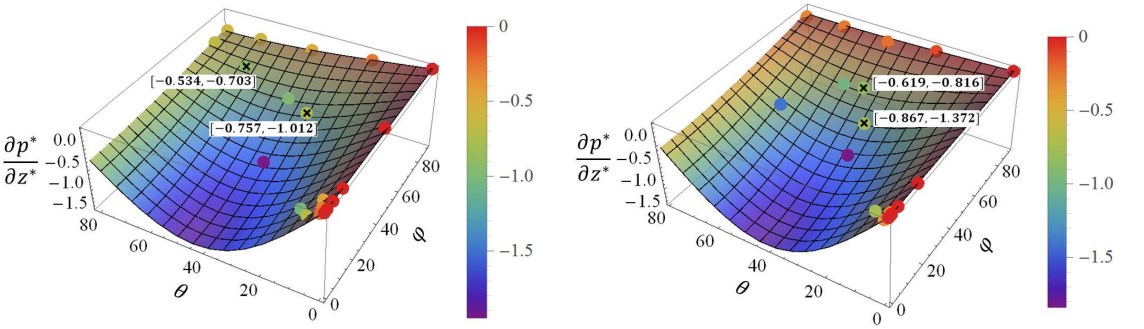

(e) z-direction pressure drop, $Re_L = 181$ (f) z-direction pressure drop, $Re_L = 8309$

Fig.4.38 Comparison of anisotropic pressure drop between model (curved surfaces) and CFD solutions (points). Two locations are labeled with brackets to give comparisons between the CFD "**x**" (first entry in the bracket) and the corresponding model results (second entry in the bracket). The locations being labeled are: $(\varphi = 55^o, \theta = 31^o)$ and $(\varphi = 75^o, \theta = 65^o)$ for $Re_L = 181$; $(\varphi = 44^o, \theta = 31^o)$ and $(\varphi = 63^o, \theta = 42^o)$ for $Re_L = 8309$.

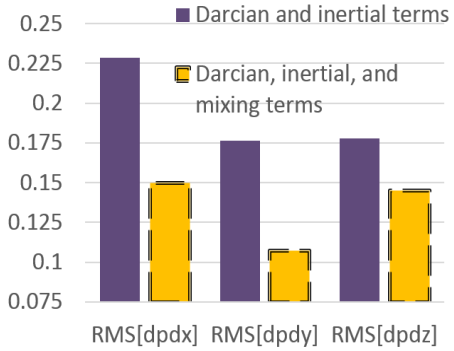

Fig.4.39 RMS values of the model with inclusion of only the Darcian and inertial terms, and of the model with inclusion of all three terms

4.2.3. Anisotropic Heat Transfer

Results of the REV calculations are analyzed for interfacial heat transfer between the fluid and the wall. The wall temperature distributions for different mean flow directions are also shown in the previous flow visualization plots. Because the wall has a uniform negative heat flux, the fluid is heating the wall and, thus, locations on the wall with high temperature values indicate higher local heat transfer coefficients. One sees that wall heat transfer effect is strong next to the regions where the flow is active. The weakest local heat transfer effect on the wall is found next to the stagnant fluid regions in Fig.4.28. Even though the mean flow direction is fixed, local flows in different regions inside the REV follow different directions, leading to complex mixing effects that enhance heat transfer, such as in the case shown by Fig.4.36 and Fig.4.37.

A correlation for anisotropic heat transfer is developed based on dimensionless numbers. The Nusselt number is a function of Reynolds number as well as angles that characterize the mean flow direction. These angles relate the pore-scale mixing effect to the macroscopic heat transfer. A volumetric heat transfer coefficient is defined as,

$$h_V = \frac{q'' a_V}{\left[\frac{1}{A}\int_{wall} T dA\right] - \langle T \rangle^f} \tag{4.55}$$

The study [46] used the following expression to model anisotropic heat transfer behavior:

$$Nu = (c_1{}^{n_c} cos^2\alpha + c_2{}^{n_c} cos^2\beta + c_3{}^{n_c} cos^2\gamma)^{\frac{1}{n_c}} + (d_1{}^{n_d} sin^2\gamma + d_2{}^{n_d} cos^2\gamma)^{\frac{1}{n_d}} Re^{0.6} Pr^{\frac{1}{3}} \tag{4.56}$$

The term $(c_1{}^{n_c} cos^2\alpha + c_2{}^{n_c} cos^2\beta + c_3{}^{n_c} cos^2\gamma)^{\frac{1}{n_c}}$ represents conduction effects in the situation of a very small Reynolds number. Other porous media heat transfer correlations have neglected the conduction effect for convenience of normalizing the Nusselt number on Prandtl number [45]. Given this, the conduction term is approximately modeled to be proportional to $Pr^{\frac{1}{3}}$ and is independent of the mean flow direction. The second term on the RHS of Eq. (4.56) depends on Reynolds number and mean flow angle, and represents convective heat transfer due to fluid inertial and mixing effects. Furthermore, this term is based only on the angle γ because it is the dominant angle for the two-dimensional and quasi-three-dimensional porous media investigated. Given this, a more generalized form for this term is adopted in the present study by including all independent angles using trigonometric functions in a quadratic form. Also, considering the fact that angles φ and θ have similar effects on volumetric heat transfer, the proposed heat transfer model for the interrupted plate medium is,

$$\frac{Nu}{Pr^{\frac{1}{3}}} = c + d_1(cos^2\varphi + cos\theta^2) Re_L{}^{n_{d_1}} + f_1(sin^2\varphi + sin^2\theta) Re_L{}^{n_{f_1}} + d_2(cos\varphi + cos\theta) Re_L{}^{n_{d_2}} + f_2(sin\varphi + sin\theta) Re_L{}^{n_{f_2}} \tag{4.57}$$

Using results from forty REV simulations for, we calculate the coefficients in Eq. (4.57):

$$c = 7.012, \quad d_1 = -2.766, \quad f_1 = -0.530, \quad d_2 = 2.685, \quad f_2 = 0.444$$

$$n_{d_1} = 0.387, \quad n_{f_1} = 0.637, \quad n_{d_2} = 0.476, \quad n_{f_2} = 0.682$$

The model is compared with CFD solutions in Fig.4.40. Two locations that are in the middle of the $\varphi - \theta$ domain are labeled by the CFD and modeled values. In general, the two are in good agreement with one another.

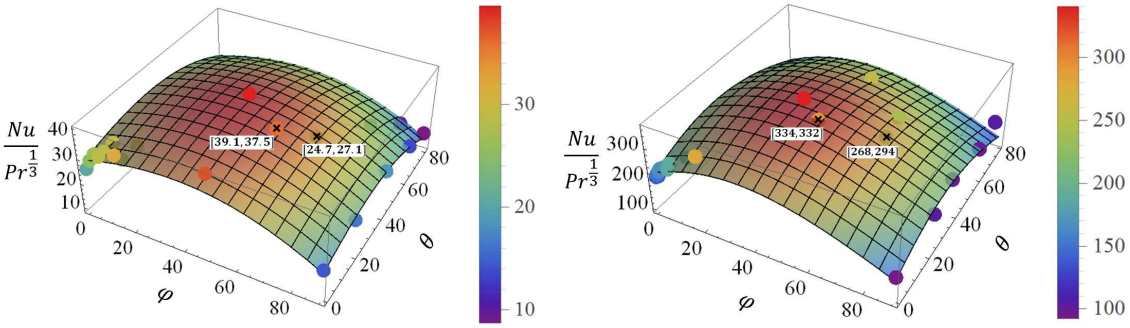

(a) $Re_L = 181$ (b) $Re_L = 8309$

Fig.4.40 Comparison of Nusselt numbers (volumetric Nu) between model (curved surfaces) and CFD solutions (points). Two locations are labeled with brackets to give comparisons between the CFD "**x**" (first entry in the bracket) and the corresponding model results (second entry in the bracket). The locations being labeled are: $(\varphi = 55^o, \theta = 31^o)$ and $(\varphi = 75^o, \theta = 65^o)$ for $Re_L = 181$; $(\varphi = 44^o, \theta = 31^o)$ and $(\varphi = 63^o, \theta = 42^o)$ for $Re_L = 8309$.

The directional characteristics for heat transfer with the interrupted plate medium have the following characteristics: (1) for a given θ, (especially for one between 0 and 65^o), heat transfer increases as φ increases from 0 to around 40^o, and then decreases as φ continues toward 90^o. The reason for the increase in heat transfer when φ increases from 0 to around 40^o is that an increasing amount of flow impinging on the plates leads to increasingly complex pore-scale fluid motion. Representative cases are shown by Figs. 9 and 10. The reason for the decrease in heat transfer when φ increases from 40^o to around 90^o is that impingement of the flow at a more directed angle onto the plate leads to more fluid stagnation. Representative cases are shown by Figs. 6 and 7, where the flow impinges on the plates at a directed angle and causes large stagnation zones, thus less heat transfer. (2) Due to identical geometric periodicity in the Oy and Oz directions, for a given φ

(especially between 0 and 65^o) heat transfer also increases as θ increases from 0 to around 40^o and then decreases as θ continues to reach 90^o. (3) Because of the aforementioned aspects, the highest heat transfer effects occur when the mean flow approaches in a direction with both φ and θ being about 33^o. The reason for this is that with this direction, the pore-scale fluid is most agitated, forming complex fluid movement in many different directions inside the REV, even though the mean flow is pointing in one specific direction. This situation is illustrated by the flow fields in Fig.4.36 and Fig.4.37. Heat transfer is enhanced by the agitated pore-scale fluid.

The proposed models are further tested against a CFD simulation for a Reynolds number that was not used for developing the models. A flow through the REV in the x-direction with a Reynolds number of 4969 is simulated using the Transition SST model, and a mesh count of 1,323,532 cells, with a maximum y+ value of 1.88 for the first layer of cells next to the wall. The $\frac{Nu}{Pr^{1/3}}$ values and the dimensionless pressure drop values resulting from the CFD simulation and the model are, respectively, 166.9 and 167.1, and -0.1217 and -0.1078. The model is relatively good.

Next, numerical heat transfer values are compared between the present interrupted-plate heat exchanger and heat exchangers studied in other references. For comparison purposes, converting dimensionless numbers to be based on the hydraulic diameter, which is twice the plate separation distance, we obtain that a Reynolds number of 249 and the $\frac{Nu_{hydraulic}}{Pr^{1/3}}$ value of 14.2 for the present interrupted-plate medium for an x-directional flow. In the study of the microfabricated involute-foil regenerator [66], the $\frac{Nu_{hydraulic}}{Pr^{1/3}}$ value of the regenerator is 16.4. Overall, the heat transfer values computed in the present study are comparable to those published for other heat exchangers.

Shown by the anisotropic heat transfer model is that the Nusselt number reaches a maximum value when the mean flow attacks the plates at particular angles. A design is thus made by tilting the plates to misalign with the chamber's axis. The tilting angles, φ and θ, are 34°, which corresponds to the maximum Nusselt number when $Re_L = 8309$.

When the flow passes through in the chamber, most of the pore-scale flows have attack angles close to 34°. The flow is agitated, and heat transfer is enhanced. Although the matrix pressure drop is greater, it is small compared to the thermodynamic gas pressure. A provisional patent for this design has been filed [83]. As shown in Fig.4.41, the exchanger matrix consists of repeated layers of separated and parallel plates stacked together, wherein the plates are separated and parallel to one another in one layer of the exchanger and perpendicular to the parallel plates in the adjacent layers, and wherein all plates are oriented parallel along a direction that is misaligned with the axial direction of the flow channel. The heat transfer rate is estimated to be about 4.5 times that of a conventional strip-fin plate-fin heat exchanger. A preliminary calculation of this tilted-interrupted-plate matrix will be shown in flowing chapter using a 1-D model.

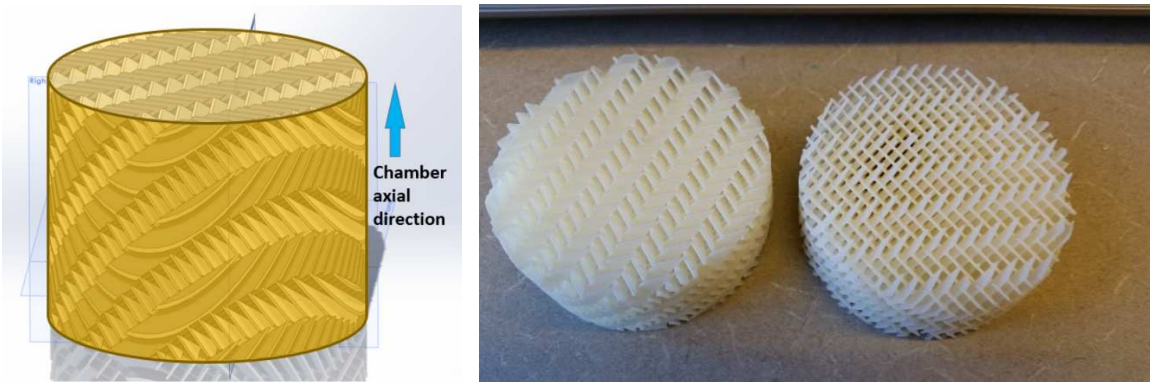

Fig.4.41 Tilted-interrupted-plate matrix design based on the anisotropic heat transfer model [83]

4.3. Summary

In this chapter, developed are heat transfer and pressure drop models for: (1) heat exchanger matrices with different shapes, and (2) anisotropic characterizations of the matrix. These models can be used in three-dimensional CFD simulation of the liquid piston chamber, and also for design analysis of the exchanger matrix shape. These topics will be addressed in

the following chapters. Based on the anisotropic model, a new exchanger design was proposed.

Chapter 5: A 1-D Numerical Model and Its Application to Thermal Design

A one-dimensional (1-D) numerical model to calculate transient temperature distributions in the liquid-piston compressor with heat exchanger inserts is developed. The 1-D model calculates energy transport by convection and conduction in both the solid matrix and the fluid phases. The Volume of Fluid (VOF) method is used to model the moving liquid-gas interface. The equations are discretized and solved by a finite difference method. Solutions of the 1-D model are validated against full CFD solutions of a two-dimensional computation domain.

The advantage of the 1-D model is that it gives fast calculations of the temperature distributions along the axial direction of the compression chamber, and thus the model can be used to compare different heat exchanger matrices and to design the porosity distributions and shape profile, in the axial direction, of a heat exchanger matrix. The objective of the design is to minimize the compression work input, or to maximize efficiency, for a given piston speed and a given overall pressure compression ratio. A design methodology is proposed based on sensitivity calculations in an iterative procedure. The sensitivity is calculated by taking the partial derivative of the objective function with respect to the change in the design parameter at each design evaluation node. In each design calculation round, the 1-D model is solved as many times as there are design evaluation nodes, and each time the design parameter at a single node is changed by a small amount. From these calculations, the sensitivity of changing the design parameter's distribution to the objective function is obtained. Based on the sensitivity, the design parameter is updated in the direction that favors the objective. Then, the procedure marches to the next round and the same calculations are completed iteratively until a final solution is reached. The design analysis shows that exchanger matrices with high porosity and coarse features should be used in the lower part of the chamber and those with low porosity and fine features should be used in the upper part of the chamber.

5.1. A 1-D Numerical Model

5.1.1. Transport Equations

The governing equations will be presented. A photo of an experimental liquid piston prototype is shown in Fig.1.2. From a modeling perspective, this chamber is considered one-dimensional; of interest to the design are the distributions of variables along the chamber's axial direction. A schematic of the 1-D liquid piston compression chamber domain is shown in Fig.5.1. Water is pumped into the chamber filled with heat exchanger elements to compress the air above the water-air interface. At the beginning of the compression process, the water-air interface starts at the bottom of the chamber.

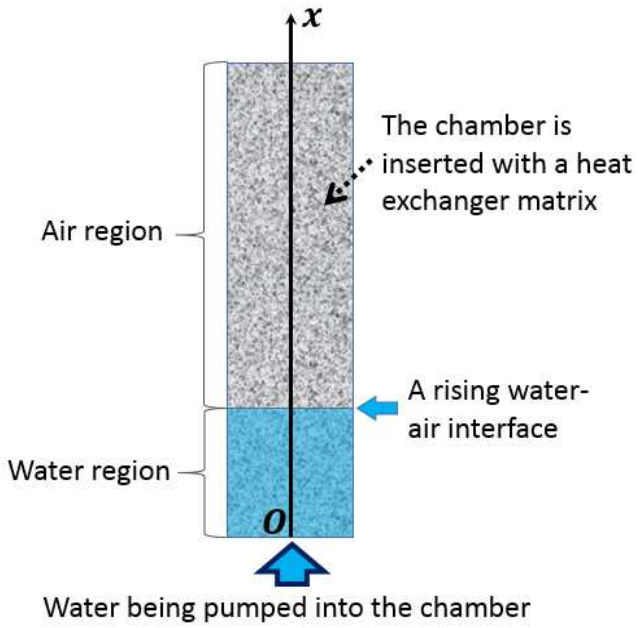

Fig.5.1 A schematic of the 1-D liquid piston chamber domain

The compression process in a liquid-piston air compressor with insertion of a heat exchanger is modeled. In the fluid region, a rising liquid-gas interface must be simulated. This is modeled using the VOF approach [22]. A volume fraction variable for each of the

water and air phases is defined as the volume concentration of that phase at a given location and time. The sum of volume fractions of both phases (air and water) equals unity.

$$\alpha_1 + \alpha_2 = 1 \tag{5.1}$$

where subscripts 1 and 2 refer to the air and the water phases, respectively. The mass conservation condition should be satisfied by each phase. Therefore, the continuity equations are:

$$\frac{\partial \alpha_1 \rho_1}{\partial t} + \frac{\partial \alpha_1 \rho_1 u}{\partial x} = 0 \tag{5.2}$$

$$\frac{\partial \alpha_2}{\partial t} + \frac{\partial \alpha_2 u}{\partial x} = 0 \tag{5.3}$$

The volume fraction functions give distributions of the two phases in the computational domain. The energy transport in the fluid phases is modeled by treating the two fluid phases as one fluid mixture, with different local fluid properties determined by the local occupation of the two phases. Therefore, one energy equations is solved for both fluids.

$$\epsilon \frac{\partial \overline{\rho c_p} T}{\partial t} + \epsilon \frac{\partial \overline{\rho c_p} u T}{\partial x} = k\epsilon \frac{\partial^2 T}{\partial x^2} + \alpha_1 \beta_1 T \left(\frac{\partial p}{\partial t} + u \frac{\partial p}{\partial x}\right) + h_V (T_s - T) \tag{5.4}$$

where the flow properties are dependent upon the two phases,

$$\overline{\rho c_p} = \alpha_1 \rho_1 c_{p,1} + \alpha_2 \rho_2 c_2 \tag{5.5}$$

$$k = \alpha_1 k_1 + \alpha_2 k_2 \tag{5.6}$$

The water is assumed to be incompressible and, thus, the pressure work term in Eq. (4) is effective only in the air phase, as when $\alpha_1 = 0$, the pressure work term becomes zero automatically. The pressure can be related to the air temperature and density by the equation of state, which will be explained later. The energy transport in the solid is given by,

$$(1 - \epsilon)\rho_s c_s \frac{\partial T_s}{\partial t} = k_s (1 - \epsilon) \frac{\partial^2 T_s}{\partial x^2} - h_V (T_s - T) \tag{5.7}$$

The velocity of the water phase at any location is the same as the water inlet velocity, given that water is incompressible. Previous 2-D CFD simulations also have shown that an exchanger matrix when used in a liquid-piston chamber results in a pressure drop along the flow direction, and has a significant effect in smoothing the flow and suppressing the development of secondary air flows [74]. As a result, the bulk air velocity is linearly distributed along the axial direction, matching the water (interface) velocity at the water-air interface, and stagnant at the top cap. The velocity field is defined accordingly. The instantaneous water-air interface location is calculated by finding the point that has a volume fraction of 0.5 for either phase. The velocity field of air and water are given by,

$$u = u(x,t) = \begin{cases} U_0, & \alpha_2 \geq 0.5 \\ U_0 \frac{L-x}{L-x_p}, & \alpha_1 > 0.5 \end{cases} \tag{5.8}$$

where the interface location, x_p , satisfies $\alpha_2(x_p) = 0.5$.

5.1.2. Boundary Conditions

The one-dimensional domain has two boundaries, the inlet and the top cap. Constant inlet and wall temperatures are assumed. Therefore, the thermal boundary conditions are:

$$T|_{x=0} = T|_{x=L} = T_s|_{x=0} = T_s|_{x=L} = T_0 \tag{5.9}$$

Given that the inlet is water and that the top cap region is occupied by air, the volume fraction values at the boundaries are:

$$\alpha_1|_{x=0} = \alpha_2|_{x=L} = 0 \tag{5.10}$$

$$\alpha_2|_{x=0} = \alpha_1|_{x=L} = 1 \tag{5.11}$$

5.1.3. Equation of State

For different occasions, two different models are used to relate pressure, density and temperature. For low pressure compression cases (up to 3MPa), the ideal gas model is used,

$$p = \rho_1 RT \tag{5.12}$$

For high pressure compression cases (up to 21MPa), a real gas model is used. The model is based on a cubic equation of state for real gas. A relation between air pressure, density, and temperature is given by [70], as:

$$p = \frac{\rho \Re T}{M - \rho \mathfrak{b}} - \frac{\mathfrak{a}\rho^2}{M^2 + \mathfrak{b}M\rho} \tag{5.13}$$

where,

$$\mathfrak{b} = \frac{0.08664 \Re T_c}{P_c} \tag{5.14}$$

$$\mathfrak{a} = \frac{0.42727 \Re^2 {T_c}^2}{P_c}\left\{1 + \mathfrak{n}\left[1 - \left(\frac{T}{T_c}\right)^{0.5}\right]\right\}^2 \tag{5.15}$$

$$\mathfrak{n} = 0.48 + 1.574\omega - 0.176\omega^2 \tag{5.16}$$

The acentric factor, ω, is taken to be 0.033. For air, the critical pressure, critical temperature and molecular weight are respectively, 3.758MPa, 132.3K and 29g/mol. The universal gas constant is 8.314J/(mol K). As the air is considered as a real gas, the specific heat is modeled using a departure specific heat [71]:

$$c_{p,1} = c_{p,1,\text{ideal}} - c_{p,1,\text{dep}} \tag{5.17}$$

$$c_{p,1,dep} = -\frac{p}{\rho T} + \frac{\Re}{M} - \frac{\frac{\partial \mathfrak{a}}{\partial T} - \frac{\mathfrak{a}}{T}}{M\mathfrak{b}} \ln\left(1 + \frac{\mathfrak{b}\rho}{M}\right) \tag{5.18}$$

The ideal specific heat for air, $c_{p,1,\text{ideal}}$, is a function of temperature based on a curve fit of the data from [72].

5.1.4. Numerical Scheme

A finite difference method is used to discretize the continuity and energy equations in section 5.1.1. The continuity equations for water and air are discretized using an explicit upwind method. They are given by:

$$\frac{{\alpha_{2,j}}^{n+1}-{\alpha_{2,j}}^{n}}{\Delta t}+\frac{{\alpha_{2,j}}^{n}{u_{2,j}}^{n}-{\alpha_{2,j-1}}^{n}{u_{2,j-1}}^{n}}{\Delta x}=0 \tag{5.19}$$

$$\frac{{\alpha_{1,j}}^{n+1}{\rho_{1,j}}^{n+1}-{\alpha_{1,j}}^{n}{\rho_{1,j}}^{n}}{\Delta t}+\frac{{\alpha_{1,j}}^{n}{\rho_{1,j}}^{n}{u_{1,j}}^{n}-{\alpha_{1,j-1}}^{n}{\rho_{1,j-1}}^{n}{u_{1,j-1}}^{n}}{\Delta x}=0 \tag{5.20}$$

The fluid energy equation is discretized using an explicit scheme, with upwind differencing on the advection term and central differencing on the diffusion term.

$$\frac{\left(\overline{\rho c_p}_j^{\mathbb{k}+1}-\alpha_{1,j}^{\mathbb{k}+1}\rho_{1,j}^{\mathbb{k}+1}R\right)T_j^{\mathbb{k}+1}-\left(\overline{\rho c_p}_j^{n}-\alpha_{1,j}^{n}\rho_{1,j}^{n}R\right)T_j^{n}}{\Delta t}$$

$$+\frac{\overline{\rho c_p}_j^{n}u_j^{n}T_j^{n}-\overline{\rho c_p}_{j-1}^{n}u_{j-1}^{n}T_{j-1}^{n}}{\Delta x}-\frac{h_V{}_j^{n}\left({T_{s,j}}^{n}-T_j^{n}\right)}{\epsilon}$$

$$=k_j^{n}\frac{T_{j-1}^{n}-2T_j^{n}+T_{j+1}^{n}}{\Delta x^2}+\frac{\alpha_{1,j}^{n}\rho_{1,j}^{n}Ru_j^{n}T_j^{n}-\alpha_{1,j-1}^{n}\rho_{1,j-1}^{n}Ru_{j-1}^{n}T_{j-1}^{n}}{\Delta x} \tag{5.21}$$

The energy transport in the solid is governed by diffusion. The solid energy equation is discretized using an implicit scheme, with central differencing in space. It is given by

$$-\frac{k_s}{\Delta x^2}{T_{j-1}}^{\mathbb{k}+1}+\left(\frac{\rho_s c_s}{\Delta t}+\frac{2k_s}{\Delta x^2}+\frac{{h_{v,j}}^{\mathbb{k}+1}}{1-\epsilon_j}\right){T_j}^{\mathbb{k}+1}-\frac{k_s}{\Delta x^2}{T_{j+1}}^{\mathbb{k}+1}$$

$$=\frac{\rho_s c_s}{\Delta t}{T_{s,j}}^{n}+\frac{{h_{v,j}}^{\mathbb{k}+1}}{1-\epsilon_j}{T_j}^{\mathbb{k}+1} \tag{5.22}$$

This equation can be written as

$$a_{s,j}{T_{j-1}}^{\mathbb{k}+1}+\beta_{s,j}{T_j}^{\mathbb{k}+1}+\chi_{s,j}{T_{j+1}}^{\mathbb{k}+1}=\gamma_{s,j} \tag{5.23}$$

where,

$$a_{s,j}=-\frac{k_s}{\Delta x^2} \tag{5.24}$$

$$\beta_{s,j}=\frac{\rho_s c_s}{\Delta t}+\frac{2k_s}{\Delta x^2}+\frac{{h_{v,j}}^{\mathbb{k}+1}}{1-\epsilon_j} \tag{5.25}$$

$$\chi_{s,j}=-\frac{k_s}{\Delta x^2} \tag{5.26}$$

$$\gamma_{s,j} = \frac{\rho_s c_s}{\Delta t} {T_{s,j}}^{n} + \frac{{h_{v,j}}^{\mathbb{k}+1}}{1-\epsilon_j} {T_j}^{\mathbb{k}+1} \tag{5.27}$$

Let N_n be the number of discretized nodes in the computational domain; 0 denotes the node at $x = 0$, and $N_n - 1$ denotes the node at $x = L$. Equation (5.23) is written in matrix form for all the nodes in the computational domain:

$$\begin{bmatrix} \beta_{s,1} & \chi_{s,1} & & & \\ a_{s,2} & \beta_{s,2} & \chi_{s,2} & & \\ & \cdots & \cdots & \cdots & \\ & & \cdots & \cdots & \chi_{s,N_n-3} \\ & & & a_{s,N_n-2} & \beta_{s,N_n-2} \end{bmatrix} \begin{bmatrix} T_{s,1} \\ T_{s,2} \\ \cdots \\ T_{s,N_n-3} \\ T_{s,N_n-2} \end{bmatrix}^{\mathbb{k}+1}$$

$$= \begin{bmatrix} \gamma_1 - a_{s,1} T_{s,0} \\ \gamma_2 \\ \cdots \\ \gamma_{N_n-3} \\ \gamma_{N_n-2} - \chi_{s,N_n-1} T_{s,N_n-1} \end{bmatrix} \tag{5.28}$$

The continuity equations are solved explicitly. The solid energy equation is solved using the Thomas algorithm. In each time step, the fluid and solid equations are iteratively solved in a coupled manner until the solution is converged, at which point, the solution at the iteration step, $\mathbb{k} + 1$, is considered to be the solution at time step, $n + 1$, and then the computation marches to the next time step.

The coupling of heat transfer between the fluids and the solid heat exchanger matrices is based on models developed in the previous chapters.

5.1.5. Solution and Validation

Solved using the 1-D model is compression in a liquid-piston compressor with a 10 PPI metal foam insert. This is the same case studied in section 3.2; the same length of the liquid piston chamber, compression speed, and physical properties as those of case Run1 in Table 3.4 are solved. The total compression time is 2.6 seconds. Water starts entering the compressor from the bottom of the chamber ($x = 0$). The interfacial heat transfer

correlation for the 10PPI metal foam follows Eq.(1.19), which is validated in section 3.1. The 1-D computation is run on a mesh with 3500 axial nodes and over 30,000 time steps ($\Delta t = 8.667 \times 10^{-5} s$). A C++ code is written to solve the governing equations.

The velocity field and the calculated volume fraction distribution of air at different times during compression are shown in Fig.5.2 and Fig.5.3. The one-dimensional VOF method can capture movement of the liquid-gas interface. In Fig.5.3, the part of the curve with $\alpha_1 = 0$ represents the instantaneous location of water, and the part of the curve with $\alpha_1 = 1$ represents the instantaneous location of air. The water-air interface lies in the transition region from $\alpha_1 = 0$ to $\alpha_1 = 1$.

The calculated temperature distributions of the fluid and solid are shown in Fig.5.4 and Fig.5.5. The water temperature during compression is maintained constant. Part of the input work during compression of air is converted into the air internal energy, causing the air temperature to rise. Since the air flow is almost stagnant in the region very close to the top cap, the heat transfer mode is mainly conduction in the near-cap region. The increase in the air internal energy due to compression is much larger than the amount of heat being transported from the air, because of low velocities of the air in that region and small thermal conductivity of air. Thus, the local air temperature is highest in the near-cap region. Meanwhile, since the top cap is isothermal, this creates a large local temperature gradient in the air. The solid heat-up is considerably less than that of the air. The part of the matrix that is solid submerged in water is being cooled effectively, and, thus, is maintained at the initial temperature. The maximum rise of the local temperature of solid is near the axial middle region of that solid portion of the matrix that is in contact with the air. It is maximum at the end of compression.

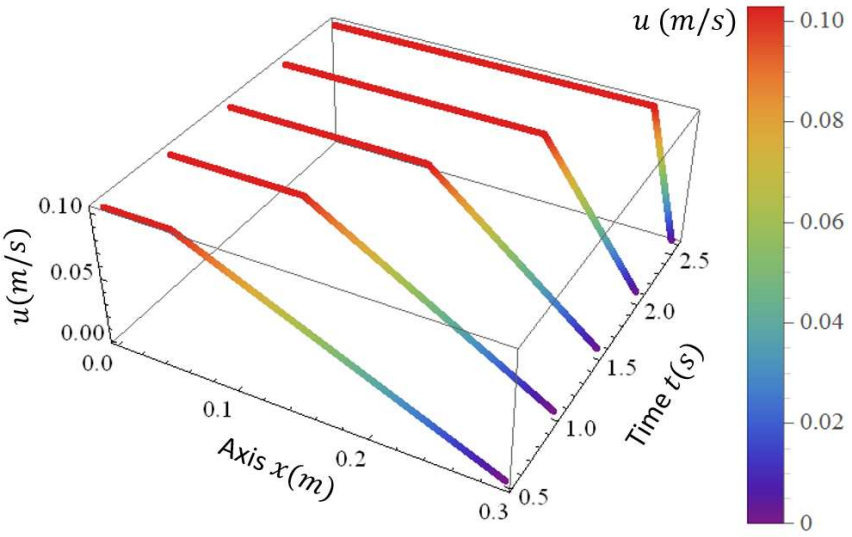

Fig.5.2 Transient 1-D velocity distributions in the liquid piston chamber

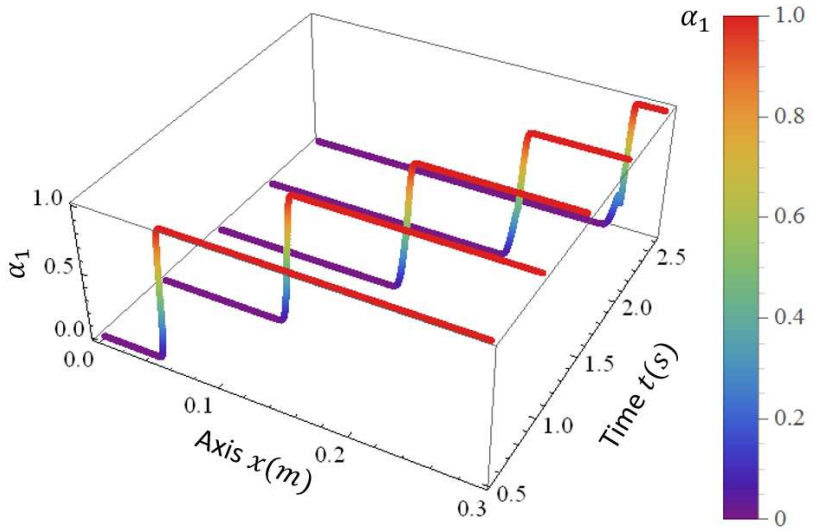

Fig.5.3 Transient volume fraction distributions in the liquid piston chamber ($\alpha_1 = 0$ represents water region; $\alpha_1 = 1$ represents air region)

The calculated temperature distributions of the fluid and solid are shown in Fig.5.4 and Fig.5.5. The water temperature during compression is maintained constant. Part of the input work during compression of air is converted into the air internal energy, causing the

air temperature to rise. Since the air flow is almost stagnant in the region very close to the top cap, the heat transfer mode is mainly conduction in the near-cap region. The increase in the air internal energy due to compression is much larger than the amount of heat being transported from the air, because of low velocities of the air in that region and small thermal conductivity of air. Thus, the local air temperature is highest in the near-cap region. Meanwhile, since the top cap is isothermal, this creates a large local temperature gradient in the air. The solid heat-up is considerably less than that of the air. The part of the matrix that is solid submerged in water is being cooled effectively, and, thus, is maintained at the initial temperature. The maximum rise of the local temperature of solid is near the axial middle region of that solid portion of the matrix that is in contact with the air. It is maximum at the end of compression.

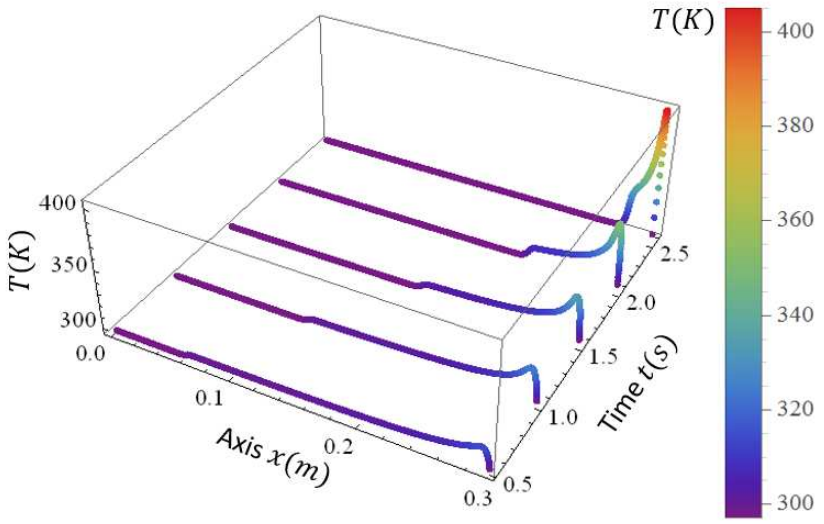

Fig.5.4 Transient 1-D fluid temperature distributions in the liquid piston chamber

For grid-independence verification, the above problem is solved on a mesh of 7000 axial nodes, and with 120,000 time steps ($\Delta t = 2.167 \times 10^{-5} seconds$). The temperature distributions of the fluid and solid calculated from the original run and from the grid

independence comparison run at the end of compression ($t = 2.6s$) are shown in Fig.5.6. The comparison shows grid independence for a grid with 3500 nodes.

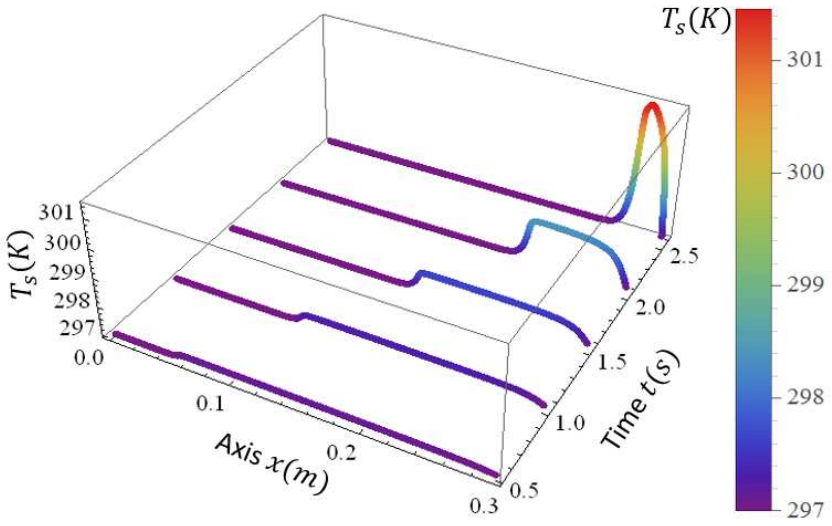

Fig.5.5 Transient 1-D solid temperature distributions in the liquid piston chamber

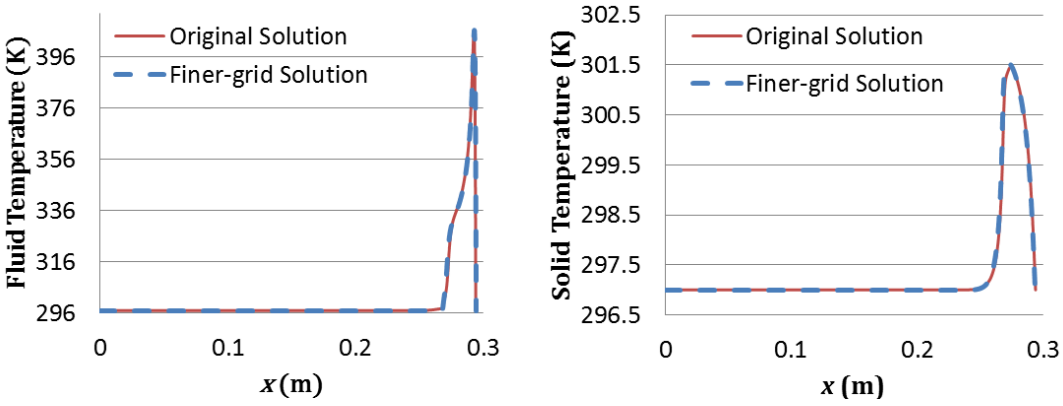

(a) Fluid temperature, $t = 2.6s$ (a) Solid temperature, $t = 2.6s$

Fig.5.6 Temperature distributions at the end of compression from the original solution and from the finer-grid solution for grid-independence verification

For validation purposes, solutions of the two-dimensional (2-D), axisymmetric CFD simulation of a liquid-piston compressor fully occupied by porous inserts are taken from section 3.2 and compared to the 1-D solutions of the present study. The two compression problems being solved are identical. The radius of the chamber is 0.0254m. The radius is not of concern to the present, 1-D computation. The fluid temperature distribution from the present 1-D solution is compared with the centerline temperature distribution from the 2-D CFD solution, and also compared to the 2-D temperature field in Fig.5.7. The comparison shows that the 1-D model can capture the important features of the transient axial temperature distribution of the fluid mixture in the chamber. The 2-D temperature fields show high temperature streaks in the region very close to the top cap. This is consistent with the 1-D solution. The physical reasons are that the flow is mostly stagnant in that region, and the increase in the internal energy added due to compression work is much greater than the energy being conducted away to the solid phase in that region. The solid temperature distributions calculated from the 1-D and 2-D solutions are shown in Fig.5.8. Comparing the 1-D solid temperature distribution and the centerline temperature distribution from the 2-D solution, one sees that the maximum local temperature difference is less than 4K. This is due to a lack of radial conduction and the cylinder side wall in the 1-D problem. The shape of the 1-D solid temperature curve correctly represents the same feature of the solid temperature distribution from the 2-D solution.

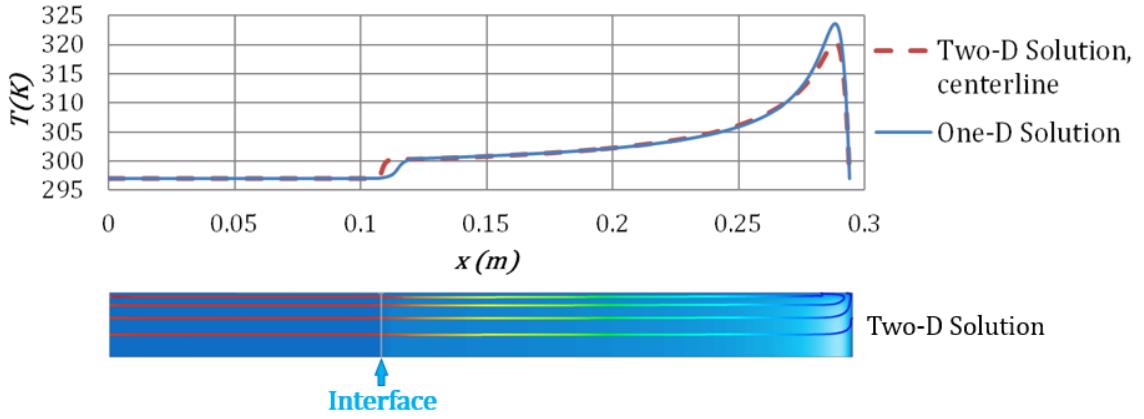

(a) Fluid temperature, $t = \frac{2}{5}t_f = 1.04\text{s}$

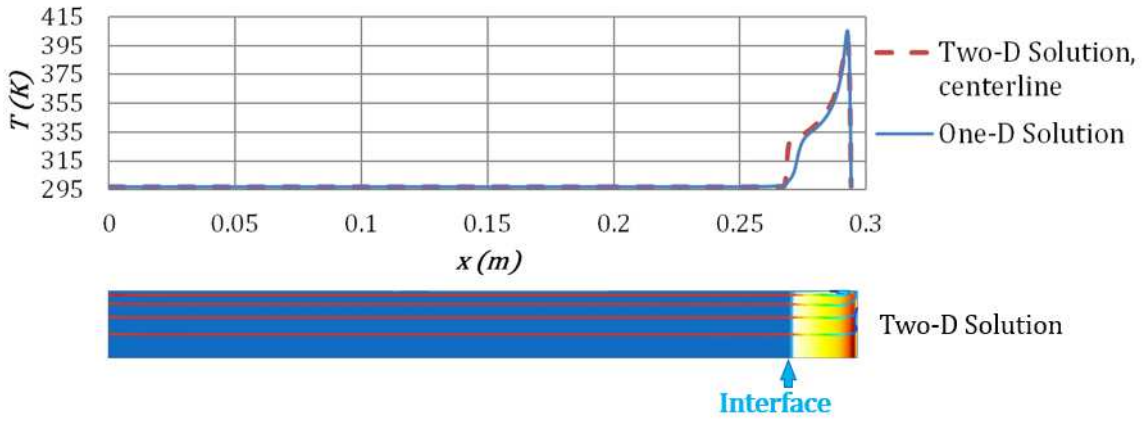

(b) Fluid temperature, $t = t_f = 2.6\text{s}$

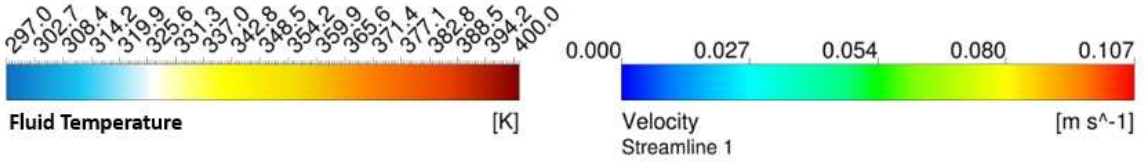

Fig.5.7 Comparisons of fluid temperature distributions between One-D solution and Two-D solution

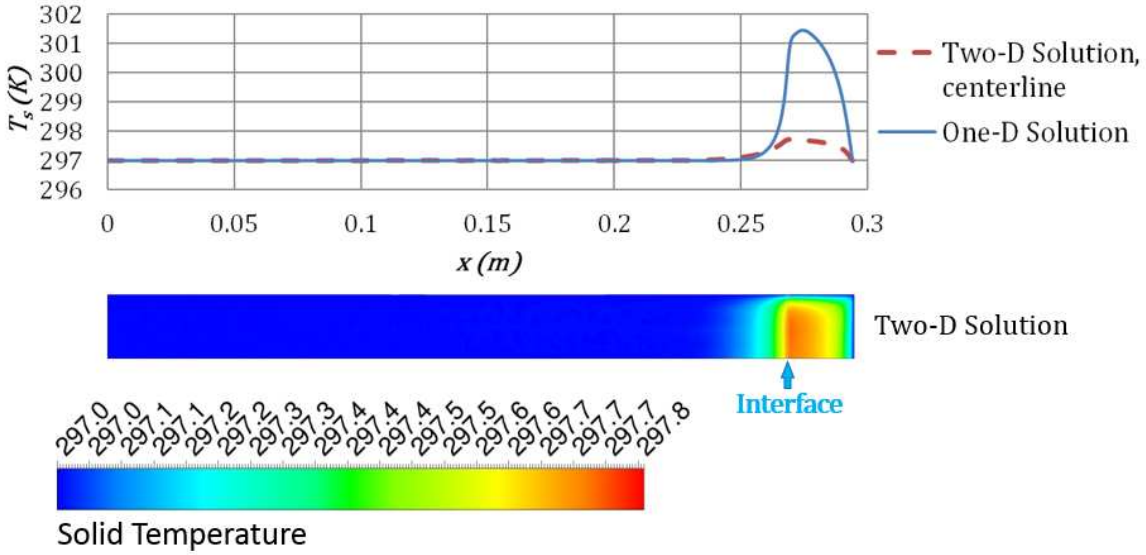

Fig.5.8 Comparisons of solid temperature distribution at $t_f = 2.6$ seconds between the One-D solution and Two-D solution

5.2. Fast Computation of Different Exchanger Matrices Based on the 1-D Model

5.2.1. Simulation Cases

In this section, the 1-D model is applied for fast calculations to investigate and compare different heat exchanger matrices. The application is targeted at a high-pressure compression chamber, which uses the same chamber as discussed in section 3.3 (or section 2.2); it has a length of 0.4826m, and the compression speed is 0.15m/s. The total compression time is 3s. The compression starts with a chamber filled with air at 7bar, and at the end of compression the pressure of air is around 210bar.

The heat exchanger matrices compared include: 10 PPI open-cell metal foam, 40 PPI open-cell metal foam, three interrupted plate exchanger matrices including two with the straight plates and one with the tilted plates (refer to Fig.4.41), and two honeycomb matrices. Characterizations of the metal foam matrices were studied in section 3.1. One of the interrupted plate matrix is REV20 (refer to Table 4.1), which has fine features: $\ell = 3mm, 2\mathscr{b} = 2.5mm, t = 0.4mm$ (which will be referred to as "I-P 3_2.5_0.4"); the other

interrupted plate matrix is REV11_1 which features an intermediate element size: $\ell = 7.5mm$, $2\mathscr{b} = 2.75mm$, $t = 0.55mm$ (which will be referred to as I-P 7.5_2.75_0.55). Two different materials are calculated for each shape, plastic and metal (steel). The tilted-interrupted-plate matrix has plate dimensions: element size: $\ell = 7.5mm$, $2\mathscr{b} = 2.75mm$, $t = 0.55mm$. The naming of the exchangers follows the same rule as introduced in the preceding section; symbols and numbers mean respectively: material, exchanger type (interrupted-plate), plate height, plate separation distance, and plate thickness. Metal, as used in some of the exchangers, refers to steel. Two honeycomb matrices are also studied. One with 1/4 inch cell size, and the other with 1/8 inch cell size. A chematic of the honeycomb matrix is shown in Fig.5.9. The honeycomb has channels with hexagonal cross sections, and the cell size refers to the distnce between two parallel walls of the hexagonal channel. For the honeycomb matrix, since the honeycomb ducts are also laid out in an interrupted fashion, a correlation for heat transfer in an entry region of a hexagonal duct is used [84],

$$Nu_{l_c} = 2f_r \left(\frac{l_c}{L_d} Re_{l_c} Pr\right)^{\frac{1}{2}} \tag{5.29}$$

where the characteristic length l_c is square root of the channel cross sectional area, L_d is the duct length which is 7.5mm in both honeycomb matrices. The definition and correlation for friction factor is given by,

$$f_r = \frac{\tau_w}{\frac{1}{2}\rho u^2} = \frac{0.564}{\left[1+\left(1.664Pr^{\frac{1}{6}}\right)^{9/2}\right]^{2/9}} \tag{5.30}$$

The wall thickness values corresponding to the 1/4in and 1/8in honeycomb matrices are, respectively, 0.143mm and 0.109mm. The heat exchanger matrices, as well as the hydro-thermal models and materials are listed in Table 5.1.

The simulations are run on a one-dimensional domain with a fine grid of 3000 cells and a time step size of $\frac{1}{12000}s$. Grid independence at 2000 cells is verified with a $\frac{1}{4000}s$

time step is verified by running the case PL-I-P-7.5_2.75_0.55 on grids of 1500, 2000, 3000 and with time steps of $\frac{1}{2000}s$, $\frac{1}{4000}s$, $\frac{1}{7000}s$, and $\frac{1}{12000}s$.

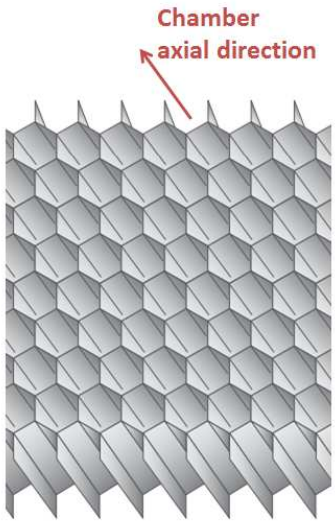

Fig.5.9 A schematic of the honeycomb matrix

5.2.2. Results

The temperature distributions in both the fluids and solid are obtained from the 1-D simulations. Results are shown in Fig.5.10 and Fig.5.11. Two times during later period of the compression process are plotted, 2.4s and 3s. The fluid temperature rises significantly from 2.4s to 3s. The air temperature near the water-air interface is low due to cooling effect of water. Above the interface, there is a sudden rise in the air temperature due to compression. Near the top cap, the air temperature reaches a peak value as the flow is stagnant.

Comparing different exchanger matrices on how well they suppress air temperature rise, the one having the best performance is the 40PPI metal foam, and the one having the worst performance is the honeycomb matrix with a quarter inch (6.3mm) cell size. The 40PPI metal foam has very fine features and large surface areas, and thus performs the best,

but practical issues arise, such as the high tendency of trapping water in the pores. The 1/4inch honeycomb is the worst because of the large cell size and very thin walls, thus providing insufficient heat transfer areas and insufficient thermal capacitance.

Table 5.1 Heat exchanger matrices in 1-D calculation

<table>
<tr><th>Cases</th><th>Pressure drop</th><th>Heat transfer</th><th>Material</th></tr>
<tr><td>10PPI Metal Foam</td><td>$K = 2.397 \times 10^{-7} m^2$
$b = 285/m$</td><td rowspan="2">Eq.(1.19)</td><td rowspan="3">Aluminum
$k_s = 205 W/(mK)$
$c_s = 871 J/(kgK)$
$\rho = 2719 kg/m^3$</td></tr>
<tr><td>40PPI Metal Foam</td><td>$K = 9.913 \times 10^{-8} m^2$
$b = 576/m$</td></tr>
<tr><td>Honeycomb-1/4</td><td rowspan="2">Eq.(5.30)</td><td rowspan="2">Eq.(5.29)</td></tr>
<tr><td>Honeycomb-1/8</td><td rowspan="4">Steel
$k_s = 14 W/(mK)$
$c_s = 502 J/(kgK)$
$\rho = 7954 kg/m^3$</td></tr>
<tr><td>Metal I-P 3_2.5_0.4</td><td>$K = 2.764 \times 10^{-7} m^2$
$b = 77.0/m$</td><td rowspan="4">Eq.(4.37)</td></tr>
<tr><td>Metal I-P 7.5_2.75_0.55</td><td>$K = 4.790 \times 10^{-7} m^2$
$b = 24.7/m$</td></tr>
<tr><td>Plastic I-P 3_2.5_0.4</td><td>$K = 2.764 \times 10^{-7} m^2$
$b = 77.0/m$</td><td rowspan="3">Plastic
$k_s = 0.17 W/(mK)$
$c_s = 1200 J/(kgK)$
$\rho = 1060 kg/m^3$</td></tr>
<tr><td>Plastic I-P 7.5_2.75_0.55</td><td>$K = 4.790 \times 10^{-7} m^2$
$b = 24.7/m$</td></tr>
<tr><td>Plastic I-P-Tilted</td><td>Eq.(4.54)</td><td>Eq.(4.57)</td></tr>
</table>

The performance of the interrupted-plate matrix ranks in the middle. The plastic tilted-interrupted-plate matrix has almost similar performance as “Metal I-P 3_2.5_0.4,” as it is made of straight metal plates featuring very small elements. If made of the same material and same elemental plate dimensions, the tilted-interrupted-plate matrix result in a reduction of 30K in the gas temperature at the end of compression. For straight plates,

smaller features have better heat transfer performance; if made of the same material, the one with a smaller element size, “I-P 3_2.5_0.4,” is better than the one with a bigger element size, “I-P 7.5_2.75_0.55.” For the same shape, the metal one performs better than the plastic one. However, the “Plastic I-P 3_2.5_0.4” is almost as good as “Metal I-P 7.5_2.75_0.55,” since the plastic has a much larger thermal capacity than air, even though it is smaller than metal.

The solids have higher temperature values in regions where they are exposed to air. The location of the peak solid temperature is above the water-air interface. As the water-air interface rises, the portion of the matrix that becomes submerged in water gets cooled; this can be shown by comparing Fig.5.11 (a) and (b). The solid temperature rise depends on porosity and material. The ones with smaller porosity and higher thermal capacity values have smaller temperature rises.

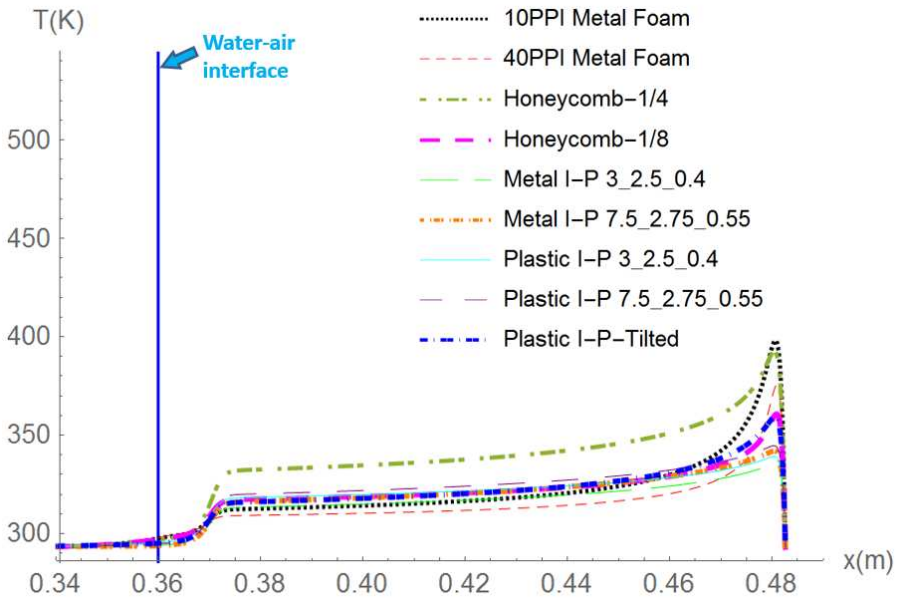

(a) time=2.4s

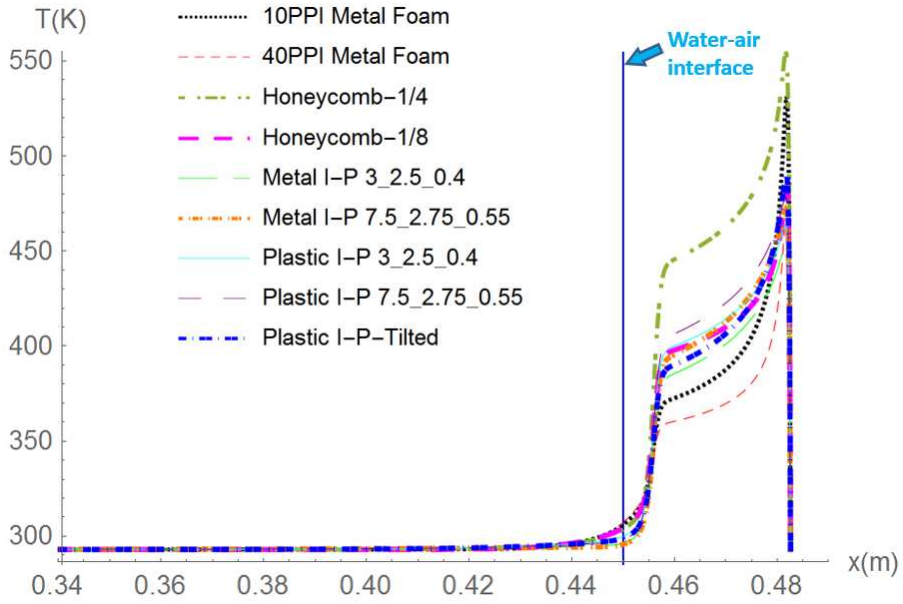

(b) time=3s

Fig.5.10 Temperature distributions in the fluids

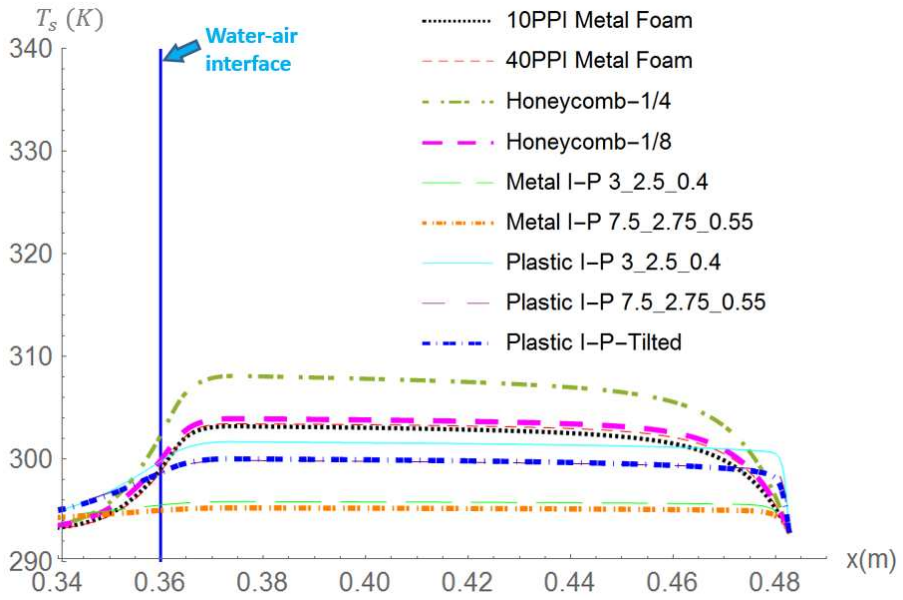

(a) time=2.4s

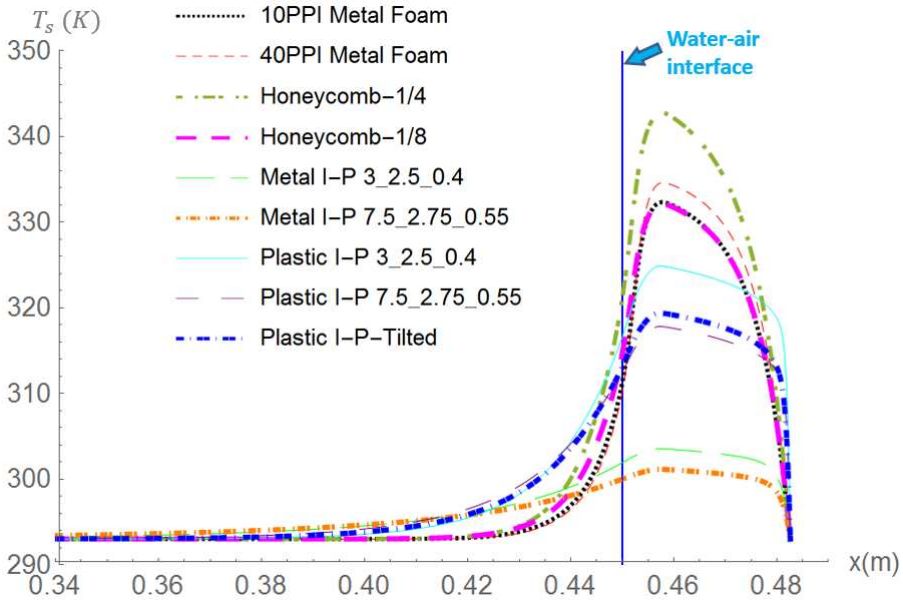

(b) time=3s

Fig.5.11 Temperature distributions in the solid

5.3. Thermal Design of Heat Exchanger Matrices Based on 1-D Model

The advantage of the 1-D model is that it gives fast and accurate calculations of the axial temperature distributions in the liquid piston compressor. Therefore, it can be used for fast comparison of applications of different matrices in the liquid-piston chamber, as shown in the previous section, and also can be used for design analyses. In this section, three design analysis problems will be addressed.

5.3.1. Design of the Porosity Distribution

The objective is to minimize the compression work input for a given overall pressure compression ratio by changing the distribution of porosity or the shape of the exchanger matrix. A design method based on sensitivity calculations is developed. It solves the flow field using the 1-D model in an iterative procedure. The sensitivity is the partial derivative of the compression work with respect to the porosity value at each design node. In each design analysis round, the 1-D model is solved as many times as there are design nodes, and each time the porosity value at a single design node is changed by a small amount. From these calculations, the sensitivity of changing the porosity distribution to the total work input (objective) is obtained. Based on this, the porosity distribution is updated in the direction that favors the objective. Then, the design procedure marches to the next round and the same calculations are completed iteratively until an optimum solution is reached. A best design of the distribution of porosity over the chamber is obtained.

5.3.1.1. Design Objective and Constraints

Addressed now is a design analysis of the distribution of porosity inside the chamber using the 1-D model. As mentioned earlier, the purpose of inserting porous media in the compressor is to reduce temperature rise during compression. From the heat transfer point of view, having a larger percentage of solid matrix, which corresponds to a lower porosity value, leads to less temperature rise of air. If the temperature rise could be minimized, less compression work would be required to maintain the air pressure at the storage pressure as the compressed air cools to the ambient temperature. On the other hand, a larger percentage of solid matrix increases flow resistance of the air and liquid piston, which requires more

compression work to overcome. Thus, the goal is to find the optimal porosity distribution for the porous medium that minimizes the work input. The porosity value in this problem is bound by the values $[0.7, 0.96]$.

A major constraint to the design problem is the power density. The power density is the storage energy per unit volume divided by the compression time. The storage energy is the amount of work output as the compressed air undergoes an isothermal expansion process. Therefore, the power density is given by:

$$\dot{Pow} = \frac{E_s}{V_0 t_f} = \frac{mRT_0(\ln(\zeta)-1+\frac{1}{\zeta})}{V_0 t_f} = \frac{\rho_0 RT_0(\ln(\zeta)-1+\frac{1}{\zeta})}{t_f} \tag{5.31}$$

In the design analysis, the power density is fixed by fixing the compression time and the pressure compression ratio. As the porosity distribution is gradually updated during design calculation procedures, the compression speed also needs to be updated accordingly such that the requirements of a fixed compression time and a fixed final pressure compression ratio are met.

The compression work during compression from $t = 0$ to $t = t_f$ is given by

$$W_{\text{comp}} = \int_0^{t_f} (P + P_{\text{r}}) U_0 A \text{dt} \tag{5.32}$$

This is the objective function that must be minimized. The compression work is done to pump the liquid piston against the thermodynamic pressure of air, P, and the flow resistance of the porous insert, P_{r}.

The instantaneous thermodynamic pressure of the air in the chamber is given by,

$$P = \frac{1}{L}\int_0^L \alpha_1 RT dx \tag{5.33}$$

The instantaneous air volume fraction and fluid temperature are variables that can be obtained by solving the 1-D model.

A general formulation of the flow resistance due to the porous medium is based on Darcian and Forchheimer terms:

$$P_r = \int_0^L \left[\frac{\mu}{K}\epsilon u + \rho b(\epsilon u)^2\right] dx \tag{5.34}$$

Note that in this problem the VOF method is used, and ρ and μ are the fluid mixture properties. In this equation, it does not account for the effect of changing porosity on the flow resistance. Ergun proposed a term, $\frac{(1-\epsilon)^2}{\epsilon^3}$, multiplied to the Darcian velocity in the Darcian resistance term, and a term, $\frac{1-\epsilon}{\epsilon^3}$, multiplied to the Darcian velocity squared in the Forchheimer resistance term [85]. Therefore, considering Ergun's equation and the resistance parameters obtained for the 10 PPI metal foam, the following equation is used to account for the effect of porosity on flow resistance,

$$P_r = \int_0^L \left[\frac{\mu}{\tilde{K}}\frac{(1-\epsilon)^2}{\epsilon^3}\epsilon u + \rho\tilde{b}\frac{1-\epsilon}{\epsilon^3}(\epsilon u)^2\right] dx \tag{5.35}$$

where, $\tilde{K} = 1.460 \times 10^{-9} m^2,\ \tilde{b} = 3275/\mathrm{m}$

After compression, the compressed air cools to the initial temperature; cooling work is done to decrease its volume while maintaining its pressure:

$$W_{\text{cool}} = (P_f - P_0)(V_f - V_0\frac{P_0}{P_f}) \tag{5.36}$$

The total input work is the sum of compression work and cooling work, which is the objective function to minimize:

$$W_{\text{in}} = \int_0^{t_f} \left\{\frac{1}{L}\int_0^L \alpha_1\rho_1 RT dx + \int_0^L \left[\frac{\mu}{\tilde{K}}\frac{(1-\epsilon)^2}{\epsilon^3}\epsilon u + \frac{1}{2}\rho\tilde{b}\frac{1-\epsilon}{\epsilon^3}(\epsilon u)^2\right] dx\right\} U_0 A \mathrm{dt} + (P_f - P_0)(V_f - \frac{V_0}{\zeta}) \tag{5.37}$$

The pressure, temperature, and volume fraction are obtained by solving the One-D model.

5.3.1.2. Design Method

The design method features an iterative procedure that involves evaluating the sensitivity of local change of $\epsilon(x)$ and optimizing $\epsilon(x)$ accordingly. First, an initial porosity distribution, $\epsilon(x)_{[0]}$ is assigned. The total work input is calculated based on Eq.(5.37), after solving the transient flow variables from the 1-D model. Then, the local sensitivity, which is the partial derivative of compression work with respect to local porosity, is evaluated at each design node according to:

$$\left(\frac{\partial W_{in}}{\partial \epsilon(x_l)}\right)_{[i]} = \left(\frac{W_{in,l}{}^{*} - W_{in}}{\Delta\epsilon}\right)_{[i]} \tag{5.38}$$

where subscripts l and $[i]$ represent local node index and iteration step, respectively. The work W_{in} is evaluated based on the current porosity distribution, $\epsilon(x)$, obtained after the previous calculation round. The term $W_{\text{in},l}{}^{*}$ is evaluated based on the porosity distribution, $\epsilon^{*}(x)$, which has a small change, $\Delta\epsilon$, at location x_l:

$$\epsilon^{*}(x_n)_{[i]} = \begin{cases} \epsilon(x_n)_{[i]} + \Delta\epsilon, & n = l \\ \epsilon(x_n)_{[i]}, & n \neq l \end{cases} \qquad n = 1,2,\dots,N \tag{5.39}$$

where N is the total number of design nodes along the axis of the chamber. Evaluating the sensitivity at each node l requires solving the 1-D model based on the porosity distribution, $\epsilon^{*}(x_n)$. After calculations of sensitivity values at all nodes are completed, the porosity distribution is updated in the direction that decreases the compression work based on the local sensitivity values. Since larger local sensitivity values indicate larger gains when optimizing the local porosity, the scheme increases or decreases the local porosity values by an amount proportional to the local sensitivity value. The local porosity values are updated based on:

$$\epsilon(x_l)_{[i+1]} = \begin{cases} 0.7, & if\ \ \epsilon(x_l)_{[i]} - \gamma\Delta\epsilon\left(\frac{\partial W_{\text{in}}}{\partial\epsilon(x_l)}\right)_{[i]} < 0.7 \\ 0.96, & if\ \ \epsilon(x_l)_{[i]} - \gamma\Delta\epsilon\left(\frac{\partial W_{\text{in}}}{\partial\epsilon(x_l)}\right)_{[i]} > 0.96 \\ \epsilon(x_l)_{[i]} - \gamma\Delta\epsilon\left(\frac{\partial W_{\text{in}}}{\partial\epsilon(x_l)}\right)_{[i]}, & otherwise \end{cases},$$

$$l = 1, 2, \dots, N \tag{5.40}$$

where γ is a parameter to control the convergence rate of the design analysis.

Because the compression time is fixed, as the porosity distribution is updated, the final pressure ratio would be different if the same compression speed were used. Therefore the compression speed must be updated to maintain the same pressure compression ratio. The objective of updating the compression speed is to minimize the pressure ratio error:

$$P_{err} = |\zeta - \zeta_{desire}| \tag{5.41}$$

The sensitivity of the compression speed to the pressure ratio error is calculated by:

$$\left(\frac{\partial P_{err}}{\partial U_0}\right)_{[i]} = \left(\frac{{P_{err}}^* - P_{err}}{\Delta U_0}\right)_{[i]} \tag{5.42}$$

where ${P_{err}}^*$ is the solution obtained for the compression speed: $U_0 + \Delta U_0$. The compression speed is then updated based on its sensitivity:

$$U_{0_{[i+1]}} = U_{0_{[i]}} - \frac{P_{err_{[i]}}}{\left(\frac{\partial P_{err}}{\partial U_0}\right)_{[i]}} \tag{5.43}$$

The aforementioned calculations are performed repeatedly until a final and optimum $\epsilon(x)$ is found.

5.3.1.3. Result

A design problem is solved to find an optimal porosity distribution, $\epsilon(x)$, that minimizes the compression work, W_{in} , for a given compression time and liquid piston speed. The porosity value is bound by $[0.7, 0.96]$. The same chamber length, compression speed and

physical properties as used in section 5.1.5 are solved in this design problem. The compression time is 2.6s. The final compression ratio is fixed at 12.94, and the power density is $64{,}020 W/m^3$ (storage energy density: $166{,}453 W/m^3$). The initial porosity distribution is 0.93 throughout the chamber. Since 1-D modeling does not include radial direction effects, the result on the work input is given on a "per volume" basis. The domain is discretized into 50 design nodes ($N = 50$) and 3500 computation nodes ($N_n = 3500$) for the One-D model. The time step size for solving the One-D model is $\Delta t = 2.167 \times 10^{-5} s$. The parameter, γ, increases with iteration step to accelerate the convergence speed for the first five design interations, and is maintained at a relatively small value for the sixth design iteration:

$$\gamma = \frac{i}{50} \tag{5.44}$$

where i is the design calculation step.

The design calculation procedure starts with $i = 0$. After three design calculation rounds, at step $i = 3$, the solution is considered to be optimal and further design calculations would result in a change of less than $1 J/m^3$ of work input, W_{in}. The work input values at every design calculation step are shown in Fig.5.12 (a). The initial work input is $183{,}224 J/m^3$. With the optimal design, the work input is $182{,}094 J/m^3$. The initial compression speed is $0.1030 m/s$. The compression speed for the optimal porosity distribution is $0.1031 m/s$. The efficiency, which is the storage energy divided by the work input, is improved from 90.79% to 91.41%.

The porosity distributions at different design calculation steps are shown in Fig.5.12 (b). The optimal porosity distribution, which is obtained at step 3, features high porosity values in approximately the first half of the chamber, low porosity values in a region close to the top cap, and a smooth transition region between the two regions. The physical reason for this design result is that high porosity values in the lower region of the chamber can more effectively reduce the pressure drag of the porous inserts, while low porosity values in the upper region can more effectively enhance heat transfer.

The sensitivity curves at different design calculation steps are shown in Fig.5.12 (c). Note that the work input sensitivity is based on the absolute work value for a unity radius of the air volume. In general, the sensitivity becomes smaller as the design calculation proceeds. By comparing the sensitivity curve to the porosity distribution at step 3, one sees that optimal solution is achieved at step 3. The local sensitivity values in the large-porosity region are negative, meaning that further design calculation in this region is possible only if the porosity values are allowed to be increased beyond the upper bound. The local sensitivity values in the upper, low-porosity region are positive, meaning that further design calculation in this region is possible only if porosity values below the lower bound are allowed. In the transition region between the high and low porosity regions, the local sensitivity values are almost all zero, meaning that optimal values have already been achieved in this region.

The optimal porosity distribution is shown in Fig.5.13. The porosity distribution in the transition region between the high and low porosity regions is fit into a polynomial. In summary, the optimal porosity distribution for this problem is:

$$\epsilon = 0.96 \qquad \text{for } x < 0.520L \qquad (5.45)$$

$$\epsilon = -22.610\left(\frac{x}{L}\right)^3 + 42.867\left(\frac{x}{L}\right)^2 - 27.394\frac{x}{L} + 6.794$$

$$\text{for } 0.520L \le x \le 0.816L \qquad (5.46)$$

$$\epsilon = 0.7 \qquad \text{for } x > 0.816L \qquad (5.47)$$

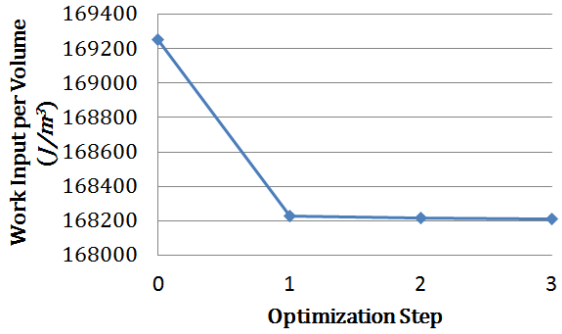

(a) Compression work values at different design calculation steps

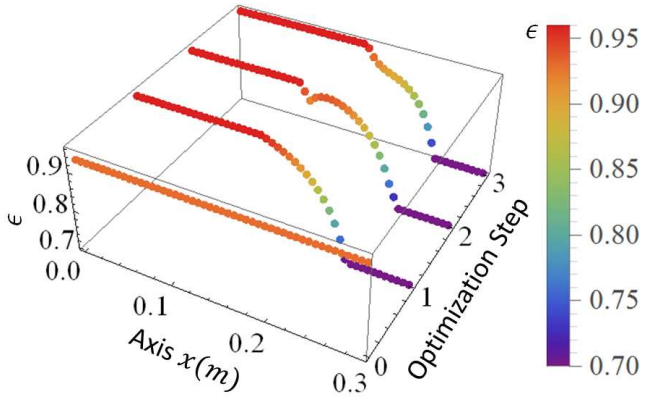

(b) Porosity distributions at different design calculation steps

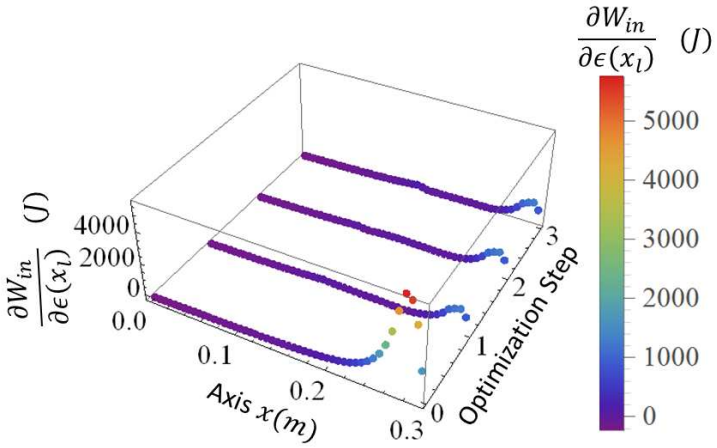

(c) Sensitivity distributions at different design calculation steps

Fig.5.12 Solutions obtained through design calculation iterations

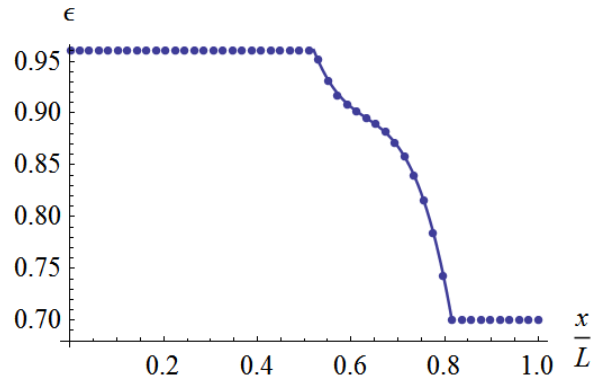

Fig.5.13 Optimal porosity distribution along the chamber axis

5.3.2. Design of the Interrupted-Plate Matrix for Low Pressure Compression

5.3.2.1. Design Objective and Constraints

A similar design analysis is done on the interrupted-plate matrix for application in the same chamber (as in section 5.3.1), for low pressure compression. The purpose of inserting the heat exchanger elements in the compressor is to reduce temperature rise during compression. From a heat transfer perspective, using smaller length scales (finer features) of the exchanger leads to enhancement in heat transfer and less temperature rise of air. When the temperature rise is reduced, less compression work would be needed to maintain the air pressure during the storage period as the compressed air cools to the ambient temperature. On the other hand, fine features of the exchanger also increases flow drag due to the resistance that liquid piston and air experience as they moving through the porous material. Thus, the design objective is to find the plate length, distance, and thickness distributions for the interrupted-plate exchanger that minimizes the total work input. The plate length, distance, and thickness values in this problem are bound by $[2mm, 15mm]$, $[2.5mm, 10mm]$, $[0.4mm, 1.6mm]$, respectively.

The objective is thus to minimize the total work input, which is the sum of compression work and cooling work, given by Eq. (5.37). The flow resistance of the interrupted-plate matrix is modeled based on Darcian and Forchheimer terms:

$$P_r = \int_0^L \left[\frac{\mu}{K}\epsilon u + \frac{F}{K^{0.5}}\rho(\epsilon u)^2\right] dx \tag{5.48}$$

The permeability and Forchheimer coefficients are given by the following equations based on interpolation of models established in the previous chapter:

$$K = \begin{cases} K_{2.5} + \frac{2\mathscr{b}-0.0025m}{0.0025m}(K_5 - K_{2.5}), & 0.0025m \le 2b < 0.005m \\ K_5 + \frac{2\mathscr{b}-0.005m}{0.005m}(K_{10} - K_5), & 0.005m \le 2b \le 0.01m \end{cases} \tag{5.49}$$

$$F = \begin{cases} F_{2.5} + \frac{2\mathscr{b}-0.0025m}{0.0025m}(F_5 - F_{2.5}), & 0.0025m \le 2b < 0.005m \\ F_5 + \frac{2\mathscr{b}-0.005m}{0.005m}(F_{10} - F_5), & 0.005m \le 2b \le 0.01m \end{cases} \tag{5.50}$$

where $K_{2.5}$, K_5, K_{10}, $F_{2.5}$, F_5, F_{10} are given by Eqns.(4.25)-(4.30). Since this is for low pressure compression, heat transfer correlation Eq.(4.35) is used. The volumetric heat transfer coefficient can be calculated based on

$$h_V = ha_V = \frac{Nu_{Dh}\mathscr{k}}{D_h} a_V \tag{5.51}$$

The plate length, plate distance, and plate thickness also determine the porosity and specific surface area of the exchanger through the following relations:

$$\epsilon = \frac{2\mathscr{b}}{2\mathscr{b}+\mathscr{t}} \tag{5.52}$$

$$a_V = \frac{4(2\mathscr{b}+\mathscr{t})\mathscr{l}+8\mathscr{b}\mathscr{t}}{2(2\mathscr{b}+\mathscr{t})^2\mathscr{l}} \tag{5.53}$$

5.3.2.2. Design Method

The design method in principle is the same as that in section 5.3.1.2. The main difference is that now three shape parameters will be designed (as opposed to one parameter in section 5.3.1); to generalize our discussion, a symbol will be used which represents all three: Θ, where $\Theta = \mathscr{l},\ 2\mathscr{b},\ and\ \mathscr{t}$. A sensitivity-based design calculation procedure is used. This is an iterative process that evaluates the sensitivity of local change of the shape parameter

$\Theta(x)$ and optimizes $\Theta(x)$ accordingly. At each design calculation round, the total work input is calculated based on the updated shape parameter distributions from the previous round using Eq.(5.37). Then, the local sensitivity, which is the partial derivative of compression work with respect to the local shape parameter value, is evaluated at each discretized design evaluation node, x_ℓ , according to:

$$\left(\frac{\partial W_{in}}{\partial \Theta(x_\ell)}\right)_{[i]} = \left(\frac{W_{in,l}{}^{*} - W_{in}}{\Delta\Theta}\right)_{[i]} \tag{5.54}$$

where subscripts ℓ and $[i]$ represent the local design evaluation node index and iteration step, respectively. On the RHS of the above equation, the work term, W_{in} , is evaluated based on the shape distribution, $\Theta(x)_{[i]}$. The work term $W_{\text{in},l}{}^{*}$ is evaluated based on the shape distribution, $\Theta^{*}(x)_{[i]}$, which has a small variation of $\Delta\Theta$ at location x_ℓ , compared to $\Theta(x)_{[i]}$. $\Theta^{*}(x)_{[i]}$ is given by:

$$\Theta^{*}(x_n)_{[i]} = \begin{cases} \Theta(x_n)_{[i]} + \Delta\Theta, & n = \ell \\ \Theta(x_n)_{[i]}, & n \neq \ell \end{cases} \qquad n = 1,2,\dots,N \tag{5.55}$$

where N is the total number of design evaluation nodes along the axis of the chamber. Evaluating the sensitivity at each node ℓ, requires solving the 1-D model based on the shape distribution, $\Theta^{*}(x_n)$. After calculations of sensitivity values at all nodes are completed, the shape parameter distribution is updated in the direction that decreases the compression work based on the local sensitivity values. Since larger local sensitivity values indicate larger gains when optimizing the shape parameter, the design calculation scheme increases or decreases the local shape parameter values by an amount proportional to the local sensitivity value, based on:

$$\Theta(x_\ell)_{[i+1]} = \begin{cases} \Theta_{low}, & if \;\; \epsilon(x_\ell)_{[i]} - \gamma\Delta\epsilon\left(\frac{\partial W_{\text{in}}}{\partial \epsilon(x_\ell)}\right)_{[i]} < \Theta_{low} \\ \Theta_{up}, & if \;\; \epsilon(x_\ell)_{[i]} - \gamma\Delta\epsilon\left(\frac{\partial W_{\text{in}}}{\partial \epsilon(x_\ell)}\right)_{[i]} > \Theta_{up} \\ \epsilon(x_\ell)_{[i]} - \gamma\Delta\epsilon\left(\frac{\partial W_{\text{in}}}{\partial \epsilon(x_\ell)}\right)_{[i]}, & otherwise \end{cases} \tag{5.56}$$

$$\ell = 1, 2, \ldots, N$$

where γ is a positive parameter to control the convergence rate of the design calculation.

As the compression time is fixed, the compression speed is updated to maintain the same pressure compression ratio throughout the design calculation procedure. The objective of updating the compression speed is to minimize the error in the final pressure ratio:

$$P_{err} = |\zeta - \zeta_{desire}| \tag{5.57}$$

The sensitivity of the compression speed to the pressure ratio error is calculated by:

$$\left(\frac{\partial P_{err}}{\partial U_0}\right)_{[i]} = \left(\frac{{P_{err}}^* - P_{err}}{\Delta U_0}\right)_{[i]} \tag{5.58}$$

where ${P_{err}}^*$ is the solution obtained for the compression speed: $U_0 + \Delta U_0$. The compression speed is then updated based on its sensitivity:

$$U_{0_{[i+1]}} = U_{0_{[i]}} - \frac{P_{err_{[i]}}}{\left(\frac{\partial P_{err}}{\partial U_0}\right)_{[i]}} \tag{5.59}$$

In each iterative step i, the design calculation sequence is: $l,\ 2b,\ t,\ U_0$. The aforementioned calculations are performed repeatedly until a final and optimum $\Theta(x)$ is found. A flow chart of the design procedure is given in Fig.5.14.

5.3.2.3. Result

Two design problems have been solved, for fast and slow compression speeds, respectively. The conditions for each problem, as well as results are given in Table 5.1. The chamber length is 0.294m in each problem. Initially, the interrupted-plate exchanger has a uniform shape throughout the chamber: $\ell = 7.5mm,\ 2b = 2.5mm,\ and\ t = 0.8mm$. For the sensitivity evaluation, the infinitesimal elements for the three shape parameters are respectively: $\Delta\ell = 0.1mm,\ \Delta(2b) = 0.075mm,\ and\ \Delta t = 0.015mm$.

The parameter is chosen to be a function that decreases with each design calculation iteration,

$$\gamma = \frac{5\lg(3i+1)+1}{40}(i+1)^{0.3} \tag{5.60}$$

An optimum design is achieved if either of the following criteria is true: (1) difference in the change of compression efficiency is less than 0.01%; or (2) the shape parameter values are already on the boundaries and further design iteration is only possible if these values go beyond the boundaries.

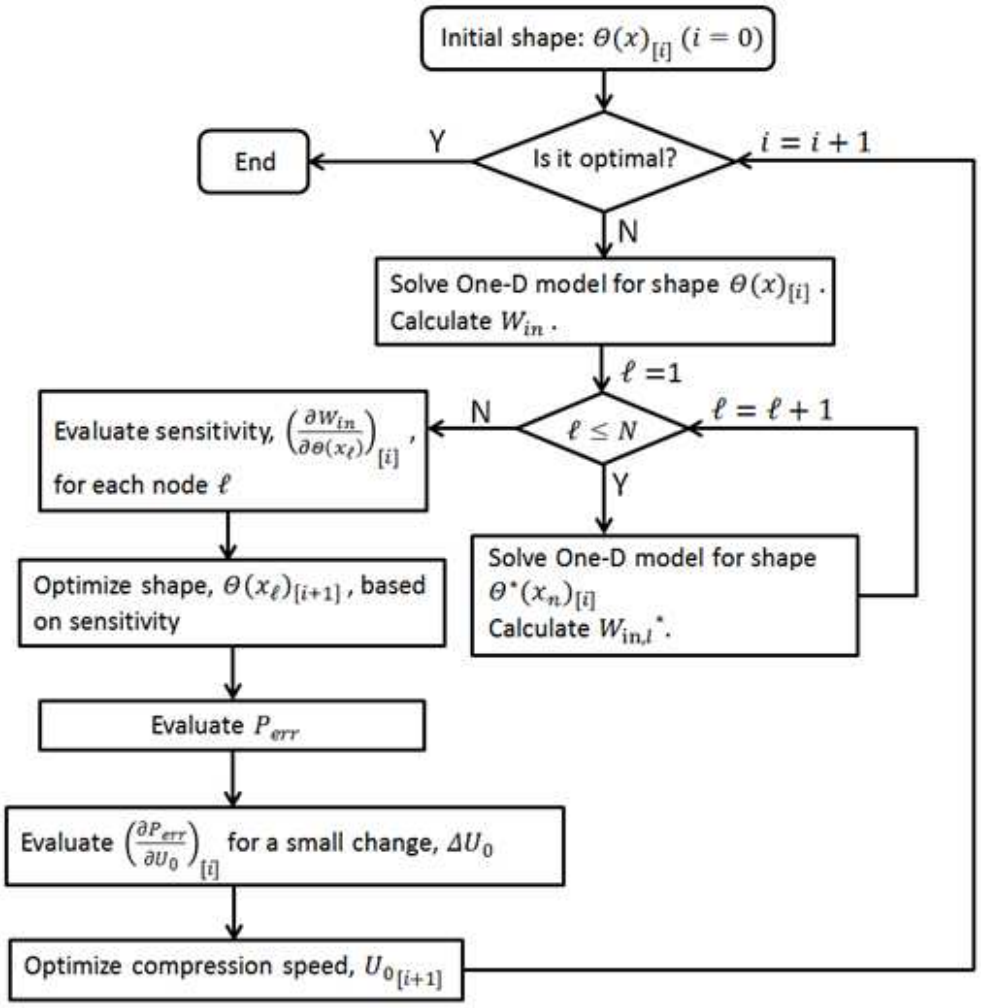

Fig.5.14 Flow chart of design calculation procedure of the interrupted-plate shape

With the optimum exchanger shape, the compression efficiency for each case has been improved by about 1% (Table 5.1). The efficiency is defined as the storage energy divided by the total work input. The power input is defined as the work input over compression time. Although the improvement on compression efficiency appears to be small, the absolute values of the reduction of power input based on the optimum design is not small, and could potentially save a large amount of energy when the system operates over long time.

Table 5.2 List of Design Analysis Cases and Results

Cases	Case 1	Case 2
Compression time (s)	1.3	2.6
Final Pressure Ratio	13.08	12.56
Storage Power per Volume (kW/m^3)	128.82	62.94
Input Power per Volume for Uniform Exchanger (kW/m^3)	140.19	66.59
Input Power per Volume for Optimized Exchanger (kW/m^3)	138.39	65.92
Reduction in the Power Input Using the Optimum Design(kW/m^3)	1.80	0.67
Compression Efficiency of Uniform Exchanger	91.9%	94.5%
Compression Efficiency of Optimized Exchanger	93.1%	95.5%
Compression Speed for Optimized Exchanger (m/s)	0.2063	0.1031

The optimal shape parameter distributions for the two cases are shown in Fig.5.15. A general trend is that smaller length scales are preferred in the upper region of the chamber while larger length scales are preferred in the lower part of the chamber. Accordingly, the result also shows that low porosity and large specific area are used in the upper part of the chamber, while high porosity and small specific area are used in the lower part of the chamber (Fig.5.16 and Fig.5.17). The physical reason for this result is that high porosity values in the lower region of the chamber can more effectively reduce the pressure drag of the porous inserts, while low porosity values in the upper region can more effectively enhance heat transfer. The fluctuations in the results are due to the fact that the exchangers already work very well, causing the sensitivity of the design calculation to be small.

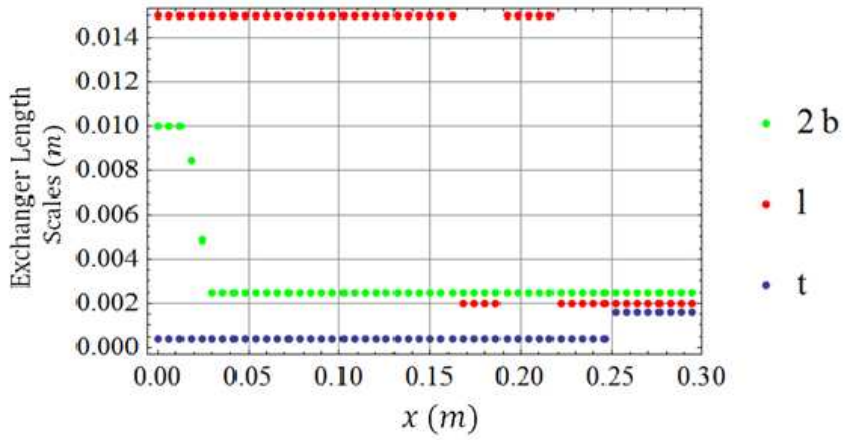

(a) Case 1, compression time=1.3s

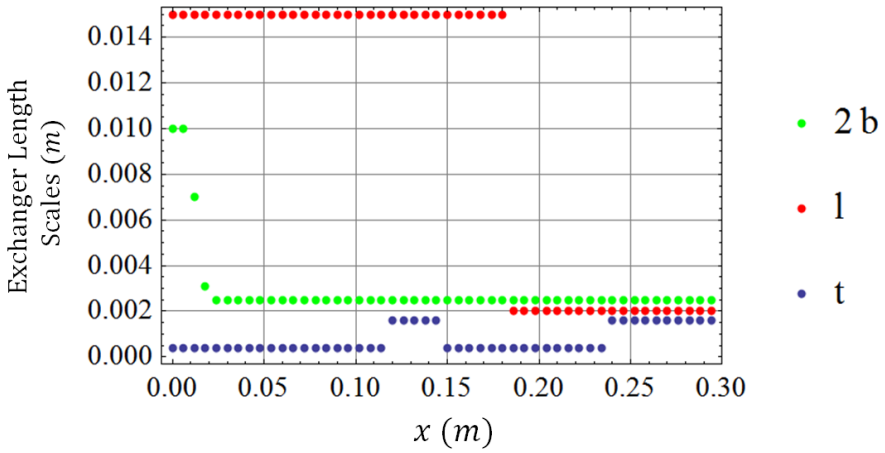

(b) Case 2, compression time=2.6s

Fig.5.15 Optimized interrupted-plate shape distribution

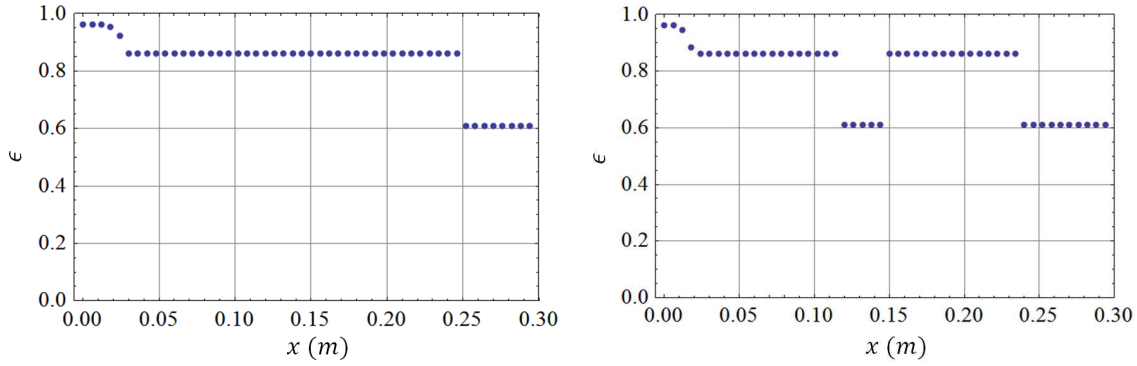

(a) Case 1, compression time=1.3s (b) Case 2, compression time=2.6s

Fig.5.16 Optimum porosity distribution

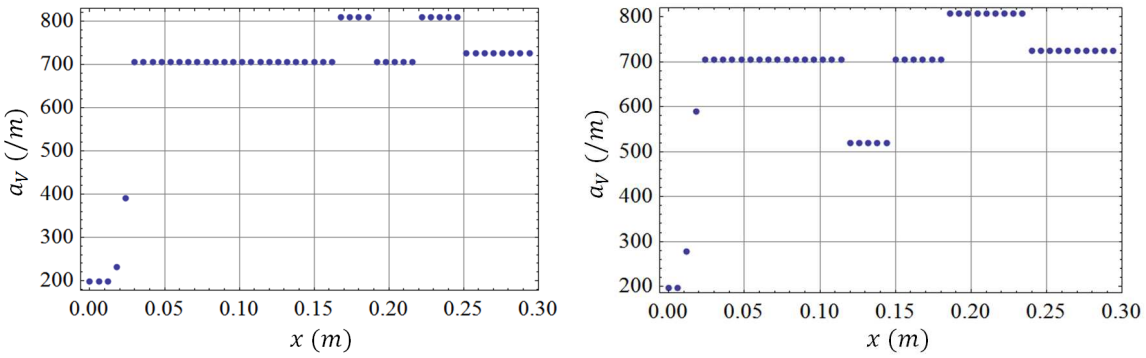

(a) Case 1, compression time=1.3s (b) Case 2, compression time=2.6s

Fig.5.17 Optimum specific area distribution

The instantaneous temperature distributions during compression processes using the uniform exchanger shape and the optimal exchanger shape are compared, as shown in Fig.5.18 - Fig.5.21. The use of denser and finer heat exchanger elements can effectively lower the air temperature in the region near the top cap during compression. This reduces the amount of input work being converted into internal energy of air and wasted during later storage period. And, because water reaches to the upper region of the chamber only near the end of the compression process, the denser heat exchanger does not cause too much extra input work to be consumed to overcome resistance. At the end of compression,

the optimal exchanger can reduce the air temperature by about 10K in both cases. The temperature rises in the exchanger solid in both cases are also shown to be reduced because of optimizing the exchanger shape.

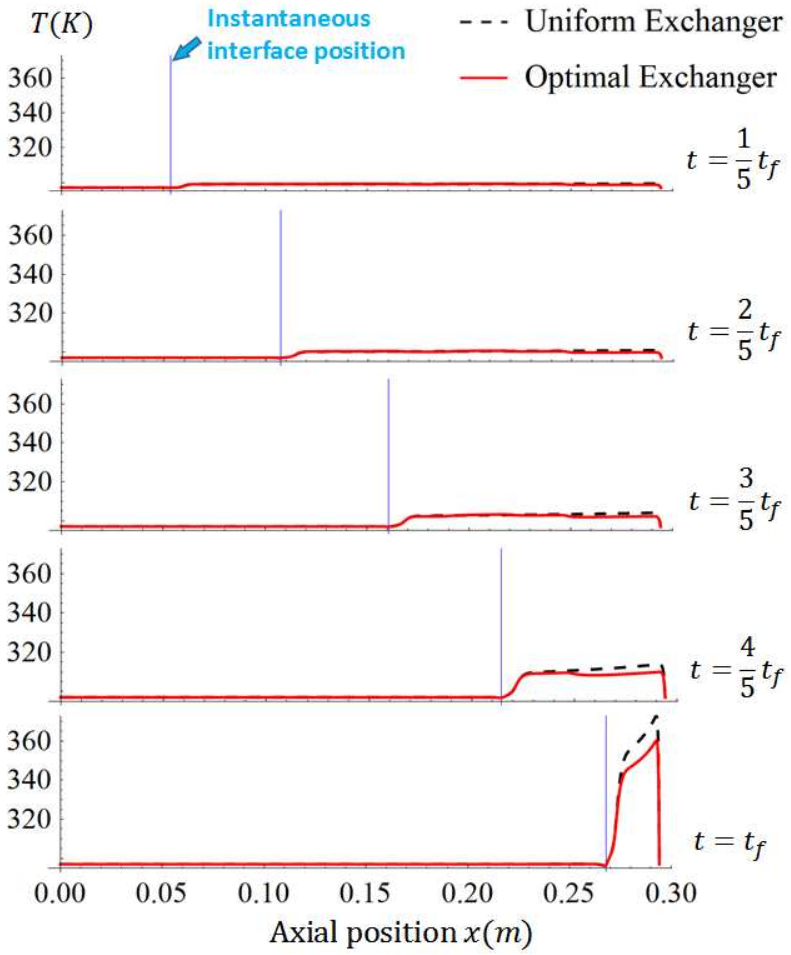

Fig.5.18 Fluid temperature distributions for compression time $t_f = 1.3s$ (comparisons between the uniform heat exchanger shape and the optimal heat exchanger shape)

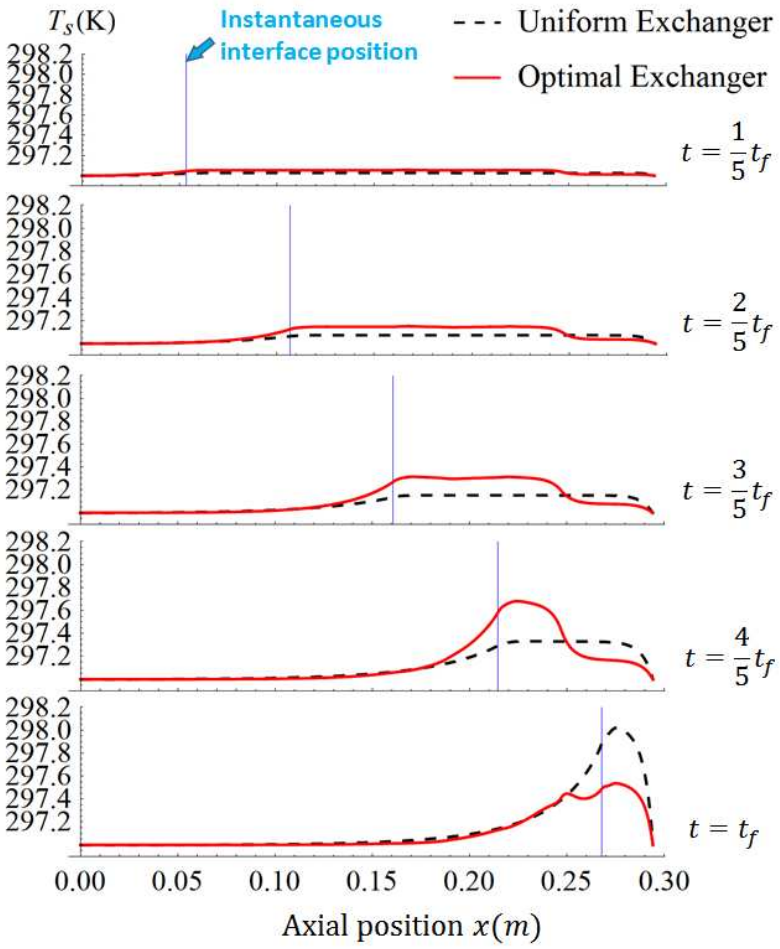

Fig.5.19 Solid temperature distributions for compression time $t_f = 1.3s$ (comparisons between the uniform heat exchanger shape and the optimal heat exchanger shape)

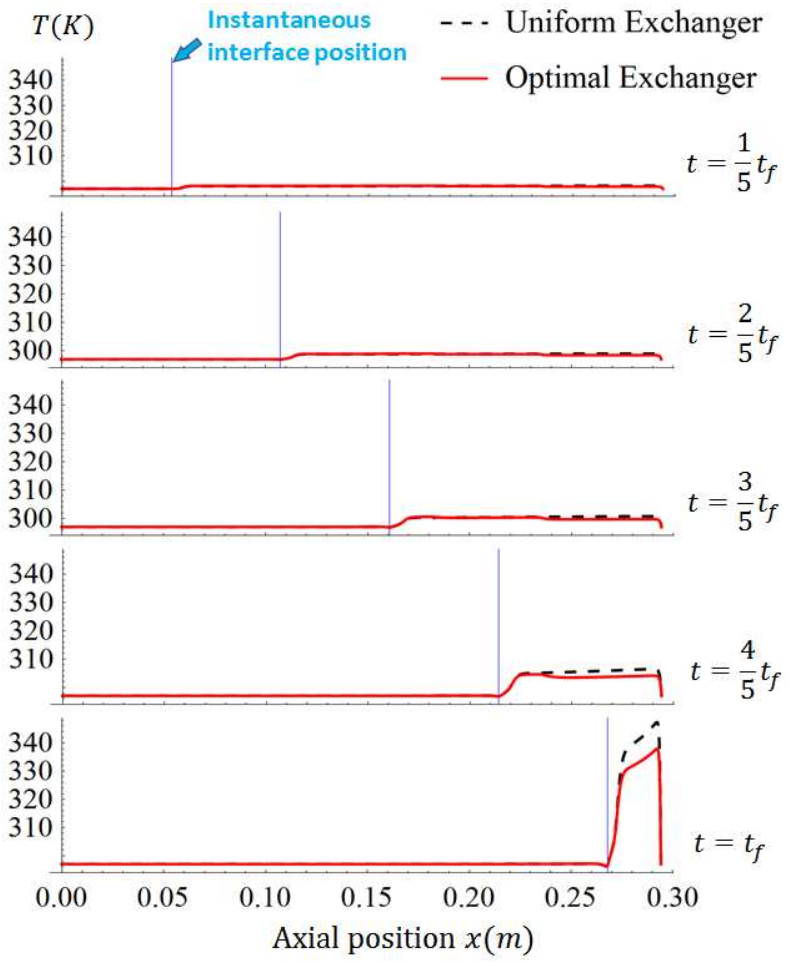

Fig.5.20 Fluid temperature distributions for compression time $t_f = 2.6s$ (comparisons between the uniform heat exchanger shape and the optimal heat exchanger shape)

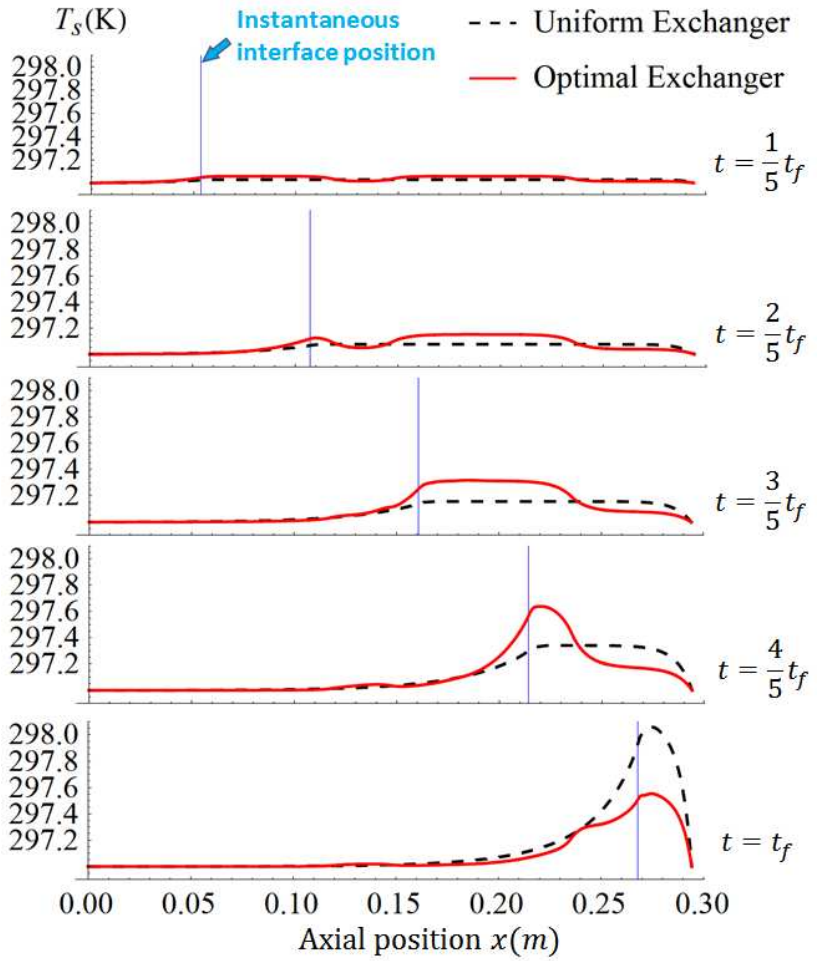

Fig.5.21 Solid temperature distributions for compression time $t_f = 2.6s$ (comparisons between the uniform heat exchanger shape and the optimal heat exchanger shape)

5.3.3. Design of the Interrupted-Plate Matrix for High Pressure Compression

An analysis focusing on a high pressure compression chamber using the interrupted plate matrix was done. The chamber has a length of 0.4826m, and the compression process goes from 7bar to 210bar in 3s. These are the same conditions as studied in section 3.3. The design calculation is the same as applied in section 5.3.2. Since compression is for high pressure, a more sophisticated heat transfer model is used, which is based on Eqns.(4.39)-(4.41). The resulting optimum design for the three shape parameters of the interrupted-

plate matrix is shown in Fig.5.22. The corresponding specific area and porosity distributions are shown in Fig.5.23. A similar trend in the design as discussed in the previous section is observed. Finer features are preferred in the upper region of the chamber to enhance heat transfer, while coarser features are preferred in the lower region to reduce pressure drop as the water piston rises.

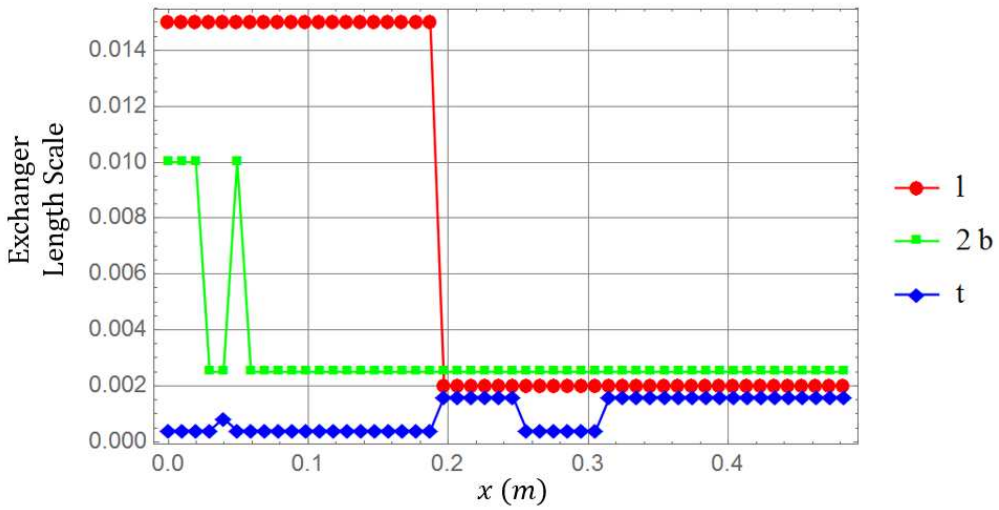

Fig.5.22 Best design of the shape parameters of the interrupted-plate exchanger used for high pressure compression

By comparing the optimum shape design with a uniform exchanger shape (REV11_1: $\ell = 7.5mm,\ 2\mathscr{b} = 2.75mm,\ t = 0.55mm$), we see a reduction of air temperature of 58.5K results by using the optimum shaped interrupted exchanger matrix. The calculated averaged air temperature for the uniform shaped interrupted plate exchanger is 472.7K, and for the optimized shape is 414.2K. The compression efficiency values for the uniform and optimized shapes are, respectively, 61.5% and 65.8%. The optimized shape results in a 4.3% increase in efficiency for the high pressure compression stage.

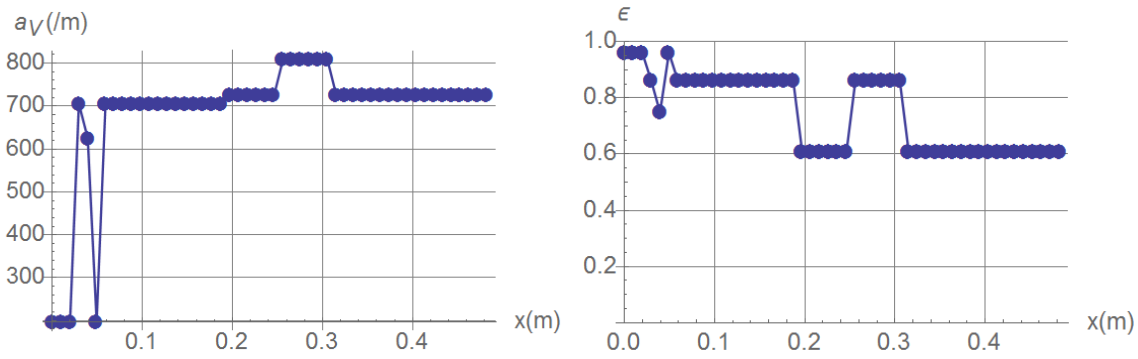

Fig.5.23 Specific area (a_V) and porosity (ϵ) corresponding to the optimal interrupted plate shape for high pressure compression

In this section, the 1-D model has been used to design the shape of the matrix, where the plates are straight, parallel to the chamber axis. A new heat exchanger matrix may be designed by combining the optimum shape as proposed in Fig.5.22 and the tilted-interrupted plate as given in Fig.4.41. As such, definitions of the exchanger's plate dimensions can be based on the optimum distribution shown in Fig.5.22 as a result of balancing heat transfer and pressure drop, and in addition, all plates can be tilted at 34° to further enhance heat transfer. Such exchanger matrices may be fabricated through 3-D printing. Blocks of different shape characteristics can be printed and stacked together in the chamber.

5.4. Further Development: a 1-D Model with an Embedded 2-D Model for Lateral Conduction in the Solid

This section presents a one-dimensional liquid-piston compressor model with an embedded two-dimensional submodel. The submodel is for calculating heat conduction in the lateral direction across a representative plate of a heat exchanger. As discussed in the previous sections in this chapter, a typical numerical model of a heat exchanger is a one-dimensional simplification of the two-energy-equation porous media model. Proposed in the present project is a one-dimensional model that incorporates the Volume of Fluid (VOF) method for application to the two-phase flow, liquid piston compressor with exchanger inserts.

Important to calculating temperature distributions in both the solid and fluid components of the mixture is heat transfer between the two, which depends on the local temperature values, geometry, and the velocity of fluid through the matrix. In the 1-D model, although the axial temperatures vary, the solid is treated as having a uniform temperature distribution across the plate at any axial location. This may be in line with the physics of flow in most heat exchangers, especially when the exchangers are made of metal with high thermal conductivity. However, it must be noted that for application to CAES, the gas temperature in the compression chamber rises rapidly during compression and the core of the solid wall may heat up to a different temperature than that of the surface, depending on the geometry, solid material of the exchanger and fluid flow situation. Therefore, a new, 1-D model with an embedded 2-D submodel is developed to consider two-dimensional heat conduction in a representative solid plate. The VOF concept is used in the model to handle the moving liquid-gas interface (liquid piston).

The model gives accurate solutions of temperature distributions in the liquid piston compression chamber. Six different heat exchangers with different length scales and different materials are simulated and compared.

5.4.1. Description of Numerical Model

5.4.1.1. Governing Equations and Numerical Scheme

As this model is an expansion to the previous 1-D model introduced in sectioon 5.1, discussion will mainly focus on the difference in the new model. In the proposed numerical model, a one-dimensional fluid domain is coupled with a two-dimensional solid domain through an interfacial heat transfer model between the fluids and the solid wall. For the fluid domain, the one dimension represents the axial direction of the compression chamber. For the two-dimensional solid domain, the one dimension is along the compressor axis and the other is across the thickness of the solid plate, perpendicular to the surface. A schematic of the computational domain and discretized cells is shown in Fig.5.24. In the actual heat exchanger, the plates are interrupted in a three-dimensional pattern; in the computation domain, only one representative plate with a fixed thickness throughout the entire

chamber's axial direction is modeled. This two-dimensional solid domain is capable of resolving heat penetration into the solid plate interior as well as the temperature distribution in the axial direction. Although it seemingly neglects the interrupting feature of the exchanger, the heat transfer correlations that couple heat transfer between a fluid and the solid surface will incorporate the effect of the interrupting feature of the exchanger plates.

The continuity equations for the air and water are given by,

$$\frac{\partial \alpha_1 \rho_1}{\partial t} + \frac{\partial \alpha_1 \rho_1 u}{\partial x} = 0 \tag{5.61}$$

$$\frac{\partial \alpha_2}{\partial t} + \frac{\partial \alpha_2 u}{\partial x} = 0 \tag{5.62}$$

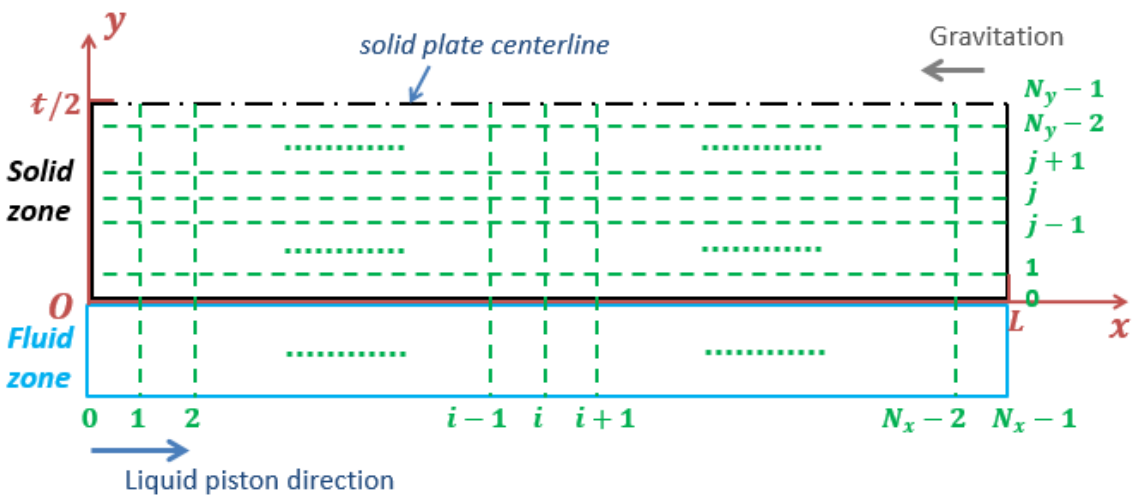

Fig.5.24 Schematic of computational domain and grid ($\frac{t}{2}$: half of the plate thickness which includes N_y nodes; L: chamber length that includes N_x nodes.)

The liquid and gas flow through a porous matrix. According to the porous media modeling principles, the energy transport in the fluid must take into account of the porosity and the interfacial heat transfer between the fluid and the solid. Also noted that this is a

two-phase flow modeled by the VOF approach, the governing equation for the energy transport in the fluid mixture (both air and water) is given by,

$$\epsilon \frac{\partial \overline{\rho c_p} T}{\partial t} + \epsilon \frac{\partial \overline{\rho c_p} uT}{\partial x} = k\epsilon \frac{\partial^2 T}{\partial x^2} + \alpha_1 \beta_1 T(\frac{\partial p}{\partial t} + u\frac{\partial p}{\partial x}) + a_V h(T_s|_{y=0} - T) \quad (5.63)$$

The water is assumed to be incompressible and, thus, the pressure work term in Eq. (4) is effective only in the air phase. The pressure can be related to air temperature and density by the equation of state.

The energy transport in the solid plate is two-dimensional, in both the compressor axial direction (x) and the direction perpendicular to the solid wall (y). The governing equation is:

$$\rho_s c_s \frac{\partial T_s}{\partial t} = k_s \frac{\partial^2 T_s}{\partial x^2} + k_s \frac{\partial^2 T_s}{\partial y^2} \quad (5.64)$$

The energy transport in the solid and fluid are coupled through interfacial heat transfer between the solid surface and the fluid domain,

$$k_s \frac{\partial T_s}{\partial y}|_{y=0} = h(T_s|_{y=0} - T) \quad (5.65)$$

Adiabatic boundary condition is applied at the centerline of the solid plate,

$$k_s \frac{\partial T_s}{\partial y}|_{y=\frac{t}{2}} = 0 \quad (5.66)$$

Other boundary conditions are:

$$T|_{x=0} = T|_{x=L} = T_s|_{x=0} = T_s|_{x=L} = T_0 \quad (5.67)$$

$$\alpha_2|_{x=0} = 1 \quad (5.68)$$

The velocity field and the real gas model used are the same as those dicussed in section 5.1.

5.4.1.2. Numerical Method

The transport equations are solved by the finite difference approach. The continuity equations for water and air are discretized using an explicit upwind method,

$$\frac{{\alpha_{2,i}}^{n+1}-{\alpha_{2,i}}^{n}}{\Delta t}+\frac{{\alpha_{2,i}}^{n}{u_i}^{n}-{\alpha_{2,i-1}}^{n}{u_{i-1}}^{n}}{\Delta x}=0 \tag{5.69}$$

$$\frac{{\alpha_{1,i}}^{n+1}{\rho_{1,i}}^{n+1}-{\alpha_{1,i}}^{n}{\rho_{1,i}}^{n}}{\Delta t}+\frac{{\alpha_{1,i}}^{n}{\rho_{1,i}}^{n}{u_i}^{n}-{\alpha_{1,i-1}}^{n}{\rho_{1,i-1}}^{n}{u_{i-1}}^{n}}{\Delta x}=0 \tag{5.70}$$

The fluid energy equation is discretized using an explicit scheme, with upwind differencing on the advection term and central differencing on the diffusive term,

$$\frac{\left(\overline{\rho c_p}_i^{n+1}T_i^{n+1}-\alpha_{1,i}^{n+1}p_i^{n+1}\right)-\left(\overline{\rho c_p}_i^{n}T_i^{n}-\alpha_{1,i}^{n}p_i^{n}\right)}{\Delta t}+\frac{\overline{\rho c_p}_i^{n}u_i^{n}T_i^{n}-\overline{\rho c_p}_{i-1}^{n}u_{i-1}^{n}T_{i-1}^{n}}{\Delta x}-$$
$$\frac{a_V h_i^{n}({T_{s,i,0}}^{n}-T_i^{n})}{\epsilon}=k\frac{T_{i-1}^{n}-2T_i^{n}+T_{i+1}^{n}}{\Delta x^2}+\frac{\alpha_{1,i}^{n}u_i^{n}p_i^{n}-\alpha_{1,i-1}^{n}u_{i-1}^{n}p_{i-1}^{n}}{\Delta x} \tag{5.71}$$

The solid energy equation is discretized using central differencing in space, and is solved using the Gauss-Seidel method.

$$\rho_s c_s\frac{{T_{s,i,j}}^{\mathbb{k}+1}-{T_{s,i,j}}^{n}}{\Delta t}$$
$$=k_s\left(\frac{{T_{s,i-1,j}}^{\mathbb{k}+1}-2{T_{s,i,j}}^{\mathbb{k}+1}+{T_{s,i+1,j}}^{\mathbb{k}}}{\Delta \mathrm{x}^2}+\frac{{T_{s,i,j-1}}^{\mathbb{k}+1}-2{Ts,i,j}^{\mathbb{k}+1}+{T_{s,i,j+1}}^{\mathbb{k}}}{\Delta \mathrm{y}^2}\right) \tag{5.72}$$

The integer $\mathbb{k}$ represents the Gauss-Seidel iteration step within a time step. The boundary conditions on the solid plate that involve heat flux equations are discretized with 2nd order differencing.

5.4.1.3. Grid Independence Verification

Simulations are done on a liquid-piston compressor for application to the high pressure compression stage of a CAES system. The compression starts with air at 700kPa and 293K. The chamber is initially full of air and has a total length of 0.4826m. Water is pumped into the chamber at a uniform speed, 0.152m/s, to compress the air. The total compression time is 3s. The final air pressure is around 21MPa.

For the grid independence study, a heat exchanger matrix, namely "PL-I-P-7.5_2.75_0.55," is simulated. The name indicates that it is a plastic (PL) interrupted-plate heat exchanger (I-P) heat exchanger featuring a plate height, plate separation distance, and plate thickness of 7.5mm, 2.75mm, and 0.55mm, respectively. The separation distance is measured between two plate surfaces facing one another. The thermal conductivity, specific heat, and density of the ABS plastic are, respectively, 0.17W/(mK), 1200J(kgK), and 1060kg/m^3. Five grids with progressively refined cell sizes and time step sizes are used for computation. Details of the grids are shown in Table 5.3.

The computation results based on different grids, compared in Fig.5.25, show that as grid resolution improves, solutions converge to the one based on the finest grid (Grid 5). Grid sets 1 and 2 give less steep air temperature rises next to the interface due to insufficient cell numbers in the x direction. They also calculate larger temperature rises on the solid wall. Grid sets 3, 4, and 5 give very close results. Grid 3 is used.

Table 5.3 Computation grids for grid independence study

	Grid 1	Grid 2	Grid 3	Grid 4	Grid 5
N_x	2001	3001	5001	6001	8001
N_y	7	13	17	27	51
Time steps	3000	6000	7500	9000	18000

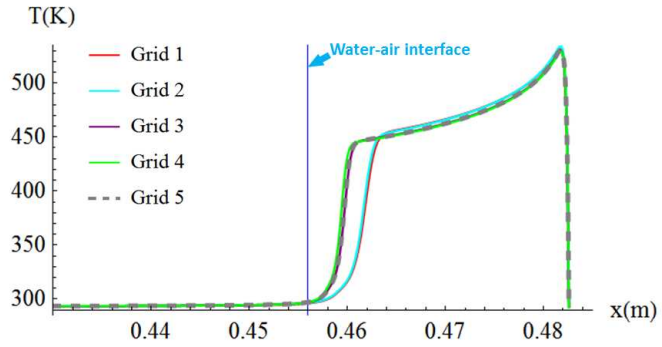

(a) Axial fluid temperature distributions

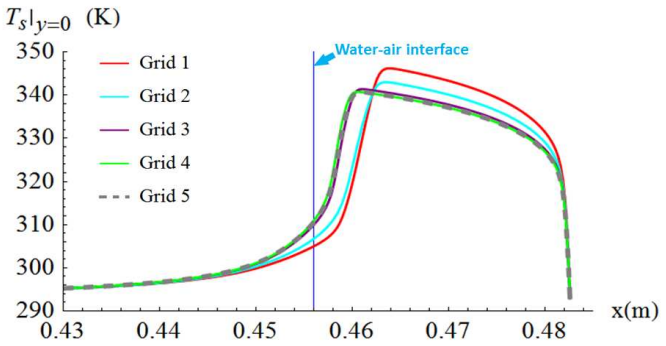

(b) Axial temperature distributions on the solid surface

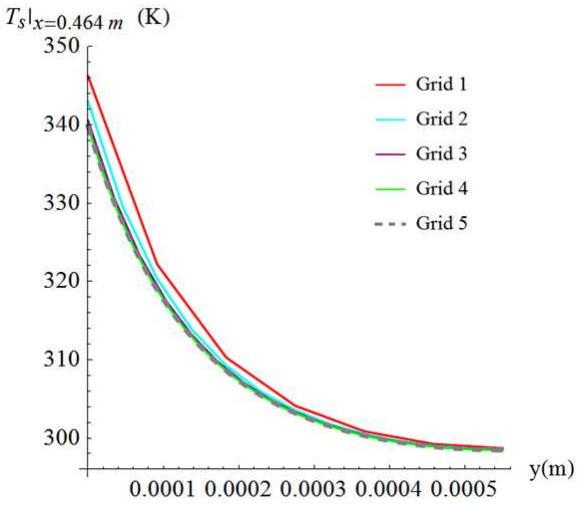

(c) Temperature distributions across the solid plate at $x = 0.464m$

Fig.5.25 Comparison of results for different grids at 3 seconds

5.4.2. Simulation Results

Six different heat exchanger matrices are studied. Four are of the interrupted-plate matrices: Metal-I-P-3_2.5_0.4, Metal-I-P-7.5_2.75_0.55, PL-I-P-3_2.5_0.4, and PL-I-P-7.5_2.75_0.55. and two honeycomb matrices with cell sizes of 1/4in (6.3mm) and 1/8in (3.2mm) (namely Honeycomb1_4 and Honeycomb1_8, respectively) are studied. The exchanger hydro-thermal properties and materials are listed in Table 5.1.

The numerical model gives detailed calculations of temperature distributions in a representative solid plate, as well as the axial fluid temperature distribution. In Fig.5.26-Fig.5.31, it is shown that air temperature rises roughly by 200K at the end of compression. The temperature rise mostly occurs in the latter period of a compression stroke since, for a constant liquid piston speed, the volume compression ratio becomes larger near the end of compression as the volume of air becomes smaller. In different exchanger matrices, the water temperature is nearly constant throughout the compression process and immediately above the water-air interface, there is a step rise of air temperature followed by continuously rising temperature that reaches a peak value at a location very close to the top cap of the chamber. The liquid and gas near the interface move together with little relative velocity so it is difficult for convective heat transfer to take place directly from air to water. Though there is a small amount of heat that is conducted from air to water across the interface, the effect of it is small in changing the water temperature near the interface region, given that water has a much larger density and heat capacity. The temperature of air rises by compression. Relative to the air far from the interface, the air temperature near the interface is nearer that of the water temperature because of faster air velocity that results in better heat transfer from air to the exchanger matrix. Near the top cap region, the air temperature reaches a maximum because of the relatively stagnant flow in that region, limiting the amount of heat transfer from air to the solid matrix.

The location of the instantaneous maximum temperature in an exchanger matrix shifts during compression as the water-air interface rises. In general, however, it is located in a

region of the matrix that is in contact with air and very near the water-air interface. The reason for this is that once a section of the matrix is immersed in water, it is cooled quickly and the section of the matrix directly above the water-air interface is farthest from the cold top cap and it also has been previously heated by air. Thus, this location has the maximum instantaneous temperature throughout the matrix.

The solid temperature distributions are affected by wall thickness and solid material. The two honeycomb matrices have only small temperature rises in the plates (Fig.5.26 and Fig.5.27), mainly because they are made of aluminum with a large thermal conductivity, which conducts the heat quickly to the cooled section at the water side of the interface. Comparison between the interrupted-plate exchangers of the same geometry but different materials (Fig.5.28 vs. Fig.5.30 or Fig.5.29 vs. Fig.5.31) shows that the use of ABS plastic, which has a low thermal conductivity, results in a much larger temperature rise on the plate surface than in the core region of the plate, while the stainless steel results in only a slightly larger temperature rise on the surface than in the core region. This difference between the ABS exchanger and the metal exchanger is caused by a difference in the conductive thermal resistances. Comparison between the interrupted-plate exchangers of the same material but different shapes (Fig.5.28 vs. Fig.5.29 or Fig.5.30 vs. Fig.5.31) show that, when the plate is thicker, the centerline temperature is lower because it takes more time for heat transfer to penetrate to the core region from the surface. The thermal conductivity also affects the axial temperature distribution in the plate. The heat penetration depths from the water-air interface location downwards into the plate section that is immersed in water are different for different materials. As shown in all the plots, the aluminum plate has the longest heat penetration depth downwards from the water-air interface, the stainless steel plate has the medium depth and the ABS plastic has the smallest penetration depth, due to the different thermal conductivities.

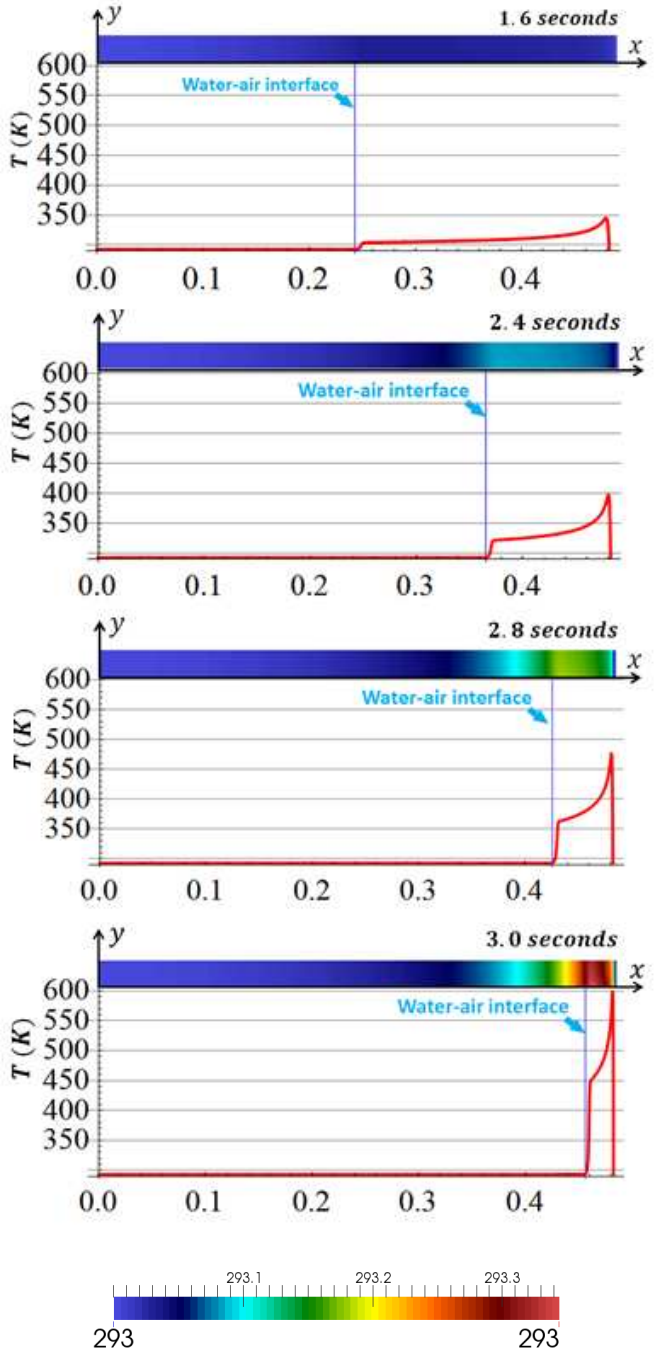

Fig.5.26 Temperature, Honeycomb1_4 (Curve represents fluid and contour plot is for solid; the y axis is scaled up 160 times)

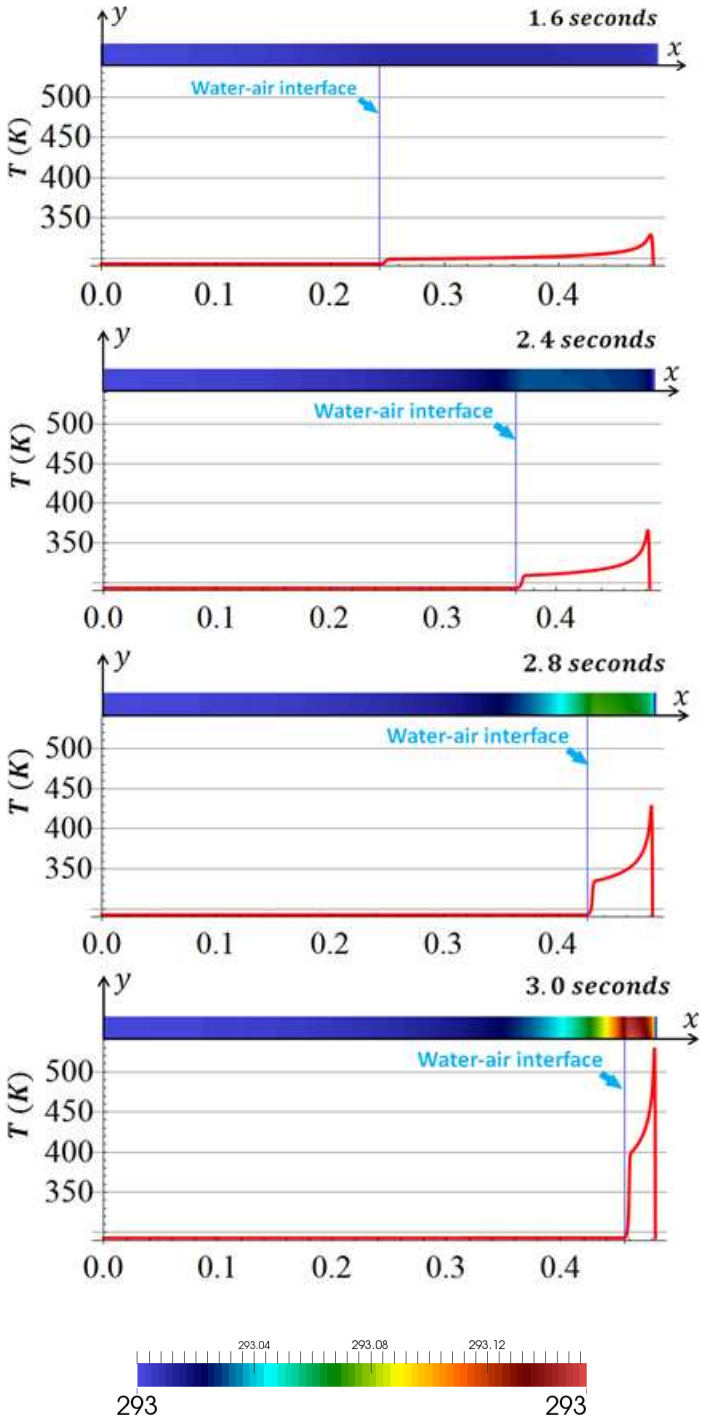

Fig.5.27 Temperature, Honeycomb1_8 (Curve represents fluid and contour plot is for solid; the y axis is scaled up 160 times)

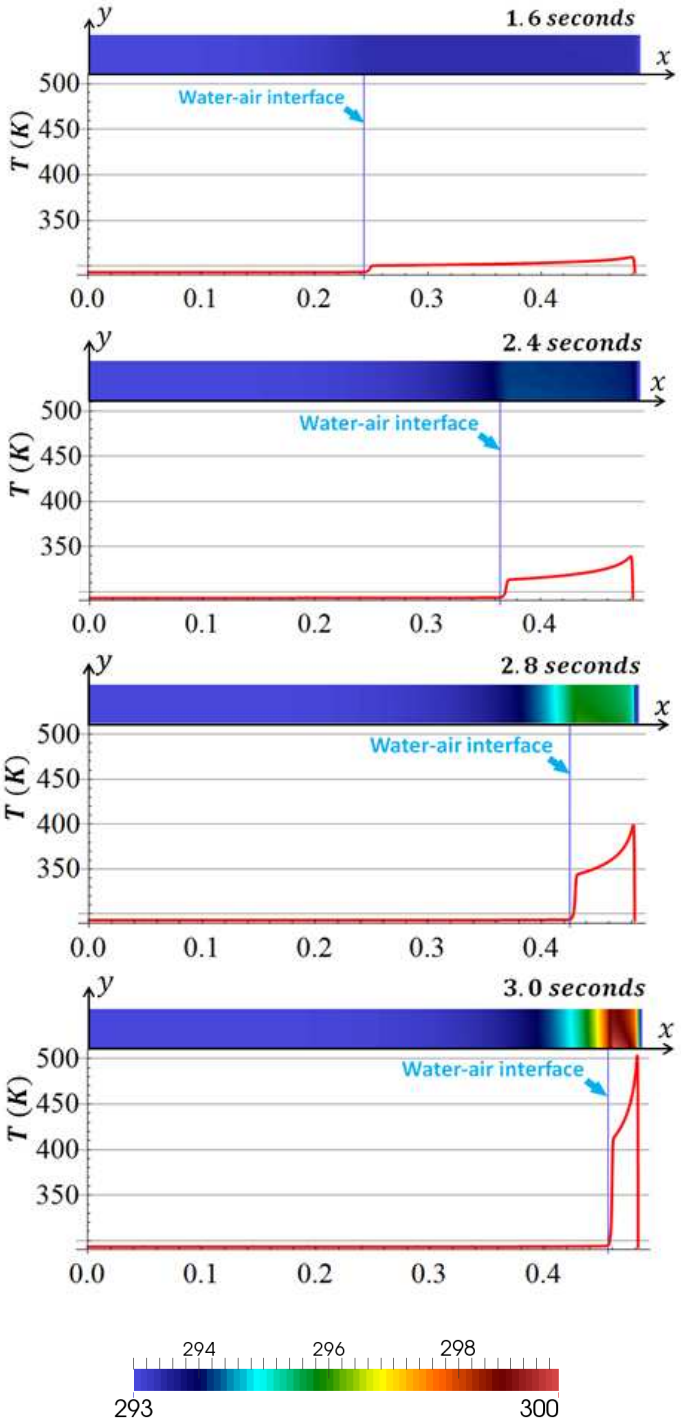

Fig.5.28 Temperature, Metal-I-P-3_2.5_0.4 (Curve represents fluid and contour plot is for solid; the y axis is scaled up 80 times)

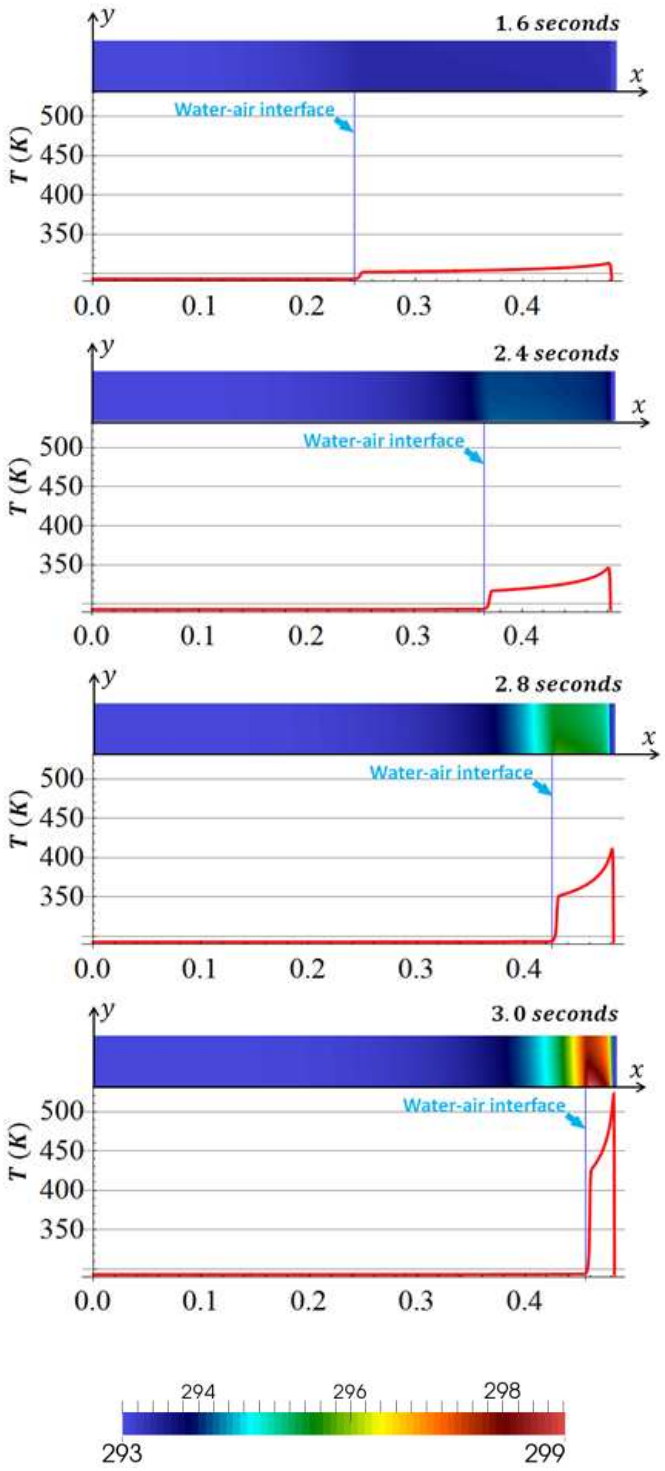

Fig.5.29 Temperature, Metal-I-P-7.5_2.75_0.55 (Curve represents fluid and contour plot is for solid; the y axis is scaled up 80 times)

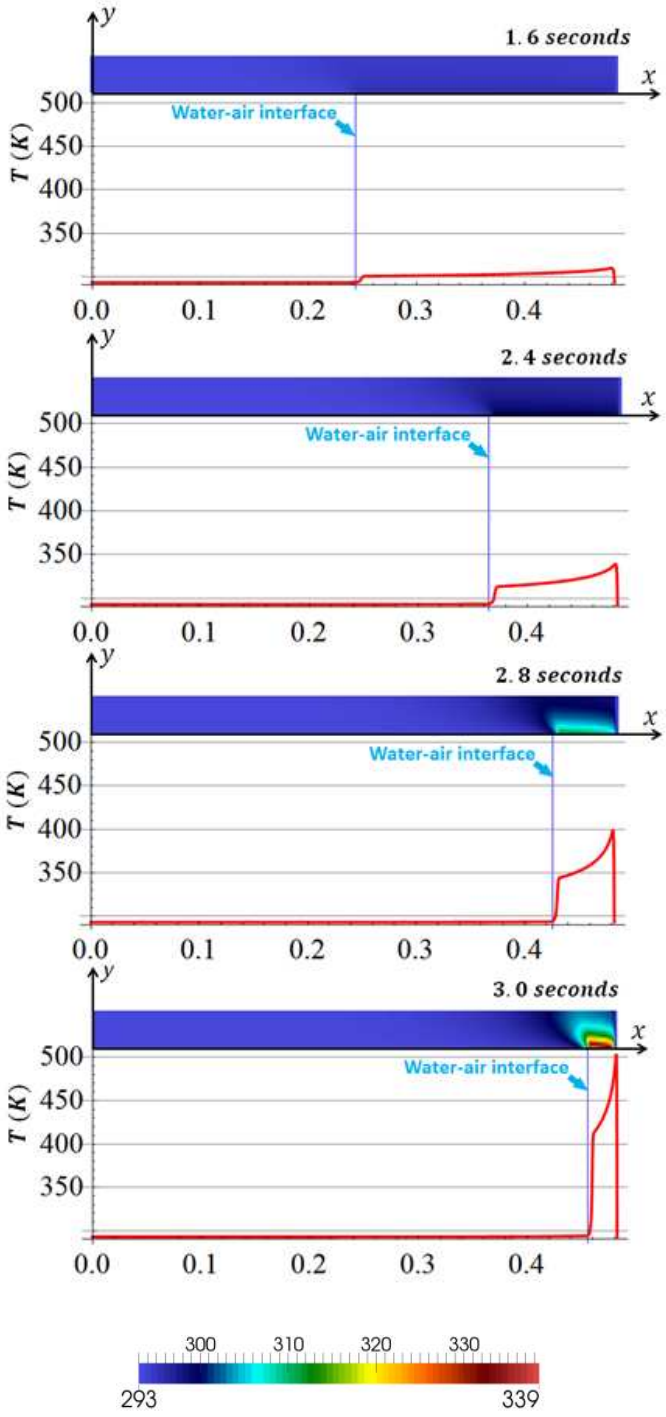

Fig.5.30 Temperature, PL-I-P-3_2.5_0.4 (Curve represents fluid and contour plot is for solid; the y axis is scaled up 80 times)

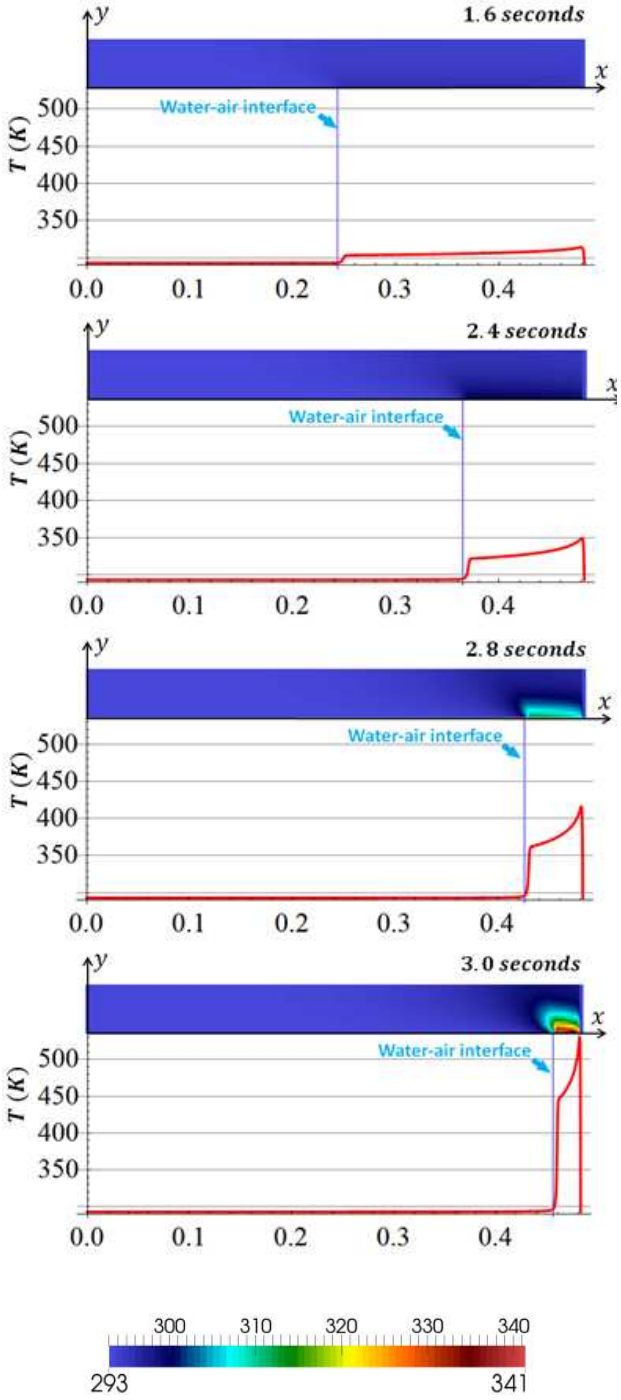

Fig.5.31 Temperature, PL-I-P-7.5_2.75_0.55 (Curve represents fluid and contour plot is for solid; the y axis is scaled up 80 times)

The bulk air temperature, or the mass-averaged air temperature, at the final compression state, is computed for each simulation case. As shown in Fig.5.32, using small exchanger features (small length scales) for the exchanger plate elements is beneficial for improving heat transfer. However, the Honeycomb1_4 matrix is an exception. Its plates are thin, yet the duct size is too large for such thin plates to have a strong heat transfer capability. The Honeycomb1_8, on the other hand, has a smaller duct size and thinner plates and, thus, has very good heat transfer capability. We can also see that, in general, metal (stainless steel) performs better than ABS plastic in the interrupted-plate exchangers, but the effect of the exchanger shape cannot be overlooked, as the plastic-made PL-I-P-3_2.5_0.4 matrix performs almost as well as the stainless-steel-made Metal-I-P-7.5_2.75_0.55 matrix. Finally, we give the porosity and specific surface area values for these matrices to relate to their heat transfer performances. The porosity and specific area values are respectively, 95.7% and 629.9/m for Honeycomb1_4, 93.6% and 1259.8/m for Honeycomb1_8, 86.2% and 768.9/m for Metal/PL-I-P3_2.5_0.4, and 83.3% and 643.1/m for Metal/PL- I-P-7.5_2.75_0.55. One can immediately see that the low temperature rise with the Honeycomb1_8 matrix is also attributable to its very large specific surface area as a result of fine plate features, while the high air temperature rise with the Honeycomb1_4 matrix is attributable to its high porosity and long fluid-to-solid transfer length.

The compression efficiencies with different exchanger matrices are computed and shown in Fig.5.33. Exchangers with lower air temperature rises generally have higher efficiency, because a lower temperature rise requires less compression work and has less thermal energy loss during the storage period. The overall difference in efficiency among the simulated exchangers is less than 4%. The storage power density values are also calculated based on the simulation results, given in Fig.5.34. The storage power density is defined as the storage energy per second of compression time, per unit mass of air. In general, the calculated power density value show promising prospects.

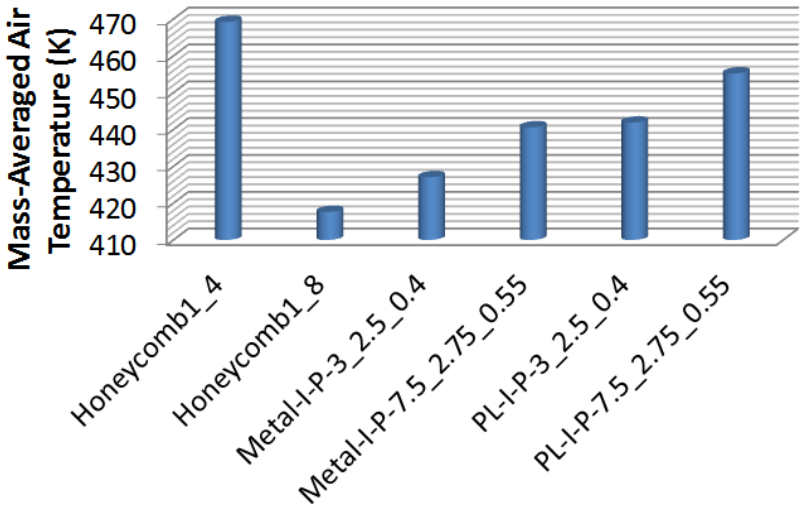

Fig.5.32 Comparison of bulk air temperatures at the final compression state among different exchanger matrices

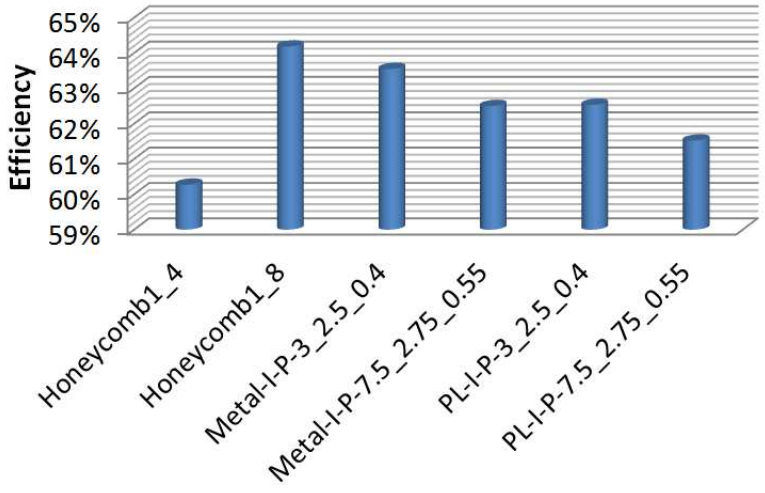

Fig.5.33 Comparison of compression efficiencies among different exchanger matrices

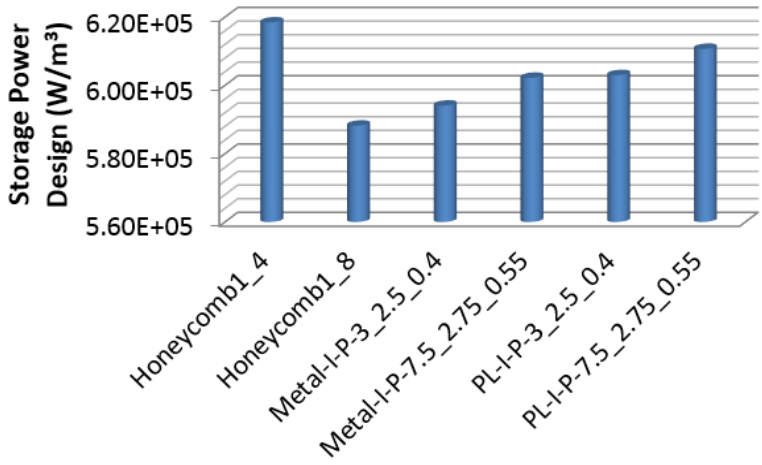

Fig.5.34 Comparison of storage power densities among different exchanger matrices

5.5. Summary

In this chapter, a 1-D model for liquid piston compression is developed. The 1-D model gives fast and accurate calculations of the axial temperature distributions in both the solid and fluids and is applied in thermal design problems to design the distribution of the heat exchanger shape. The design analysis shows that, in general, fine shape features are preferred in the upper region of the compression chamber, while coarser features are preferred in the lower region of the compression chamber. The 1-D model is then expanded to include a sub-2-D model which, in addition to calculating the axial solid temperature distribution, calculates the lateral temperature distribution across a representative exchanger plate element.

Chapter 6: Global Scale 3-D Simulations of Liquid Piston Compression with Interrupted-Plate Matrices

In this chapter, 3-D CFD simulations are done to simulate compression processes in a liquid piston chamber with and without insertion of the interrupted plate exchanger matrices. Several different interrupted plate matrices are simulated and compared. The 3-D simulations provide detailed results for understanding of the physics of the compression process and for quantifying the performance of different interrupted plate matrix designs with application to liquid piston compression. The simulations are also compared with experiments.

6.1. Numerical Procedure

Studied is a compression process for high-pressure compression (same conditions as discussed in section 2.2). Compression starts with air at 7bar and ends when it is compressed to 210 bar. The chamber has a length of 0.4826m and a radius of 0.0381m. The compression speed is 0.15m/s. The compression time is around 3s; slight variations in the total compression times exist among different simulation cases due to different heat transfer conditions leading to different rates in the pressure rise.

In the CFD simulation, the chamber with the exchanger insert is modeled as a continuum region. No internal walls of the porous media are created in the computational mesh, but their hydrothermal effects are modeled using closure terms in the transport equations. This method is always used in modeling porous media flow, as discussed in Chapter 1. The modeling approach, including the governing equations, are outlined in section 1.3. The same approach has already been applied in section 3.2 for 2-D simulations of liquid piston chambers with metal foam inserts. In this chapter, 3-D simulations are done; the closure models for the flow resistance (pressure drop) and heat transfer that were developed in Chapter 4 are applied in the global-scale liquid piston simulation.

The computational domain is discretized mainly using quadrilateral cells, with some triangular prisms appearing occasionally near the central region of the domain. The grid

has a total number 2,542,000 cells. The cell divisions numbering 130 are used on the circumference of the cylinder wall. The height of the cells adjacent to the wall is 0.00022m, which is $\frac{1}{173}$ of the cylinder radius. The cell height increases with the location from the wall with a growth rate exponent of 1.05. In the axial direction, there are 400 divisions. The cell length in the axial direction uniformly decreases from the inlet to the top cap, with the top cap cell being $\frac{1}{6}^{\text{th}}$ the length of the bottom cell. A view of the top region of the mesh is shown in Fig.6.1.

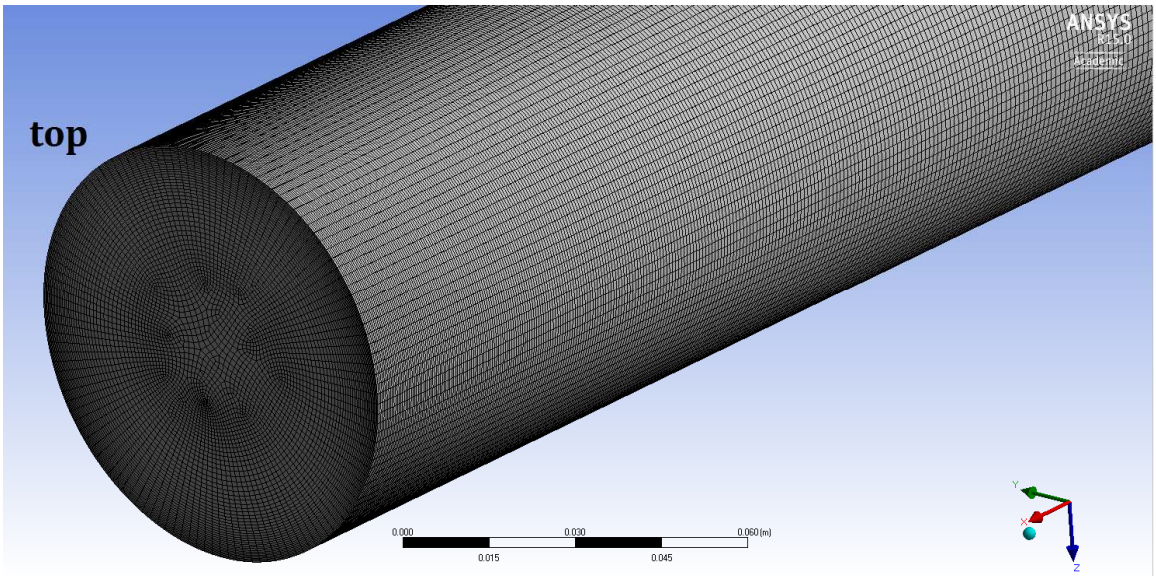

Fig.6.1 Computation mesh for 3-D CFD simulation

Numerical simulations are done using finite-volume-based, commercial CFD solver ANSYS Fluent. For simulations of heat exchanger inserts, a scalar transport function representing the energy transport in the solid matrix is implemented through User-Defined-Function scripts that interface with the VOF model of the solver. The transient formulation is based on a first order implicit scheme. The time step size is 0.00005s. Spatial derivatives are discretized based on a second order upwind scheme. The SIMPLE algorithm is used. The convergence criteria for the residuals the are set to 10^{-9}.

6.2. No-Insert Case

A case is simulated without any exchanger insert in the chamber to give comparisons to cases with exchanger inserts that will be shown later. The simulation is based on a RANS formulation using a Transition SST model [80], which is a four-equation model, solving for a turbulence kinetic energy, turbulence dissipation rate, onset of transition, and a momentum boundary layer thickness Reynolds number. It that takes into account transition from laminar to turbulent regimes. The model is available in the commercial software ANSYS Fluent. The maximum y+ value for the first layer of cells next to the wall is 16 in this simulation.

The air regions at different times during compression are shown in Fig.6.2 to Fig.6.7. Plotted are the instantaneous water-air interface (shown by the cross-sectional disk), the streamlines and the fluid temperature distribution (shown on the horizontal plane). The air in the chamber experiences a high temperature rise during compression, especially in the later part. Air very near the water-air interface is cooled. Although there is heat transfer from air to water, as shown by the axial temperature gradient in the air above the interface, water maintains almost a constant temperature, since it has a large thermal capacity. There is no generation of water vapor. The air temperature rise is most rapid near the very end of compression (from 2.5s to 2.95s), as the constant-speed compression results in a high volume ratio change near the end of compression. Also shown by the simulation is a big vortex ring forming in the chamber. During compression, most of the air in the core region of the chamber flows from bottom to top with a gradually decreasing speed as it approaches the top cap. Very near the top cap, part of the air flow stagnates, and the rest follows a recirculation pattern that runs from the top to the bottom in a layer between the wall and the core flow. This secondary flow phenomenon is most significant near the later period of compression as the air space becomes short and wide.

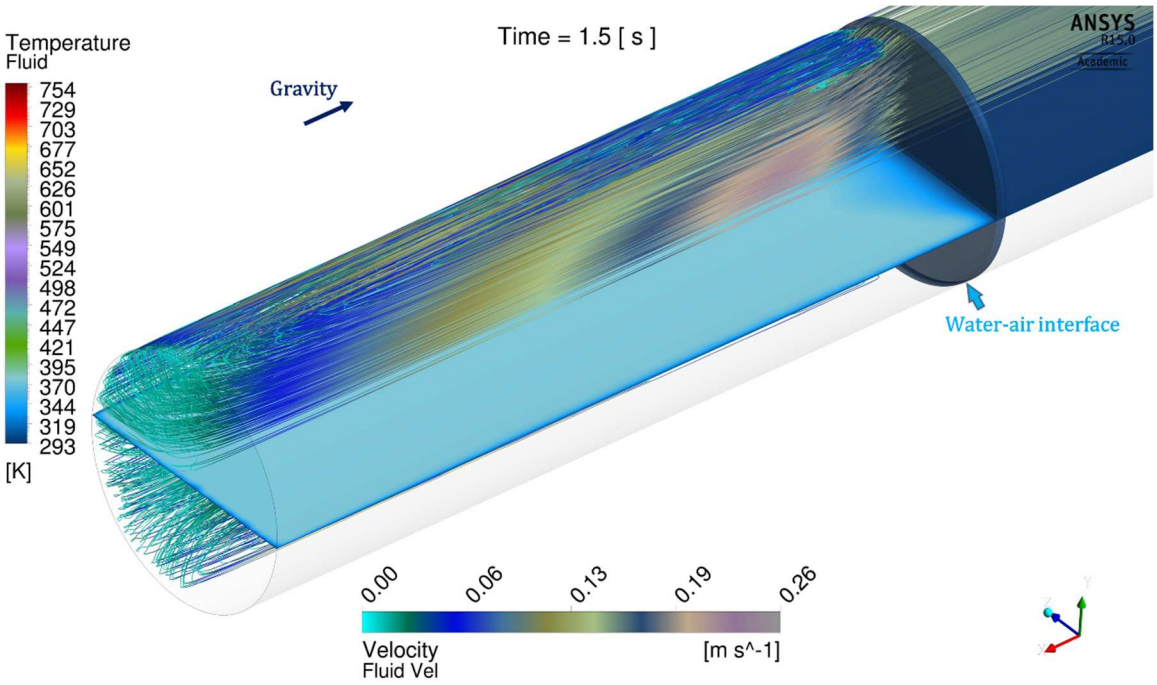

Fig.6.2 Fluid temperature and streamlines of no-insert case, t=1.5s

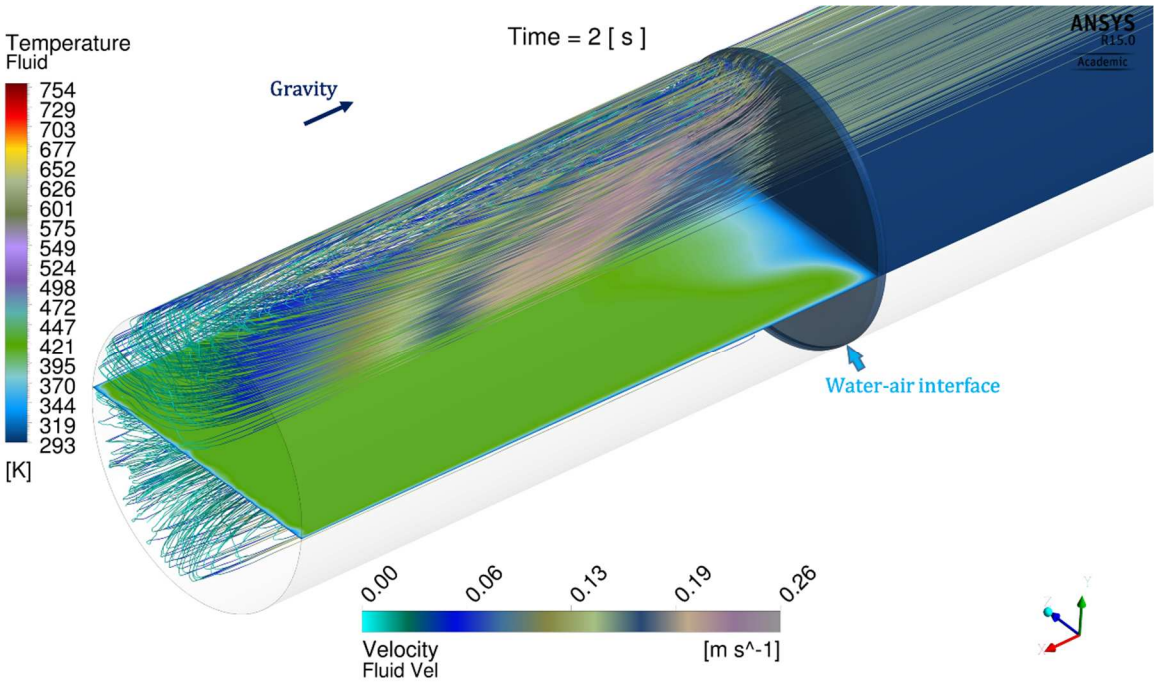

Fig.6.3 Fluid temperature and streamlines of no-insert case, t=2s

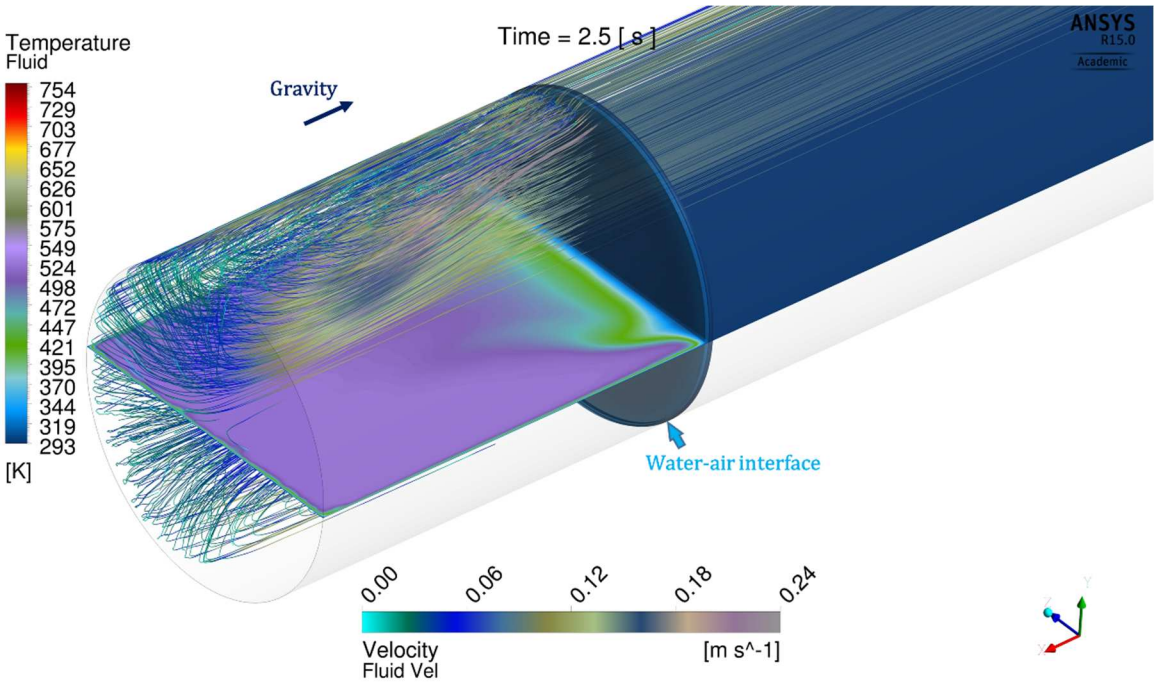

Fig.6.4 Fluid temperature and streamlines of no-insert case, t=2.5s

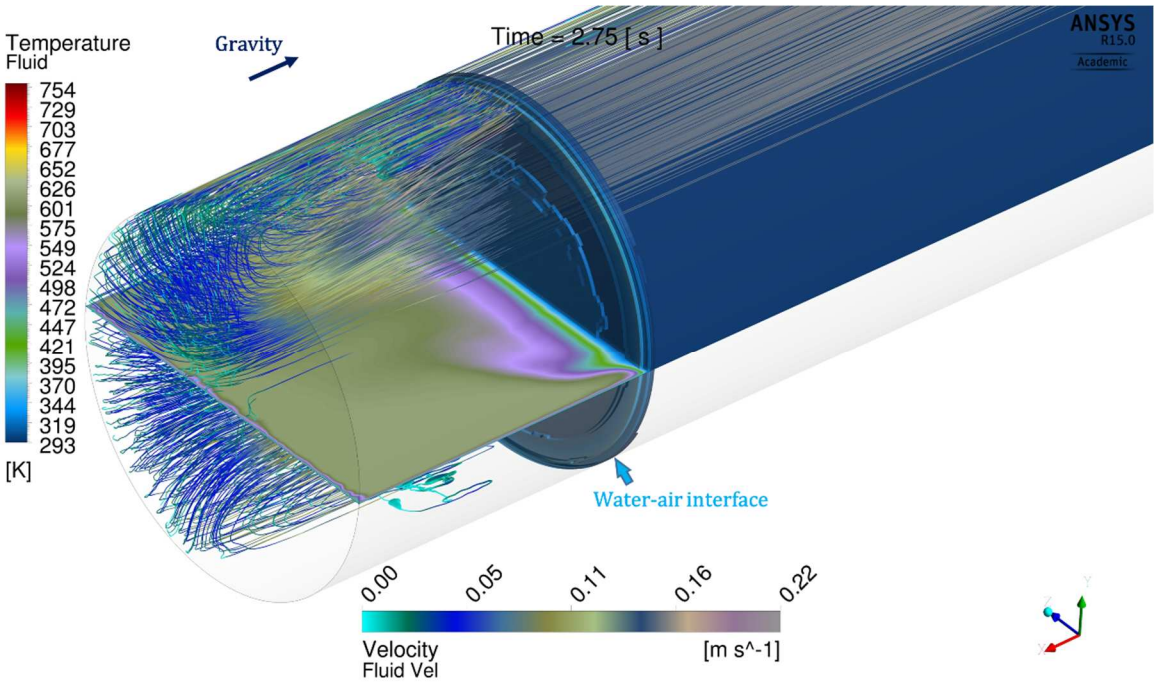

Fig.6.5 Fluid temperature and streamlines of no-insert case, t=2.75s

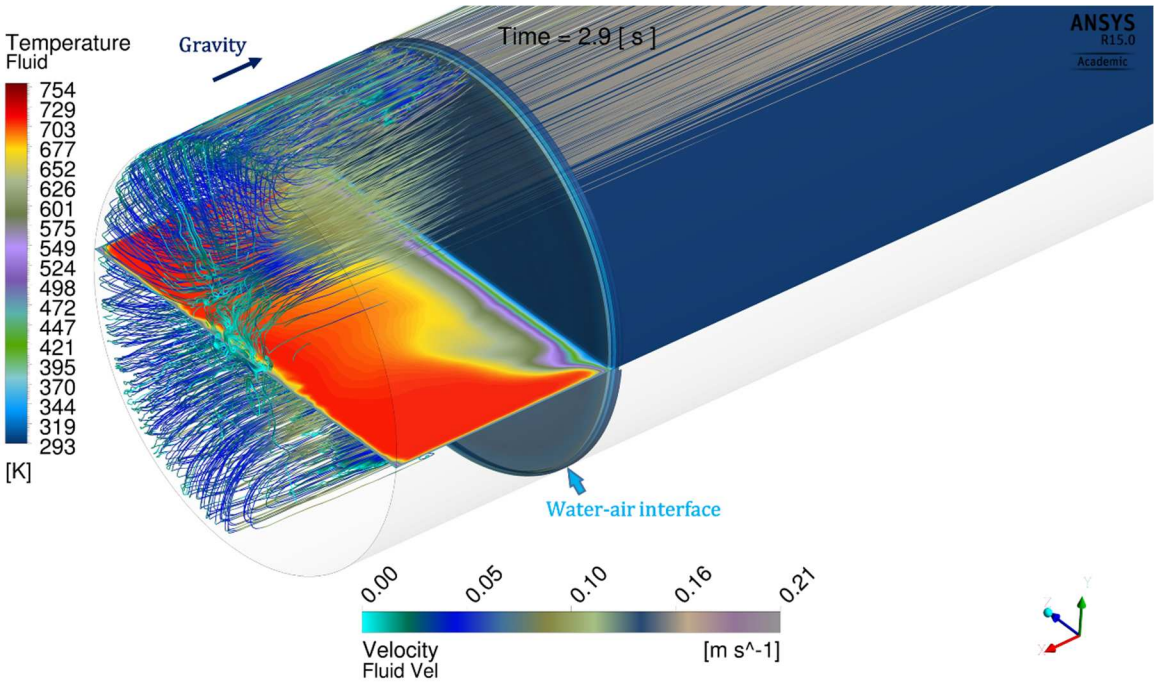

Fig.6.6 Fluid temperature and streamlines of no-insert case, t=2.9s

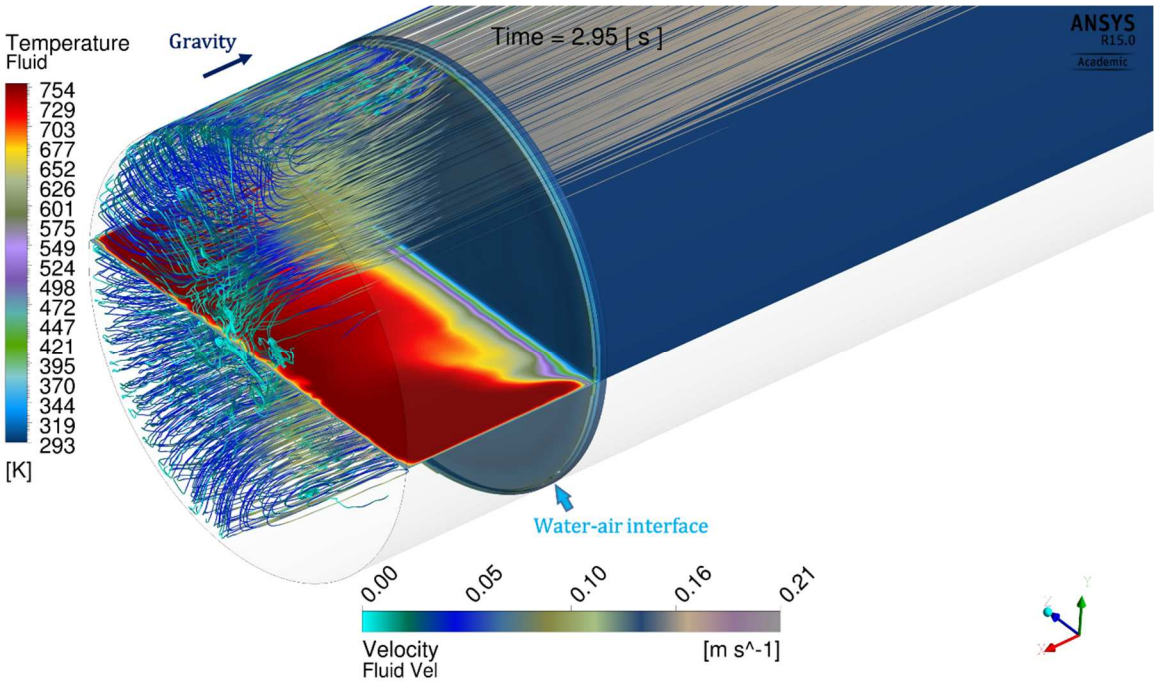

Fig.6.7 Fluid temperature and streamlines of no-insert case, t=2.95s

6.3. Plastic Interrupted Plate with Uniform Shape Distribution

In this section, liquid piston compression in a chamber with an interrupted plate heat exchanger matrix is simulated. The interrupted plate matrix has the following plate height, separation distance, and plate thickness: $\ell = 7.5mm$, $2b = 2.75mm$, $t = 0.55mm$ (refer to Fig.4.1 for schematics of the parameters). The compression chamber occupied by the matrix is modeled as a continuum region, employing the anisotropic pressure drop and heat transfer models developed in section 4.2. They are implemented in the commercial CFD solver through User-Defined-Function scripts. The simulated heat exchanger matrix has a material property of plastic with the following thermal properties: $k_s = 0.17W/(mK)$, $c_s = 1200J/(kgK)$, $\rho = 1060kg/m^3$ (from Table 5.1).

The fluid temperature distributions and streamlines are shown in Fig.6.8 to Fig.6.13. The streamlines in the air are straightened, which is a major difference from the previous no-insert case where a vortex ring feature was observed. It shows that the porous matrix has a flow resistance effect that eliminates opportunities for forming large-scale secondary flows. Due to the use of the exchanger matrix, the overall air temperature rise is much smaller compared to the previous case where there was no matrix insert. At the end of compression, peak air temperature values of 549K are observed only in a few locations very near the top cap; the peak temperature is also 200K lower than that of the previous case where no matrix was used. The average air temperature at the end is 459.7K, which is 244K lower than the no-insert case. Near the end of compression (after 2.9s), a more uniform gradient in the temperature distribution along the chamber axis is observed in the air. Starting from the water-air interface the air temperature is low and it rapidly increases as the interface moves towards the top cap. The reason is that the heat transfer from the air to the solid matrix is dependent upon Reynolds number, and the local Reynolds number of air decreases towards the top cap along the axial direction. Thus, the peak temperature is observed near the top cap due to flow stagnation. The air temperature distribution can be changed, if a different exchanger, with an optimum design were used. This will be shown in further discussions in this chapter.

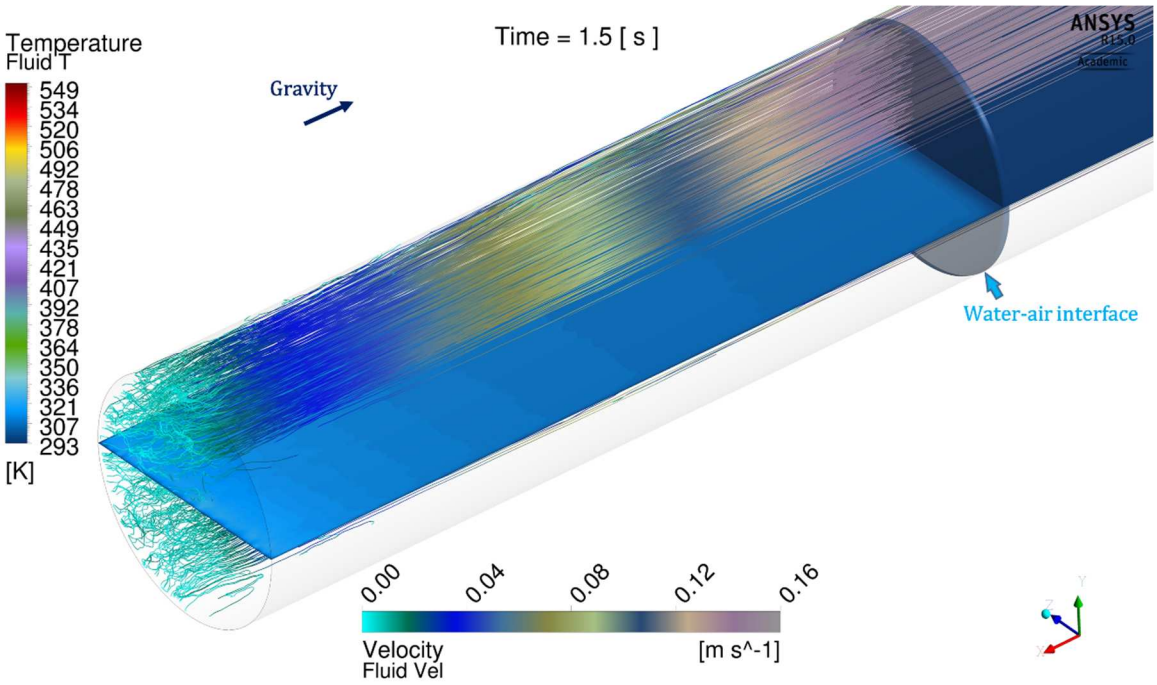

Fig.6.8 Fluid temperature and streamlines of uniform plastic matrix, t=1.5s

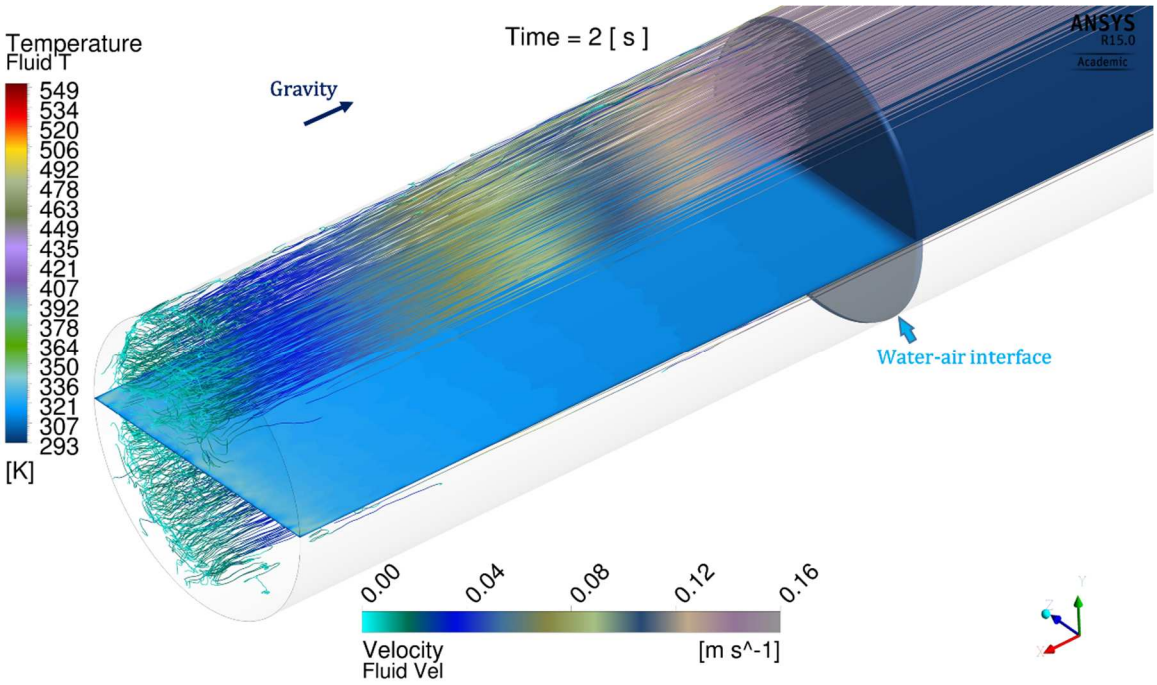

Fig.6.9 Fluid temperature and streamlines of uniform plastic matrix, t=2s

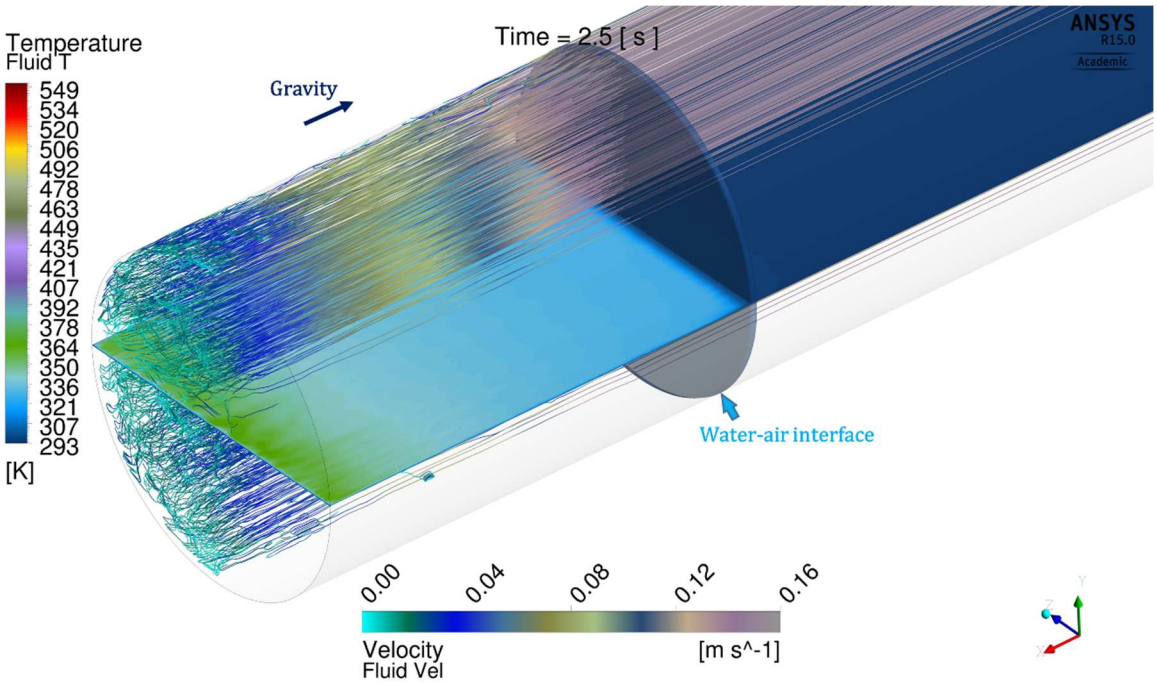

Fig.6.10 Fluid temperature and streamlines of uniform plastic matrix, t=2.5s

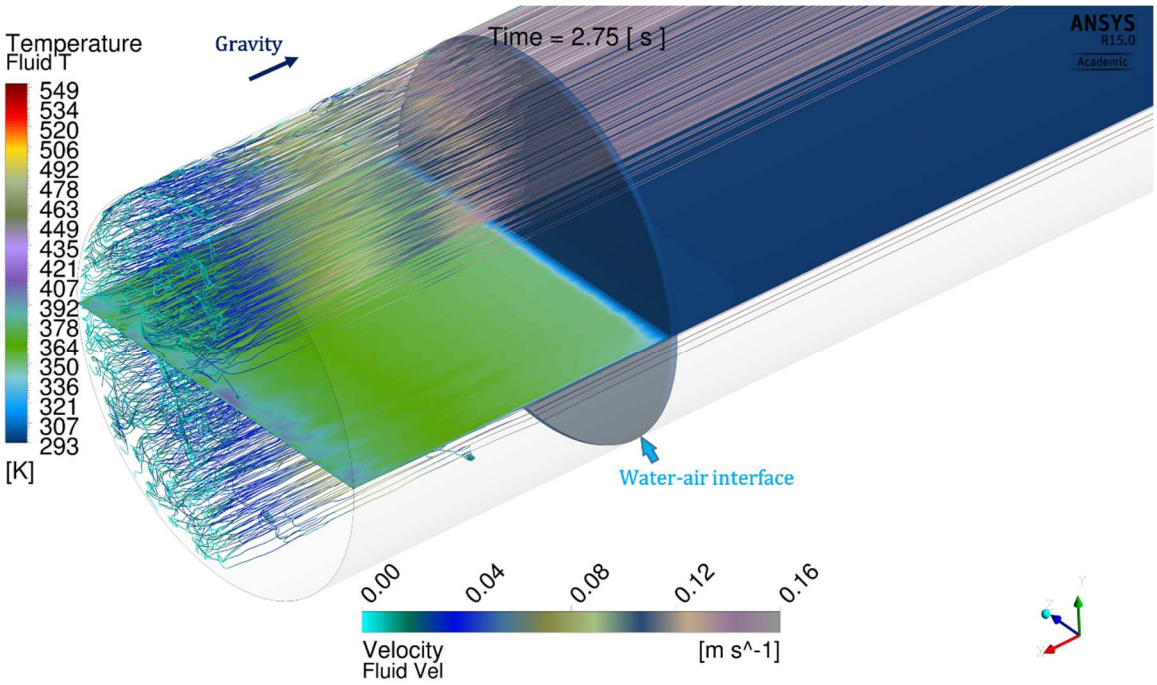

Fig.6.11 Fluid temperature and streamlines of uniform plastic matrix, t=2.75s

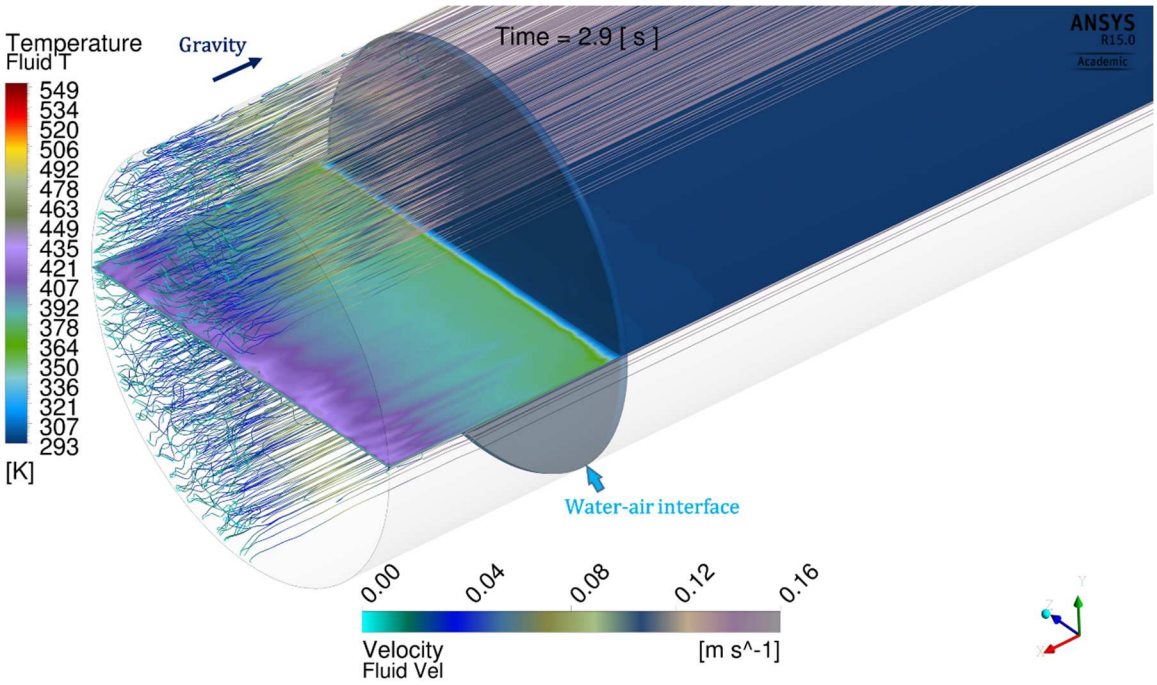

Fig.6.12 Fluid temperature and streamlines of uniform plastic matrix, t=2.9s

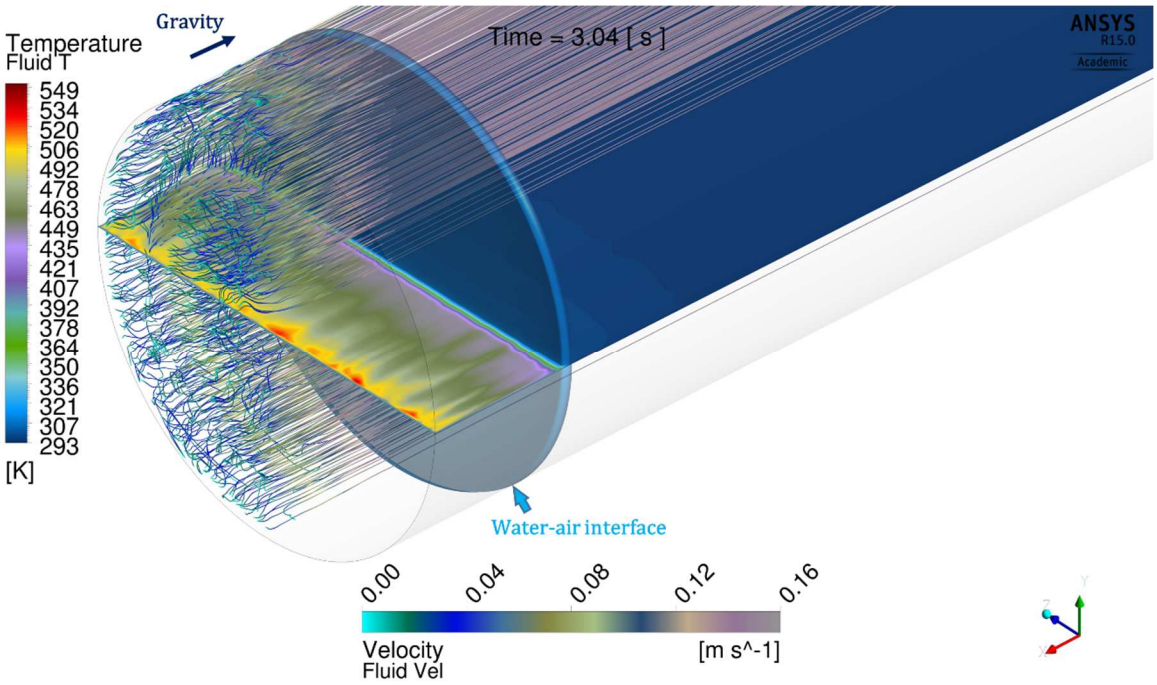

Fig.6.13 Fluid temperature and streamlines of uniform plastic matrix, t=3.04s

The temperature distributions in the solid matrix are shown by the horizontal planes in Fig.6.14 to Fig.6.19. The most rapid temperature rise in the solid matrix is observed also near the very end of the compression. After about 2.5s, the peak temperature in the solid is observed in a location above the water-air interface. This is because the air in this region is most active and transfers a large amount of heat to the solid. As water rises, the solid matrix is submerged and cooled by water. As shown in the plots, the region of the solid submerged in water has a temperature decrease in the axial direction as one moves from the interface towards the bottom of the chamber.

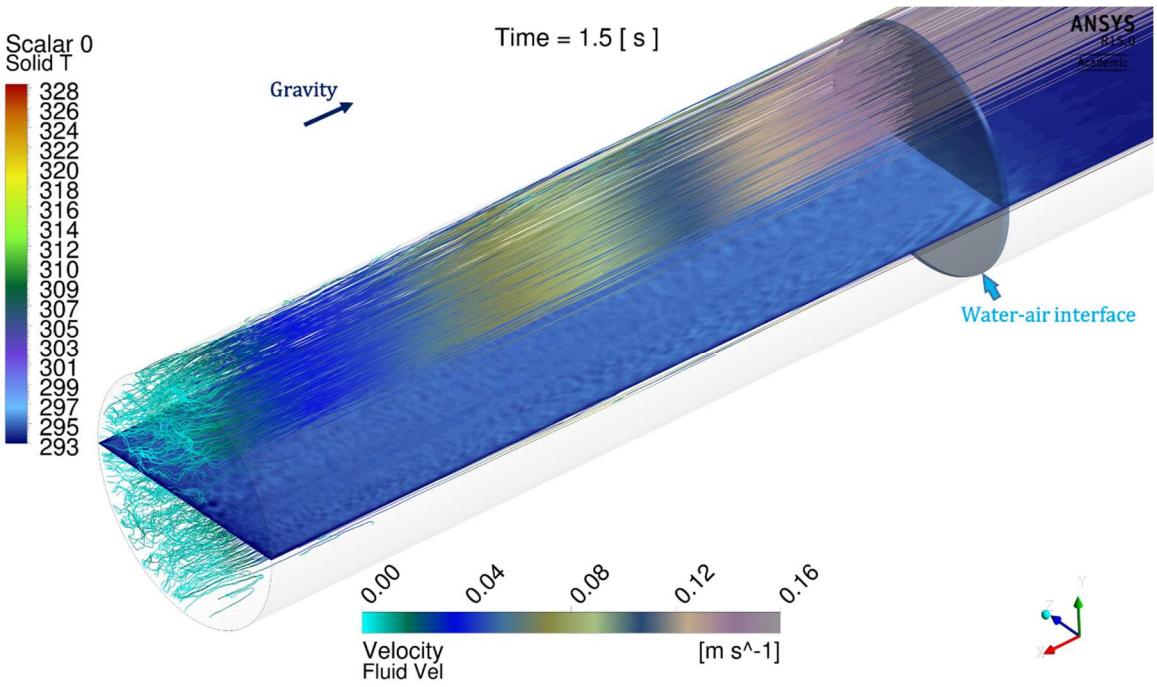

Fig.6.14 Solid temperature and streamlines of uniform plastic matrix, t=1.5s

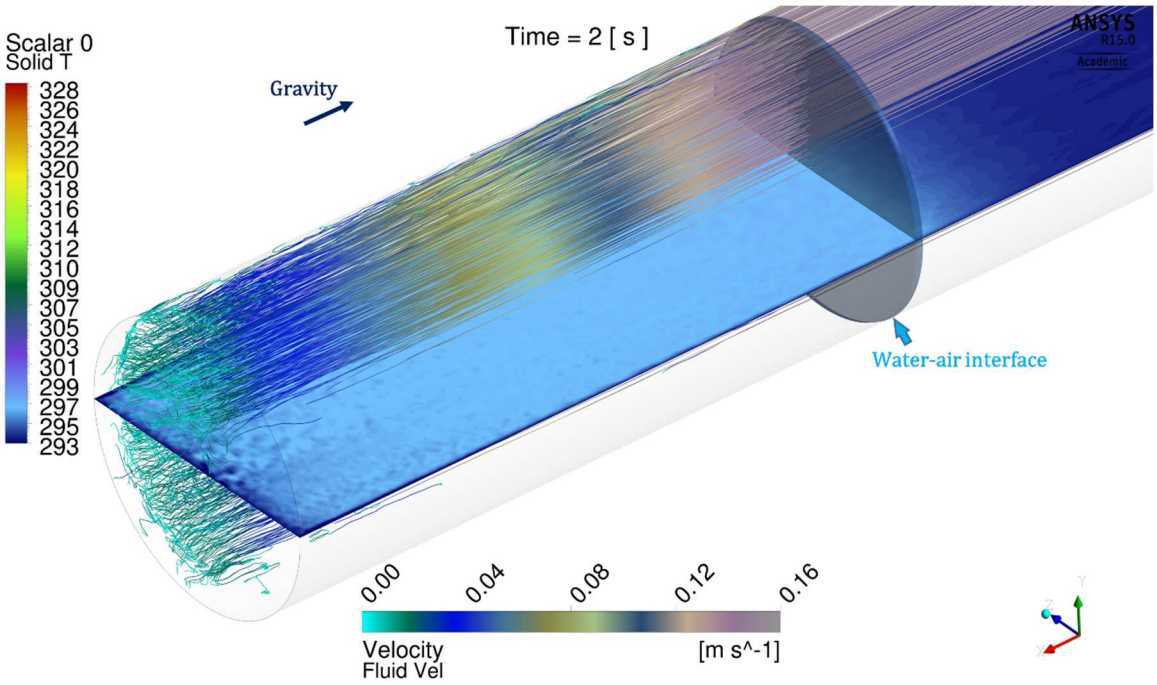

Fig.6.15 Solid temperature and streamlines of uniform plastic matrix, t=2s

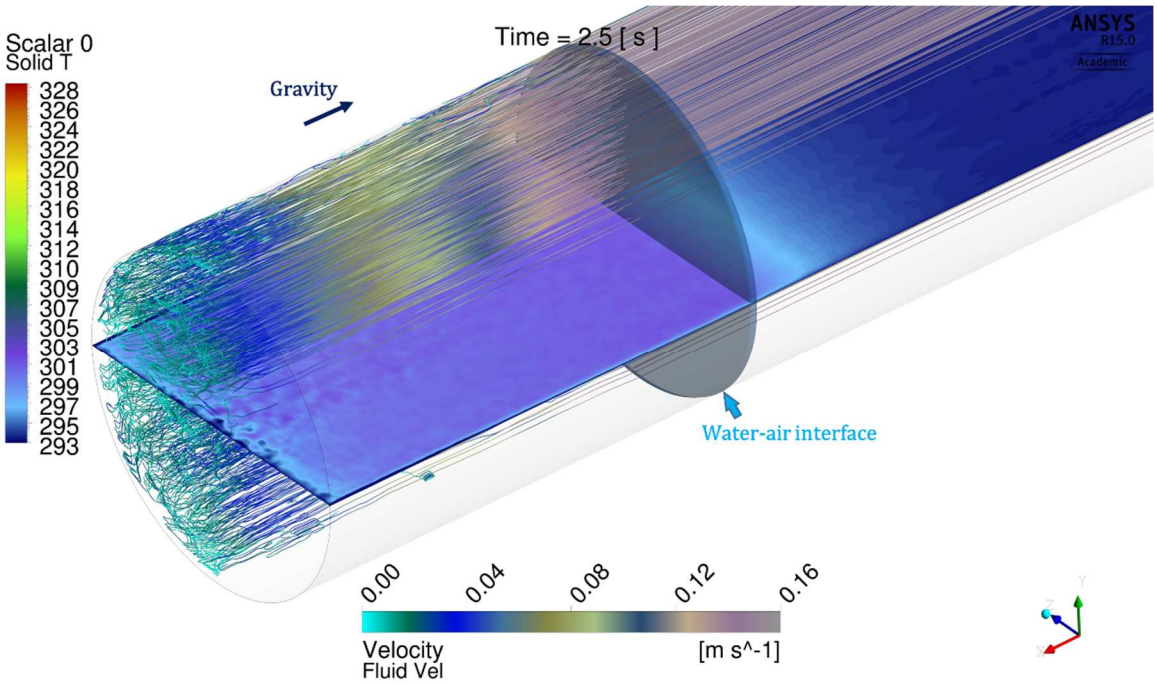

Fig.6.16 Solid temperature and streamlines of uniform plastic matrix, t =2.5s

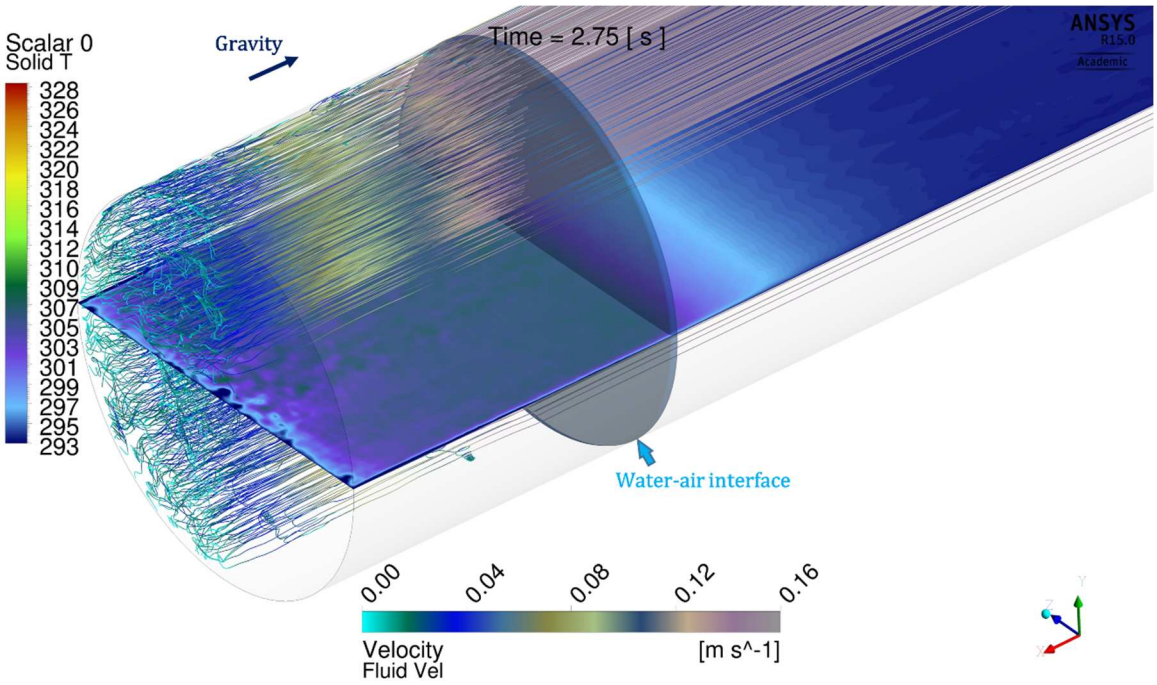

Fig.6.17 Solid temperature and streamlines of uniform plastic matrix, t=2.75s

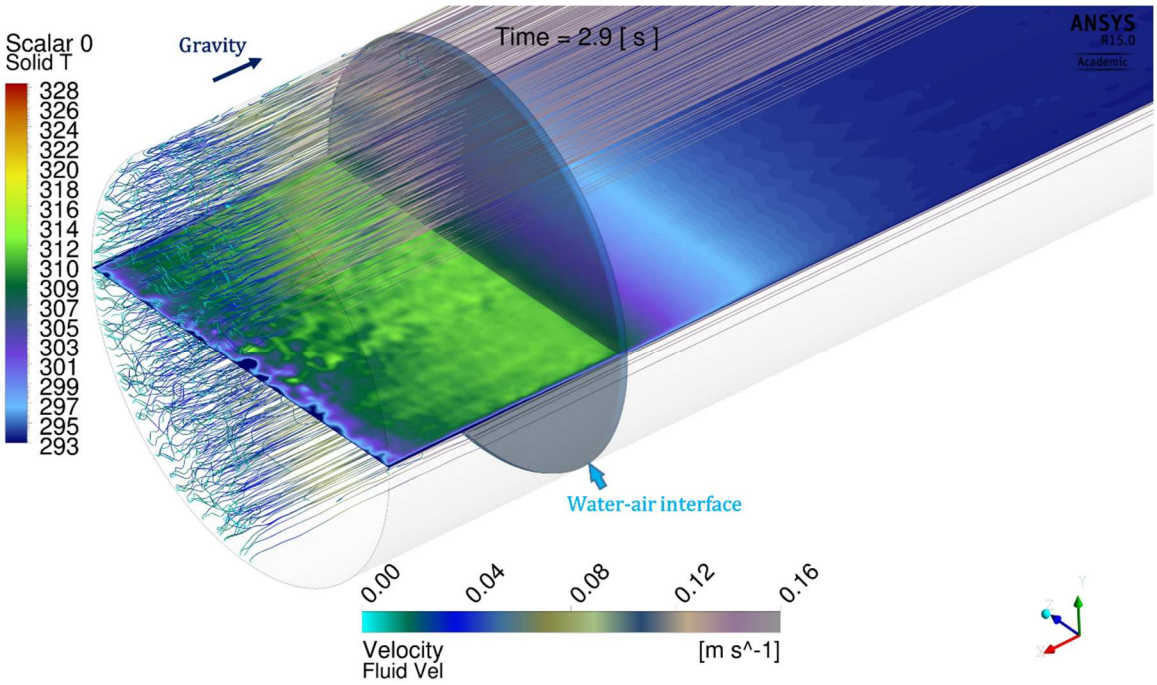

Fig.6.18 Solid temperature and streamlines of uniform plastic matrix, t=2.9s

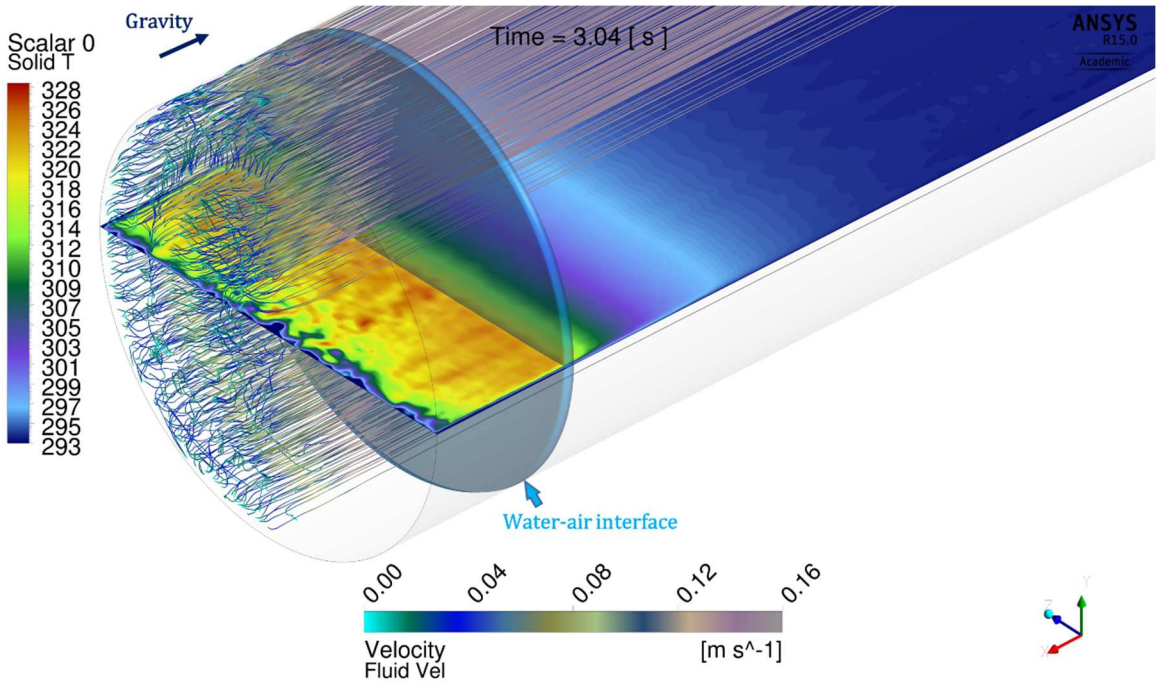

Fig.6.19 Solid temperature and streamlines of uniform plastic matrix, t=3.04s

6.4. Metal Interrupted Plate with Uniform Shape Distribution

In this section the same heat exchanger matrix shape as studied in the previous section is simulated (REV11_1), but with a material of steel. The thermal properties of steel are (from Table 5.1): $k_s = 14W/(mK)$, $c_s = 502J/(kgK)$, $\rho = 7954kg/m^3$. Although the dimensionless heat transfer depends on the flow distribution, which is affected by the shape of the exchanger, the metal exchanger is expected to have an improvement on the performance as a result of high thermal capacity (ρc_s). Simulation of the metal heat exchanger utilizes the same technique and numerical procedure as used in the previous section.

The CFD results of streamlines, fluids temperature, and solid temperature distributions at different times are given in Fig.6.20 to Fig.6.31. The flow streamline features are almost the same as the previous plastic interrupted plate matrix simulation; the streamlines are straitened due to the resistance effect of the matrix, and the air speed

decreases almost linearly in the axial direction moving from the water-air interface towards the top cap. The fluid (water and air) temperature distributions also show similar features to those of the previous plastic matrix. The main difference is that the peak air temperature at the end of compression is 15K lower in the metal matrix case, as metal has a larger thermal capacity than plastic (comparing Fig.6.25 and Fig.6.13). The temperature distributions in the metal exchanger matrix exhibits some differences from those in the plastic matrix. As metal has a higher thermal conductivity than plastic, a longer thermal penetration lengths are observed in the metal matrix in regions below the water-air interface. This is beneficial for transferring the heat from the compressed air through the exchanger matrix to the water.

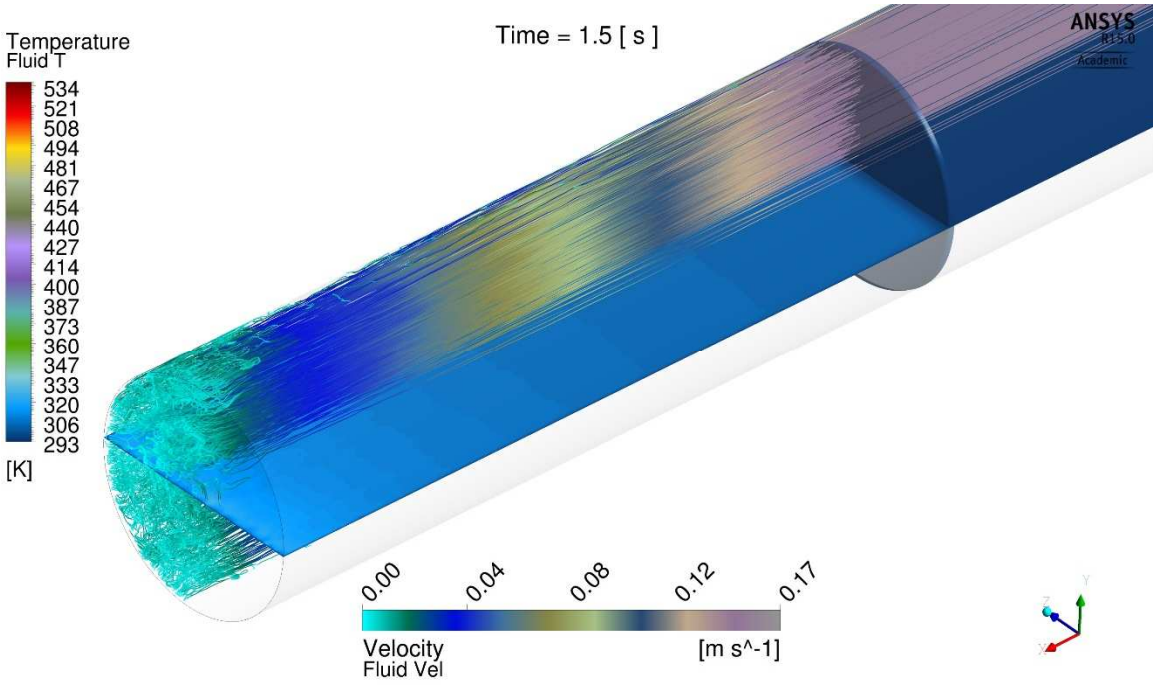

Fig.6.20 Fluid temperature and streamlines of uniform metal matrix, t=1.5s

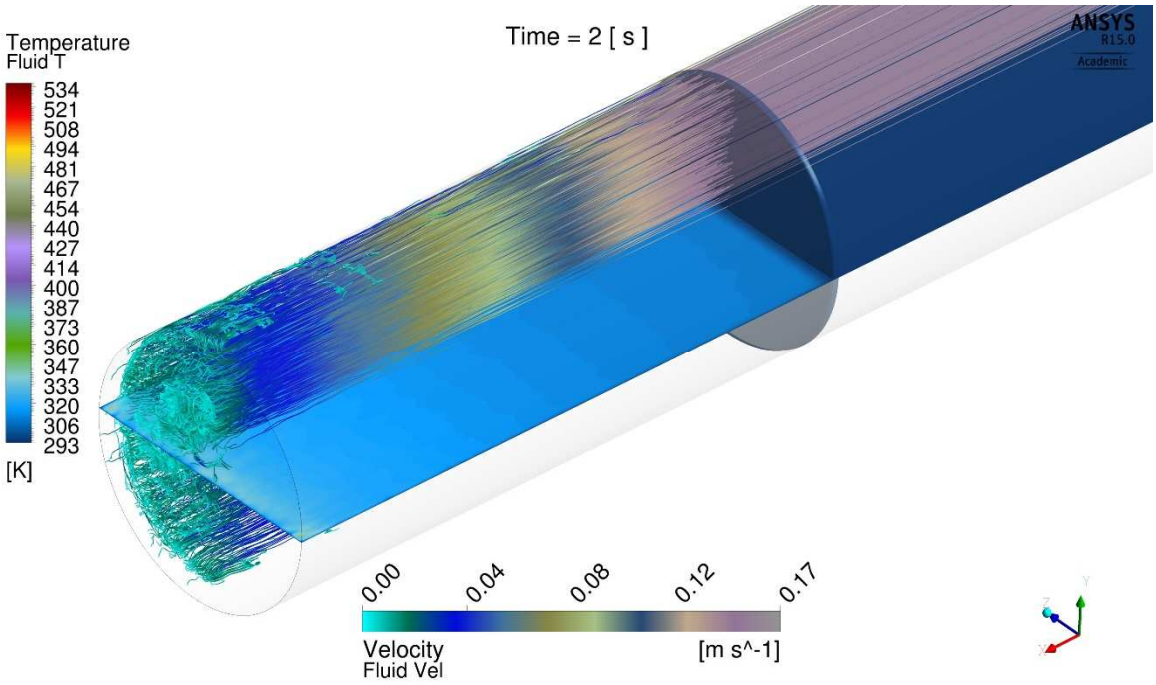

Fig.6.21 Fluid temperature and streamlines of uniform metal matrix, t=2s

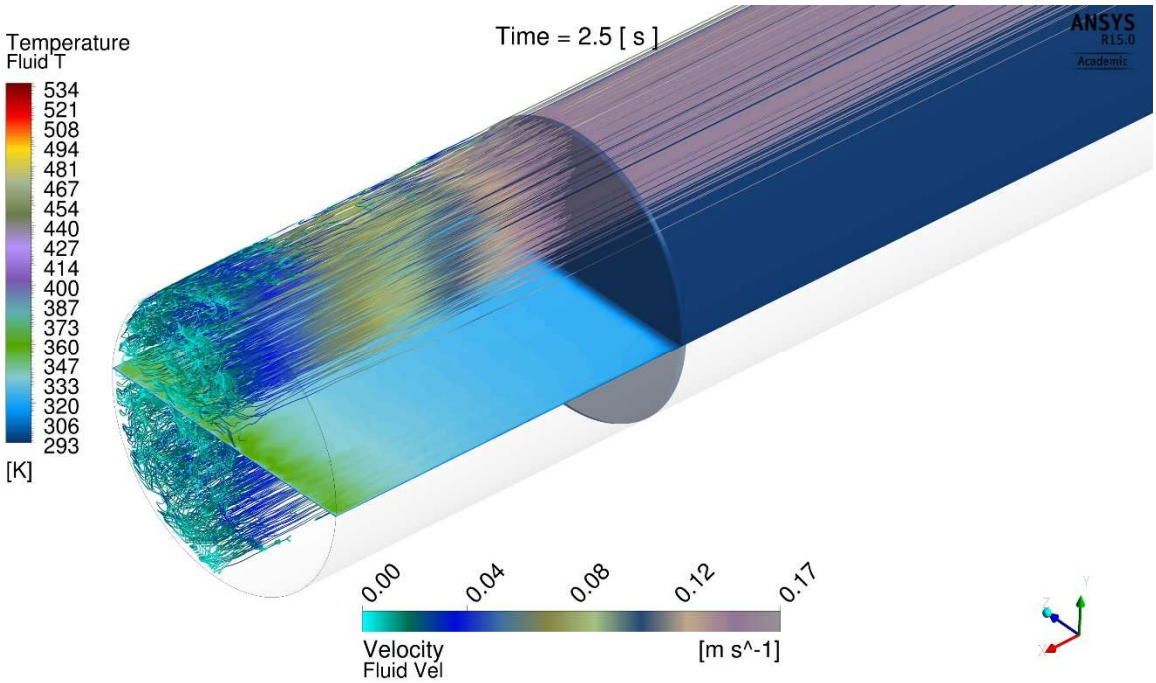

Fig.6.22 Fluid temperature and streamlines of uniform metal matrix, t=2.5s

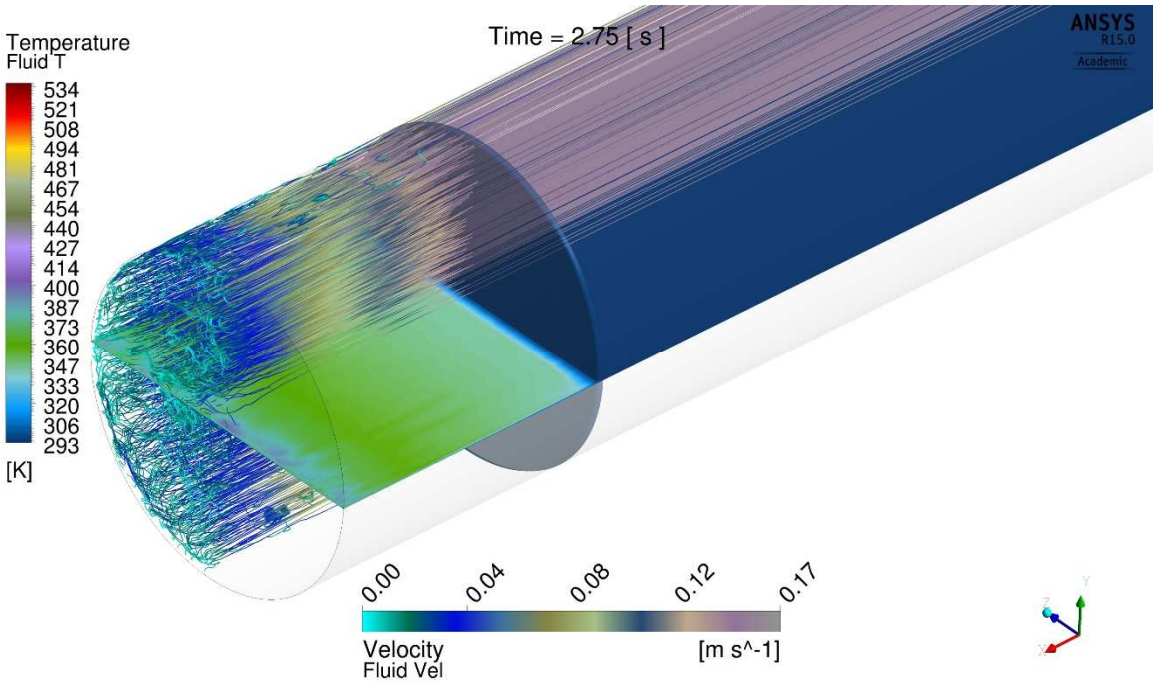

Fig.6.23 Fluid temperature and streamlines of uniform metal matrix, t=2.75s

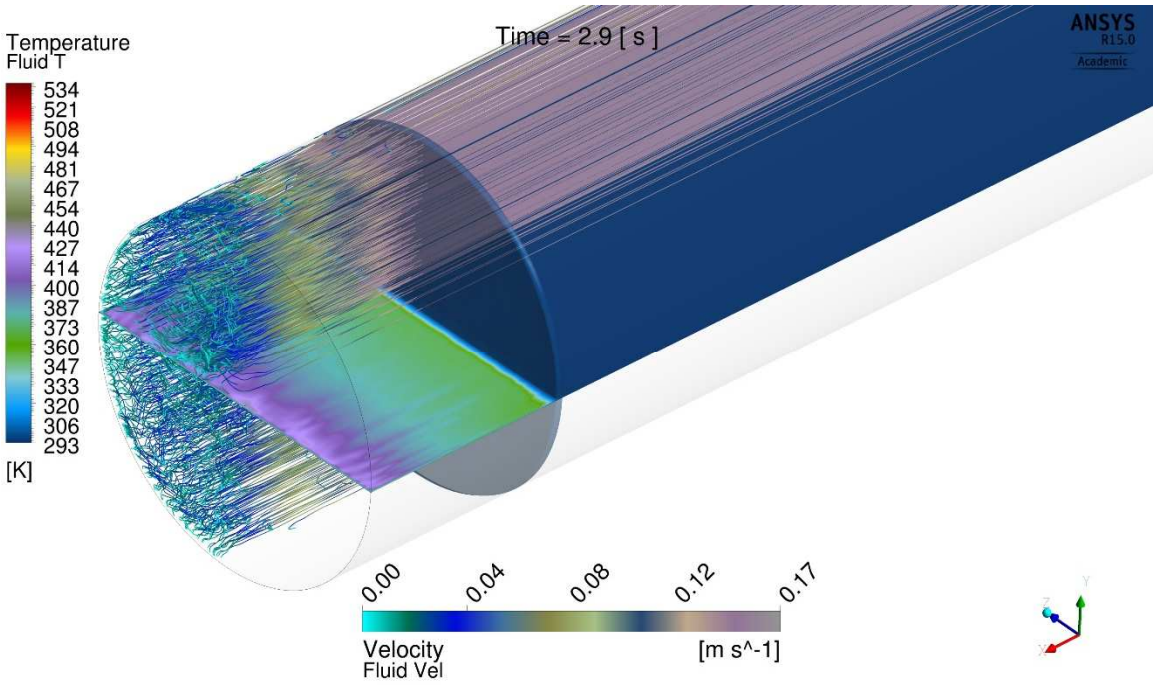

Fig.6.24 Fluid temperature and streamlines of uniform metal matrix, t=2.9s

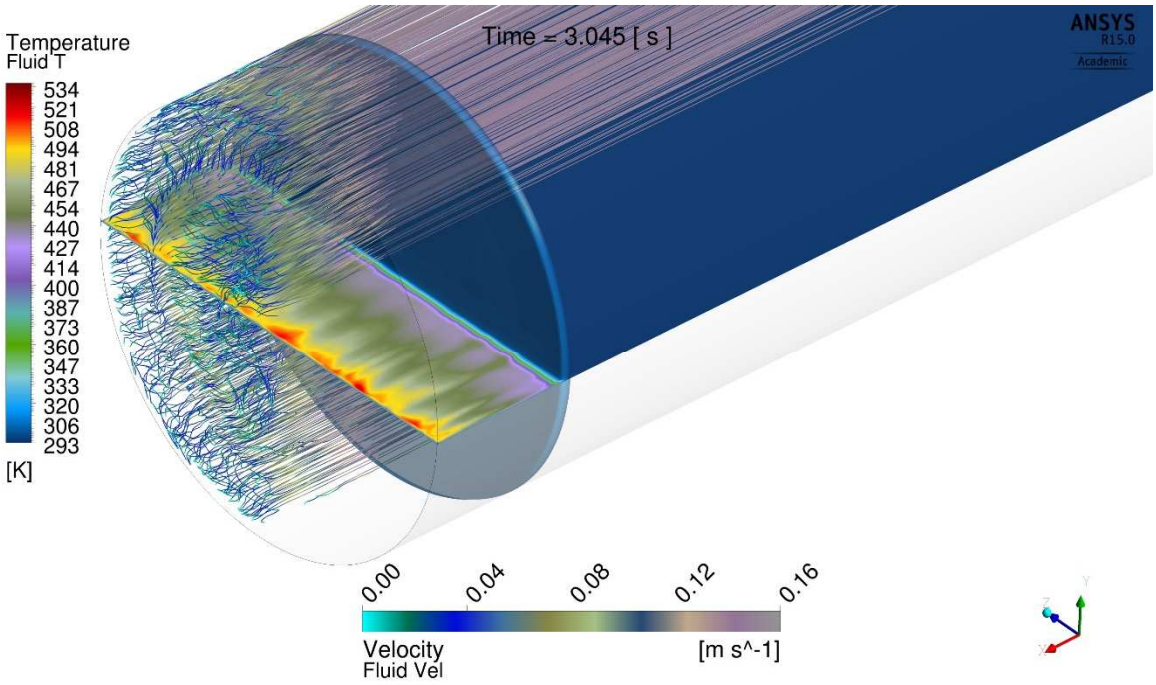

Fig.6.25 Fluid temperature and streamlines of uniform metal matrix, t=3.045s

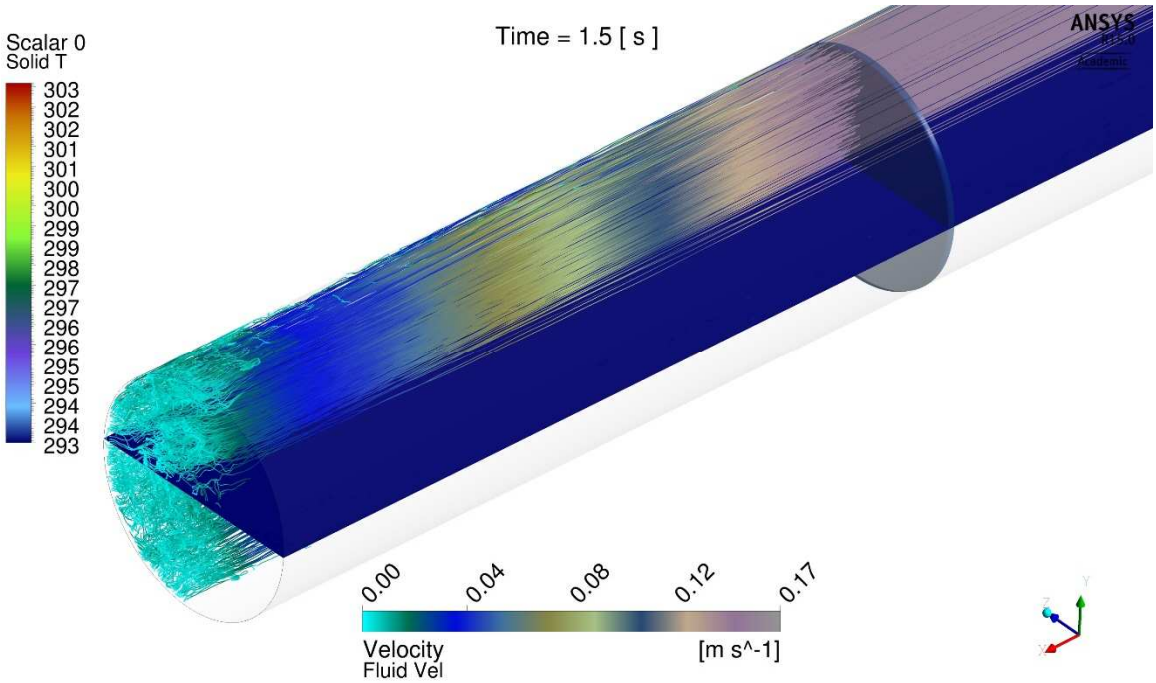

Fig.6.26 Solid temperature and streamlines of uniform metal matrix, t=1.5s

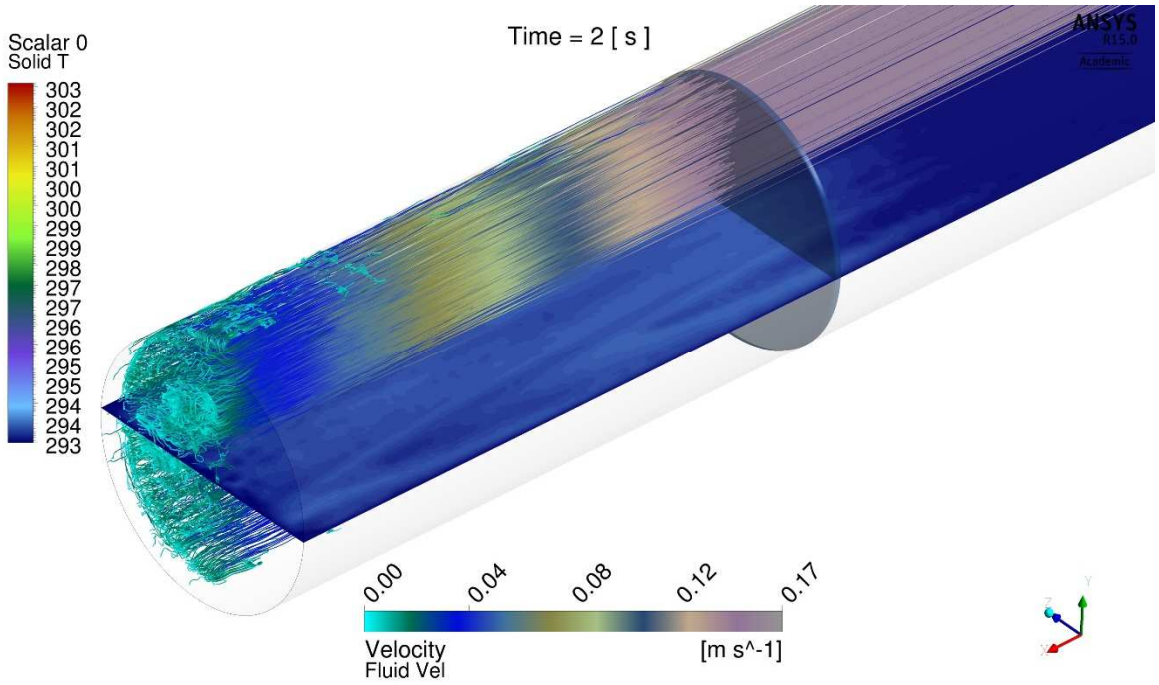

Fig.6.27 Solid temperature and streamlines of uniform metal matrix, t=2s

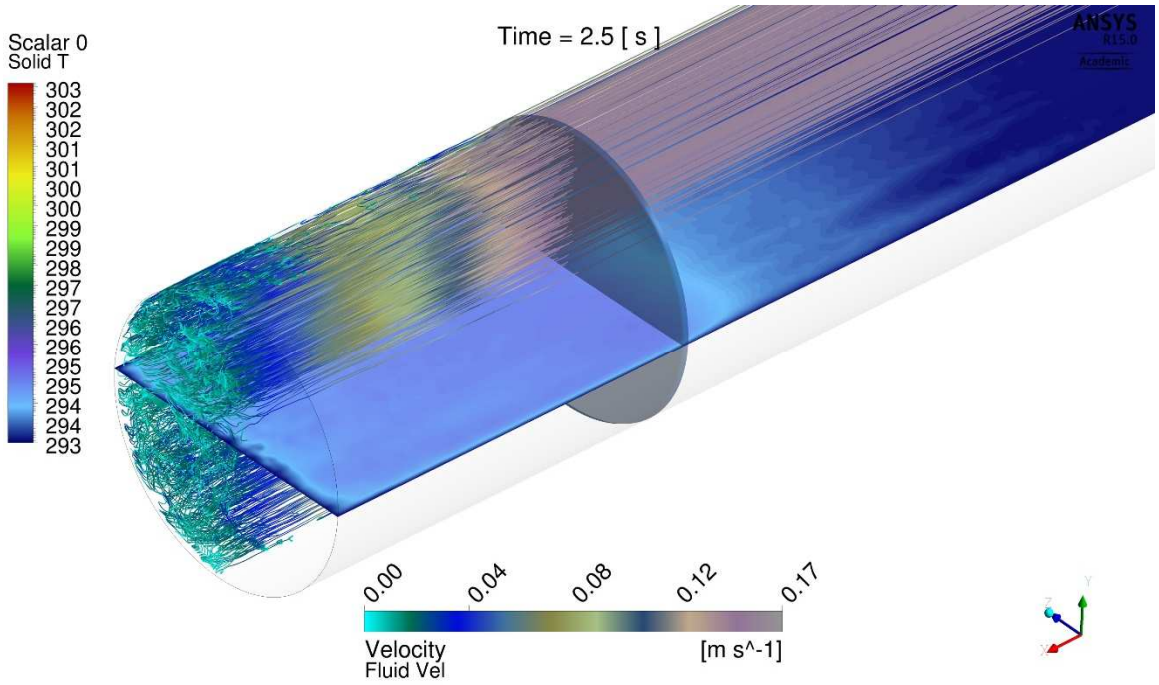

Fig.6.28 Solid temperature and streamlines of uniform metal matrix, t=2.5s

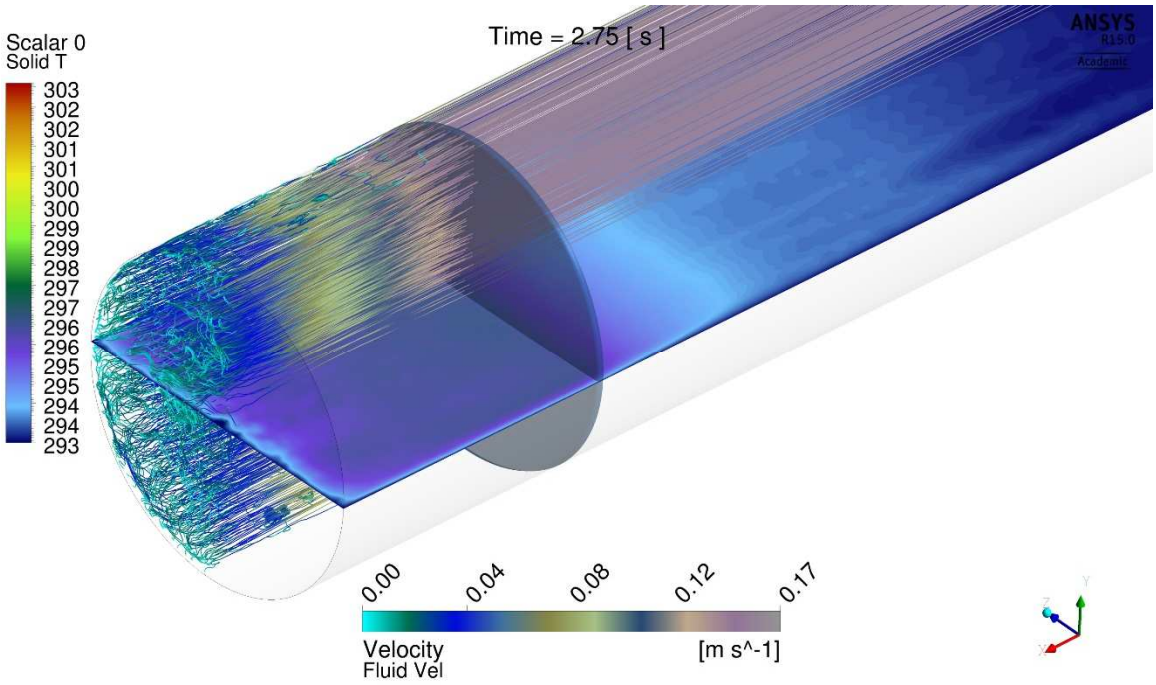

Fig.6.29 Solid temperature and streamlines of uniform metal matrix, t=2.75s

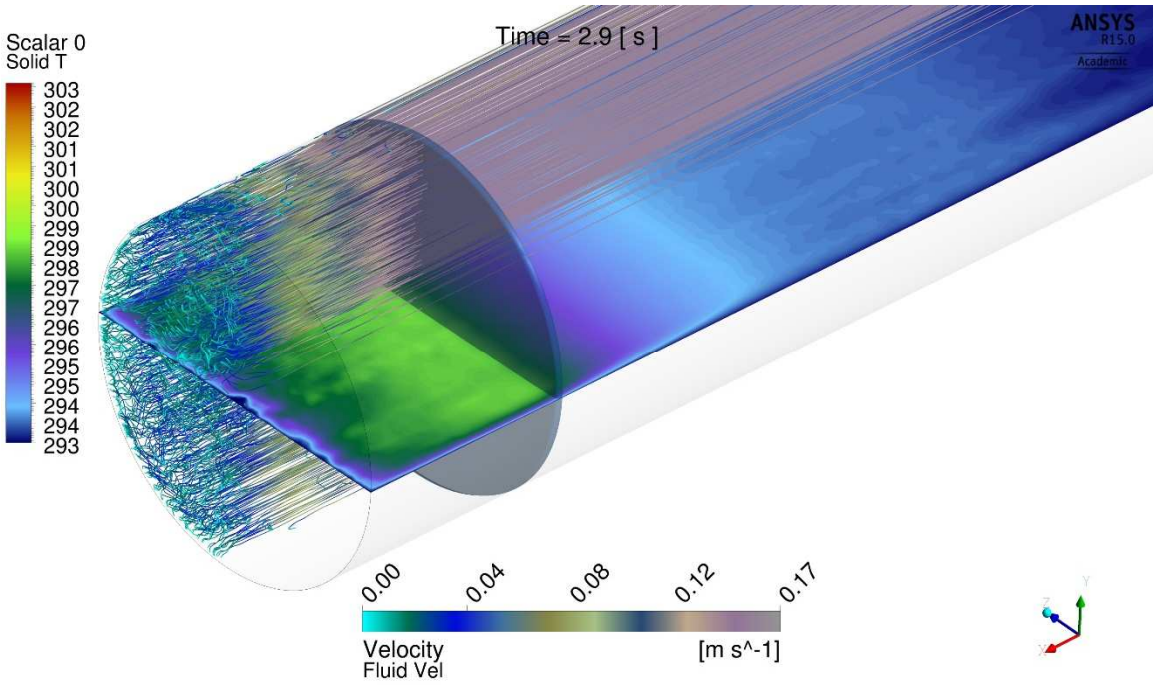

Fig.6.30 Solid temperature and streamlines of uniform metal matrix, t=2.9s

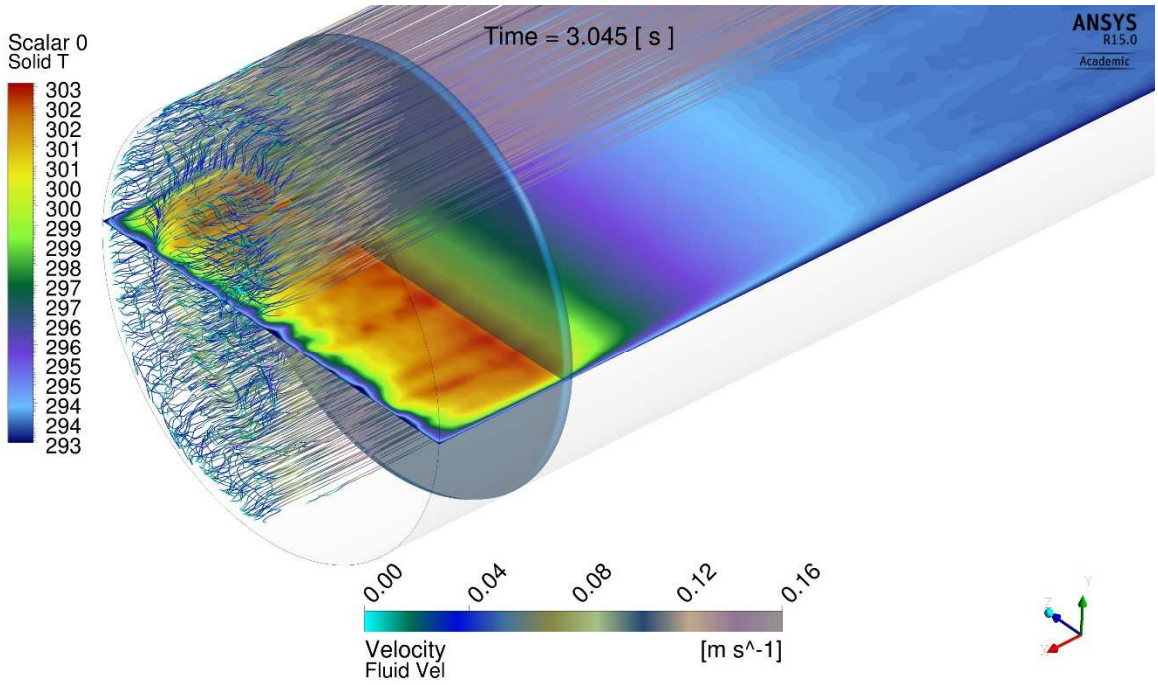

Fig.6.31 Solid temperature and streamlines of uniform metal matrix, t=3.045s

6.5. Plastic Interrupted Plate Matrix with an Optimum Shape Design

An optimum shaped interrupted plate matrix is simulated. The shape of the exchanger matrix varies along the axis of the chamber. It is based on the thermal design analysis in section 5.3.3, with the optimal shape distributison given in Fig.5.23. The simulated exchanger material is plastic.

The transient process of compression are illustrated by Fig.6.32 to Fig.6.43. At the end of compression, the peak air temperature with the optimal exchanger matrix is 502K, which is 47K lower than the uniform plastic matrix, and 32K lower than the uniform metal matrix. The air temperature distribution also appears different from the previous two uniform matrix cases. Because of the optimum shape that allocates matrix with finer features near the top cap to enhance heat transfer, the high temperature gas layer near the top cap is thinner, and the temperature distribution is more uniform in the remainder of the gas region (comparing Fig.6.37 to Fig.6.25 and Fig.6.13).

The transient temperature distribution in the solid matrix is significantly different from those of the uniform exchanger cases. During compression, different portions of the matrix heats at different rates (Fig.6.38). The optimum design fully utilizes the cooling capability of the liquid piston, while balancing the pressure drop and heat transfer of the exchanger matrix. As shown in Fig.6.38, a middle portion of the matrix heats up quickly, but soon is cooled as the water level continues to rise above it. Although made of plastic, the optimum design outperforms the metal matrix of a uniform shape distribution in lowering the gas temperature.

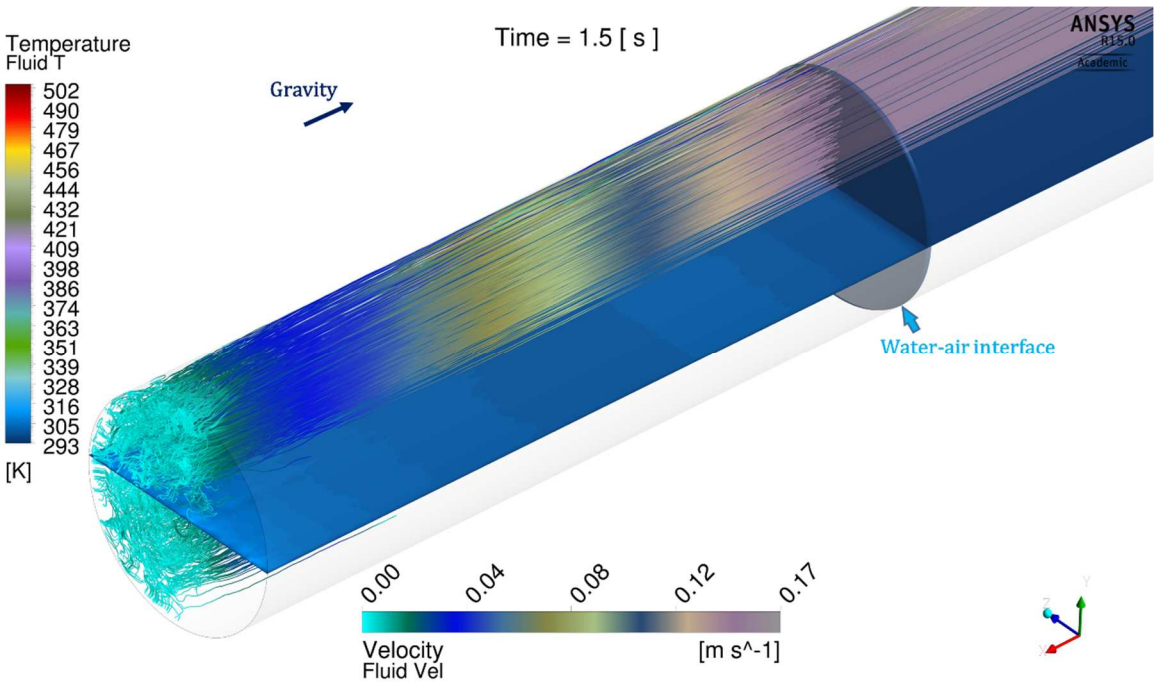

Fig.6.32 Fluid temperature and streamlines of non-uniform plastic matrix, t=1.5s

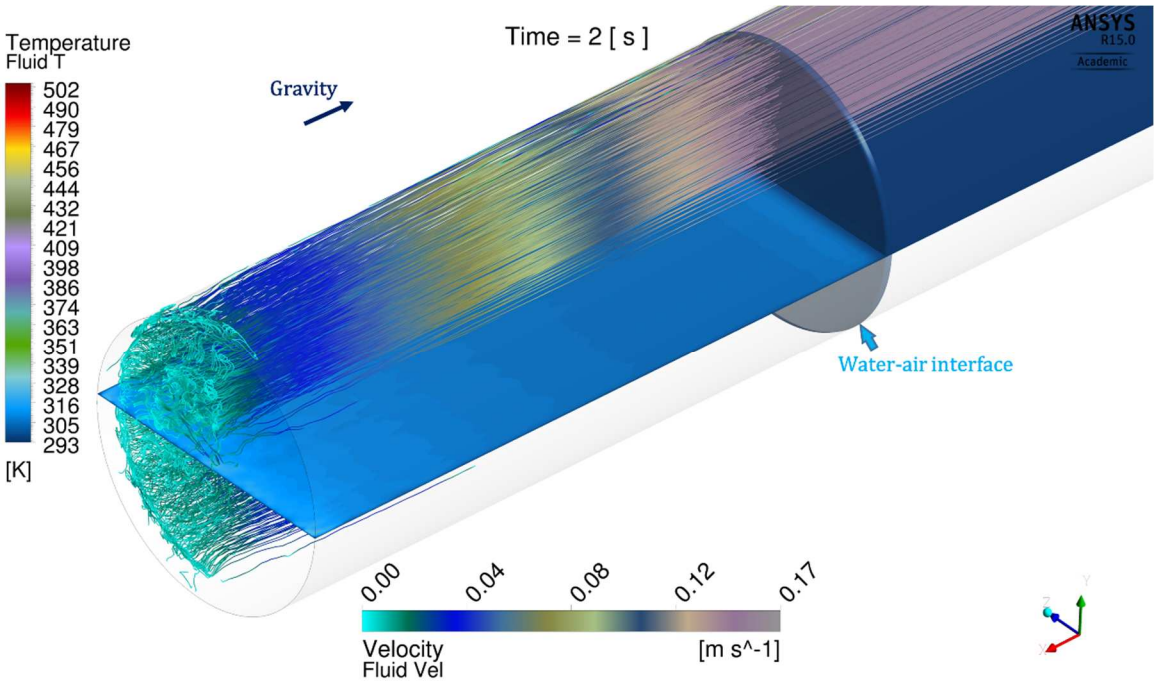

Fig.6.33 Fluid temperature and streamlines of non-uniform plastic matrix, t=2s

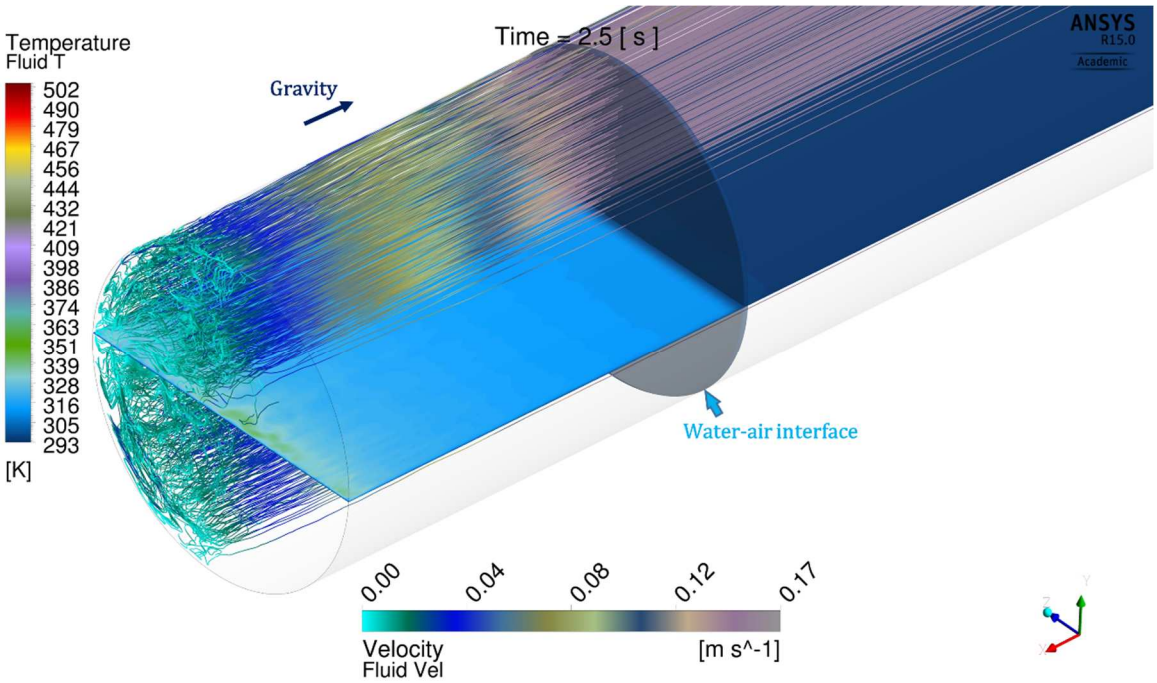

Fig.6.34 Fluid temperature and streamlines of non-uniform plastic matrix, t=2.5s

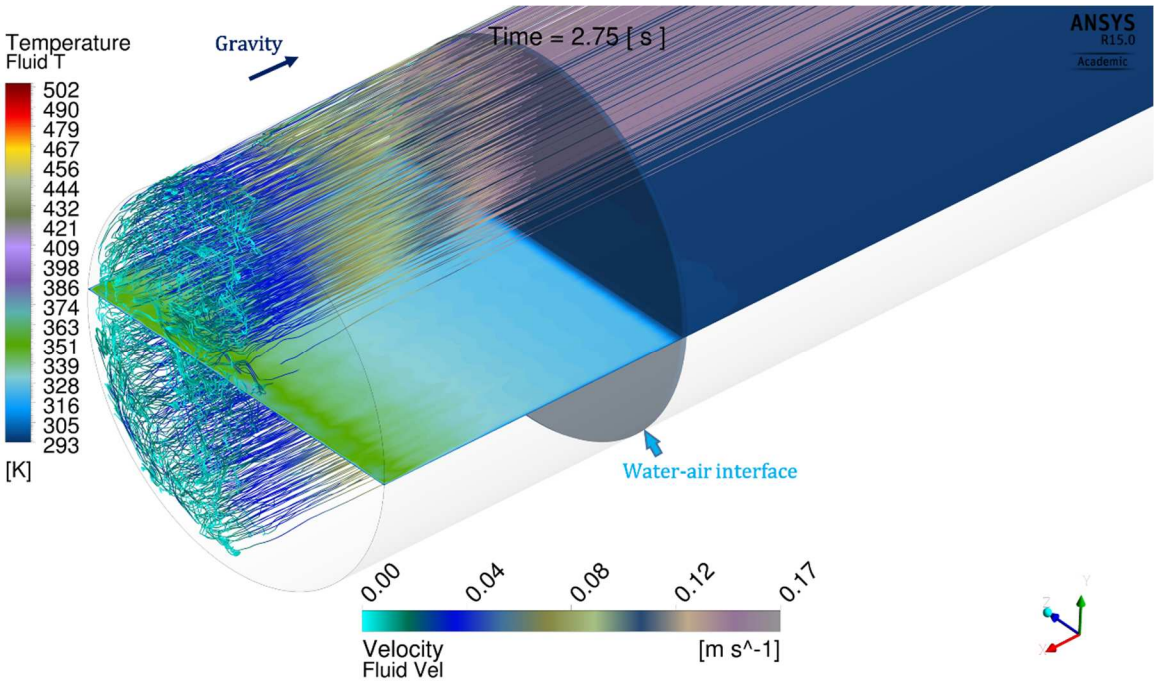

Fig.6.35 Fluid temperature and streamlines of non-uniform plastic matrix, t=2.75s

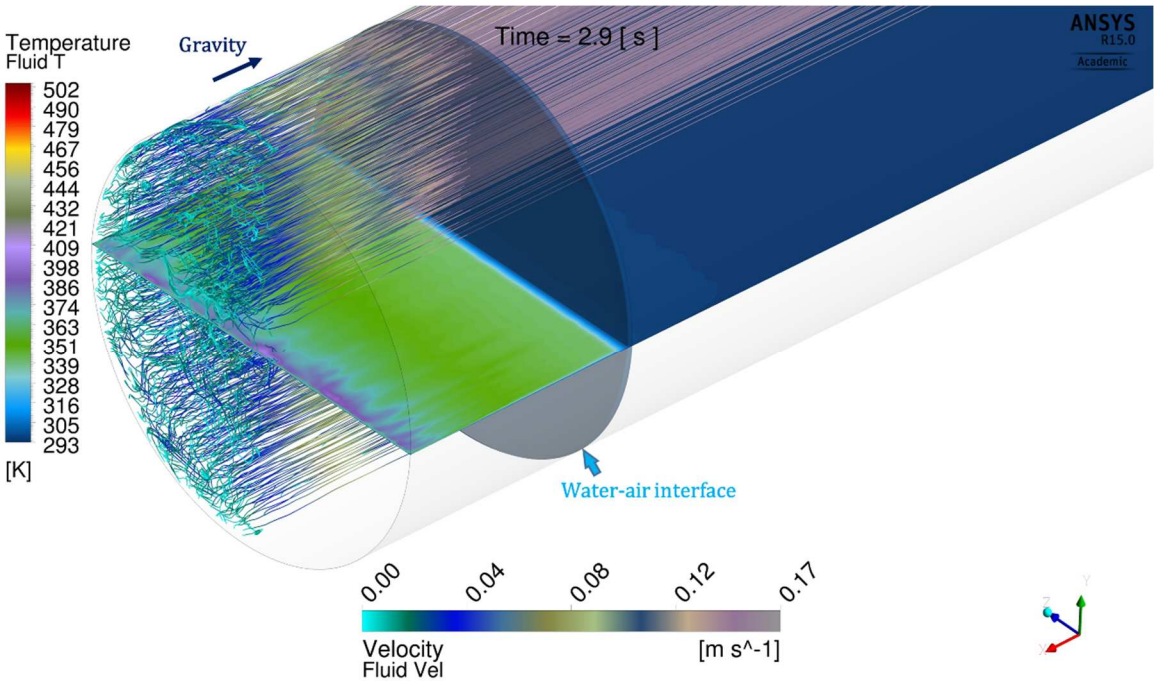

Fig.6.36 Fluid temperature and streamlines of non-uniform plastic matrix, t=2.9s

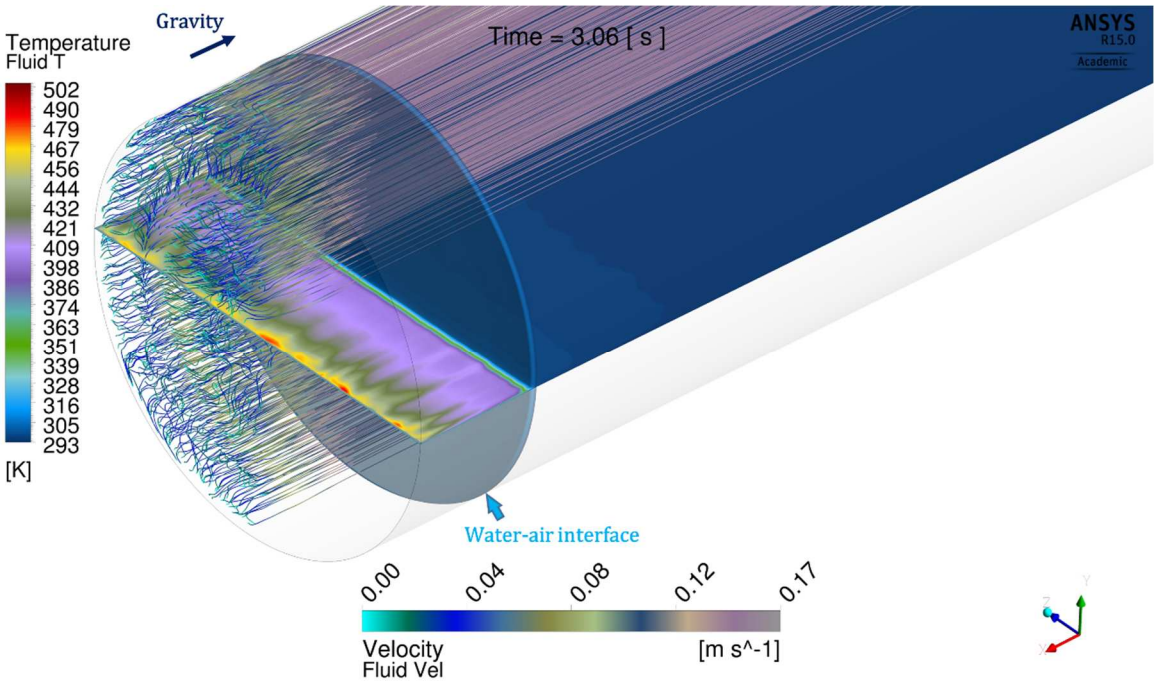

Fig.6.37 Fluid temperature and streamlines of non-uniform plastic matrix, t=3.06s

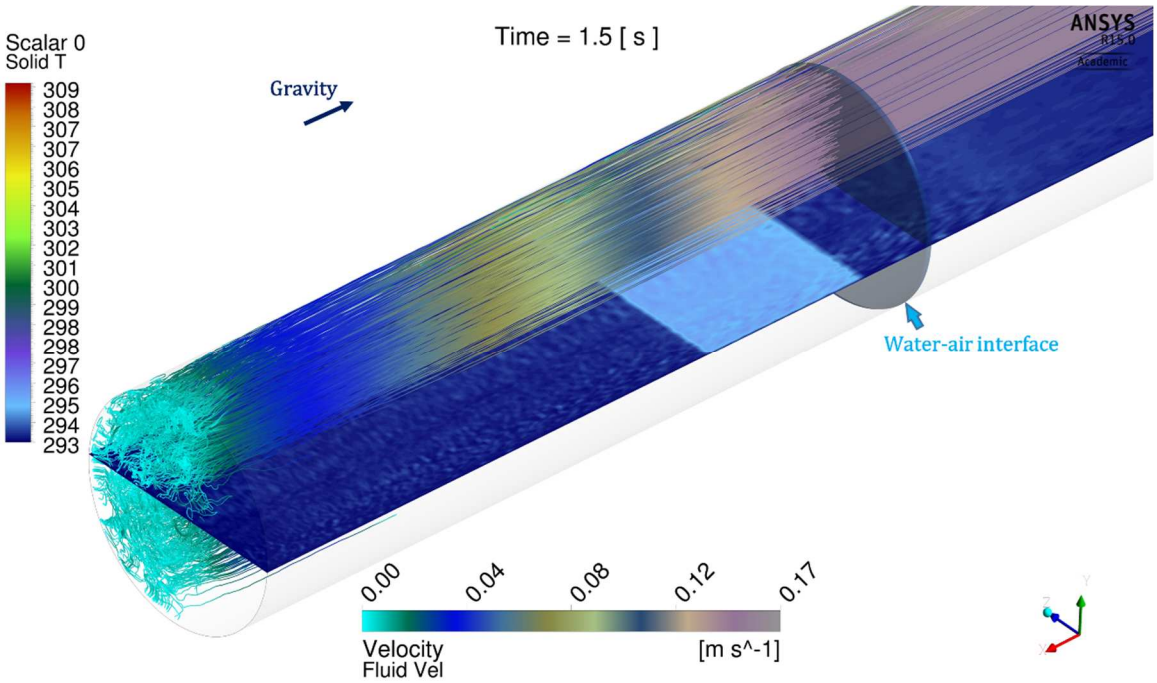

Fig.6.38 Solid temperature and streamlines of non-uniform plastic matrix, t=1.5s

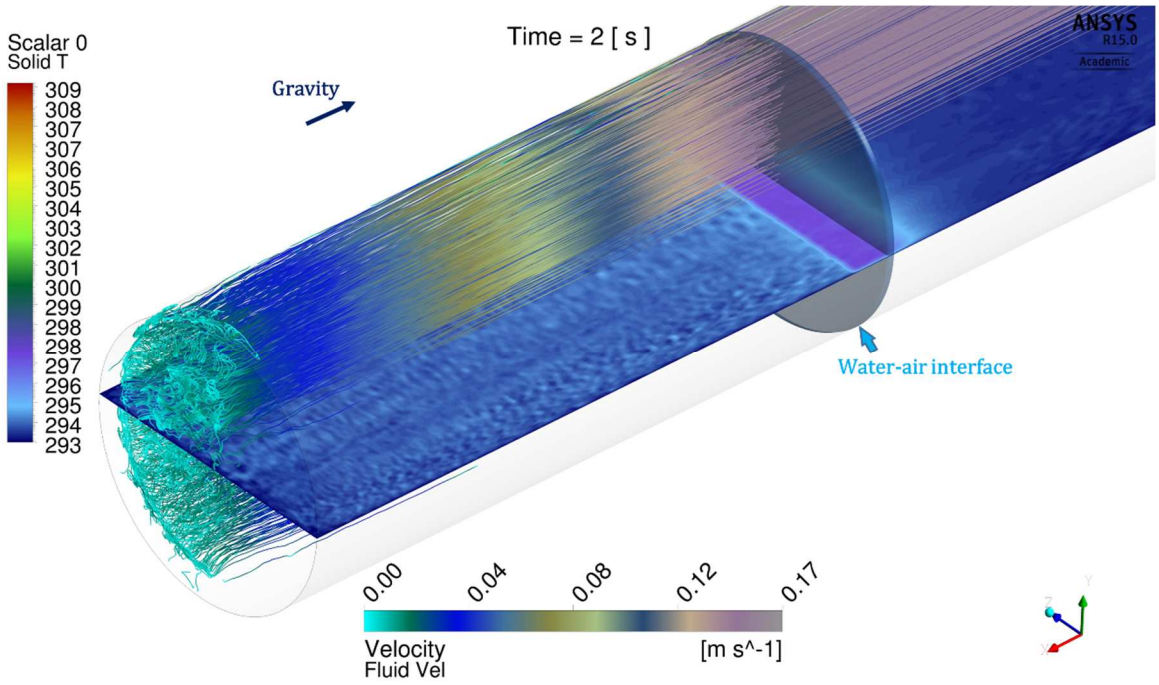

Fig.6.39 Solid temperature and streamlines of non-uniform plastic matrix, t=2s

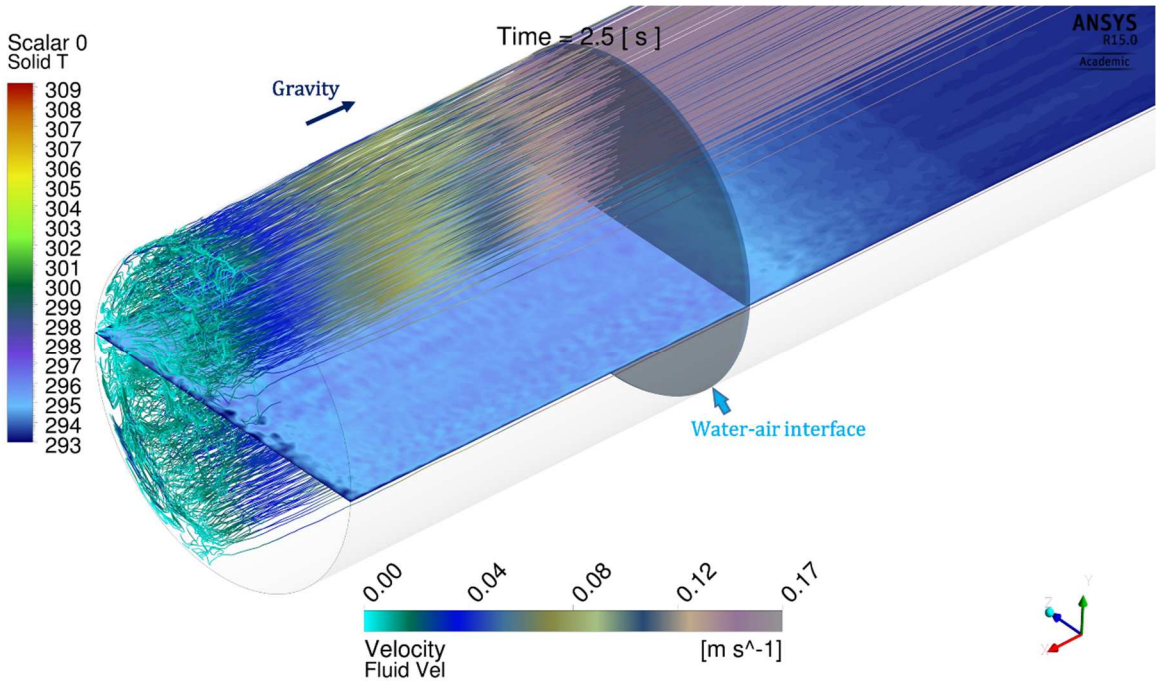

Fig.6.40 Solid temperature and streamlines of non-uniform plastic matrix, t=2.5s

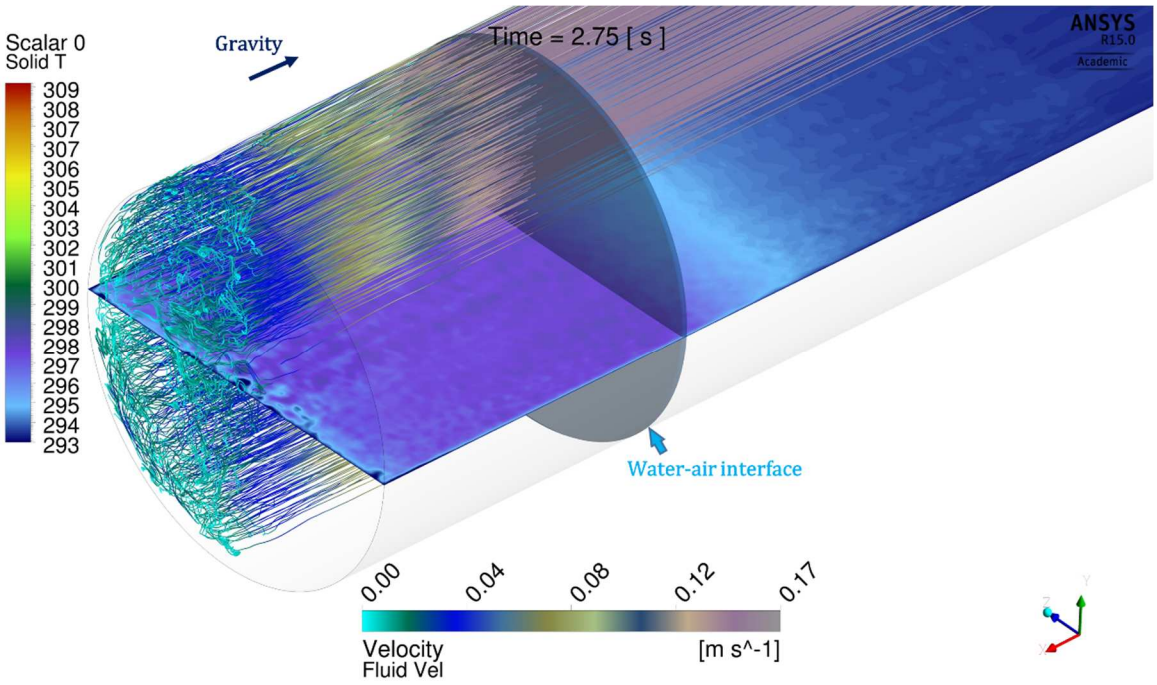

Fig.6.41 Solid temperature and streamlines of non-uniform plastic matrix, t=2.75s

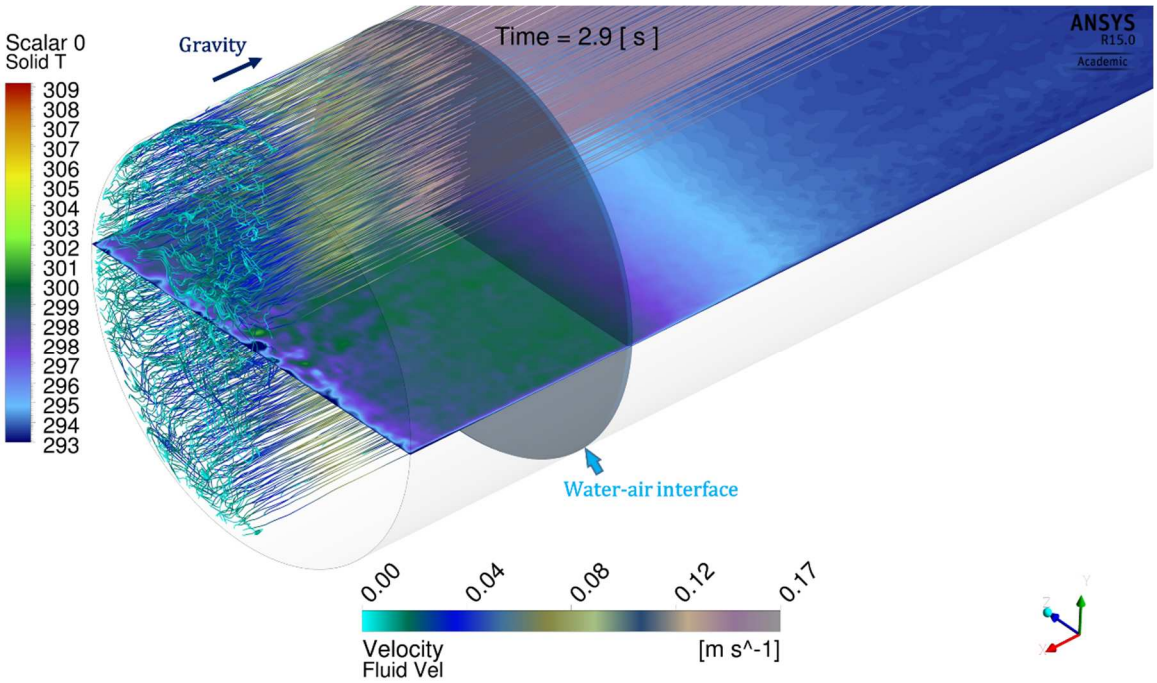

Fig.6.42 Solid temperature and streamlines of non-uniform plastic matrix, t=2.9s

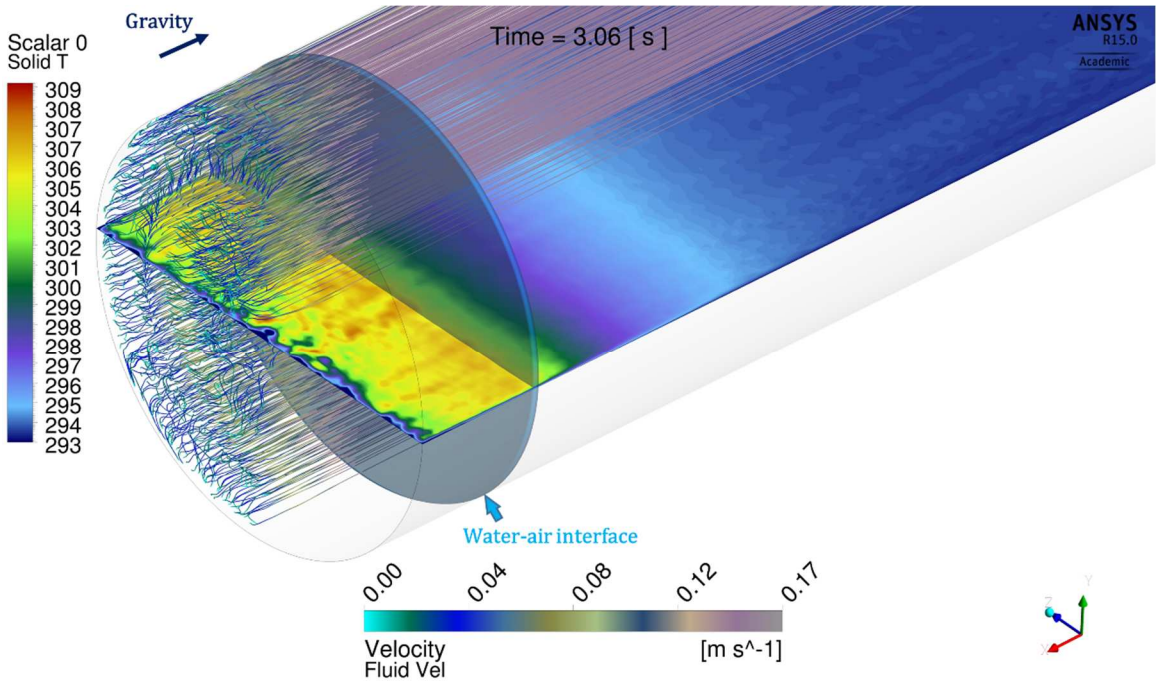

Fig.6.43 Solid temperature and streamlines of non-uniform plastic matrix, t=3.06s

6.6. Comparison to Experiments

For validation, two of the 3-D CFD simulations are compared to liquid piston compression experiments conducted at the University of Minnesota [86]. In the experiment, the compressor chamber is made of a steel cylinder to sustain pressure up to 210bar; water is pumped into the chamber from the bottom. Three-D printed, plastic interrupted plate matrices are inserted in the chamber. A picture of the chamber is shown in Fig.6.44. The instantaneous gas pressure and volume during compression are measured. The pressure is measured by the pressure transducer installed on the top cap of the chamber. The instantaneous gas volume is obtained by measuring the displacement of the piston that pumps water into the compressor using an encoder (not shown in Fig.6.44). Although a thermocouple was installed on the top cap, it was used only for measuring the initial temperature and the final equilibrium temperature, instead of the transient gas temperature.

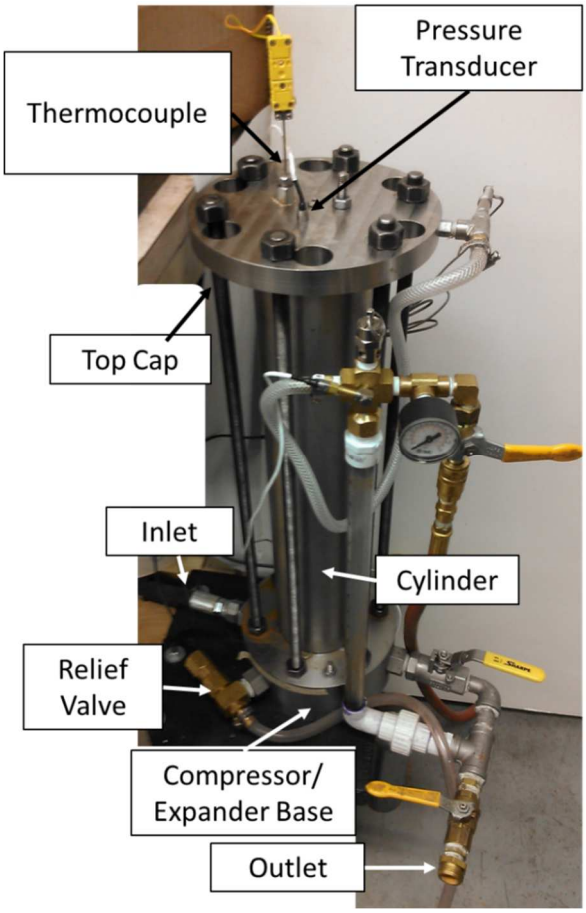

Fig.6.44 A picture of the experimental liquid piston compressor chamber (picture taken from [86])

In [85], results of experimental runs for compression processes at different speeds are compared by normalizing the instantaneous pressure and volume data with respect to their initial values. Data taken from [86] are compared with two CFD simulation runs: no-insert case (sections 6.2), and uniform distributed exchanger (section 6.3). In the CFD simulations, the flow rates for the no-insert and uniform insert cases are, respectively: 684cc/s and 570cc/s. They are compared with experimental runs of a no-insert case with a 600cc/s flow rate and a uniform insert case with a 500cc/s flow rate. The initial gas volumes in the CFD runs and in the experiments are also slightly different. For the no-insert case, the initial gas volumes in the CFD simulation and in the experiment are, respectively,

2201cc and 2228cc. For the uniform insert case, the initial gas volumes in the CFD simulation and in the experiment are, respectively, 1834cc and 1591cc. The CFD and experimental results are compared by normalizing instantaneous pressure and volume with respect to their corresponding initial values, shown in Fig.6.45. Overall agreement is found between CFD and experiments. One main uncertainty in the experiment is a decreased piston velocity near the end of the compression. As shown in Fig.6.46 taken from [86], for an experimental run targeting at 600cc/s constant flow rate, the actual flow rate drops significantly once pressure is over 100bar (or when the dimensionless pressure is over 14). This explains the discrepancy in Fig.6.45 between CFD and experiment at high pressure values, as CFD always has a constant flow rate throughout the entire compression process. For the uniform insert case, the CFD simulation is done based on a porous media modeling approach which couples the energy transport in the fluids and solid through the developed heat transfer correlations. The agreement between the experiments and CFD indicates that the heat transfer correlations developed in Chapter 4 can well characterize featrues of the interrupted plate exchanger when applied to liquid piston compression.

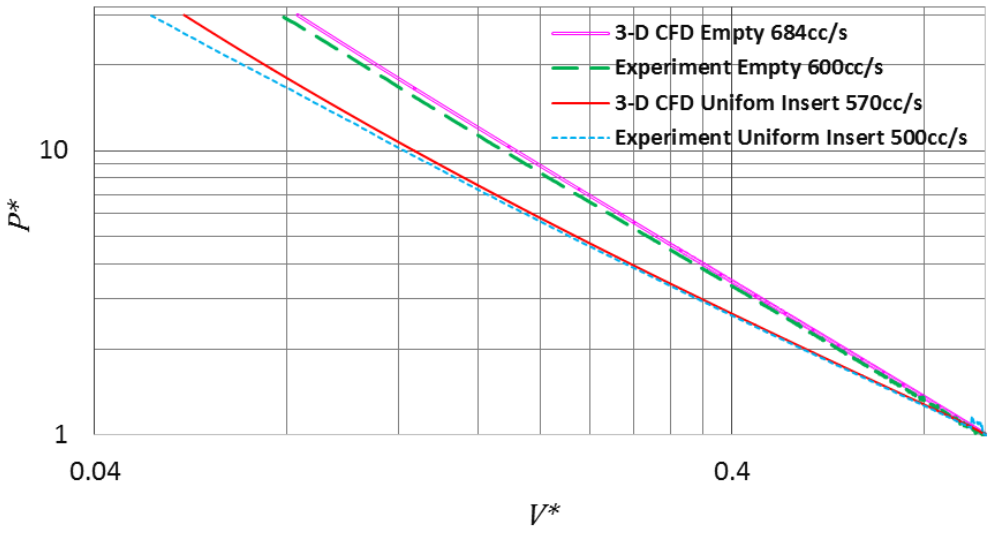

Fig.6.45 Comparison of 3-D CFD simulation results to experimental data (experimental data taken from [86])

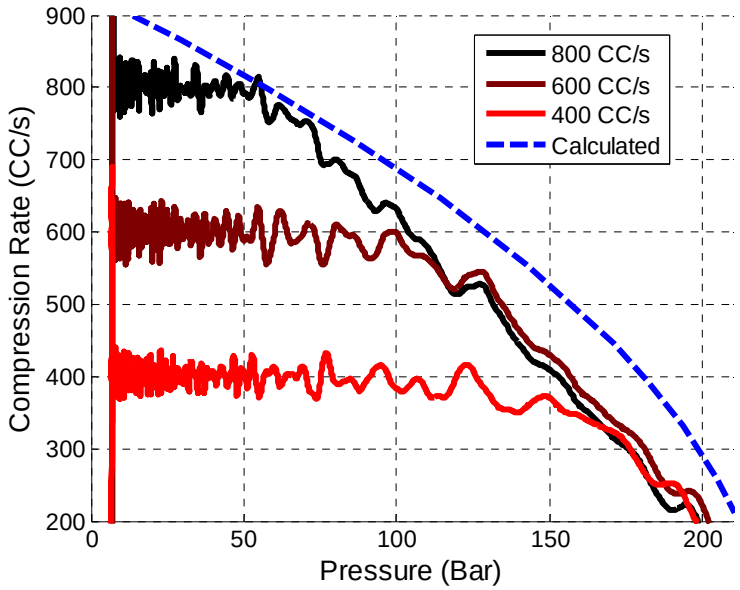

Fig.6.46 Actual compression volume flow rates in the experiment (taken from [86])

6.7. Summary

Three-D CFD simulations have been done for four cases, no-insert, uniform plastic and metal matrices, and an optimal plastic matrix. During compression, the work input to the compressor (from the pump) depends on the instantaneous thermodynamic pressure rise of air and the pressure drop across the matrix insert. The pressure at the liquid piston inlet represents the sum of these two pressure resistances. For the four cases, the inlet pressure are compared and shown in Fig.6.47. The pressure rise is most rapid with the case where no heat exchanger matrix is used. For the cases utilizing exchanger matrices, the one with the optimal matrix has the smallest slope of pressure vs. time, indicating less compression work is required.

The average air temperature at the end of compression and the compression efficiency are calculated for each case. The numerical values are listed in Table 6.1 and comparisons

are shown in Fig.6.48. For reference, the storage power values are also calculated and given in Table 6.1. Overall, the interrupted-plate heat exchanger matrices can significantly reduce the temperature rise of compressed air. Using metal (steel) as the material for the complete matrix only provides small improvement in the thermal performance: the overall temperature rise is reduced by less than 10K with the complete metal matrix. This is because convective heat transfer depends on the shape of the matrix, and for the same shape, plastic already has a sufficiently large thermal capacity for absorbing heat from the hot air. The result also shows that using an optimal shaped matrix made with plastic has superior thermal performance to the uniform metal exchanger matrix. The final air temperature of the optimal shape exchanger case is 36K lower than that of the uniform steel exchanger case. Plastic exchanger matrices also has lower cost than metal matrices.

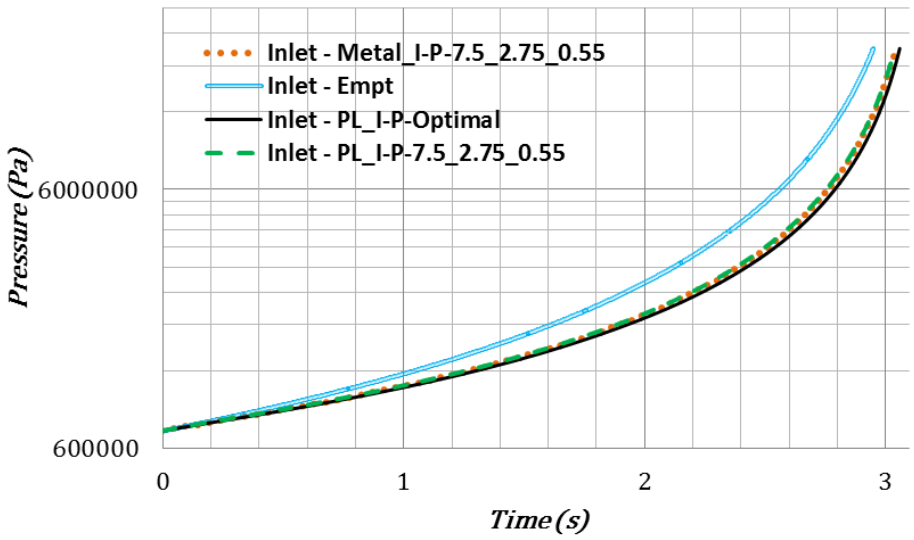

Fig.6.47 Inlet pressure vs. time for different exchangers and no-exchanger chamber

Table 6.1 Final air temperature and efficiency for different cases

	T_f (K)	η	Storage power (W)
No-insert	703.6	0.437	1182
PL_I-P-7.5_2.75_0.55	459.7	0.617	1147
Metal_I-P-7.5_2.75_0.55	450.3	0.628	1145
PL_I-P-Optimal	414.2	0.654	1139

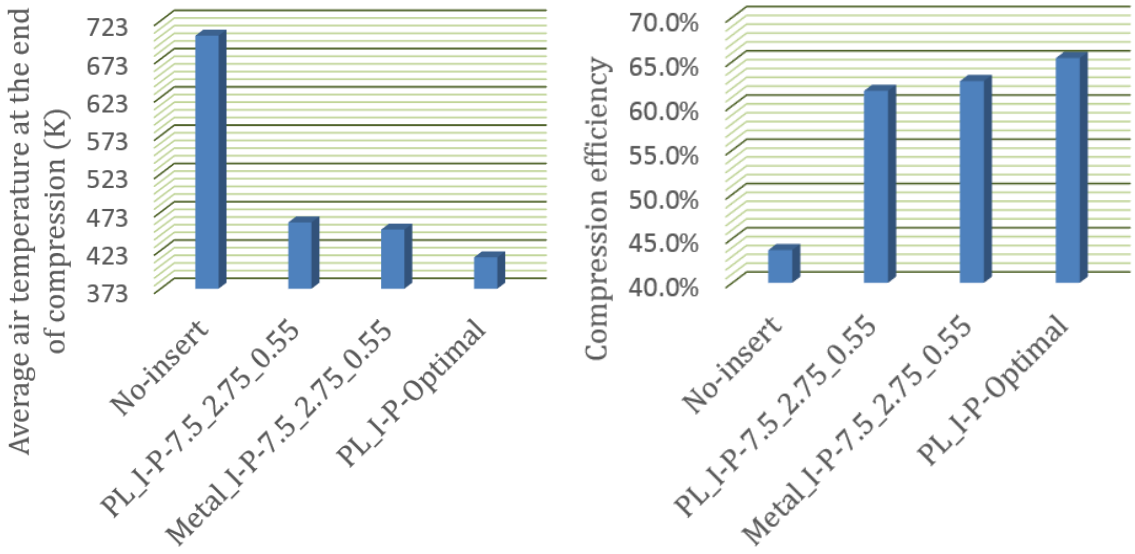

Fig.6.48 Comparisons of final air temperature and compression efficiency among different 3-D simulations

Chapter 7: Conclusions

The present research has developed and utilized simulation tools to understand the physics of fluid flow in a liquid-piston compressor, and provided insight into design. CFD simulations show high temperature rise during compression of air when no heat transfer elements are used. Heat exchanger matrices are thus applied. Two types of exchangers have been investigated in detail, the metal foam and interrupted-plate matrices. As such, numerical models that characterize the heat transfer and pressure drop of the exchangers are established, and enhanced heat transfer processes for application to Compressed Air Energy Storage (CAES) are found.

Metal foam matrices (10PPI and 40PPI) are commercially available. They represent isotropic porous media. Flow resistance models based on the Darcian and inertial terms are developed by taking pressure drop measurements of flow through metal foam blocks. A heat transfer correlation is confirmed by using a 0-D numerical model to quickly evaluate different porous media heat transfer correlations in the literature and compare results to the measured instantaneous pressure and volume data during liquid piston compression. Using the hydro-thermal models, global scale CFD simulations on the liquid piston chamber inserted with metal foam matrices are conducted. The results show that the metal foam effectively suppresses temperature rise during compression. The flow field is affected by the layout of the metal foam as secondary flows are eliminated in regions where the foam is inserted. The CFD method of modeling metal foam inserts in the liquid piston compressor has also been combined with a design exploration to study the effects of varying the profile of cross-sectional diameter along the chamber's axial direction. The analysis shows that when the chamber is longer and has steeper changes in the cross-sectional diameter, the flow is more agitated and, thus, better heat transfer results.

The second type of exchanger studied in detail is a high-efficiency, low pressure drop, and anisotropic interrupted-plate medium. It features plates stacked in an interrupted fashion and offers flexibility to design the shape. The hydro-thermal models that characterize the heat transfer and pressure drop are developed through large numbers of

numerical simulations focusing on the REV (or unit cell) models of the matrices. Two characteristic lengths have been used in the dimensionless groups for developing the heat transfer correlations. The use of the hydraulic diameter treats the exchanger matrix as flow channels while the use of the characteristic pore size treats the matrix as a porous medium providing a volumetric heat transfer rate. Models based on both characteristic lengths are developed and validated. The simulation results show that Nusselt number typically increases with Reynolds number. However, when different shapes of the exchanger REV models are investigated, the Nusselt number values scatter at the same Reynolds number, indicating that a second parameter representing the shape's effect on heat transfer is necessary. This parameter is proposed to be the ratio of the plate height over separation distance, $\frac{\ell}{2\mathscr{b}}$. For a Reynolds number less than 10,000, a small increase in the Nusselt number is observed while $\frac{\ell}{2\mathscr{b}}$ increases from 0.8 to 6; for a relatively large Reynolds number, the Nusselt number increases rapidly as $\frac{\ell}{2\mathscr{b}}$ increases from 0.8 to 3.5. Numerical visualizations also show that for a large Reynolds number, when $\frac{\ell}{2\mathscr{b}}$ is 2.73, the flow is more agitated than the cases when the $\frac{\ell}{2\mathscr{b}}$ values are 0.833 and 6. By varying the mean flow angles in CFD simulations of the unit cell, anisotropic hydro-thermal characterization of the interrupted-plate matrix has also been completed. The CFD results show that although the mean flow points at a certain direction, the pore-scale flows tend to avoid direct impingement on the plates, thus run in different directions, leading to strong mixing effects, which are beneficial for heat transfer. Traditionally, the Darcian and inertial terms are used in the modeling of the anisotropic pressure drop. Proposed in the present study is an additional term that captures flow mixing and separation effects at off-axial directions. Evaluation of the RMS values shows that the addition of this term provides an improved accuracy over a model based only on the Darcian and inertial terms. Anisotropic heat transfer models are developed from the REV simulations and a maximum heat transfer is achieved when the flow attacks the plates with an angle of around 34°. A design for the

next-generation exchanger matrix has been proposed wherein the plates are tilted to misalign from the chamber's axis.

Using the detailed hydro-thermal models developed from CFD simulations, design analyses on the shape of the heat exchanger matrix have been done to further improve the performance of the heat exchanger. A simplified 1-D numerical model is developed that requires much less computational resources, and is capable of providing fast and accurate solutions of axial temperature distributions in the liquid piston chamber with heat exchanger inserts. Using the 1-D model, the porous medium shape distributions in the liquid-piston compressor chambers are analyzed. The optimum distribution based on the design analysis presented herein shows that coarse features are favored in the lower portion of the chamber and fine features are favored in the upper region of the chamber. This is the result of balancing among the trade-offs between pressure drop and heat transfer. In general, depending on the final pressure ratio, using an exchanger matrix can improve the CAES compression efficiency by 20 to 40%, and using an optimum design of the exchanger can improve the efficiency by another 1 to 4%. A further development of the 1-D model incorporates a sub-2-D model that calculates heat conduction in the lateral direction across a heat exchanger plate. The results show that for metal heat exchangers, the instantaneous surface temperature of the plate is very close to its core temperature. For plastic exchangers, the surface temperature is higher than the core temperature, yet not substantial to damage the exchanger surface. Plastic exchangers are shown to be sufficient as a result of its high heat capacitance compared to that of air.

Detailed 3-D simulations on the liquid piston chambers are completed to investigate the performance of no-insert chambers and chambers with interrupted-plate matrices of uniform and optimum distributions. CFD simulations on the REV models have provided detailed flow resistance and heat transfer correlations, which are incorporated into a set of volume-averaged transport equations that treats the porous region as a continuum in the 3-D simulations. The simulation results show detailed flow fields in the chamber during compression, and proved the effectiveness of using the exchanger matrices. A vortex ring is formed in the gas space when no insert is present, whereas the gas flow is straightened

when exchanger matrices are present. Without any heat transfer medium, the final gas temperature after compression is 704K. A uniform, plastic matrix results in a reduction of 244K in the final gas temperature. A uniform, metal matrix further reduces the final temperature by only 10K, whereas an optimum-shaped, plastic exchanger matrix reduces it by 46K. This comparison shows the importance of designing the heat exchanger shape to provide effective heat transfer in regions that demand most amount of heat transfer and to reduce the pressure drop in the other regions.

Preliminary investigations on the compression/expansion piston trajectories have been done. An improvement in efficiency is achieved if a fast-slow-fast piston trajectory is adopted for compression. Further detailed optimization may be done to obtain better efficiency improvements. Simulations on expansion processes indicate that, when the chamber is inserted with an exchanger matrix, a faster piston speed is favored in the beginning of the expansion, whereas, when the chamber is not inserted with a matrix, a slower piston speed is favored at the beginning.

Using the numerical tools, several design concepts have been investigated in this study, including varying the chamber's cross-sectional shape profile, designing a non-uniformly shaped exchanger matrix, and tilting the plates of the exchanger matrix. An ultimate liquid piston may be built combining all these concepts. If manufacturing cost can be justified, a gourd-like chamber shape can be applied. In general, the chamber should be long, having a varying cross-sectional diameter, with a maximum diameter in the middle of the axis and a minimum on the top. In the chamber, interrupted-plate matrices must be used. In the present research, investigations have been done, separately, on tilting the plates of a matrix with a uniform shape distribution, and on varying the shape distribution of straight plates. They result in similar performance improvements for the same pressure compression ratios. In the ultimate design, the two can be combined: the plates can be tilted, and also have coarse dimensional features in the lower region of the chamber and fine features in the upper region. Further studies may be done to conduct a detailed optimization including all the aforementioned aspects, as well as the piston trajectory control.

The following fundamental areas may also be investigated in future research:

(1) Although preliminary simulations on the no-insert chambers show that condensation and evaporation have little effects on the overall gas temperature or efficiency, the interaction of the condensed water droplets with air and with the exchanger surfaces and the forming of water films on theses surfaces during high pressure conditions are complex phenomena, and detailed studies are required to fully understand them.

(2) Observations on the liquid piston experiments show that sometimes water tends to be trapped in the exchanger matrix; preliminary analysis shows that three types of trapping mechanisms may be present, trapping at the junctions of the plates, as a film on the surface, and bridging between plates. Fully understanding these phenomena requires experiments to characterize the surface properties and also to investigate the effects of the shape and pore size on the trapping of water.

Reference

[1] P. Sullivan, W. Short and N. Blari, "Modeling the Benefits of Storage Technologies to Wind Power," in *AWEA Wind Power 2008 Conference*, Houston, TX, June 2008.

[2] F. Crotogino, K. Mohmeyer and R. Scharf, "Huntorf CAES: More than 20 Years of Successful Operation," Orlando, FL, Apr. 2001.

[3] "History of First U.S. Compressed-Air Energy Storage (CAES) Plant (110 MW 26h): Volume 2: Construction," Electric Power Research Institute, May 1994.

[4] M. Nakahamkin, M. Chiruvolu, M. Patel, S. Byrd and R. Schainker, "Second Generation of CAES Technology – Performance, Operations, Economics, Renewable Load Management, Green Energy," in *PowerGen International Conference*, Las Vegas, NV, Dec 2009.

[5] P. Y. Li, J. Van de Ven and C. Sancken, "Open Accumulator Concept for Compact Fluid Power Energy Storage," in *2007 International Mechanical Engineering Congress and Exposition*, 2007.

[6] J. Van de Ven and P. Y. Li, "Liquid Piston Gas Compression," *Applied Energy,* vol. 86, no. 10, pp. 2183-2919, 2009.

[7] "U. S. Offshore Wind Energy: A Path Forward," U. S. Offshore Wind Collaborative, Oct. 2009.

[8] P. Y. Li, E. Loth, T. W. Simon, J. D. Van de Ven and S. E. Crane, "Compressed Air Energy Storage for Offshore wind Turbines," in *2011 International Fluid Power Exhibition*, Las Vegas, NV, Mar. 2011.

[9] B. Yan, J. Wieberdink, F. Shirazi, P. Y. Li, T. W. Simon and J. D. Van de Ven, "Experimental Sutdy of Heat Transfer Enhancement in a Liquid Piston Compressor/Expander Using Porous Media Inserts," *Applied Energy,* vol. 154, pp. 40-50, 2015.

[10] A. Rice, "Heat Transfer Enhancement in a Cylindrical Compression Chamber by Way of Porous Inserts and the Optimization of Compression and Expansion Trajectories for Varing Heat Transfer Capabilities," in *M.S. Thesis*, Minneapolis, University of Minnesota, June, 2011, p. 66.

[11] R. J. Tabaczynski, D. P. Hoult and J. C. Keck, "High Reynolds Number Flow in a Moving Corner," *Journal of Fluid Mechanics,* vol. 42, pp. 249-255, 1970.

[12] M. Niikanjam and R. Greif, "Heat Transfer during Piston Compression," *Journal of Heat Transfer,* vol. 100, pp. 527-530, 1978.

[13] R. Grief, T. Namba and M. Nikanjam, "Heat Transfer during Piston Compression Inclusing Side Wall and Convective Effects," *International Journal of Heat and Mass Transfer*, vol. 22, pp. 901-907, 1978.

[14] J. Polman, "Heat Transfer in a Piston-Cylinder System," *International Journal of Heat and Mass Transfer,* pp. 184-187, 1980.

[15] D. R. Buttsworth, "Heat Transfer during Transient Compression: Measurements and Simulations," *Shock Waves,* vol. 12, no. 1, pp. 87-91, 2002.

[16] G. F. Hohenberg, "Advanced Approaches for Heat Transfer Calculations," *Diesel Enginer Thermal Load,* pp. 61-79, 1979.

[17] A. G. Catto and A. T. Prata, "A Numerical Study of Instantaneous Heat Transfer During Compression and Expansion in Piston-Cylinder Geometry," *Numerical Heat Transfer, Part A,* vol. 38, pp. 281-303, 2000.

[18] A. Mohammadi, M. Yaghoubi and M. Rashidi, "Analysis of Local Convective Heat Transfer in a Spark Ignition Engine," *International Communications in Heat and Mass Transfer,* vol. 35, pp. 215-224, 2008.

[19] E. L. Pereira, C. J. Deschamps and F. A. Ribas, "Numerical Analysis of Heat Transfer inside the Cylinder of Reciprocating Compressors in the Presence of Suction and Discharge Processes," in *International Compressor Engineering Conference at Purdue,* West Lafayette, IN, 2010.

[20] Y. Li and S. Kong, "Coupling Conjugate Heat Transfer with in-Cylinder Combustion Modeling for Engine Simulation," *International Journal of Heat and Mass Transfer,* vol. 54, pp. 2467-2478, 2011.

[21] U. Lekic and B. W. Kok, "Heat Transfer and Fluid Flows in Gas Springs," *The Open Thermodynamics Journal,* vol. 4, pp. 13-26, 2010.

[22] W. Hirt and B. D. Nichols, "Volume of Fluid (VOF) Method for Dynamics of Free Boundaries," *Journal of Computational Physics,* vol. 39, pp. 201-225, 1981.

[23] M. Isshii, Thermo-Fluid Dynamic Theory of Two-Phase Flow, Paris: Eyrolles, 1975.

[24] S. Osher and J. A. Sethian, "Fronts Propagating with Curvature-Dependent Speed: Algorithms Based on Hamilton-Jacobi Formulations," *Journal of Computational Physics,* vol. 79, pp. 12-49, 1988.

[25] W. H. Lee , "A Pressure Iteration Scheme for Two-Phase Modeling," *Technical Report LA-UR 79-975. Los Alamos Scientific Lab,* 1979.

[26] J. C. Slattery, "Single-Phase Flow through Porous Media," *AIChE Journal,* vol. 15, pp. 866-872, 1969.

[27] W. G. Gray and K. O'Neill, "On the General Equations for Flow in Porous Media and Reduction to Darcy's Law," *Water Resources Research,* vol. 12, no. 2, 1976.

[28] K. Vafai and C. L. Tien, "Boundary and Inertial Effects on Flow and Heat Trasnfer in Porous Media," *International Journal of Heat and Mass Transfer,* vol. 24, pp. 195-203, 1981.

[29] K. Vafai, "Convective Flow and Heat Transfer in Variale Porosity Media," *Journal of Fluid Mechanics,* vol. 147, pp. 233-259, 1984.

[30] C. T. Hsu, "Dynamic Modeling of Convective Heat Transfer in Porous Media," in *Handbook of Porous Media (2nd Edition),* Taylor and Fracis Group, 2000, pp. 39-80.

[31] C. T. Hsu, "On Pressure-Velocity Correlation of Steady and Oscillating Flows in Regenerators Made of Wire Screens," *Transactions of the ASME,* vol. 121, pp. 52-56, Mar. 1999.

[32] M. Sozen and T. Kuzay, "Enhanced Heat Transfer in Round Tubes with Porous Inserts," *International Journal of Heat and Fluid Flow,* vol. 17, pp. 124-129, 1996.

[33] E. Sozer and W. Shyy, "Modeling of Fluid Dynamics and Heat Transfer through Porous Media for Liquid Rocket Propulsion," in *Transactions of the 43rd AIAA/ASME/SAE/ASEE Joint Propulsion Conference & Exhibit*, July 2007.

[34] N. Zahi, A. Boughamoura, H. Dhahri and S. B. Nasrallah, "Flow and Heat Transfer in a Cylinder with a Porous Insert along the Compression Stroke," *Journal o Porous Media,* vol. 11, no. 2008, pp. 525-540, 2008.

[35] Z. F. Huang, A. Nakayama, K. Yang, C. Yang and W. Liu, "Enhancing Heat Transfer in the Core Flow by Using Porous Medium Insert in a Tube," *International Journal of Heat and Mass Transfer,* vol. 53, pp. 1164-1174, 2010.

[36] W. Lu, C. Y. Zhao and S. A. Tassou, "Thermal Analysis on Metal-Foam Filled Heat Exchangers. Part I: Metal-Foam Filled Pipes," *International Journal of Heat and Mass Transfer,* vol. 49, pp. 2751-2761, 2006.

[37] M. B. Saito and M. J.S. de Lemos, "Laminar Heat Transfer in a Porous Channel Simulated with a Two-Energy Equation Model," *International Communications in Heat and Mass Transfer,* vol. 36, pp. 1002-1007, 2009.

[38] Y. P. Du, Z. G. Qu, C. Y. Zhao and W. Q. Tao, "Numerical Study of Conjugated Heat Transfer in Metal Foam Filled Double-Pipe," *International Journal of Heat and Mass Transfer* , vol. 53, pp. 4899-4907, 2010.

[39] C. Xu, Z. Song, L. Chen and Y. Zhen, "Numerical Investigation on Porous Media Heat Transfer in a Solar Tower Receiver," *Renewable Energy,* vol. 36, pp. 1138-1144, 2011.

[40] F. Kuwahara, F. Nakayama and H. Koyama, "A Numerical Sutudy of Thermal Dispersion in Porous Media," *Journal of Heat Transfer,* vol. 118, pp. 756-761, 1996.

[41] N. Wakao and S. Kaguei, Heat and Mass Transfer in Packed Beds, New York: Gorden and Breach, 1982.

[42] F. Kuwahara, M. Shirota and A. Nakayama, "A Numerical Study of Interfacial Convective Heat Transfer Coefficient in Two-Energy Equation MOdel for Convection in Porous Media," *Internaltional Journal of Heat and Mass Transfer,* vol. 44, pp. 1153-1159, 2001.

[43] A. A. Zukauskas, "Convective Heat transfer in Cross-Flow," in *Handbook of Single-Phase Convective Heat Transfer*, New York, Wiley, 1987.

[44] A. Nakayama, K. Ando, C. Yang, C. Sano, F. Kuwahara and J. Liu, "A Study on Interstitial Heat Transfer in Consolidated and Unconsolidated Porous Media," *Heat and Mass Transfer,* vol. 45, no. 11, pp. 1365-1372, 2009.

[45] K. Kamiuto and S. S. Yee, "Heat Transfer Correlations for Open-Cellular Porous Materials," *International Communications of Heat and Mass Transfer,* vol. 32, pp. 947-953, 2005.

[46] A. Nakayama, F. Kuwahara and T. Umemoto, "Heat and Fluid Flow within an Anisotropic Porous Medium," *Transactions of ASME,* vol. 124, pp. 746-753, Aug. 2002.

[47] F. L. Dullien, Porous Media: Fluid Transport and Pore Structure, Academic Press, 1979.

[48] A. Nakayama, F. Kuwahara and T. Hayashi, "Numerical Modeling for Three-Dimensional Heat and Flow through a Bank of Cylinder in Yaw," *Journal of Fluid Mechanics,* vol. 498, pp. 139-159, 2004.

[49] A. A. Alshare, P. J. Strykowski and T. W. Simon, "Modeling of Unsteady and Steady Fluid Flow, Heat Transfer, and Dispersion in Porous Media Using Unit Cell Scale," *International Journal of Heat and Mass Transfer,* vol. 53, pp. 2294-2310, 2010.

[50] A. A. Alshare, T. W. Simon and P. J. Strykowsky, "Simulations of Flow and Heat Transfer in a Serpentine Heat Exchanger Having Dispersed Resistance with Porous-Continuum and Continuum Models," *International Journal of Heat and Mass Transfer,* vol. 53, pp. 1088-1099, 2010.

[51] J. Willmott, "Digital Computer Simulation of a Thermal Regenerator," *International Journal of Heat and Mass Transfer,* vol. 7, pp. 1291-1302, 1964.

[52] F. W. Larsen, "Rapid Calculation of Temperature in a Regenerative Heat Exchager Haing Arbitrary Initial Solid and Entering Fluid Temperatures," *International Journal of Heat and Mass Transfer,* vol. 10, pp. 149-168, 1967.

[53] P. Razelos and M. K. Benjamin, "Computer Model of Thermal Regenerators with Variable Mass Flow Rates," *International Journal of Heat and Mass Transfer,* vol. 21, pp. 735-743, 1978.

[54] A. Hill and A. J. Willmott, "Accurate and Rapid Thermal Regenerator Calculations," *International Journal of Heat and Mass Transfer,* vol. 32, no. 3, pp. 465-476, 1989.

[55] J. W. Howse, G. A. Hansen, D. J. Cagliostro and K. R. Muske, "Solving a Thermal Regenerator Model Using Implicit Newton-Krylov Methods," *Numerical Heat Transfer, Part A,* vol. 38, pp. 23-44, 2000.

[56] H. Klein and G. Eigenberger, "Approximate Solutions for Metallic Regenerative Heat Exchangers," *International Journal of Heat and Mass Transfer,* vol. 44, pp. 3533-3563, 2001.

[57] M. Galle, D. W. Agar and O. Watzenberger, "Thermal N2O Decomposition in Regenerative Heat Exchanger Reactors," *Chemical Engineering Science,* vol. 56, pp. 1587-1959, 2001.

[58] G. F. Nellis and S. A. Klein, "Regenerative Heat Exchangers with Significant Entrained Fluid Heat Capacity," *International Journal of Heat and Mass Transfer,* vol. 49, pp. 329-340, 2006.

[59] A. A. Greco and A. Maiorino, "A Dimensionless Nemerical Analysis for the Optimization of an Active Magnetic Regenerative Refrigerant Cycle," *International Journal of Energy Research,* vol. 37, pp. 1475-1487, 2013.

[60] G. Kolios, D. Luss, R. Garg and G. Viswanathan, "Efficient Computation of Periodic State of Cyclic Fixed-Bed Process," *Chemical Engineering Science,* vol. 101, pp. 90-98, 2013.

[61] I. Ruhlich and H. Quack, "Inverstigations on Regenerative Heat Exchangers," in *Cryocoolers Part 4*, 2002, pp. 265-274.

[62] V. K. Cheeda, R. V. Kumar and G. Nagarajan, "Design and CFD Analysis of a Regenerator for a Turboshaft Helicopter Engine," *Aerospace Science and Engineering,* vol. 12, pp. 524-534, 2008.

[63] R. C. Tew, J. E. Cairelli, M. B. Ibrahim, T. W. Simon and D. Gedeon, "Overview of NASA Multi-Dimensional Stirling Convertor Code Development and Validation Effort," NASA/TM-2002-21997, Dec. 2002.

[64] R. Tew, M. Ibrahim, D. Danila, T. Simon, S. Mantell, L. Sun, D. Gedeon, K. Kelly, J. Mclean, G. Wood and S. Qiu, "A Microfabricated Involute-Foil Regenerator for Stirling Engines," NASA/TM-2007214973, 2007.

[65] R. Tew, M. Ibrahim, D. Danila, T. W. Simon, S. Mantell, L. Sum, D. Gedeon, K. Kelly, J. Mclean, G. Wood and S. Qiu, "A Microfabricated Involute-Foil Regenerator for Stirling Engines," *NASA/CR-2009-215516,* June 2009.

[66] L. Sun, T. W. Simon, S. C. Mantell, M. B. Ibrahim, D. Gedeon and R. Tew, "Thermo-fluid Experiments Supporting Microfabricated Regenerator Development for a Stirling Sapce Power Engine," in *7th International Energy Conversion Engineering Conference,* Denver, CO, Aug. 2009.

[67] R. I. Issa, "Solution of Implicit Discretized Fluid Flow Equations by Operator-Splitting," *Journal of Computational Physics,* vol. 62, pp. 40-65, 1986.

[68] S. V. Patankar, Numerical Heat Transfer and Fluid Flow, Washington, D.C.: Hemisphere, 1980.

[69] R. D. Rauch, J. T. Batira and N. Y. Yang, "Spatial Adaption Procedures on Unstractured Meshes for Accurate Unsteady Aerodynamic Flow Computations," Technical Report AIAA-91-1106, 1991.

[70] G. Soave, "Equilibrium Constant from a Modified Redlich-Kwong Equation of State," *Chemical Engineering Science,* vol. 27, pp. 1197-1203, 1972.

[71] R. H. Aunger, "A Fast, Accurate Real Gas Equation of State for Fluid Dynamics Analysis Applications," *Journal of FLuids Engineering,* vol. 117, pp. 277-281, 1995.

[72] "Air Properties," The Engineering ToolBox, [Online]. Available: http://www.engineeringtoolbox.com/air-properties-d_156.html. [Accessed Sep 2014].

[73] B. Yan, Compression/Expansion within a Cylindrical Chamber: Application of a Liquid Piston and Various Porous Inserts, M.S. Plan A Thesis. Department of Mechanical Engineering, University of Minnesota, 2013.

[74] C. Zhang, J. Wieberdink, F. Shirazi, B. Yan, T. W. Simon and P. Y. Li, "Numerical Investigation of Metal-Foam Filled Liquid Pistong Compressor Using a Two-Energy Equation Forumation Based on Experimentally Validated Models," in *Proceedings of the ASME International Mechanical Engineering Congress and Exposition*, San Diego, CA, Nov 2013.

[75] G. Taguchi, T. Yokoyama and Y. Wu, "Taguchi Methods: Design of Experiments," in *Quality Engineering Series, Vol. 4*, Tokyo, ASI Press, 1993.

[76] W. Xia, H. Y. Hsu and L. X. Kong, "A CFD-Aided Experimental Study on Bending of Micro Glass Pipettes," *Journal of Mechanical Science and Technology,* vol. 21, pp. 1338-1343, 2007.

[77] Q. Wang, Q. Chen and M. Zeng, "A CFD-Taguchi Combined Method for Numerical Investigation of Natural Convection Cooling Performance of Air-Core Reactor with Noise Reducing Cover," *Numerical Heat Transfer, Part A,* vol. 55, pp. 1116-1130, 2009.

[78] C. Zhang, J. H. Wieberdink, F. A. Shirazi, B. Yan, T. W. Simon and P. Y. Li, "Numerical Investigation of Metal-Foam Filled Liquid Piston Compressor Using a Two-Energy Equation Formulation Based on Experimentally Validated Models," in *ASME 2013 International Mechanical Engineering Congress and Exposition*, San Diego, CA, Nov. 2013.

[79] P. J. O'Rourke and F. V. Bracco, "Two Scaling Transformations for the Numerical Computation of Multidimensional Unsteady Laminar Flames," *Journal of Computational Physics,* vol. 33, no. 2, pp. 185-203, 1979.

[80] F. R. Menter, R. B. Langtry, S. R. Likki, Y. B. Suzen, P. G. Huang and S. Volker, "A Correlation Based Tansition Model Using Local Variables Part 1 - Model Formulation," *Journal of Turbomachinery,* vol. 128, pp. 413-422, July 2006.

[81] D. K. Lily, "A Proposed Modification of the Germano Subgrid-Scale Closure Model," *Physics of Fluids,* vol. 4, pp. 633-635, 1992.

[82] M. L. Shur, P. R. Spalart, M. K. Strelets and A. K. Travin, "A Hybrid RANS-LES Approach with Delayed DES and Wall-Modelled LES Capabilities," *International Journal of Heat and Fluid Flow,* vol. 29, no. 6, pp. 1638-11649, 2008.

[83] T. W. Simon and C. Zhang, "Plate Heat Exchanger". USA Patent Provisional Application for Patent, U11.12-0237, 2014.

[84] Y. S. Muzychka and M. M. Yovanovich, "Laminar Flow Friction and Heat Transfer in Non-Circular Ducts and Channels Part II- Thermal Problem," Compact Heat

Exchangers, A Festschrift on the 60th Birthday of Ramesh K. Shah, Grenoble, France, Aug. 2002.

[85] S. Ergun, "Fluid Flow through Packed Columns," *Chemical Engineering Progress*, vol. 48, pp. 89-94, 1952.

[86] J. H. Wieberdink, "Increasing Efficiency and Power Density of a Liquid Piston Air COmrpessor/Expander with Porous Media Heat Transfer Elements," University of Minnesota, M.S. Thesis, Minneapolis, MN, 2014.